

## Abstract

### Controlling Complex Light Propagation and Statistics

Nicholas Bender

2021

In this dissertation, a methodology for experimentally creating and controlling random light in free space and in diffusive media is presented.

In free space, we develop and demonstrate the ability to arbitrarily customize the intensity statistics and spatial-correlations of spatially-incoherent light. First, we present a general method for customizing the intensity statistics of speckle patterns on a target plane. Specifically, we show that by judiciously modulating the phase-front of a monochromatic laser beam, we can experimentally generate speckle patterns with arbitrarily-tailored intensity probability-density functions. Then, we experimentally demonstrate and theoretically develop a general method for creating fully-developed speckles with strong ‘non-local’ intensity correlations. The tailored correlations are considered non-local because the functional form of the spatial intensity correlations can be arbitrarily manipulated without altering the field correlations. Afterward, we develop an experimental method for customizing the intensity probability density function of speckle patterns while simultaneously introducing non-local spatial correlations among the speckle grains. The various families of tailored speckle patterns –created by our general method– can exhibit radically different topologies, statistics, and variable degrees of spatial order. Irrespective of their distinct statistical properties, however, all of these speckles are created by appropriately encoding high-order correlations into the phase front of a monochromatic laser beam with a spatial light modulator. In addition to our experimental demonstration, we explore both the theoretical and practical limitations on the extent to which the intensity PDF and the spatial intensity correlations can be manipulated concurrently in a speckle pattern. Fi-

nally, we perform a proof of principle super-resolution imaging demonstration; where we design and create bespoke speckle patterns for parallelized nonlinear pattern-illumination microscopy based on fluorescence photoswitching. In our demonstration, we obtain a spatial resolution three times higher than the diffraction limit of the illumination optics in our setup. Furthermore, we show that tailored speckles vastly outperform standard speckles, and therefore, customized speckles are a potent tool in parallelized super-resolution microscopy.

In diffusive media, we demonstrate the ability to coherently control wave transport through –and throughout– multiple scattering systems. We develop a unique experimental platform based on the synthesis of nanofabricated on-chip structures and interferometric wavefront-shaping. With our setup, we investigate the fluctuations and correlations of transmission eigenchannel depth-profiles in optical diffusive media. Specifically, we find that the depth profiles of high-transmission eigenchannels exhibit low realization-to-realization fluctuations. Furthermore, our experimental and numerical studies reveal the existence of inter-channel correlations, which are significant for low-transmission eigenchannels. Next, using our experimental platform’s unparalleled access to the optical field inside on-chip diffusive structures; we introduce and experimentally investigate the deposition matrix,  $\mathcal{Z}$ : which maps any input wavefront to its internal field distribution over a specific region. Concurrently, we develop a theoretical formalism to predict the ultimate limitations on energy deposition at any depth inside a diffusive medium. Finally, we introduce the remission matrix,  $\mathcal{R}$ , which maps the wavefronts input over a finite region of a diffusive medium’s surface to the resulting diffusive waves re-emitted from a displaced region on the same surface. Furthermore, we experimentally demonstrated that remission eigenchannels can enhance the remitted signal strength without sacrificing the penetration-depth of the collected light.

# Controlling Complex Light Propagation and Statistics

A Dissertation  
Presented to the Faculty of the Graduate School  
Of  
Yale University  
In Candidacy for the Degree of  
Doctor of Philosophy

By  
Nicholas Bender

Dissertation Director: Professor Hui Cao

December 2021

Copyright © 2021 by Nicholas Bender

All rights reserved.

## Acknowledgments

First and foremost, I would like to thank my advisor Professor Hui Cao. I am humbled to have had the opportunity to learn from her. Her dedication and knowledge, in teaching and research, is inspirational. That working together has been fun, is a bonus.

I would also like to thank Professor Hong Tang and Professor Owen Miller for their advice throughout my graduate studies; as well as for agreeing to be on my thesis committee. Furthermore, I would like to thank Professor Joseph Goodman for agreeing to be my external reader.

I would like to single out, and express my deepest gratitude to Professor Hasan Yilmaz. I could not ask for a better mentor –and friend– to work with in the lab.

While a graduate student at Yale, I have been incredibly fortunate to work with –and learn from– some truly fantastic people. I am grateful to have collaborated with Professor Alexey Yamilov, Professor Yaron Bromberg, Professor Chai Wade Hsu, Professor Arthur Goetschy, Professor Joerg Bewersdorf, and Mengyuan Sun. I have learned a lot from them, and greatly appreciate their hard work! As a member of Hui’s research group, I have been lucky to get to know the following spectacular individuals: Dr. Stefan Bittner, Dr. Wen Xiong, Dr. Yaniv Eliezer, Dr. Chun-Wei Chen, KyungDuk Kim, SeungYun Han, Liam Shaughnessy, and Samuel Halladay. I also greatly appreciate the group’s administrative supporters: Maria Rao, Giselle Maillet, and Alexander Bozzi. Obviously, I would also like to thank the funding sources for my research: Yale University, the Office of Naval Research (ONR), and the National Science Foundation (NSF).

Outside of Yale, I owe a debt of gratitude to Professor Tsampikos Kottos and Professor Hamidreza Ramezani for encouraging me to study physics: while I was an undergraduate student at Wesleyan University. I would like to thank my parents for supporting my decision to pursue a PhD, and patiently listening (or at least politely nodding) when I attempted to explain what I was researching.

Finally, I would like to thank my wife, and best-friend for the past decade, Eleonore Bayles.

# Contents

<b>1</b>	<b>Introduction</b>	<b>1</b>
1.1	Coherent Wavefront Shaping . . . . .	1
1.2	Random Light In Free Space . . . . .	2
1.3	Random Light In Diffusive Media . . . . .	5
<b>2</b>	<b>Customizing Speckle Intensity Statistics</b>	<b>9</b>
2.1	Introduction . . . . .	9
2.2	Experimental Setup . . . . .	11
2.3	Method . . . . .	12
2.3.1	Local Intensity Transformation . . . . .	12
2.3.2	Experimental Speckle Generation . . . . .	15
2.4	Customized Speckle Patterns . . . . .	19
2.5	Statistical Properties Of Customized Speckle Patterns . . . . .	21
2.5.1	Phase-PDF & Spatial Correlations . . . . .	21
2.5.2	Higher-Order Statistics . . . . .	23
2.5.3	Intensity-Moment Analysis . . . . .	25
2.6	Axial Propagation . . . . .	27
2.7	Discussion & Conclusion . . . . .	29

<b>3</b>	<b>Introducing Non-Local Correlations Into Laser Speckles</b>	<b>30</b>
3.1	Introduction . . . . .	30
3.2	Enhanced Non-Local Correlation Length . . . . .	32
3.3	Anisotropic Long-Range Correlations . . . . .	35
3.4	Origins Of Non-Local Correlations . . . . .	39
3.5	Axial Evolution Of Speckle Correlations . . . . .	42
3.6	Discussion & Conclusion . . . . .	43
<b>4</b>	<b>Creating And Controlling Complex Light</b>	<b>45</b>
4.1	Introduction . . . . .	45
4.2	Method . . . . .	46
4.3	Example Customized Speckles . . . . .	51
4.4	Higher-Order Statistics Analysis . . . . .	51
4.5	Theoretical Limitations . . . . .	54
4.6	Experimental Realizations . . . . .	62
4.7	Discussion & Conclusion . . . . .	64
<b>5</b>	<b>Circumventing The Optical Diffraction Limit With Customized Speckles</b>	<b>67</b>
5.1	Introduction . . . . .	67
5.2	Experimental Setup . . . . .	69
5.2.1	Optical Setup . . . . .	69
5.2.2	Purified Protein Sample Preparation . . . . .	71
5.3	Photoconversion Fluorescence Microscopy . . . . .	71
5.4	Quantitative Analysis . . . . .	73
5.4.1	Fluorescent Spot Measurement . . . . .	73
5.4.2	Fluorescent Spot Properties . . . . .	75
5.5	Customized Speckle Statistics . . . . .	77

5.6	Vortex Characteristics . . . . .	79
5.7	Protein Photoconversion Simulation . . . . .	81
5.8	Optical Sectioning . . . . .	85
5.9	Live Sample Demonstration . . . . .	86
5.9.1	Photonconverting Live Yeast Cells With Customized Speckles . . . . .	86
5.9.2	Live Yeast Cell Culture & Preparation . . . . .	87
5.10	Discussion & Conclusion . . . . .	87
<b>6</b>	<b>Fluctuations And Correlations Of Transmission Eigenchannels In Diffusive Media</b>	<b>90</b>
6.1	Introduction . . . . .	90
6.2	Experimental Setup . . . . .	92
6.3	Determination Of Sample Transport Parameters . . . . .	94
6.4	Measurement Procedure . . . . .	96
6.5	Transmission Eigenchannel Depth-Profiles . . . . .	97
6.6	Transmission Eigenchannel Fluctuations . . . . .	99
6.7	Transmission Eigenchannel Correlations . . . . .	103
6.8	Discussion & Conclusion . . . . .	104
<b>7</b>	<b>Depth-Targeted Energy Deposition Deep Inside Scattering Media</b>	<b>105</b>
7.1	Introduction . . . . .	105
7.2	Deposition Matrix . . . . .	108
7.3	Numerical Simulation & Analytical Model . . . . .	109
7.4	Measurement Of Deposition Eigenchannels . . . . .	114
7.5	Two Mechanisms For Energy Deposition . . . . .	115
7.6	Discussion & Conclusions . . . . .	118

<b>8</b>	<b>Remission Eigenchannels Inside Diffusive Scattering Media</b>	<b>120</b>
8.1	Introduction . . . . .	120
8.2	Experimental Samples . . . . .	122
8.3	Remitted Random Light . . . . .	125
8.4	Remission Matrix . . . . .	126
8.5	Experimentally Measuring Remission Eigenchannels . . . . .	127
8.6	Discussion & Conclusion . . . . .	133
<b>9</b>	<b>Conclusion</b>	<b>134</b>
<b>A</b>	<b>Random Light In Free Space</b>	<b>137</b>
A.1	Transmission-Matrix Measurement . . . . .	137
A.1.1	Four-Phase Plus One-Amplitude Measurement . . . . .	138
A.1.2	Building A Transmission Matrix . . . . .	139
A.2	Transmission Matrix Validation . . . . .	143
A.3	Effect Of Transmission Matrix Error On Customized PDFs . . . . .	145
<b>B</b>	<b>Random Light In Disordered Media</b>	<b>149</b>
B.1	On-Chip Nano Fabrication Process . . . . .	149
B.2	Disordered Waveguide Design . . . . .	156
B.3	Optical Setup . . . . .	156
B.4	Fluctuations & Correlations of Transmission Eigenchannels . . . . .	158
B.4.1	Transmission Matrix Measurement . . . . .	159
B.4.2	Transmission Eigenchannel Profile Measurement . . . . .	160
B.4.3	Transmission Eigenchannel Numerical Simulations . . . . .	161
B.4.4	Identification Of Experimental Transmission Eigenchannels . . . . .	164
B.4.5	Transmission Eigenchannel Variance . . . . .	165

B.5	Deposition Eigenchannels . . . . .	166
B.5.1	Deposition Eigenchannel Numerical Simulations . . . . .	166
B.5.2	Analytical Predictions . . . . .	169
B.5.3	Upper Edge Of $p(\zeta)$ . . . . .	176
B.5.4	Deposition Eigenchannel Experimental Measurements . . . . .	177
	<b>Bibliography</b>	<b>182</b>

# List of Figures

1.1	<b>An example of Rayleigh speckles.</b> . . . . .	3
2.1	<b>A caricature of the experimental setup.</b> Light reflected by a spatial light modulator is Fourier transformed by a lens, and then imaged onto a detector. . . . .	11
2.2	<b>A physically impossible intensity PDF.</b> The black curve is the original desired PDF, and the blue curve is the numerically obtained one after a local intensity transformation algorithm. Their difference (shaded area) is due to the limited range of the spatial frequencies in the speckle pattern. . . . .	14
2.3	<b>Example customized speckles.</b> A Rayleigh speckle pattern (a) and customized speckle patterns with distinct intensity statistics (b-e). In the top row, each pattern is 504 $\mu\text{m}$ by 504 $\mu\text{m}$ , and the maximum intensity is normalized to 1. The associated PDF, shown in the lower row, is uniform (b), linearly increasing (c), peaked at a non-zero intensity (d), and bimodal (e), over a predefined range of intensity. The red solid curves are experimental data, the blue dashed curves are from numerically generated target speckle patterns. Both are the result of spatial and ensemble averaging over 50 independent speckle patterns. . . . .	19

2.4 **The topological change of a customized speckle pattern.** A Rayleigh speckle pattern in (a) is transformed to the speckle pattern in (b) via a local intensity transformation. Application of a digital low-pass Fourier filter results in the pattern in (c). Multiple iterations of intensity transformations and filtering result in the final pattern in (d) which obeys the desired intensity PDF and spatial frequency constraints. The maximum intensity is normalized to 1. . . . . 20

2.5 **Characteristics of customized speckle patterns.** (a) The phase histogram of the speckled fields demonstrates that they are all fully developed. (b) The spatial field correlation function  $|C_E(|\Delta\mathbf{r}|)|^2$  and (c) the spatial intensity correlation function  $C_I(|\Delta\mathbf{r}|)$ , of the customized speckles, remain the same as in Rayleigh speckles. In (a-c), the four customized speckle patterns have constant (black), linearly increasing (red), unimodal (blue), bimodal (green) PDFs, and the purple is for Rayleigh speckles. (d) Comparing  $|C_E(|\Delta\mathbf{r}|)|^2$  (black curve) to  $C_I(|\Delta\mathbf{r}|)$  (blue dashed curve), both averaged over the 5 curves in (b) and (c) respectively, to confirm they have the same correlation width. . . . . 22

2.6	<b>Some higher-order statistical properties of the customized speckle patterns with a bimodal intensity PDF.</b>	(a) The spatially averaged intensity PDF $P_S(I)$ of 2500 speckle patterns verifies that the speckle patterns are stationary. (b) The ensemble-averaged intensity PDF $P_E(I)$ –within the area of a single speckle grain– for each spatial position in a pattern confirms the speckles are ergodic. (c) The complex-amplitude joint-PDF for the speckled field $P(\text{Re}[E], \text{Im}[E])$ displays circular non-Gaussian statistics. (d) The joint PDF for two intensities $P(I_1, I_2)$ at spatial positions separated by approximately one speckle grain size (twice the spatial intensity correlation width) are uncorrelated. The results in (c,d) are obtained from averaging over space and 100 speckle patterns, a digital low-pass Fourier filter is applied to remove noise. . . . .	24
2.7	<b>Evolution of customized speckle patterns upon axial propagation.</b>	The intensity PDF at the Fourier plane of the SLM ( $z = 0$ ) is linearly increasing (a) and bimodal (e). The distance from the Fourier plane is $R_l/5$ (b, f), $(2/5)R_l$ (c, g), and $(10/7)R_l$ (d, h). . . . .	28
3.1	<b>Enhancing non-local correlations in speckles.</b>	A Rayleigh speckle pattern (a,c) with $C_I(\Delta r) =  C_E(\Delta r) ^2$ (e), is compared to an “enlarged Rayleigh” speckle pattern (b,d) with $C_I(\Delta r)$ much broader than $ C_E(\Delta r) ^2$ (f). The non-local intensity correlations, $C_{NL}(\Delta r)$ , have comparable strength to the local correlations, $C_L(\Delta r) =  C_E(\Delta r) ^2$ , in (f). The correlation functions in (e,f) are obtained by averaging over 100 independent speckle patterns. Similar to the Rayleigh speckle pattern, the customized speckle field is fully developed with a uniform phase distribution between 0 and $2\pi$ .	33

3.2	<p><b>Creating speckle patterns with spatially oscillating, anisotropic long-range intensity correlations.</b> The intensity correlation function <math>C_I(\Delta\mathbf{r})</math> (a), determines the Fourier amplitude profile of <math>I(\mathbf{r})</math> (b). An experimentally generated speckle intensity-pattern <math>I(\mathbf{r})</math> (c) possessing the correlations given in (a), and the corresponding phase profile <math>\theta(\mathbf{r})</math> (d). <math>\theta</math> is uniformly distributed between 0 and <math>2\pi</math>, confirming that the speckle pattern is fully developed. The local intensity correlation function <math>C_L(\Delta\mathbf{r})</math> (e) has a maximum value of 1, while the non-local intensity correlation function <math>C_L(\Delta\mathbf{r})</math> (f) has a maximum/minimum value of <math>\pm 0.1</math>. The correlation functions in (a,e,f) are obtained by averaging over 100 speckle patterns. The origins in (a,b,e,f) are located at the plots' centers. . . . .</p>	36
3.3	<p><b>Tuning the speckle contrast independently from the spatial intensity correlation function.</b> Two experimentally generated speckle patterns (a,c) with congruent intensity correlation functions (b,d). The intensity contrast is 0.68 in (a) and 1.35 in (c). The origin for (b) and (d) is located at the center of the plots. . . . .</p>	37
3.4	<p><b>Introducing spatially simple anisotropic non-local correlations into speckles.</b> The spatial intensity correlation function (a) is sparse. The local correlation function (b) has a maximum amplitude of 1, while the non-local correlation function (c) has a maximum/minimum amplitude of <math>\pm 0.2</math>. An ordered intensity pattern <math>g(\mathbf{r})</math> (d), produced by the Gerchberg Saxton algorithm, is convolved with super-Rayleigh speckle pattern <math>J(\mathbf{r})</math> (e) to generate a speckle intensity-pattern <math>I(\mathbf{r})</math> (f) with the desired non-local correlations given in (c). The correlation functions in (a,b,c) are obtained by averaging over 100 speckle patterns and the origins are located at the plots' centers. . . . .</p>	39

3.5	<b>Axial evolution of a customized speckle pattern.</b> An example customized speckle pattern (a), on the plane of customization $z = 0$ , is juxtaposed with its corresponding spatial intensity correlation function (d). The speckle pattern (b) and its intensity correlation function (e), after axially propagating to $z = R_l/3$ , are presented. At this distance, the magnitude of the non-local correlations has reduced by half. The speckle pattern (c) and its intensity correlation function (f) are shown after further propagation to $z = 2R_l/3$ . At this point, the non-local correlations are completely erased and only the local correlations remain. The correlation functions in (d,e,f) are obtained by averaging over 100 different speckle patterns, and the origins are located at the center of the plots. . . . .	42
4.1	<b>Speckle customization method.</b> We show a flowchart visualization of our speckle customization method. $I_D(\mathbf{r})$ represents an intensity pattern obeying the desired PDF and $\tilde{I}(\mathbf{r})$ is an intensity pattern with the desired correlations. . . . .	46

4.2	<b>Example customized speckle pattern.</b>	A customized speckle pattern is shown in (a) with a spatially sparse intensity correlation function (b) and a unimodal intensity PDF (c). In (b) $C_{\max} = 0.15$ and $C_{\min} = -0.03$ . In (c) the intensity PDF of the experimentally created speckles (purple solid line) closely follows the target intensity PDF (black dashed line). The local intensity correlation function (d) remains the same as that of a Rayleigh speckle pattern, indicating that the modification of the spatial intensity correlation function is the result of introducing non-local correlations into the speckle pattern. To obtain (b-d) we ensemble average over 100 independent speckle patterns to obtain the PDF and the correlation functions. The origin of (b) and (d) is located at the center of each plot. . . . .	50
4.3	<b>Higher-order statistics.</b>	Some high-order statistical properties of the family of customized speckle patterns in Fig. 4.2 are presented. In (a) the complex joint PDF of the speckled field reveals that the speckle patterns are circular non-Gaussian and therefore fully developed. In (b-d) we show the joint intensity PDF, $P(I_1, I_2)$ , of $I_1$ and $I_2$ sampled at spatial locations separated by $\Delta\mathbf{R} = (60 \mu\text{m}, 60 \mu\text{m})$ , $(0, 100 \mu\text{m})$ , and $(100 \mu\text{m}, 0)$ respectively. In (b) the intensity values are uncorrelated and thus the joint intensity PDF is independent, while in (c,d) the encoded non-local correlations result in a dependent joint PDF. To obtain these results we use an ensemble of 5000 customized speckle patterns. . . . .	53
4.4	<b>A flowchart illustration of separate control over the speckle correlations and intensity PDF.</b>	The phase-only SLM generates the speckle pattern $I(r)$ , whose Fourier transform is $J(\rho) = \mathcal{F}[I(\mathbf{r})]$ . The Fourier amplitude, $ J(\rho) $ , is modulated to manipulate $C_I(\Delta\mathbf{r})$ and the phase, $\text{Arg}[J(\rho)]$ , can be used to tailor the intensity PDF. . . . .	56

4.5 **The effect of reconstructing an intensity PDF from different numbers of its moments.** An example PDF,  $P(I)$ , with a finite range of intensity is shown in (a). The Fourier spectrum of  $P(I)$  is plotted in (b), demonstrating that the PDF has a limited number of non-zero Fourier components. (c) shows the PDF reconstruction error of (a) as a function of the number of intensity moments used for reconstruction. Two examples of reconstructed PDFs are shown in (d); they are created using 8 intensity moments and 17 intensity moments. . . . . 59

4.6 **Two customized speckle patterns (a,b) with different intensity PDFs (c,d) but identically shaped spatial intensity correlation functions are shown in (e,f).** In (a) we present a measured speckle pattern adhering to both the PDF shown in (c), which is flat over a pre-defined range of  $I/\langle I \rangle$ , and the diagonally oscillating spatial intensity correlation function shown in (e). In (b) we present a measured speckle pattern with the same shaped intensity correlation function (f), but obeying a different intensity PDF (d), which increases linearly over a pre-defined  $I/\langle I \rangle$  range. In (e)  $C_{\max} = 0.32$  and  $C_{\min} = -0.09$  while in (f)  $C_{\max} = 0.14$  and  $C_{\min} = -0.04$  due to the different PDFs. We ensemble average over 100 independent speckle patterns to obtain the PDF and correlation functions in (c-f). The origin of (e) and (f) is located at the center of each plot. . . . . 61

4.7 **Two customized speckle patterns with the same intensity PDF but different spatial intensity correlation functions are shown.** In (a) we present a measured speckle pattern adhering to both the bimodal intensity PDF shown in (c) and the isotropic oscillating correlation function shown in (e). In (b) we present a measured speckle pattern also adhering to a bimodal PDF (d) but possessing anisotropic ‘checkerboard’ correlations shown in (f). In (g,h) we show the corresponding non-local correlations. In (e)  $C_{\max} = 0.29$  and  $C_{\min} = -0.05$  while in (f)  $C_{\max} = 0.30$  and  $C_{\min} = -0.12$ . We ensemble average over 100 independent speckle patterns, to obtain the PDFs and correlation functions in (c-h). The origins of (e-h) are located at the center of each plot. . . . . 63

5.1 **Experimental setup.** The experimental setup used for nonlinear speckle-illumination microscopy is shown. We use a phase-only SLM to generate a customized speckle pattern which illuminates and photoconverts a fluorescent sample. . . . . 70

5.2 **Customizing speckles for nonlinear pattern illumination.** An experimentally recorded speckle pattern that illuminates and photoconverts a uniform fluorescent protein sample is shown in (a). Within the white box the speckles obey delta statistics and outside they obey Rayleigh statistics. In (b), an experimentally recorded image of the fluorescence from the unconverted regions shows isometric and isotropic spots produced by the vortices in the delta speckles; while the region photoconverted by the Rayleigh speckles features large, irregular, and interconnected fluorescent grains. . . . . 72

5.3 **Circumventing the diffraction limit.** A diffraction-limited spot of the 405 nm illumination/photoconversion optics is presented in (a). In (b), an example fluorescent spot produced by a vortex in the delta speckle pattern is illustrated. Its size is much smaller than the diffraction-limited spot. Its shape can be fit by an ellipse of major axis width  $a = 6.1 \mu\text{m}$  and minor axis width  $b = 5 \mu\text{m}$ . The aspect-ratio,  $b/a$ , histogram of all fluorescent spots produced by the delta speckles is shown in (c). The inset illustrates an ellipse with the average aspect ratio  $\langle b/a \rangle = 0.86$ . In (d), the box-plot analysis of the major and minor axes widths is shown. The white line marks the mean value, and the black whiskers represent the upper and lower bounds of the data. The edges of the blue and red shaded regions mark the upper and lower quartiles (25%, 75%) of the ensemble. The green dashed line indicates the FWHM of the diffraction-limited spot in (a). . . 74

5.4 **Customized Speckle Statistics.** An example delta speckle pattern is presented in (a) and the corresponding phase distribution of its complex field is shown in (b). The phase is randomly distributed between  $-\pi$  and  $\pi$ , indicating that the speckle pattern is fully developed. The intensity PDF (purple solid line) of the delta speckle pattern is shown in (c) and compared with a Rayleigh PDF (green dashed line). The spatial correlation functions of the intensity (red dashed line) and the field (blue solid line) in the delta speckle pattern are shown in (d). The spatial fluctuations of the intensity are faster than those of the field. The anti-correlation ( $C_I < 0$ ) originates from the bright ring surrounding each vortex core. The plots both in (c) and (d) are obtained from an ensemble of 100 speckle patterns. 76

5.5 **Optical Vortex Characteristics.** Two example vortices from a delta speckle pattern, (a), and from a Rayleigh speckle pattern, (b), are shown. While the vortices in the delta speckles are nearly circular, the Rayleigh speckles' vortices have highly irregular shapes. This property is reflected in (c) where we plot the average intensity profile of light around vortices in 1,000 delta speckle patterns (purple solid line) and around vortices in 1,000 Rayleigh speckle patterns (green dashed line). The edge of the purple and green shaded regions indicates one standard deviation away from the corresponding mean profile. In (d), we plot the probability density of the equal-intensity contours' aspect-ratio around the vortices in 1,000 delta speckle patterns (purple) next to the theoretical prediction for Rayleigh speckle patterns (green). . . . . 80

5.6 **Photoconversion simulation.** When a delta speckle pattern is used for photoconversion (a), the unconverted regions near the vortices quickly evolve into isotropic and isomeric islands as seen in (b) at  $t = 1/q$ . At long timescales the islands remain, as shown in (c) where  $t = 10/q$ , yet they have considerably smaller size and higher spatial frequencies (d). When a Rayleigh speckle pattern is used for photoconversion (e), an interconnected web forms instead of isolated islands at  $t = 1/q$  as shown in (f). Even at long time scales isolated and isotropic islands are rarely seen in (g) and fewer high-spatial frequencies are present when compared to (c), as shown in (h). The power spectra in (d,h) are ensemble-averaged over 100 realizations, and normalized to have a mean value of 1 over the spatial frequencies plotted. Note, the values at  $k = 0$  are not plotted. . . . . 82

5.7 **Axial Propagation.** Axial intensity cross-sections,  $I(x = x_0, y, \Delta z)$ , of both delta (a) and Rayleigh (c) speckles are juxtaposed with a simulation of the corresponding unconverted protein density in a uniform sample,  $\rho(x = x_0, y, \Delta z, 10/q)$ , (b,d) over one Rayleigh axial-decorrelation length  $R_l$ . In (e), the axial intensity correlation function  $C_I(\Delta z)$  of the delta speckles (purple line) is three times narrower than that of the Rayleigh speckles (green dashed line). In (f), the axial correlation function of the unconverted protein density  $C_\rho(\Delta z)$  generated by delta speckles (purple line) has almost same width as that generated by Rayleigh speckles (green dashed line). We ensemble average over the propagation of 100 speckle patterns to create the curves in (e,f). . . . . 84

5.8 **Photoconversion of live yeast cells with a customized speckle pattern.** In (a), we present an optical image of the fluorescent light emitted from a sample of live yeast cells before they are photoconverted by the delta speckle pattern shown in (b). The white circles in (b) indicate the vortices which overlap with the yeast cells. An image of the fluorescent light emitted by the live-cell sample after photoconversion is shown in (c). The red circles in (c) correspond to the white circles in (b). . . . . 86

6.1 **Waveguide structure and optical setup.** A composite SEM image of a diffusive waveguide is shown in (a). The matrix mapping the field in the buffer region to the end region,  $t_{\text{buff} \rightarrow \text{end}}$ , is related to the matrices  $t_{\text{slm} \rightarrow \text{buff}}$  and  $t_{\text{slm} \rightarrow \text{end}}$ . In (b) the simplified sketch of the experimental setup illustrates how we wavefront shape a laser beam with a spatial light modulator (SLM) while performing an interferometric measurement of the light scattered out of the waveguide. . . . . 93

6.2	<b>Determining the sample transport parameters.</b>	Determining the transport mean free path $\ell_t$ and the diffusive dissipation length $\xi_a$ of the diffusive waveguides by fitting the experimentally-measured average depth profile for random incident wavefronts, $\langle I(z) \rangle$ , (blue) to theoretical predictions from the diffusion equation (red). . . . .	95
6.3	<b>Depth profiles of transmission eigenchannels.</b>	High ( $\alpha = 1$ ) and low ( $\alpha = 20$ ) transmission eigenchannel profiles are presented in (a,b) while the 22 measured eigenchannel profiles are juxtaposed in (c). The experimentally measured profiles (blue lines) agree well with the profiles calculated from numerical simulations using the transmission matrix $t$ (black dashed lines) and the matrix $t_{\text{buff} \rightarrow \text{end}}$ (red lines). . . . .	98
6.4	<b>Eigenchannel fluctuations.</b>	In (a), the spatially-averaged depth-profile fluctuations of the eigenchannels, $\tilde{C}_\alpha$ , increase monotonically with the channel index $\alpha$ . The green dashed line indicates the experimentally observed fluctuations for random incident wavefronts: 0.59. In (b), experimentally observed depth-resolved intensity fluctuations, $\text{var}[I_\alpha(z)]$ , of high ( $\alpha = 1$ ) and low ( $\alpha = 20$ ) transmission eigenchannels (circles) are closely reproduced by the numerical simulations of transmission eigenchannels from $t_{\text{buff} \rightarrow \text{end}}$ (solid lines) and $t$ (dashed lines). In (c), $\text{var}[I_\alpha(z)]$ is divided by $\langle I_\alpha(z) \rangle^2$ for the high/low-transmission eigenchannels of $t$ . In (d-e), the experimentally-observed and numerically-calculated depth-resolved intensity fluctuations for individual eigenchannels show how $\text{var}[I_\alpha(z)]$ evolves with $\alpha$ . . . . .	100

6.5 **Inter-channel correlations.** The covariance  $\tilde{C}_{\alpha\beta}$  between any two pairs of eigenchannels,  $\alpha$  and  $\beta$ , is calculated from experimental data (a) and numerical simulations (b,c). The cumulative covariance  $\sum_{\beta \neq \alpha} \tilde{C}_{\alpha\beta}$  exceeds the variance  $\tilde{C}_{\alpha\alpha}$  in (d). The blue symbols represent experimental data and red lines represent numerical simulations based on  $t_{\text{buff} \rightarrow \text{end}}$ . . . 102

7.1 **Schematic of the experimental platform for investigating energy deposition in a diffusive system.** A spatial light modulator (SLM) shapes the incident wavefront of a monochromatic laser beam, and the field distribution inside a two-dimensional disordered waveguide is probed from above. This setup allows measurement of the deposition matrix that relates the incoming field pattern to the spatial field distribution inside a target region (marked by the cyan box). Selective coupling of light into the deposition eigenchannels can enhance or suppress energy inside the target region, as confirmed by the CCD camera image of the spatial intensity distribution. 107

**7.2 Numerical simulation and analytic prediction of deposition eigenvalues.** (a) Probability density function of normalized deposition eigenvalues  $\zeta / \langle \zeta \rangle$  for a thin slice at varying depths  $z_D$  inside a diffusive waveguide (see inset). Analytical FRM predictions (solid lines) agree with numerical simulations (dots) averaged over 1000 disorder configurations. For most depths,  $P(\zeta / \langle \zeta \rangle)$  is very different from the bimodal distribution of the transmission eigenvalues  $P(\tau / \langle \tau \rangle)$ , although it converges to bimodal at the end (shaded area at  $z_D/L = 1$ ). The theoretical prediction for the upper edge of  $P(\zeta)$ , which sets the limit for energy enhancement  $\langle \zeta_{\max} \rangle / \langle \zeta \rangle$ , is marked by dashed purple line in the horizontal plane. (b) Energy enhancement in two diffusive waveguides (WG1, WG2), given by the ratio of the largest ensemble-averaged deposition-eigenvalue  $\langle \zeta_{\max} \rangle$  over the mean eigenvalue  $\langle \zeta \rangle$ , increases with depth  $z_D$  and reaches its maximum at  $z_D/L \sim 3/4$ . Analytical predictions for the upper edge of  $P(\zeta / \langle \zeta \rangle)$  (solid lines) are compared to numerical data (symbols). The energy enhancement  $\langle \tau_{\max} \rangle / \langle \tau \rangle$  exceeds the transmission enhancement  $\langle \zeta_{\max} \rangle / \langle \zeta \rangle$  (horizontal dotted line) at most depths. In (a), the waveguide (WG1) has a length  $L = 50 \mu\text{m}$ , width  $W = 15 \mu\text{m}$ , and transport mean free path  $\ell_t = 3.3 \mu\text{m}$ . (b) includes a second waveguide (WG2) of  $L = 50 \mu\text{m}$ ,  $W = 30 \mu\text{m}$ , and  $\ell_t = 1.6 \mu\text{m}$ . . . . . 110

7.3 **Experimental measurement of deposition eigenchannels.** (a) A composite scanning electron microscope (SEM) image of a disordered waveguide of width  $W = 15 \mu\text{m}$ . Randomly distributed air holes (each 100 nm in diameter) are etched throughout a designated  $L = 50 \mu\text{m}$  long region. Superimposed are four target regions used for energy deposition; each is  $10 \mu\text{m} \times 10 \mu\text{m}$ . (b,c) The depth profiles (cross-section integrated intensities) of two deposition eigenchannels with enhanced and suppressed energies in the target region  $R_1$  centered at depth  $z_D = 10 \mu\text{m}$  (b), and  $R_2$  at  $z_D = 20 \mu\text{m}$  (c) are shown. The experimental data (red circle, purple diamond) agrees with the numerical simulations (red solid line, purple dotted line). The black dashed line is the averaged intensity profile generated by random input wavefronts. Each experimental data point is averaged over  $\Delta z = \ell_t$  to reduce fluctuations. (d,e) The experimentally measured energy enhancement in the target region  $\eta_t$  (blue-circles) and in the surrounding area  $\eta_s$  (brown-diamonds) of two deposition eigenchannels  $\alpha = 2$  (d) and  $\alpha = 24$  (e) are compared with numerical data (light-blue and orange lines): for the case of energy deposition into four target regions centered at 10, 20, 30, and 40  $\mu\text{m}$ . In (d) the green line corresponds to  $35C_2(z_D)$ , and its agreement with the experimental/numerical results of  $\eta_t(z_D)$  confirms the essential contribution of long-range intensity correlations to energy deposition. . . . . 113

7.4	<b>Relation between deposition eigenchannels and transmission eigenchannels.</b>	(a,c) The projection of a deposition eigenchannel with index $\alpha = 1$ (a) or 25 (c) onto transmission eigenchannels with index $\beta$ gives the coefficients $d_{\alpha\beta}$ . Four curves denote $ d_{\alpha\beta} ^2$ for four target regions $R_1 - R_4$ [inset of (a)] in the same disordered waveguide as in Fig. 7.3. (b,d) Comparison between the coherent sum (red/purple) and incoherent (green) sum of the transmission eigenchannels describing deposition eigenchannel profiles, with coefficients given in (a,c). For each deposition region, the enhancement/suppression above/below the random input intensity profile (black dashed line) has two distinct contributions from selective excitation of transmission eigenchannels (green areas) and constructive/destructive interference between them (cyan areas). . . . .	116
8.1	<b>Remission eigenchannel concept.</b>	By coherently controlling the wavefront of light injected into a slab-geometry diffusive-medium with a spatial light modulator; we can couple into a remission-eigenchannel to enhance the signal of the emitted light, without sacrificing the penetration depth. We can directly observe the spatial profile of the remission-eigenchannel by capturing the light scattered out-of-plane with a CCD camera. . . . .	122
8.2	<b>On-chip diffusive-slab SEM images.</b>	A SEM image of the full on-chip slab-geometry diffusive system used in our experiments is shown in (a). Magnifying by an order of magnitude, in (b) the 15 $\mu\text{m}$ -wide input waveguide is shown at the buffer-region diffusive-region interface. Further magnification shows the trigonal photonic-crystal lattice of air holes (radius = 155 nm, lattice constant = 440 nm) and examples of the randomly arranged 100-nm-diameter holes in the diffusive region. . . . .	123

- 8.3 **Remission of random input wavefronts.** The average intensity pattern produced by random input wavefronts  $\langle I(y, z) \rangle$  is shown in (a). An example conditional probability distribution,  $\langle I(y, z) \rangle \langle I(y + \Delta y, z) \rangle$ , of remitted random light is presented in (b) for  $\Delta y = 25\ell_t$ . The black dots represent the maxima of  $\langle I(y, z) \rangle \langle I(y + \Delta y, z) \rangle$  along the  $z$ -axis, for each value of  $y$ , and the purple curve is the best fit of an ellipse to the data. The ellipse gives the trajectory of randomly-generated remitted-light traveling from the input to the displaced region. In (c) the trajectory of remitted light in the  $(y, z)$  plane is plotted as a function of separation  $\Delta y$ . . . . . 125
- 8.4 **Field-reconstruction matrix validation.** An experimentally measured intensity distribution within the diffusive slab –generated by a random phase pattern on the SLM– is presented in (a) next to the field-reconstruction matrix prediction (b). The intensity patterns have a Pearson correlation coefficient of 0.94 without any data manipulation or noise reduction. . . . . 128
- 8.5 **Remission eigenchannel intensity distribution.** An example ensemble-averaged remission eigenchannel intensity distribution is shown in (a) for a remission region displaced  $\Delta y = 17.2\ell_t$  along the input surface. For reference, the trajectory of the random-light-generated conditional probability distribution from the input to the emission region (white dashed curve) is shown. To illustrate the directionality of remission eigenchannels, and their ability to redistribute energy *inside* the diffusive system, in (b) we show the difference between the lower and upper remission eigenchannel intensity distributions:  $\langle I_{+\Delta y}(y, z) \rangle - \langle I_{-\Delta y}(y, z) \rangle$ . For reference, the corresponding random-light conditional probability distributions are shown. . . . . 130

8.6	<b>Difference between remission eigenchannels and random illumination patterns.</b> In (a-c), the ensemble-averaged “open” remission eigenchannel pattern subtracted by the ensemble-averaged random input pattern $\langle I_{\Delta y}(y, z) \rangle - \langle I(y, z) \rangle$ is shown for a target region (black square) located at $\Delta y = 12.5\ell_t, 18.8\ell_t, \& 25\ell_t$ away from the input source. The solid-green lines show the trajectory of the conditional probability distribution generated by random light, in each panel, while the black dashed lines show the trajectory the remission eigenchannel’s conditional probability distribution. . . . .	132
A.1	<b>Transmission matrix validation.</b> An example customized speckle pattern predicted by our transmission matrix (a) is juxtaposed with the corresponding experimentally measured speckle pattern (b). The difference between the two intensity patterns is 9.7%. In (c) we compare the intensity PDF of predicted speckle patterns, green dashed line, with the intensity PDF of the corresponding measured speckle patterns, purple solid line, for an ensemble of 100 speckles patterns like those shown in (a) and (b). The difference between the two intensity PDFs is 3.7%. In (d) we present a measured image of the speckles in both the target region and the junkyard region. The white square denotes the boundary of the target region. . . .	144
A.2	<b>Measured speckle pattern error in Chapter 2.</b> The statistical distribution of $(I_e - I_d)/\sqrt{I_d}$ , extracted from the experimental data in Chapter 2 (symbols), is fit well by the Gaussian distribution $G(I_e, I_d)$ in Eq. A.19 (lines). The fitting parameter is given by $a = 0.020$ for the uniform PDF (black), $a = 0.019$ for the linearly increasing PDF (red), $a = 0.037$ for the PDF with a single peak (blue) and $a = 0.029$ for the bimodal PDF (green).	146

A.3	<b>Predicted effect of error on PDFs.</b> The deviation (shaded area) of the intensity PDF (blue solid line) from the target one (black dashed line) is reproduced numerically by Eq. A.21. (a-d) for the four PDFs shown in Fig. 2.5. . . . . .	147
B.1	<b>Scanning electron microscope (SEM) images of a 2D diffusive waveguide.</b> In (a) we show a composite SEM image which outlines the structures we etch into a silicon-on-insulator wafer when fabricating our structures. A SEM image of the interface between the buffer and diffusive regions is marked by the blue dashed line in (b). Close-up images of the photonic crystal sidewall and randomly-distributed holes are shown in (c) and (d). . . . . .	155
B.2	<b>A depiction of our experimental setup.</b> Monochromatic light from our laser is linearly polarized and split into two beams. One beam illuminates the phase modulating surface of a spatial light modulator (SLM), while the other is used as a reference beam. The SLM is used to control the input wavefront in our diffusive waveguide structures. A beam splitter merges the light collected from the top of our sample with the reference beam on an IR CCD. The focal length of the three lenses used in this setup are: $f_1 = 400$ mm, $f_2 = 75$ mm, and $f_3 = 100$ mm. . . . . .	157
B.3	<b>Waveguide structure and full-field measurement.</b> A composite SEM image of a diffusive waveguide is shown in (a). In (b) the 2D intensity pattern of a measured high-transmission eigenchannel is shown. Using our interferometric setup, we can reconstruct the phase of the light field inside the diffusive waveguide in (c). In (b-c) the edges of the diffusive region are marked by the vertical dashed lines. . . . . .	159

**B.4 Transmission eigenvalue mapping.** Calculated transmission eigenvalues, as a function of eigenchannel index  $\alpha$ , are shown in (a). In (b), we show the mapping between the experimentally-measured eigenchannel profiles with index  $\alpha_E$  and the first 22 (in the order of decreasing transmittance) eigenchannels with index  $\alpha$  found in the numerical simulations based on the  $t_{\text{buff} \rightarrow \text{end}}$  matrix. . . . . 164

**B.5 Transmission eigenchannel variance comparison.** We compare the variance of eigenchannel profiles calculated with the normalized intensity (purple solid line) to the intensity variance normalized by the mean intensity  $\langle \text{var}[\tilde{I}_\alpha(z)] / \langle \tilde{I}_\alpha(z) \rangle^2 \rangle_z$  squared (green dashed line). They show similar growth with the eigenchannel index  $\alpha$ . . . . . 165

**B.6 Comparison between deposition eigenvalue definitions.** Comparison of the eigenvalue distributions  $p(\zeta)$  of the operators  $\mathcal{Z}^\dagger \mathcal{Z}$  defined by Eq. (7.1) and Eq. (7.2), evaluated at different depths  $z_D/L$  of a disordered waveguide (length  $L = 50 \mu\text{m}$ , width  $W = 30 \mu\text{m}$ , transport mean free path  $\ell = 3.3 \mu\text{m}$ ). Noticeable differences are observed only at  $z_D$  very close to  $L$ , where  $p(\zeta)$  converges to the bimodal distribution of transmission eigenvalues for the operator  $\mathcal{Z}^\dagger \mathcal{Z}$  defined by Eq. (7.2) only. The two distributions still coincide for  $z_D/L = 0.95$  (panel 5), which corresponds to  $L - z_D < \ell$ . . . . . 168

**B.7 Width-dependence of deposition eigenvalues.** Deposition eigenvalue distribution  $p(\zeta)$  at depth  $z_D = 0.8L$  of a disordered waveguide of length  $L = 50 \mu\text{m}$  and width  $W = 15, 30, 50 \mu\text{m}$ . Analytical FRM predictions (solid black lines) are compared with numerical results (dots) obtained from the solution of the wave equation for  $10^3$  realizations of the disordered waveguide with a transport mean free path  $\ell = 3.3 \mu\text{m}$ . The distribution of the largest eigenvalue  $p(\zeta_{\text{max}})$  is superimposed (red dots connected by red line) to reveal the convergence of  $\zeta_{\text{max}}$  towards the upper edge of  $p(\zeta)$  in the limit  $g = N \langle \tau \rangle \gg 1$  ( $W = 15, 30, 50 \mu\text{m}$  correspond to  $g = 5, 10, 15$ ). The value  $\langle \zeta_{\text{max}} \rangle$  is indicated with dashed vertical line. . . . . 170

**B.8 Width-dependence of maximum deposition eigenvalues.** Symbols (circles, squares, triangles) represent the ensemble average of the largest deposition eigenvalue  $\langle \zeta_{\text{max}} \rangle$  at different depth  $z_D/L$  for three waveguide width  $W = 10, 30, 60 \mu\text{m}$ . Other parameters are identical to the parameters in Fig. B.7. Solid lines of matched colors are analytical predictions for the upper edge of  $p(\zeta)$  evaluated with the numerical mean  $\langle \zeta \rangle$  and variance  $\text{Var}[\zeta]$ . The agreement between the numerical data and the analytical predictions improves with increasing waveguide width. . . . . 172

**B.9 FRM filtering ratio.** (a) Effective filtering ratio  $m = \langle \tau \rangle / \langle \zeta(z_D) \rangle$  of the FRM model versus depth  $z_D/L$ . Numerical results (dots) are compared with the analytical prediction  $m = 1 / [2(1/\langle \tau \rangle - 1)(1 - z_D/L) + 1]$  (solid lines with matched colors); (b) Variance  $\text{var}[\zeta/\langle \zeta \rangle] = \langle \zeta^2 \rangle / \langle \zeta \rangle^2 - 1$  of the eigenvalue distribution  $p(\zeta)$  vs. depth  $z_D/L$ . Numerical results (dots) are compared with intensity fluctuations  $NC_2(z_D) + 1$  evaluated analytically (solid lines of matched colors) for two values of transport mean free path  $\ell = 1.6, 3.3 \mu\text{m}$ . The disordered waveguide dimensions are  $L = 50 \mu\text{m}$  and  $W = 15 \mu\text{m}$ . . . . . 175

**B.10 Experimental measurement of deposition eigenchannels.** A composite SEM image of an on-chip disordered waveguide is presented in (a) with a delineation of the buffer region and a deposition region superimposed. In (b-e) the maximally enhancing/suppressing (red-dots/purple-diamonds) deposition eigenchannel profiles, measured experimentally, are juxtaposed with numerically simulated profiles (red-solid and purple-dashed lines): for four target regions centered at 10, 20, 30, and 40  $\mu\text{m}$ . . . . . 180

# List of Tables

2.1	Intensity moments of speckle patterns with different intensity PDFs .	25
-----	---	----

# Chapter 1

## Introduction

The goal of this dissertation is to develop a methodology for experimentally creating and controlling random light in free space and in diffusive media. In free space, the objective is to arbitrarily customize the intensity statistics and spatial-correlations of spatially-incoherent light [1–4]. In diffusive media, the aim is coherently controlling wave transport through –and throughout– multiple scattering systems [5,6]. In both cases, the lynchpin is coherent wavefront shaping.

### 1.1 Coherent Wavefront Shaping

Any static linear scattering-system, from a lens to a diffusive medium, will have a deterministic response to a given input wavefront. In principle, therefore, the response of a static linear scattering-system to any input complex-field can be mapped by a linear operator. Furthermore, this response operator can be represented by a “field reconstruction” matrix which transforms any input wavefront into the corresponding response field-pattern generated by the system: where both wavefronts are defined by complex-valued vectors. The response field pattern of interest can range from a transmitted wavefront, to a reflected wavefront, to the internal field distribution of the system. In practice, a field reconstruction

matrix can be experimentally measured using a phase-only spatial light modulator (SLM) and a CCD camera. Using the  $10^6$  phase-modulating pixels on a SLM, a complete-set of input wavefronts can be generated and sequentially illuminate a system to produce a complete set of response wavefunctions: which can be interferometrically measured by the CCD. With a field reconstruction matrix and the ability to precisely control the input wavefront of a system, a diverse range of both fundamental and applied physics research is possible.

## 1.2 Random Light In Free Space

In free space, spatially random light fields have the hallmark appearance of intricate –yet highly irregular– mosaics of diffraction-limited speckle grains. Because of their speckled appearance, random light fields are commonly referred to as speckle patterns. A speckle pattern can be characterized by the twofold complexity of its optical field. On one hand, the spatial-distribution of light in a speckle pattern is sufficiently *complicated* that speckles are described by a statistically stationary and ergodic random process. In this context, stationarity requires the statistical properties of an ensemble of speckle patterns to be the same as those of an individual speckle pattern within the ensemble. Ergodicity requires the statistical properties of two spatial positions –separated by more than one speckle grain size– to be independent and identical to those of the ensemble. On the other hand, speckle patterns are categorized by the joint probability-density function (PDF) of their *complex*-valued field. For example, a speckle pattern is said to be “fully developed” if its joint PDF is circularly invariant. In a fully-developed speckle pattern, therefore, the phase PDF is uniformly distributed between 0 and  $2\pi$ . Additionally, in a fully-developed speckle pattern the amplitude and phase profiles are statistically independent. Rayleigh speckles –the most common family of speckle patterns– obey a circular-Gaussian field PDF which results in

a negative exponential intensity PDF. See Fig. 1.1 for an example. Furthermore, they only possess short-ranged spatial intensity correlations which are determined by the average speckle grain shape: which is dictated by the diffraction limit. For more information on standard speckle patterns, consult Refs. [7–11].

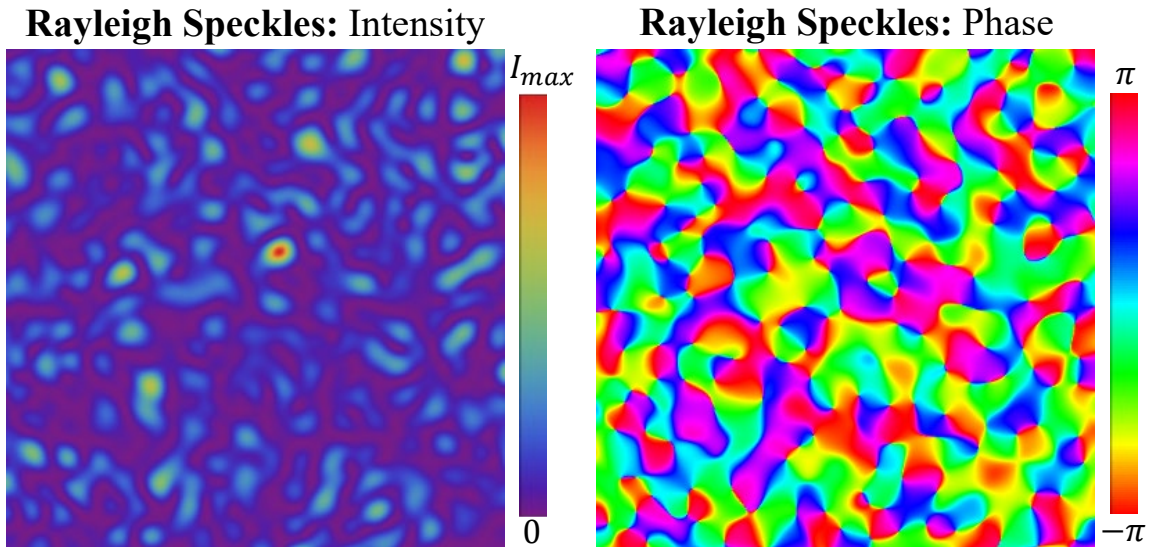


Figure 1.1: **An example of Rayleigh speckles.**

Until recently, Rayleigh intensity statistics were considered close to a universal property of speckle patterns. This is because in most cases, non-Rayleigh speckles can be classified as either under-developed (the sum of a small number of scattered waves, or the phases of the waves are not fully randomized) or partially-coherent (the sum of incoherent partial waves) [12–20]. In both cases, the diversity of the intensity PDF’s functional-form is limited. Similarly, adherence to the Siegert relation is another common assumption made about random light fields. Specifically, that the spatial intensity correlation function of a complex-field is proportional to the squared magnitude of the spatial field correlation function: also known as the local correlation function. Based on this assumption, the spatial intensity correlation function of a speckle pattern is typically modified by altering the local correlation function: via amplitude modulation of the field’s Fourier compo-

nents [2, 15, 21–31]. Because the local correlation function is effectively the diffraction-limited point spread function of a system, this approach can be quite limiting in terms of the range of possible correlation functions. Despite these limitations on controlling the PDF and spatial-correlations of speckle patterns, there has been a plethora of interest in creating speckle patterns with tailored statistics and correlations [29, 30, 32–39]. This is due to the many potential applications of customized speckles. In structured-illumination imaging, for example, tailored speckles can be used for dynamic speckle illumination microscopy [40, 41], super-resolution imaging [42, 43], and as pseudo-thermal light sources for high-order ghost imaging [44–46]. Furthermore, a general method for customizing the statistics, topology and spatial order of laser speckle patterns would be a valuable tool for synthesizing optical potentials for cold atoms [47], microparticles [48–51], and active media [52–54].

In the second chapter of this dissertation, a general method for arbitrarily customizing the intensity PDF of a speckle pattern on a target plane is presented. By judiciously modulating the phase-front of a monochromatic laser beam with a SLM, different families of speckle patterns with tailored intensity PDFs can be experimentally generated. Relative to Rayleigh speckles, the customized speckles exhibit radically different topologies yet maintain the same spatial correlations. Additionally, the customized speckles are fully developed, ergodic, and stationary: with circular non-Gaussian statistics for the complex field.

In the third chapter, a method for creating fully-developed speckles with strong non-local intensity correlations is experimentally demonstrated and the resulting speckles are theoretically analyzed. This technique is denoted “introducing non-local correlations” because the functional form of the spatial intensity correlations can be arbitrarily tailored without altering the field correlations. Furthermore, the introduction of non-local correlations can be accomplished while preserving the circular-Gaussian field-statistics of a

speckle pattern.

In the fourth chapter, an experimental method for customizing the intensity probability density function (PDF) of speckle patterns –while simultaneously introducing non-local spatial correlations among the speckle grains– is presented. The various families of fully-developed tailored speckle-patterns created by this method can exhibit radically different topologies, statistics, and variable degrees of spatial order. Irrespective of the distinct statistical properties, all of the speckle patterns are created by appropriately encoding high-order correlations into the phase front of a monochromatic laser beam with a spatial light modulator. In addition to the experimental demonstration, both the theoretical and practical limitations on the extent to which the intensity PDF and the spatial intensity correlations can be manipulated concurrently in a speckle pattern are explored.

In the fifth chapter, a family of “delta” speckle patterns are designed and used for parallelized nonlinear pattern-illumination microscopy: based on fluorescence photoswitching. In the proof-of-principle experimental demonstration, a spatial resolution three times higher than the diffraction limit of the illumination optics is obtained. In addition to the demonstration, the manner in which the delta speckles outperform standard speckles is illustrated: establishing that delta speckles are a potent tool in parallelized super-resolution microscopy.

### **1.3 Random Light In Diffusive Media**

Controlling random wave scattering in disordered systems is essential in a wide range of applications involving light, microwaves, and acoustic waves [55, 56]: such as deep-tissue imaging [57, 58], optogenetically controlling neurons [59, 60], non-invasive ultrasound surgery [61], and optimization of photoelectrochemical processes in strongly-scattering systems [62]. The fundamental challenge to overcome in disordered systems is the mul-

multiple scattering of waves, which results in a diffusive spread of the wave energy. For light, when a coherent wave enters a disordered system the photons scatter in random directions and, as a function of depth, the number of unscattered photons decays to zero exponentially. Past a certain depth –called the transport mean free path ( $\ell_t$ )– the photons are equally likely to travel in any direction [55, 56, 58, 63–68]. For visible light this transition from a beam into a diffuse glow occurs at  $\ell_t \approx 1$  mm in living cells [69],  $\ell_t \approx 10$  m in clouds [70], and  $\ell_t \approx 1$   $\mu\text{m}$  in white paint [71]. Until recently, the transport mean free path has been a fundamental barrier preventing non-invasive wave-based applications deep within disordered systems.

## Transmission Eigenchannels

Generally, studies aimed at controlling wave scattering through a diffusive system rely on the field transmission matrix,  $t$ , of the system: which maps the incident waves to the transmitted waves [5, 71–80]. The utility of the transmission matrix lies in its ability to connect input wavefronts to the corresponding output wavefronts. Specifically, the eigenvectors of  $t^\dagger t$  are the orthogonal set of input wavefronts which excite a set of disorder-specific wavefunctions –spanning the system– known as the transmission eigenchannels: each with a transmittance given by the corresponding eigenvalue  $\tau$ . One of the striking theoretical predictions of diffusive systems is the bimodal distribution of the transmission eigenvalues: with maxima at  $\tau = 0$  and  $\tau = 1$  [56, 81–86]. While transmission eigenvalues are intensely studied topics, transmission eigenchannels are relatively unstudied: due to the simultaneous theoretical and experimental complexity of the task.

The sixth chapter of this dissertation experimentally explores transmission eigenchannels inside nano-fabricated planar diffusive waveguides. The individual depth profiles of transmission eigenchannels *within* diffusive systems are directly observed, and the second order statistics are studied. The depth profiles of high-transmission eigenchannels

are shown to exhibit low realization-to-realization fluctuations. Furthermore, the experimental and numerical studies reveal the existence of inter-channel correlations, which are significant for low-transmission eigenchannels.

## **Energy Deposition Eigenchannels**

A significant challenge in fundamental physics and practical applications is depositing energy into a target region *deep* inside a diffusive system. Currently, it is known that coherently controlling the incident wavefront allows diffraction-limited focusing inside a diffusive system [64, 65, 87–91]. Typically, the appropriate incident wavefront is obtained via the time-reversal principle [92]: that the phase conjugate of an output field generated by a point source will focus back to that point [64]. Targets in many applications like neurons or early-stage tumors, however, are much larger than an optical-diffraction-limited focal spot and therefore wavelength-scaled light focusing does not correspond to maximal energy deposition into an extended target. Since the optimal spatial field distribution across the target is not known *a priori*, neither time reversal nor phase conjugation can be used to find the optimal incident wavefront. Furthermore, while feedback-based iterative optimization of the input wavefront [65] is efficient at reaching the global maximum when focusing light [93]; currently, this is not the case for energy delivery into a target of arbitrary size and shape.

In the seventh chapter the “deposition matrix” is introduced relating any input wavefront to its internal field distribution over a specified region inside the system. Deposition matrices are experimentally measured in diffusive waveguides and their eigenstates are excited to enhance/suppress the energy within different extended target regions. In addition to the experimental demonstration, a theoretical formalism for prediction the energy enhancement is developed.

## Remission Eigenchannels

Diffusive-waves have been used for sensing and imaging [94–103] in a diverse variety of random media: ranging from the earth’s crust [104–106] to the human brain [101, 107–109]. Often, in theoretical investigations and lab-based experiments, waves transmitted through diffusive media are utilized and studied for imaging and sensing. In many real-world applications, however, transmitted waves are unavailable and directly reflected waves cannot penetrate beyond one transport mean-free-path into the system. Therefore, in many applications remitted waves must be used: diffusive waves actively generated by an external source and emitted from the medium on the same side, from a separate location.

In the eighth chapter, an experimental study on diffusive-wave remission eigenchannels in open disordered systems is presented. The remission matrix,  $\mathcal{R}$ , of a diffusive system is introduced; which maps the wavefronts input over a finite region of a diffusive medium’s surface to the resulting diffusive waves re-emitted from a displaced region on the same surface. Using a modified version of the on-chip platform and experimental setup presented in Chapters 6 & 7, various remission matrices are experimentally measured. Subsequently, the individual remission eigenstates are excited, and their spatial structures are observed as a function of separation between the input and remission regions. We show that “open” remission eigenchannels enhance the output signal without sacrificing the light’s penetration-depth into the system.

# Chapter 2

## Customizing Speckle Intensity Statistics

### 2.1 Introduction

<sup>1</sup>Speckle formation is a phenomenon inherent to both classical and quantum waves. Characterized by a random granular structure, a speckle pattern arises when a coherent wave undergoes a disorder-inducing scattering process. As discussed in Chapter 1, the statistical properties of a speckle pattern are generally considered universal –commonly referred to as Rayleigh statistics– featuring a circular-gaussian distribution for the complex-field joint probability density function, and a negative-exponential intensity probability density function (PDF) [7–10]. Typically, non-Rayleigh speckles are classified as either under-developed (either the sum of a small number of scattered waves, or the phases of these waves are not fully randomized) or partially-coherent (the sum of incoherent partial waves) [12–20]. In both cases, the diversity of the intensity PDF’s functional form is limited. Recently, however, a simple method of creating non-Rayleigh speckle patterns with a phase-only spatial light modulator (SLM) was developed [33]. High-order correlations were encoded into the field by the SLM, leading to a redistribution of the light intensity

---

<sup>1</sup>The chapter material is primarily taken from reference [1]: Nicholas Bender, Hasan Yilmaz, Yaron Bromberg, and Hui Cao, “Customizing speckle intensity statistics”, *Optica*, vol. 5, 595-600, (2018).

among the speckle grains in the far-field. In this method, the speckle pattern could either possess an intensity PDF with a tail decaying slower or faster than a negative-exponential function. It was not known, however, if it was possible to have an intensity PDF of any functional form, such as increasing with intensity, or double-peaked at specific values.

In this chapter, we present a general method for tailoring the intensity statistics of speckle patterns by modulating the phase front of a laser beam with a SLM. Starting with a Rayleigh speckle pattern, we numerically apply a local intensity transformation to obtain a new speckle pattern which is governed by a target intensity PDF. Subsequently this pattern is experimentally generated in the far field of the SLM, where the requisite phase modulation is determined numerically via a nonlinear optimization algorithm. Via this process, we can create speckle patterns governed by arbitrary intensity PDFs: within a predefined intensity-range of interest. Such speckle patterns exhibit distinct topologies relative to Rayleigh speckles, while retaining the same spatial correlation length. A thorough study of the statistical properties reveals that the different ensembles of speckles created are unique relative to previously studied families of speckle patterns. Despite being fully-developed, ergodic, and stationary, the joint complex-field PDFs of the speckle patterns are circular non-Gaussian; with higher-order intensity moments differing from those of Rayleigh speckles. Both the intensity statistics and speckle topology evolve with beam propagation away from the target plane, wherein the speckle patterns eventually revert back to Rayleigh speckles. The technique outlined in this chapter provides a versatile framework for customizing speckle patterns for varied applications in microscopy, imaging and optical manipulation.

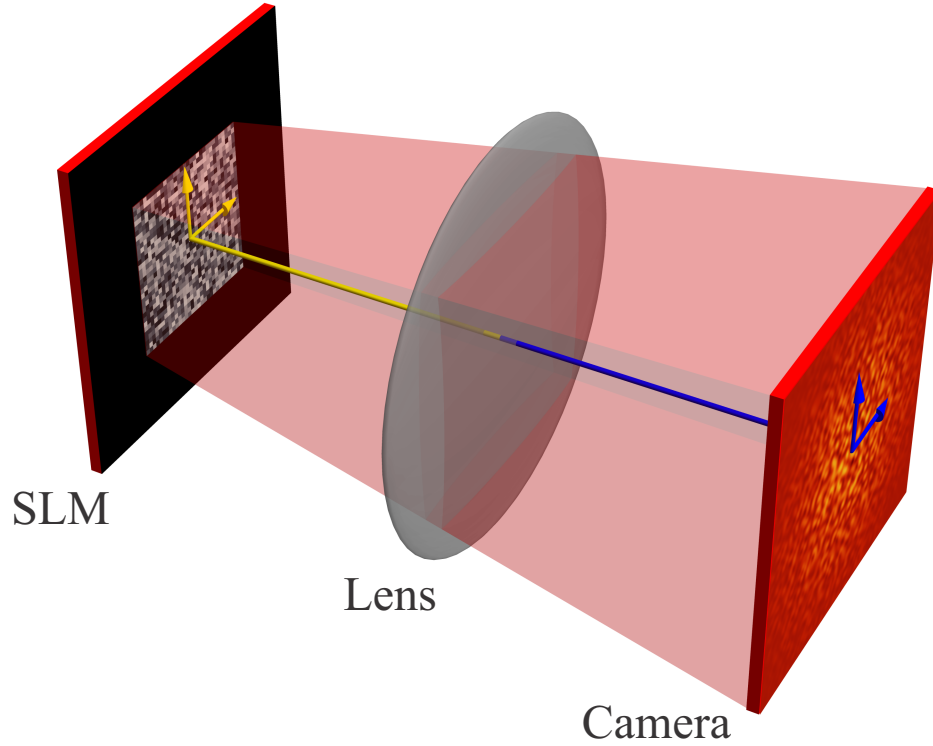


Figure 2.1: **A caricature of the experimental setup.** Light reflected by a spatial light modulator is Fourier transformed by a lens, and then imaged onto a detector.

## 2.2 Experimental Setup

The experimental setup described in this section, and characterized in Fig. 2.1, is used in the following four chapters to create customized speckle patterns. A reflective, phase-only SLM (Hamamatsu LCoS X10468) is illuminated with a linearly-polarized monochromatic laser beam with a wavelength  $\lambda = 642$  nm (Coherent OBIS). The laser beam is expanded and clipped by an iris to uniformly illuminate the SLM phase modulation region. The central part of the phase modulating region of the SLM is partitioned into a square array of  $32 \times 32$  macro-pixels, each consisting of  $16 \times 16$  pixels. The pixels on the SLM can modulate the incident light's phase between the values of 0 and  $2\pi$  in increments of  $2\pi/170$ . However, a small portion of reflected light from the SLM is unmodulated. To bypass the unmodulated light, we write a horizontal binary-phase diffraction-grating within each

macropixel –with a grating period of 8 pixels– and work with the light diffracted to the first-order. The remaining illuminated pixels outside the central square diffract the laser beam away from the target plane via a vertical phase-grating. The SLM is placed at the front focal plane of a lens,  $f = 500$  mm, and the intensity pattern at the back focal plane is recorded by a charge-coupled device (CCD) camera (Allied Vision Prosilica GC660). The laser beam incident upon the SLM is linearly polarized and the incident angles on the camera are too small to introduce a significant polarization component in the axial direction. Thus, the light waves incident on the camera can be modeled as scalar waves. To a good approximation, the field pattern on the camera chip is the Fourier transform of the field on the SLM surface.

## 2.3 Method

### 2.3.1 Local Intensity Transformation

Next, we describe how to determine a target speckle intensity-pattern governed by an arbitrary intensity-PDF. When a random phase pattern (uniformly-distributed between 0 and  $2\pi$ ) is displayed on the SLM, the intensity pattern recorded by the camera is a Rayleigh speckle pattern. We numerically perform a local intensity transformation on a recorded Rayleigh speckle pattern which converts it into a speckle intensity-pattern governed by the desired PDF,  $F(\tilde{I})$ . The intensity PDF of the Rayleigh speckle pattern,  $P(I) = \exp[-I/\langle I \rangle]/\langle I \rangle$ , can be related to the target PDF,  $F(\tilde{I})$ , by:

$$P(I)dI = F(\tilde{I})d\tilde{I}. \quad (2.1)$$

This relation is the starting point for determining the local intensity transformation  $\tilde{I} = f(I)$ , which is applied to the intensity values of a Rayleigh speckle pattern to create a new

speckle pattern with the desired PDF. To solve for the specific intensity transformation associated with the PDF  $F(\tilde{I})$ , we write Eq. 2.1 in integral form with  $\langle I \rangle = 1$ :

$$\int_0^I e^{-I'} dI' = \int_{\tilde{I}_{\min}}^{\tilde{I}} F(\tilde{I}') d\tilde{I}'. \quad (2.2)$$

Evaluating the integrals and solving for  $\tilde{I}$  as a function of  $I$  gives the desired local intensity transformation  $\tilde{I} = f(I)$ . In addition to altering the intensity PDF, such a transformation provides the freedom to regulate the maximum and minimum intensity values of the transformed pattern. We may arbitrarily set  $\tilde{I}_{\max}$  or  $\tilde{I}_{\min}$ , as long as the following normalization conditions hold:

$$\int_{\tilde{I}_{\min}}^{\tilde{I}_{\max}} F(\tilde{I}') d\tilde{I}' = 1 \quad (2.3)$$

and

$$\langle \tilde{I} \rangle = \int_{\tilde{I}_{\min}}^{\tilde{I}_{\max}} \tilde{I}' F(\tilde{I}') d\tilde{I}' = \langle I \rangle. \quad (2.4)$$

This regulatory ability is useful in practical applications, such as those using speckle illumination, where without altering the total power of illumination the maximal intensity value can be set below the damage threshold of a sample or the minimum intensity value can be set to exceed the noise floor.

The local intensity transformation is typically nonlinear and therefore produces spatial frequency components that are higher than those in the original pattern, and therefore, outside the range of spatial frequencies accessible in the experiment. Nevertheless, these components can be removed from the intensity pattern by applying a digital low-pass Fourier filter, where the allowed frequency window is a square.<sup>2</sup> The high frequency cut-off of the filter is determined by the average value of the maximum spatial-frequency

---

<sup>2</sup>See Chapter 4 for a more sophisticated technique.

component present in Rayleigh speckle patterns generated by our setup. The resulting filtered-pattern, however, will have an intensity PDF,  $\tilde{F}(I)$ , slightly deviating from the target one,  $F(\tilde{I})$ . Such deviations can be eliminated by applying an additional scalar intensity transformation,  $\tilde{I} = \tilde{f}(I)$ , that is obtained from

$$\int_{I_{\min}}^I \tilde{F}(I')dI' = \int_{\tilde{I}_{\min}}^{\tilde{I}} F(\tilde{I}')d\tilde{I}'. \quad (2.5)$$

The process of performing a local intensity transformation, and subsequently applying a digital low-pass Fourier filter, can be iteratively repeated as a conventional Gerchberg-Saxton algorithm [110] until the target PDF is obtained for a speckle pattern obeying the spatial frequency restrictions. Repetition of this procedure with different initial patterns of Rayleigh speckles creates a statistical ensemble of independent customized intensity patterns which possesses the same PDFs. It is important to note, however, that certain PDFs cannot be generated experimentally because of the finite range of spatial frequencies allowed in a speckle pattern due to the diffraction limit. One example, is the black

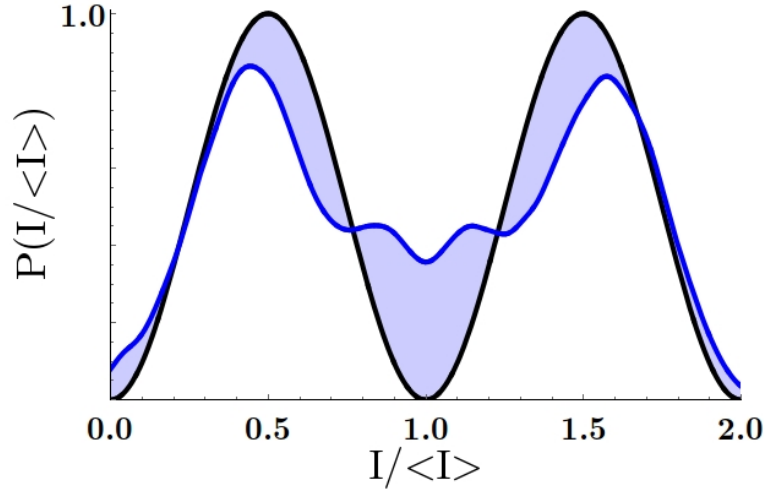


Figure 2.2: **A physically impossible intensity PDF.** The black curve is the original desired PDF, and the blue curve is the numerically obtained one after a local intensity transformation algorithm. Their difference (shaded area) is due to the limited range of the spatial frequencies in the speckle pattern.

bimodal intensity PDF shown in Fig. 2.2. The original function used to generate this PDF is  $\sin^2(\pi I/\langle I \rangle)$  over the intensity range  $0 \leq I \leq 2$ , and 0 elsewhere. This PDF is not physically possible for classical light because if  $P(I/\langle I \rangle)$  is zero –or has a discontinuity at any intensity value in-between the minimum and maximum values– it requires a corresponding discontinuity in the spatial profile of the speckle pattern. Consequently, when  $\sin^2(\pi I/\langle I \rangle)$  is used in the iterative PDF transformation algorithm, the resulting PDF converges to the blue curve plotted in Fig. 2.2. The blue shading in this figure highlights the regions where deviations occur, primarily centered around  $I/\langle I \rangle = 1$ , where  $\sin^2(\pi I/\langle I \rangle) = 0$ .

### 2.3.2 Experimental Speckle Generation

Having created an ensemble of intensity patterns obeying a desired PDF, the next step is to determine the phase patterns –which when displayed on the SLM– generate the desired intensity patterns on the camera plane.

#### Speckle Spatial-Sampling

Assuming the SLM consists of a  $N \times N$  array of macro-pixels, a discrete Fourier transform gives a  $N \times N$  array of independent elements, each representing a speckle grain. To avert the effects of aliasing and uniquely define the spatial profile measured by the camera, it is necessary to sample the speckle pattern at or above the Nyquist limit. This means every speckle grain should be sampled at least twice along each spatial axis. Thus the  $N \times N$  speckles generated on the camera chip must be sampled by at least  $2N \times 2N$  points when defining a target intensity pattern to create. It is important to note, however, that this  $2N \times 2N$  intensity array –representing a speckle pattern– contains correlations between adjacent elements. Furthermore, higher spatial-sampling does not alter the information content of the pattern, and therefore, we can record the experimentally measured

speckle patterns well above the Nyquist limit with the CCD camera:  $\sim 6$  camera pixels per speckle grain along each axis. Because the phases on the SLM are transcendently related to the intensity values on the Fourier plane, there is no closed form solution for the  $N^2$  independent phases of the SLM macropixels to generate the minimally required  $4N^2$  partially correlated intensity values of the target speckle pattern. Thus, we have to find the solution numerically. To facilitate the convergence to a solution, we reduce the area we attempt to control –on the camera plane– to the central quarter region representing the Fourier transform of the phase modulating region of the SLM.

### **Field Transmission Matrix**

Experimentally the Fourier relation between the field reflected off the SLM and that in the camera plane is only approximate. We characterize the precise relation by measuring the field transmission matrix. In addition to encapsulating the experimental imperfections induced by optical misalignment, SLM surface curvature, lens aberrations, and nonuniform laser illumination of the SLM, employing the transmission matrix provides a general formalism that can be adapted to other setups (e.g., holographic optical tweezers [111]) or to tailor the speckle statistics on a different plane than the Fourier. It also enables speckle tailoring after a disordered scattering medium; however, the degree to which this can be accomplished will depend on the number of degrees-of-freedom in the customization plane. In this work, the transmission matrix is measured with a common path interference method akin to those in [72, 79, 112]; for details see Appendix A. Briefly, the phase modulating region of the SLM is divided into two equal parts. We sequentially display a series of orthogonal phase patterns on one part while keeping the phase pattern on the second part fixed, which generates a reference pattern. Simultaneously, we record the resulting interference patterns on the camera. Subsequent to this, we exchange the role of each part and repeat the measurement. Using all the interference patterns we can construct a linear

mapping between the field on the SLM and the field on the camera: namely, the transmission matrix. The measured transmission matrix only slightly deviates from a discrete Fourier transform in our setup. For a given phase pattern displayed on the SLM, the average differences between the speckle intensity-pattern measured by the CCD camera and that predicted by the field transmission matrix is less than 10%.

### Non-Linear Optimization Algorithm

Using the measured transmission matrix with a nonlinear-optimization algorithm, we find a solution for the SLM phase array which generates a given target intensity pattern in the camera plane. To find a solution for the SLM phase array, we numerically minimize the difference between the target pattern,  $\tilde{I}(\mathbf{r})$ , and the intensity pattern,  $I_M(\mathbf{r})$ , obtained after applying the field transmission matrix to the SLM phase array: as a function of the SLM phases. Specifically, the intensity pattern generated by the transmission matrix is given by

$$I_M(\mathbf{r}) = \left| \sum_n t_n(\mathbf{r}) e^{i\theta_n} \right|^2, \quad (2.6)$$

where  $\theta_n$  represents the phase displayed on the  $n^{\text{th}}$  SLM pixel and  $t_n(\mathbf{r})$  is the element of the transmission matrix mapping the  $n^{\text{th}}$  SLM pixel to the  $\mathbf{r}$  position on the camera. The cost function we use in our algorithm,

$$\sum_{\mathbf{r}} |\tilde{I}(\mathbf{r}) - I_M(\mathbf{r})|^2, \quad (2.7)$$

is minimized by tuning the SLM phases:  $\theta_n$ . Furthermore, the gradient of our cost function can easily be defined by taking the derivative with respect to  $\theta_n$ . We use the original SLM phase-pattern –that generates the Rayleigh speckle pattern used to seed the local intensity transformation– as the initial condition in our algorithm. Because the  $N^2$  intensity values in the target region are partially correlated, the number of degrees of freedom in the target

region is effectively less than the number of degrees of freedom we have available on the SLM. Due to this we can use a local-search algorithm, the Broyden-Fletcher-Goldfarb-Shanno (BFGS) algorithm, [113, 114] to solve for the SLM phase array and will always obtain a solution in a relatively short amount of time. For example, using *Matlab* on a laptop with an *Intel i7-4910MQ* processor (2.9 GHz base frequency) and  $N = 32$ ; it takes about 45s on average to obtain a SLM phase-array which generates a customized speckle pattern. In the process of solving for a SLM phase array, our local-search algorithm appropriately encodes high-order correlations into the phase values of the SLM phase array.

Irrespective of the specific optimization method used to generate a phase pattern on the SLM –which creates customized speckles on the camera plane– the problem is non-convex and the search’s parameter-space is vast. Therefore, while it is possible to directly search for a SLM phase-pattern which generates a customized speckle pattern with the desired statistical properties –without using a target intensity pattern– this approach is not necessarily ideal. For example, if such a method fails to converge to an acceptable solution it would be difficult to determine if this was because the algorithm was not optimal or if the desired statistics were fundamentally impossible to encode into a speckle pattern. By partitioning our method into two steps –first generating a speckled intensity pattern with the desired statistics and then creating the speckle pattern with the SLM– this can be differentiated. Furthermore, this division reduces the parameter space of our search for a solution while also enabling us to use a *local*, as opposed to a *global*, search algorithm. As a result, our algorithm always converges to an acceptable solution in a reasonable amount of time.

## 2.4 Customized Speckle Patterns

Examples of experimentally generated speckle patterns with customized intensity statistics are shown in Figs. 2.3(b-e) with  $\langle I \rangle$  normalized to 1. In (b) the speckle pattern was designed to have a uniform intensity PDF, between the predefined intensity range of  $I = 0$  and  $I = 2$ . This example illustrates that it is possible to create speckle patterns with non-decaying PDFs in addition to confining the speckle intensities within a finite range. Taking this one step further in (c), we first make the PDF increase linearly with intensity,  $P(I) = I$ , then have it drop rapidly to zero above the specified threshold of  $I = \sqrt{2}$ . To demonstrate that our method is not restricted to monotonic functions, in (d) we create a speckle pattern with a unimodal intensity PDF given by  $\sin[(\frac{\pi}{2})I]^2$  between  $I_{\min} = 0$  and  $I_{\max} = 2$ . To further increase the complexity of the speckle statistics, (e) shows an example of a bimodal PDF.

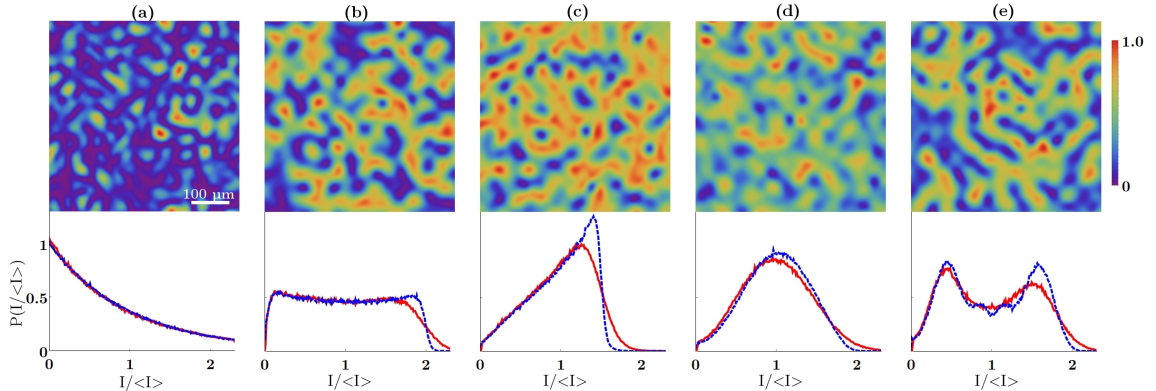


Figure 2.3: **Example customized speckles.** A Rayleigh speckle pattern (a) and customized speckle patterns with distinct intensity statistics (b-e). In the top row, each pattern is  $504 \mu\text{m}$  by  $504 \mu\text{m}$ , and the maximum intensity is normalized to 1. The associated PDF, shown in the lower row, is uniform (b), linearly increasing (c), peaked at a non-zero intensity (d), and bimodal (e), over a predefined range of intensity. The red solid curves are experimental data, the blue dashed curves are from numerically generated target speckle patterns. Both are the result of spatial and ensemble averaging over 50 independent speckle patterns.

In all cases, the experimentally generated speckle patterns possess intensity PDFs which follow the target functional form over the intensity ranges of interest and converge to zero, quickly, outside. Small deviations between the experimental PDFs and the target ones are caused by error in the transmission matrix measurement due to experimental noise and temporal decorrelations. We modeled these effects and numerically reproduced the deviations (see Appendix A for a full description of our model). Our model describes why the deviations are stronger at higher intensity values or where the PDF varies rapidly with intensity.

Additionally, Fig. 2.3 illustrates how the topology of the customized speckle patterns changes in accordance with the PDF. The spatial intensity profile of a Rayleigh speckle pattern in (a) can be characterized as a random interconnected web of dark channels surrounding bright islands. Conversely for speckles with a linearly increasing PDF in (c), the spatial intensity profile is an interwoven web of bright channels with randomly dispersed dark islands. Similarly, the spatial structure of speckles with a bimodal PDF in (e) consists of interlaced bright and dim channels. The continuous network of high intensity in the customized speckle pattern, which is absent in the Rayleigh speckle pattern, will be useful for controlling the transport of trapped atoms or microparticles in optical potentials.

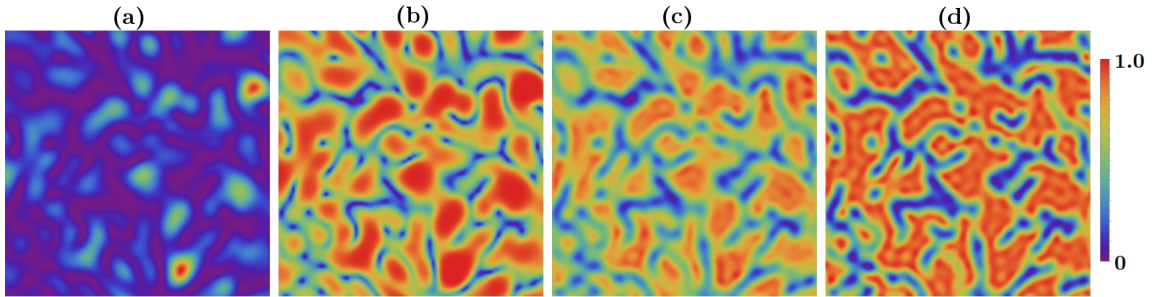


Figure 2.4: **The topological change of a customized speckle pattern.** A Rayleigh speckle pattern in (a) is transformed to the speckle pattern in (b) via a local intensity transformation. Application of a digital low-pass Fourier filter results in the pattern in (c). Multiple iterations of intensity transformations and filtering result in the final pattern in (d) which obeys the desired intensity PDF and spatial frequency constraints. The maximum intensity is normalized to 1.

The topological changes in the customized speckles result from the local intensity transformation and digital low-pass Fourier filtering. An example of this transformation is shown in Fig. 2.4. The original Rayleigh speckle pattern in (a) has a maximal probability-density of vanishing intensity,  $I = 0$ , leading to the dark channels surrounding bright islands in the spatial profile of the speckle pattern. Application of a local intensity transformation –to make the PDF increase linearly with intensity and then rapidly converge to zero above a threshold– results in the speckle pattern shown in (b). Due to the enhanced probability-density of high intensity and reduced probability-density of low intensity, the bright grains are enlarged while the dark channels are narrowed. The application of a digital low-pass Fourier filter blurs the narrow dark lines in between the bright grains (c). After iterating the process of a local intensity transformation followed by a low-pass filter, neighboring bright grains are merged to form channels that encompass dark islands (d).

## 2.5 Statistical Properties Of Customized Speckle Patterns

In this section, we analyze the statistical properties of the customized speckle patterns to illustrate their stark difference relative to previously studied speckles.

### 2.5.1 Phase-PDF & Spatial Correlations

We start by verifying that the speckle patterns are fully developed and the phase distribution,  $\Phi(\theta)$ , of the generated speckled fields is uniform over a range of  $2\pi$ . To find  $\Phi(\theta)$ , we use the measured transmission matrix and the SLM phase-patterns to recover the fields associated with the intensity patterns recorded by the CCD camera. Figure 2.5(a) plots  $\Phi(\theta)$  in the target region for the four customized PDFs shown in Figure 2.3(b-e), in addition to the case of a Rayleigh PDF. All cases have nearly constant values over  $[0, 2\pi]$ , thus our speckle patterns are fully developed. This property differentiates our speckle patterns

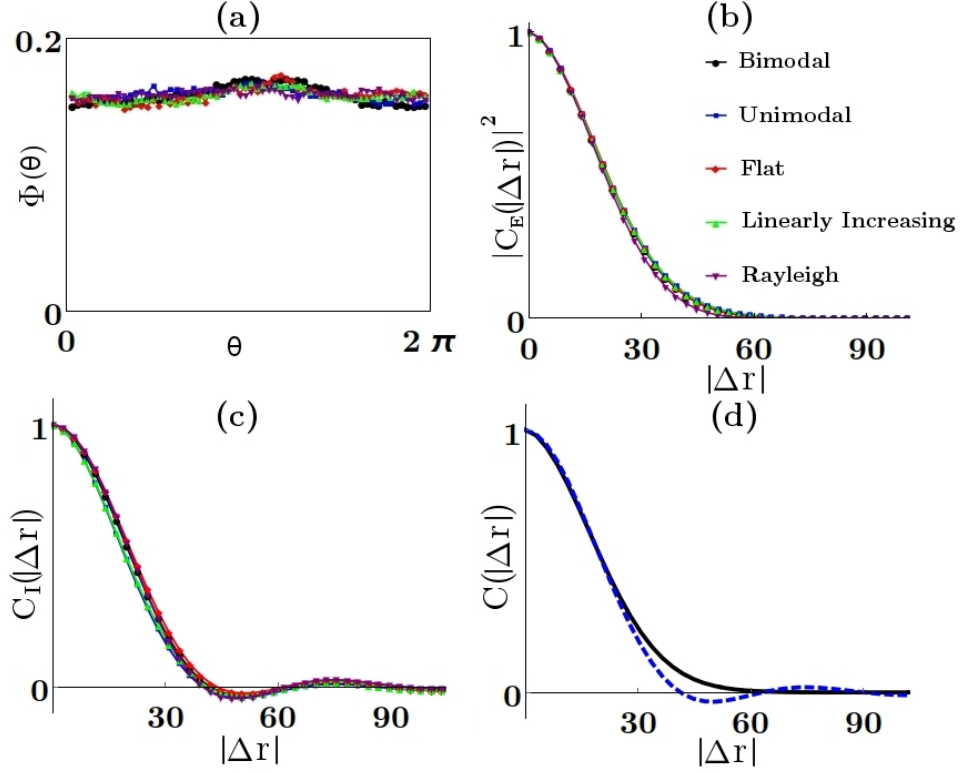


Figure 2.5: **Characteristics of customized speckle patterns.** (a) The phase histogram of the speckled fields demonstrates that they are all fully developed. (b) The spatial field correlation function  $|C_E(|\Delta \mathbf{r}|)|^2$  and (c) the spatial intensity correlation function  $C_I(|\Delta \mathbf{r}|)$ , of the customized speckles, remain the same as in Rayleigh speckles. In (a-c), the four customized speckle patterns have constant (black), linearly increasing (red), unimodal (blue), bimodal (green) PDFs, and the purple is for Rayleigh speckles. (d) Comparing  $|C_E(|\Delta \mathbf{r}|)|^2$  (black curve) to  $C_I(|\Delta \mathbf{r}|)$  (blue dashed curve), both averaged over the 5 curves in (b) and (c) respectively, to confirm they have the same correlation width.

with a unimodal PDF, shown in Figure 2.3(d), from partially developed speckle patterns which possess a similar intensity PDF [8].

Next, we check whether additional spatial correlations are introduced into the customized speckle patterns, relative to Rayleigh speckles. To this end, we calculate the 2D spatial correlation function of the speckled field:  $C_E(\Delta \mathbf{r}) = \langle \tilde{E}(\mathbf{r})\tilde{E}^*(\mathbf{r} + \Delta \mathbf{r}) \rangle / \langle \tilde{I} \rangle$ . As shown in Fig. 2.5(b), the customized speckles have a field correlation function similar to a Rayleigh speckle pattern. This means the way we tailor the speckle statistics does not affect the spatial field-correlation function. Furthermore, the 2D spatial intensity-correlation

function,  $C_I(\Delta\mathbf{r}) = (\langle \tilde{I}(\mathbf{r})\tilde{I}(\mathbf{r} + \Delta\mathbf{r}) \rangle - \langle \tilde{I} \rangle^2) / (\langle \tilde{I}^2 \rangle - \langle \tilde{I} \rangle^2)$ , plotted in Fig. 2.5(c) for the four customized speckles, has the same width as a Rayleigh speckle pattern. Hence, we can manipulate the speckle intensity-PDF without altering the spatial correlation length.

Similar to the Rayleigh speckles, the customized speckle patterns have the same width for  $\langle |C_E(\Delta\mathbf{r})|^2 \rangle$  and  $\langle C_I(\Delta\mathbf{r}) \rangle$ , as shown in Fig. 2.5(d). Relative to  $\langle |C_E(\Delta\mathbf{r})|^2 \rangle$ , however,  $\langle C_I(\Delta\mathbf{r}) \rangle$  exhibits small oscillations on the tail. These are attributed to the low-pass Fourier filtering of the intensity pattern, which we use to remove the high spatial frequency components introduced during the nonlinear transformation of a Rayleigh speckle pattern. For confirmation of this, we applied the digital low-pass Fourier filter to Rayleigh speckle patterns and the same oscillations appeared in the spatial intensity correlation function, shown in Fig. 2.5(c).

## 2.5.2 Higher-Order Statistics

Now we investigate whether the generation of tailored speckle patterns can be described statistically as a stationary and ergodic process. For a target intensity PDF, we numerically create 2500 speckle patterns consisting of 2500 speckle grains each. Fig. 2.5(a,b) shows the results for the bimodal PDF. In (a), the intensity PDF obtained for each of the 2500 ensembles is invariant as a function of ensembles, indicating the speckle patterns are stationary. In (b), the ensemble-averaged intensity PDF for individual spatial positions in the speckle patterns is also invariant as a function of spatial position and statistically identical to (a), demonstrating the ergodicity of the speckle patterns.

Figure 2.6(c) shows the joint complex-field PDF of the bimodal speckles is circular non-Gaussian, in contrast to the circular Gaussian PDF of Rayleigh speckles. Circularity reflects the fact that the amplitude and phase of the speckled field  $E$  –at a single point in space– are uncorrelated [8, 10]. Figure 2.6(d) shows the joint PDF  $P(I_1, I_2)$  for two speckle intensities at locations separated by more than the average speckle grain size.

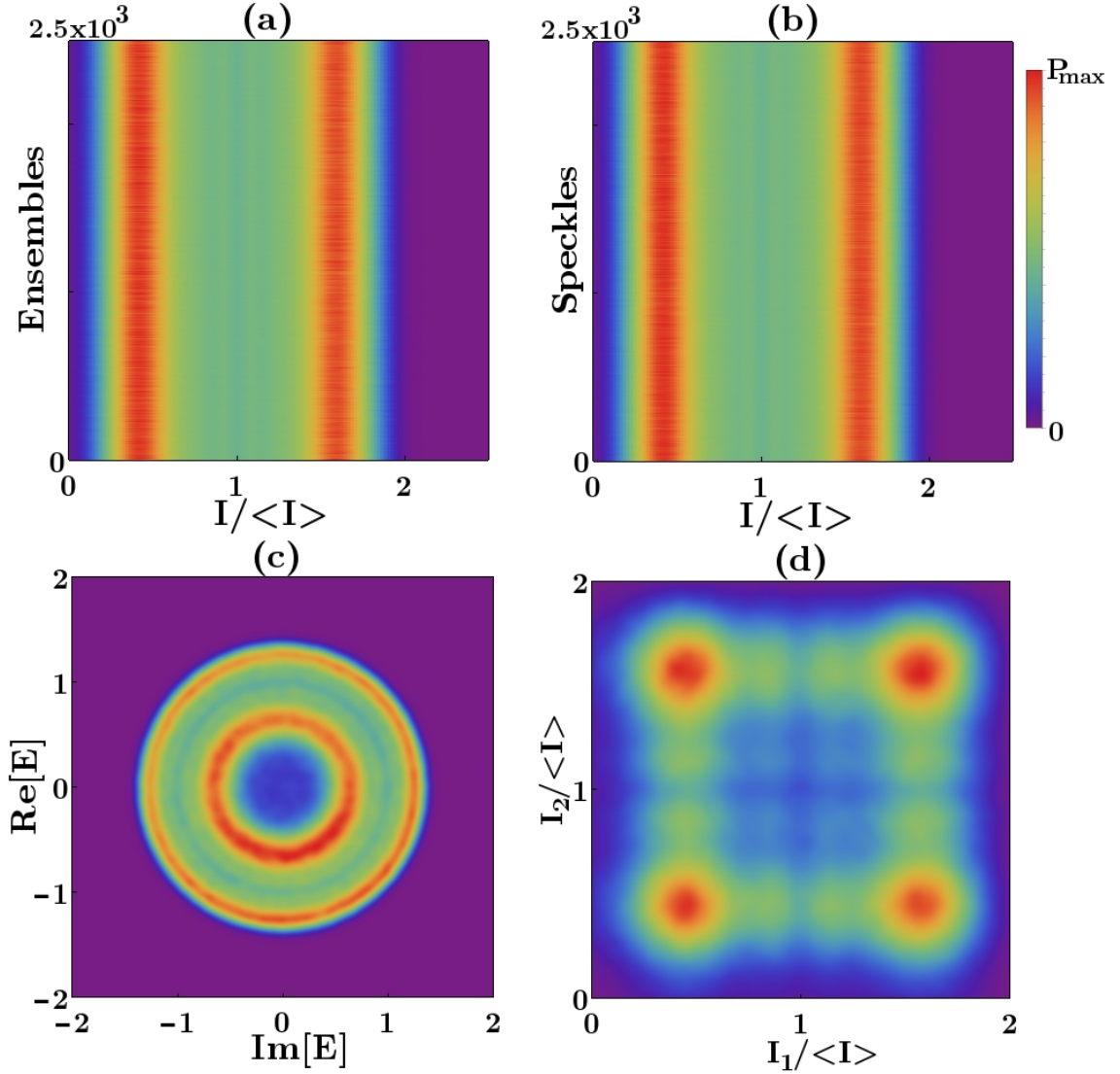


Figure 2.6: **Some higher-order statistical properties of the customized speckle patterns with a bimodal intensity PDF.** (a) The spatially averaged intensity PDF  $P_S(I)$  of 2500 speckle patterns verifies that the speckle patterns are stationary. (b) The ensemble-averaged intensity PDF  $P_E(I)$  –within the area of a single speckle grain– for each spatial position in a pattern confirms the speckles are ergodic. (c) The complex-amplitude joint-PDF for the speckled field  $P(\text{Re}[E], \text{Im}[E])$  displays circular non-Gaussian statistics. (d) The joint PDF for two intensities  $P(I_1, I_2)$  at spatial positions separated by approximately one speckle grain size (twice the spatial intensity correlation width) are uncorrelated. The results in (c,d) are obtained from averaging over space and 100 speckle patterns, a digital low-pass Fourier filter is applied to remove noise.

Because  $P(I_1, I_2) = P(I_1)P(I_2)$  the two intensities are statistically independent, which is consistent with the spatial correlation length of the speckled intensity. The other types of customized speckle patterns display similar characteristics.

### 2.5.3 Intensity-Moment Analysis

The non-Gaussian statistics of the tailored speckle patterns also emerge in their high-order intensity moments,  $\langle I^n \rangle = \int_0^\infty I^n P(I) dI$ , which differ from those of Rayleigh speckles: shown in Table 2.1. For the case of Rayleigh speckles generated by a Gaussian-random process, the high-order moments are related by  $\langle I^n \rangle = n! \langle I \rangle^n$  [9]. For the customized speckles,  $\langle I^n \rangle$  deviates from  $n! \langle I \rangle^n$ , because of high-order correlations among the partial waves that generate these patterns [33].

Table 2.1: **Intensity moments of speckle patterns with different intensity PDFs**

PDF	$\langle I \rangle$	$\langle I^2 \rangle$	$\langle I^3 \rangle$	$\langle I^4 \rangle$	$\langle I^5 \rangle$	$\langle I^6 \rangle$
Negative Exponential	1.00	2.00	6.00	24.0	120	720
Constant	1.00	1.35	2.06	3.39	5.87	10.51
Linearly Increasing	1.00	1.16	1.45	1.92	2.64	3.77
Unimodal	1.00	1.18	1.55	2.22	3.40	5.50
Bimodal	1.00	1.29	1.9	2.99	4.93	8.42

The nature of the high-order correlations dictating the divergence from Rayleigh statistics in the higher-order intensity moments can be illustrated in a relatively straightforward manner with the second-order intensity moment  $\langle I^2 \rangle$ . Consider a 1D speckled field  $E(r)$ , of length  $L$ , with spatial Fourier components,  $\varepsilon(\rho)$ , where  $\rho$  corresponds to the spatial position on the SLM plane:

$$E(r) = \frac{1}{\sqrt{L}} \sum_{\rho=0}^{L-1} \varepsilon(\rho) e^{i \frac{2\pi}{L} r \rho}. \quad (2.8)$$

With this expression, the second moment can be written as:

$$\langle I^2 \rangle = \langle E(r)E^*(r)E(r)E^*(r) \rangle_r \quad (2.9)$$

$$= \left\langle \frac{1}{L^2} \sum_{\rho_1, \rho_2, \rho_3, \rho_4=0}^{L-1} \varepsilon(\rho_1)\varepsilon^*(\rho_2)\varepsilon(\rho_3)\varepsilon^*(\rho_4)e^{i\frac{2\pi r}{L}(\rho_1-\rho_2+\rho_3-\rho_4)} \right\rangle_r. \quad (2.10)$$

The quadruple summation can be broken into 4 terms

$$\langle I^2 \rangle = \mathcal{I}_1 + \mathcal{I}_2 + \mathcal{I}_3 + \mathcal{I}_4 \quad (2.11)$$

where the subindex of  $\mathcal{I}_n$  indicates the number of independent indices in the summation contributing to the term. For example,  $\mathcal{I}_1$  consists of elements in the sum where  $\rho_1 = \rho_2 = \rho_3 = \rho_4$ , and  $\mathcal{I}_4$  consists of elements in the sum where  $\rho_1 \neq \rho_2 \neq \rho_3 \neq \rho_4$ . While the expressions are a tad cumbersome, they are simplified considerably by spatial averaging and using the Kronecker-delta identity  $\delta(\rho, \rho') = 1/L \sum_{r=0}^{L-1} \exp[i2\pi r(\rho - \rho')/L]$  to obtain the following after re-indexing:

$$\begin{aligned} \mathcal{I}_1 &= \frac{1}{L^2} \sum_{\rho_1=0}^{L-1} |\varepsilon(\rho_1)|^4 \\ \mathcal{I}_2 &= \frac{2}{L^2} \sum_{\substack{\rho_1, \rho_2=0 \\ \rho_1 \neq \rho_2}}^{L-1} |\varepsilon(\rho_1)|^2 |\varepsilon(\rho_2)|^2 \\ \mathcal{I}_3 &= \frac{2}{L^2} \Re \left[ \sum_{\substack{\rho_1, \rho_2=0 \\ \rho_1 \neq \rho_2}}^{L-1} \varepsilon(\rho_1)^2 \varepsilon^*(\rho_2) \varepsilon^*(2\rho_1 - \rho_2) \right] \\ \mathcal{I}_4 &= \frac{1}{L^2} \sum_{\substack{\rho_1, \rho_2, \rho_3=0 \\ \rho_1 \neq \rho_2 \neq \rho_3}}^{L-1} \varepsilon(\rho_1)\varepsilon^*(\rho_2)\varepsilon(\rho_3)\varepsilon^*(\rho_1 - \rho_2 + \rho_3). \end{aligned} \quad (2.12)$$

Of the four terms,  $\mathcal{I}_1$  and  $\mathcal{I}_3$  converge to zero while  $\mathcal{I}_2$  converges to  $2\langle I \rangle^2$  as a function of  $1/L$ . So, for large speckle patterns the second moment of the intensity is approximately

given by:

$$\langle I^2 \rangle \simeq 2\langle I \rangle^2 + \frac{1}{L^2} \sum_{\substack{\rho_1, \rho_2, \rho_3=0 \\ \rho_1 \neq \rho_2 \neq \rho_3}}^{L-1} \varepsilon(\rho_1) \varepsilon^*(\rho_2) \varepsilon(\rho_3) \varepsilon^*(\rho_1 - \rho_2 + \rho_3). \quad (2.13)$$

The equation demonstrates that the presence of high-order correlations in the Fourier-components of the speckle pattern enable the intensity statistics to deviate from Raleigh statistics. While the expression for the higher-order correlations required to modify  $\langle I^2 \rangle$  has been derived, other higher intensity moments will have functionally different higher-order correlations. For example,  $\langle I^3 \rangle$  will require additional 6-th order correlations between the Fourier components of the field and  $\langle I^4 \rangle$  will require additional 8-th order relations.

## 2.6 Axial Propagation

Finally, we study how the tailored speckle patterns evolve as they propagate axially along the z-axis. Our method gives the target PDF for speckle patterns on the Fourier plane of the SLM. Outside of the Fourier plane, however, the intensity statistics and topology may change. In the case of a Rayleigh speckle pattern, the spatial pattern changes upon propagation while the intensity PDF remains a negative exponential. We define  $R_l$  as the axial correlation length of the intensity pattern, which corresponds to the Rayleigh range and gives the longitudinal length of a single speckle grain. In our setup, this corresponds to translating the CCD camera  $\approx 1$  cm away from the Fourier plane. Alternatively, the speckle pattern can be propagated by multiplying the phase-pattern on the SLM by a quadratic phase-parabola, with a scalar prefactor proportional to the propagation along  $z$ . Experimentally, we verified that the two techniques are equivalent up to  $3R_l$  away from the Fourier-plane of the SLM.

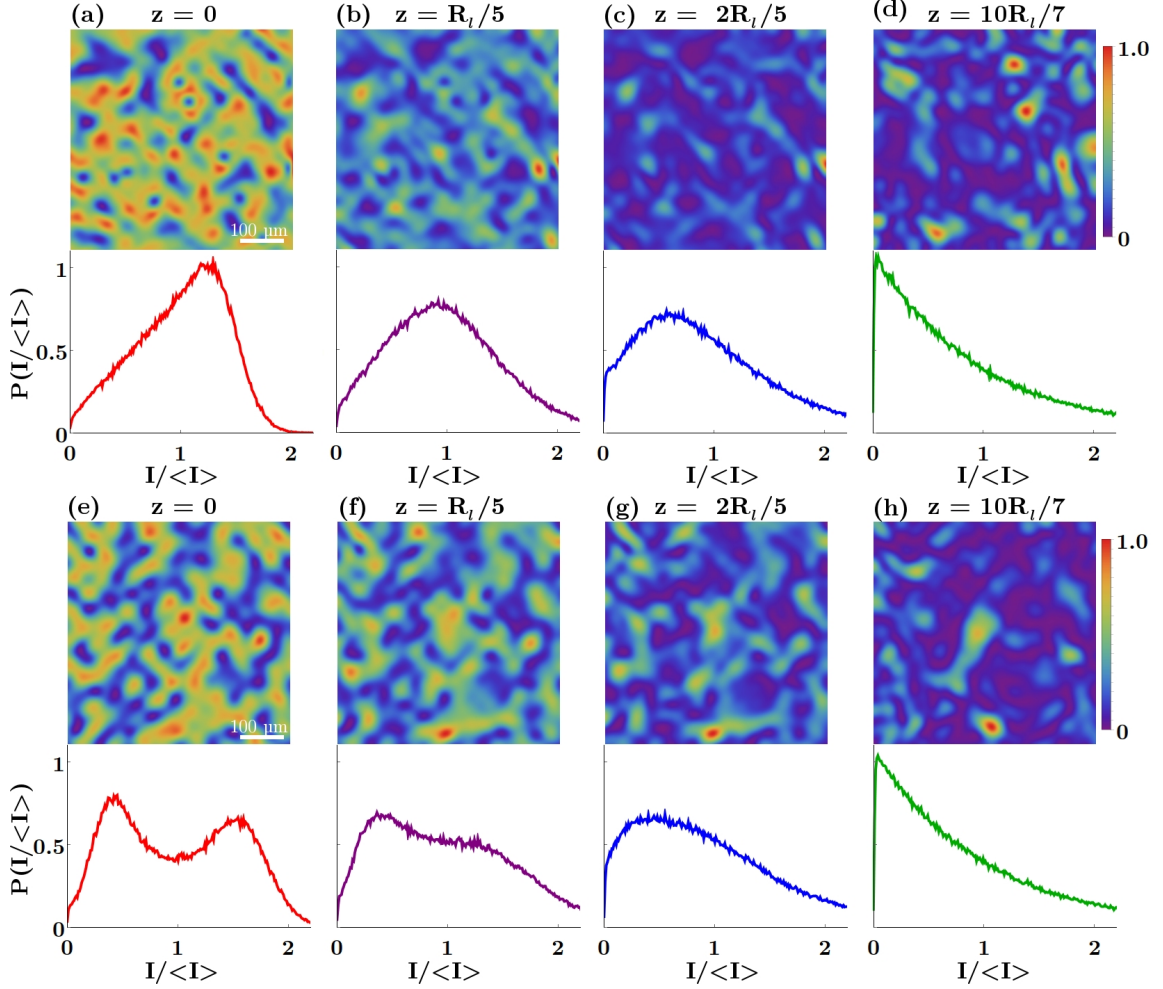


Figure 2.7: **Evolution of customized speckle patterns upon axial propagation.** The intensity PDF at the Fourier plane of the SLM ( $z = 0$ ) is linearly increasing (a) and bimodal (e). The distance from the Fourier plane is  $R_l/5$  (b, f),  $(2/5)R_l$  (c, g), and  $(10/7)R_l$  (d, h).

The top row of Fig. 2.7 shows the axial evolution of speckles that have a linearly increasing PDF at the Fourier plane,  $z = 0$ , in (a). As the speckle pattern propagates to  $z = R_l/5$ , the PDF becomes bell-shaped in (b). With further propagation, the maximum of the PDF migrates to a smaller intensity value, as shown in (c) for  $z = (2/5)R_l$ , until it reaches  $I = 0$ . The speckles revert to Rayleigh statistics at  $z \approx R_l$ , beyond which the PDF maintains a negative exponential, as shown in (d) for  $z = (10/7)R_l$ . The topology of the speckle pattern evolves together with the intensity PDF: the interconnected web of bright channels first attenuates upon propagation, then breaks into isolated islands.

In Fig. 2.7(e-f), we show the axial evolution of a speckle pattern with a bimodal PDF at  $z = 0$  in (e). As the pattern propagates to  $z = R_l/5$  in (f), the peaks are asymmetrically eroded, with the high intensity peak diminishing first. Further propagation to  $z = (2/5)R_l$  results in a unimodal PDF in (g). Once the axial distance  $z$  exceeds  $R_l$ , the speckles return to Rayleigh statistics, as shown in (h) for  $z = (10/7)R_l$ . A corresponding change of speckle topology is seen: the bright channels disappear first, then the dim channels fracture, while neighboring dark islands merge to form channels. Therefore, axial propagation, within the range of  $R_l$ , alters the intensity PDF and the speckle topology.

This behavior can be understood in the Fresnel approximation, where the axial propagation of a field pattern adds a quadratic phase to its spatial Fourier spectrum [8]. Because the changes in the intensity PDF result from high-order correlations encoded into the phases of the Fourier components, the phase parabola accompanying axial-propagation erodes away the customized statistics as the speckles propagate axially (along  $z$ -axis).

## 2.7 Discussion & Conclusion

In conclusion, we have presented a general method for customizing speckle intensity-statistics using a phase-only SLM. The generated speckle patterns possess radically different intensity PDFs and topologies relative to Rayleigh speckles. However, they are fully developed speckles which maintain the basic characteristics of stationarity and ergodicity. Their unusual statistical properties engender a new type of speckle pattern with non-Gaussian statistics. Our method is versatile and compatible with a broad range of optical setups. Given the plethora of potential applications, it paves the way for new directions in both fundamental research (many-body physics in random optical potentials with tailored statistics) and applied research (speckle-illumination-based imaging and speckle optical tweezers).

# Chapter 3

## Introducing Non-Local Correlations Into Laser Speckles

### 3.1 Introduction

<sup>1</sup>A bedrock principle of statistical physics is the Siegert equation, which relates the first and second-order correlation functions. It is the foundation of common techniques such as Hanbury-Brown Twiss interferometry [115] and dynamic light scattering [116]. Despite its general use, it is not universal. In quantum optics, for example, photon anti-bunching violates the Siegert equation. This violation has been widely explored in studies of non-classical light [117]. For classical wave transport in mesoscopic systems, the violation of the Siegert equation is a hallmark of non-local correlations. Not only do non-local correlations reflect a proximity to Anderson localization, they are also responsible for universal conductance fluctuations [118]. Non-local correlations originating from crossed scattering paths in a disordered medium [119–128], however, are significantly weaker than the local correlations.

While previous mesoscopic physics studies have retrieved information about disor-

---

<sup>1</sup>The chapter material is primarily taken from reference [2]: Nicholas Bender, Hasan Yilmaz, Yaron Bromberg, and Hui Cao, “Introducing non-local correlations into laser speckles”, *Optics Express*, vol. 27, 6057-6067, (2019).

dered systems from speckle correlations in scattered light [129]; this chapter explores the inverse process, namely, we design the scattering structure itself to obtain desired speckle intensity-correlations in the far field. In particular, we aim to enhance and manipulate non-local correlations by drastically, yet controllably, violating the Siegert relation so the local-correlations are unaffected. The simplest “scattering” structure –which can be facilely controlled– is a spatial light modulator (SLM) in the configuration described in Chapter 2. Although incident light is scattered once by the SLM, we have shown in the previous chapter that arbitrary correlations can be encoded among the SLM pixels. Such correlations can be significantly stronger and more versatile than correlations built among partial waves during the process of multiple scattering in a random medium.

In this chapter, we experimentally demonstrate that the speckle intensity-correlation length can be augmented to significantly exceed the field correlation length, with non-local intensity correlations comparable in strength to the local intensity correlations. Furthermore, we show that it is possible to arbitrarily tailor the long-range intensity correlation function –for example making it anisotropic and oscillating– while keeping the field correlation function isotropic and untouched. Finally, a theoretical analysis reveals that the non-local intensity correlations in the far-field speckle patterns originate from high-order phase correlations encoded into the light field on the SLM plane.

The ability to manipulate the intensity correlations of speckles has a plethora of potential applications. Speckle illumination has been used for computational imaging and compressive sensing. In this context, tailoring the speckle correlations would be essential for “smart” illumination of the target [130]. In speckle-based fluorescence microscopy, the spatial intensity correlation function corresponds to the point spread function [131, 132], and thus customizing speckle correlations enables one to engineer the point spread function. Furthermore, laser speckle patterns with designed intensity correlations can be used as bespoke disordered optical-potentials in transport studies of cold atoms [133], colloidal

particles [134], and active media [53].

In this chapter we will define the spatial intensity correlation function as:

$$C_I(\Delta\mathbf{r}) \equiv \langle I(\mathbf{r})I(\mathbf{r} + \Delta\mathbf{r}) \rangle / \langle I(\mathbf{r}) \rangle \langle I(\mathbf{r} + \Delta\mathbf{r}) \rangle - 1 = C_L(\Delta\mathbf{r}) + C_{NL}(\Delta\mathbf{r}). \quad (3.1)$$

Here  $C_L(\Delta\mathbf{r})$  is the local correlation function, and it is related to the field correlation function,  $C_E(\Delta\mathbf{r}) \equiv \langle E(\mathbf{r})E^*(\mathbf{r} + \Delta\mathbf{r}) \rangle / \langle |E(\mathbf{r})|^2 \rangle$ , by  $C_L(\Delta\mathbf{r}) = |C_E(\Delta\mathbf{r})|^2$  [8, 10, 11, 120].  $C_{NL}(\Delta\mathbf{r})$  represents the non-local correlation [135], and it vanishes when the Siegert relation holds:  $C_I(\Delta\mathbf{r}) = |C_E(\Delta\mathbf{r})|^2$ .

Previous studies dedicated to altering speckle intensity-correlations [15, 21–27, 38, 136] generally rely on the Siegert relation, and modulate the spatial field correlations. It is more challenging to violate the Siegert relation and control the intensity correlations without affecting the field correlations. Such a modification requires the field and intensity to fluctuate spatially on different length scales. Although speckled-speckles produced by double scattering have  $C_I(\Delta r) \neq |C_E(\Delta r)|^2$ , the difference  $C_I(\Delta r) - |C_E(\Delta r)|^2$  representing the non-local intensity correlations  $C_{NL}(\Delta r)$  is rather small [31, 137]. In the near-field zone of a scattering medium, the Siegert relation does not hold, but the speckles are not fully developed and have a low contrast [138]. Here we develop a flexible yet robust method to introduce arbitrary non-local intensity correlations into fully-developed speckle patterns without altering the field correlations.

## 3.2 Enhanced Non-Local Correlation Length

First, we demonstrate how to increase the intensity correlation length of the speckles in the far field of the SLM in our setup without altering the field correlation length. We begin by measuring a generic Rayleigh speckle pattern, Figs. 3.1(a & c), created in the far

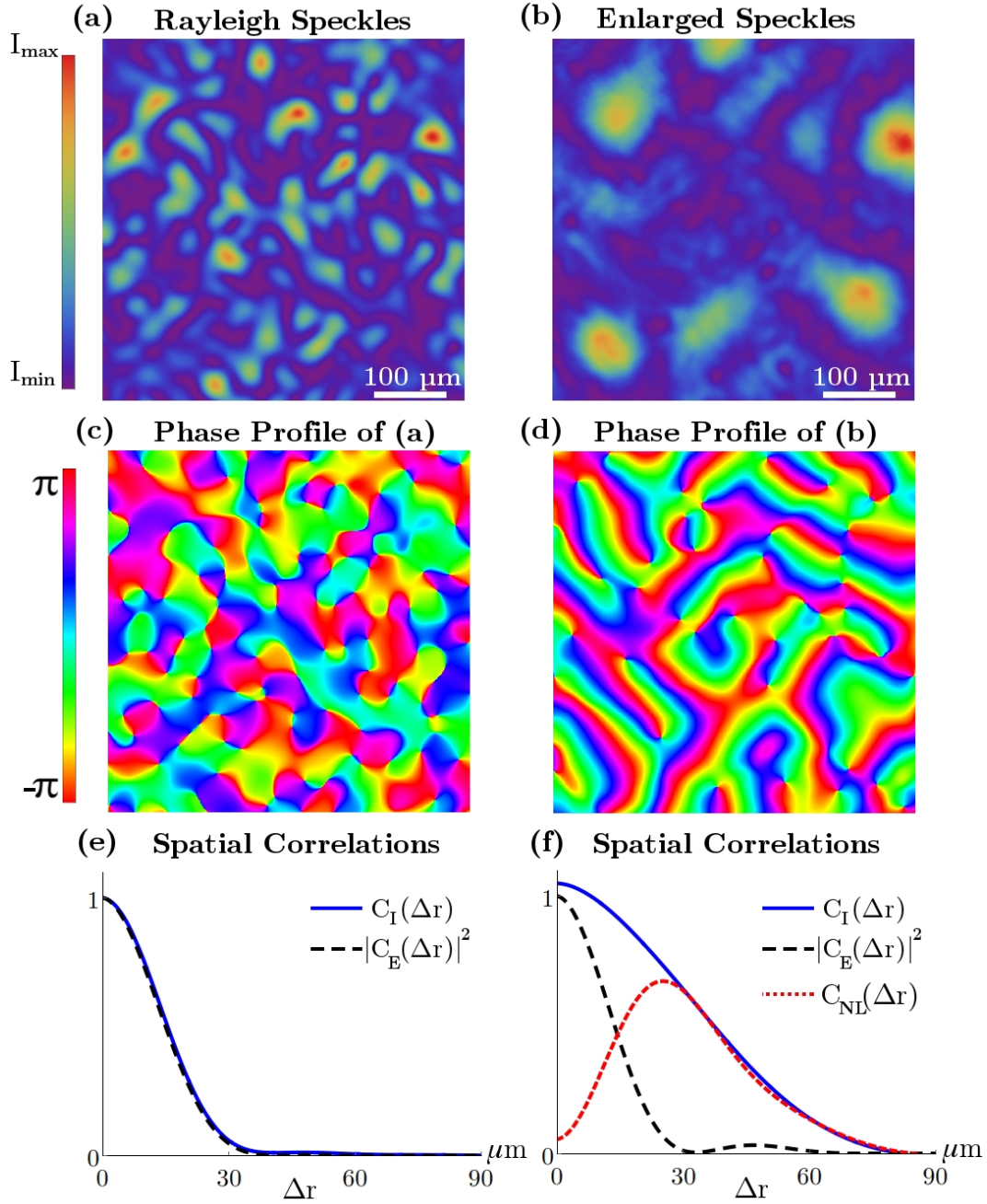


Figure 3.1: **Enhancing non-local correlations in speckles.** A Rayleigh speckle pattern (a,c) with  $C_I(\Delta r) = |C_E(\Delta r)|^2$  (e), is compared to an “enlarged Rayleigh” speckle pattern (b,d) with  $C_I(\Delta r)$  much broader than  $|C_E(\Delta r)|^2$  (f). The non-local intensity correlations,  $C_{NL}(\Delta r)$ , have comparable strength to the local correlations,  $C_L(\Delta r) = |C_E(\Delta r)|^2$ , in (f). The correlation functions in (e,f) are obtained by averaging over 100 independent speckle patterns. Similar to the Rayleigh speckle pattern, the customized speckle field is fully developed with a uniform phase distribution between 0 and  $2\pi$ .

field with a random phase pattern is displayed upon the SLM. In this case, the speckled field obeys a circular Gaussian probability density function for the complex amplitudes, and possesses only short-range intensity correlations,  $C_I(\Delta r) = |C_E(\Delta r)|^2$ , as confirmed in Fig. 3.1(e). We then magnify the speckled intensity-pattern numerically by a factor  $\alpha$  to increase the intensity correlation length by the same factor. We use the nonlinear-optimization algorithm presented in Chapter 2 to determine a phase pattern –which upon application to the SLM– generates the enlarged speckled intensity pattern on the camera plane. Again, to facilitate the convergence to a solution, we reduce the area we attempt to control –on the camera plane– to the central quarter of the region representing the Fourier transform of the phase modulating region of the SLM. Since the SLM does not change the field amplitude –due to the Wiener-Khinchin theorem– the spatial field correlation function in the CCD plane remains identical to that of the unmagnified speckle pattern. Therefore, so do the local intensity correlations  $C_L(\Delta r) = |C_E(\Delta r)|^2$ .

After finding the appropriate two-dimensional (2D) SLM phase-patterns we display them, and record the speckle patterns incident upon the CCD camera. Figure 3.1(b & d) present one demonstration of an “enlarged Rayleigh” speckle pattern. The intensity fluctuates on a length scale  $\alpha = 2.5$  times longer than the Rayleigh pattern in Fig. 3.1(a). While the width of  $C_I(\Delta r)$  is increased 2.5 times,  $|C_E(\Delta r)|^2$  remains the same as the original Rayleigh speckles, as shown in Fig. 3.1(f). This means that the speckled field, more precisely, the phase of the field plotted in Fig. 3.1(d), fluctuates faster in space than the intensity: on average. Still, the phase pattern is significantly modified relative to that of a Rayleigh speckle pattern such as in Fig. 3.1(c). It exhibits distinct features such as elongated equiphase lines, which can be seen in Fig. 3.1(d). Nevertheless, these features are masked by the spatial averaging inherent to calculating the field correlation function. The dramatic difference between  $C_I(\Delta r)$  and  $|C_E(\Delta r)|^2$  demonstrates the profound non-local intensity correlations present in the speckle pattern.

Since the Rayleigh speckles are magnified by the same factor  $\alpha = 2.5$  in both  $x$  and  $y$  directions, the intensity correlation functions, both  $C_L$  and  $C_{NL}$ , are isotropic and depend only on  $\Delta r = |\Delta \mathbf{r}| = \sqrt{(\Delta x)^2 + (\Delta y)^2}$ . Figure 3.1(f) compares  $C_{NL}(\Delta r)$  to  $C_L(\Delta r)$  and  $C_I(\Delta r)$ . Unlike  $C_L$ ,  $C_{NL}$  does not decay monotonically with  $\Delta r$ , instead it rises to its maximum when  $C_L$  almost dies out, and subsequently  $C_{NL}$  dominates the functional form of  $C_I(\Delta r)$ . The maximum value of  $C_{NL}$  is comparable to that of  $C_L$  at  $\Delta r = 0$ . In this example, the speckle intensity-correlations become long-ranged but remain isotropic, namely, the correlation lengths are identical in both the  $x$  and  $y$  directions. We can easily make the correlations anisotropic, by setting the amplification factor in  $x$  different from that in  $y$ , thereby tuning the intensity correlation lengths in  $x$  and  $y$  separately.

### 3.3 Anisotropic Long-Range Correlations

Next, we demonstrate how to synthesize speckles with significantly more complex spatial intensity correlations. Figure 3.2(a) shows  $C_I(\Delta \mathbf{r})$  with an oscillating non-local correlation function  $C_{NL}(\Delta \mathbf{r}) = (1/10) \cos[(\Delta x + \Delta y)/20]$ , where  $x$  and  $y$  are spatial coordinates. To generate speckles possessing such correlations, we first find speckle intensity-patterns  $I(\mathbf{r})$  which adhere to the desired  $C_I(\Delta \mathbf{r})$ . Since the Fourier transform of  $I(\mathbf{r})$  is related to that of  $C_I(\Delta \mathbf{r})$  by  $\mathcal{F}[C_I(\Delta \mathbf{r}) + 1] = |\mathcal{F}[I(\mathbf{r})]|^2$ ,  $|\mathcal{F}[I(\mathbf{r})]|$  is known. As plotted in Fig. 3.2(b), it is a sparse function. We then solve for  $I(\mathbf{r})$  with a Gerchberg-Saxton algorithm. Starting with a Rayleigh speckle intensity-pattern,  $J(\mathbf{r})$ , we modify the amplitude of its Fourier components, such that  $|\mathcal{F}[J(\mathbf{r})]|$  is equal to  $|\sqrt{\mathcal{F}[C_I(\Delta \mathbf{r}) + 1]}|$ , without altering the phase values. The inverse Fourier transform of the modified Fourier spectrum gives a complex valued function for  $\tilde{J}(\mathbf{r})$ . Since intensity values must be positive real numbers, we ignore the phase values and set  $\tilde{J}(\mathbf{r}) = |\tilde{J}(\mathbf{r})|$ .

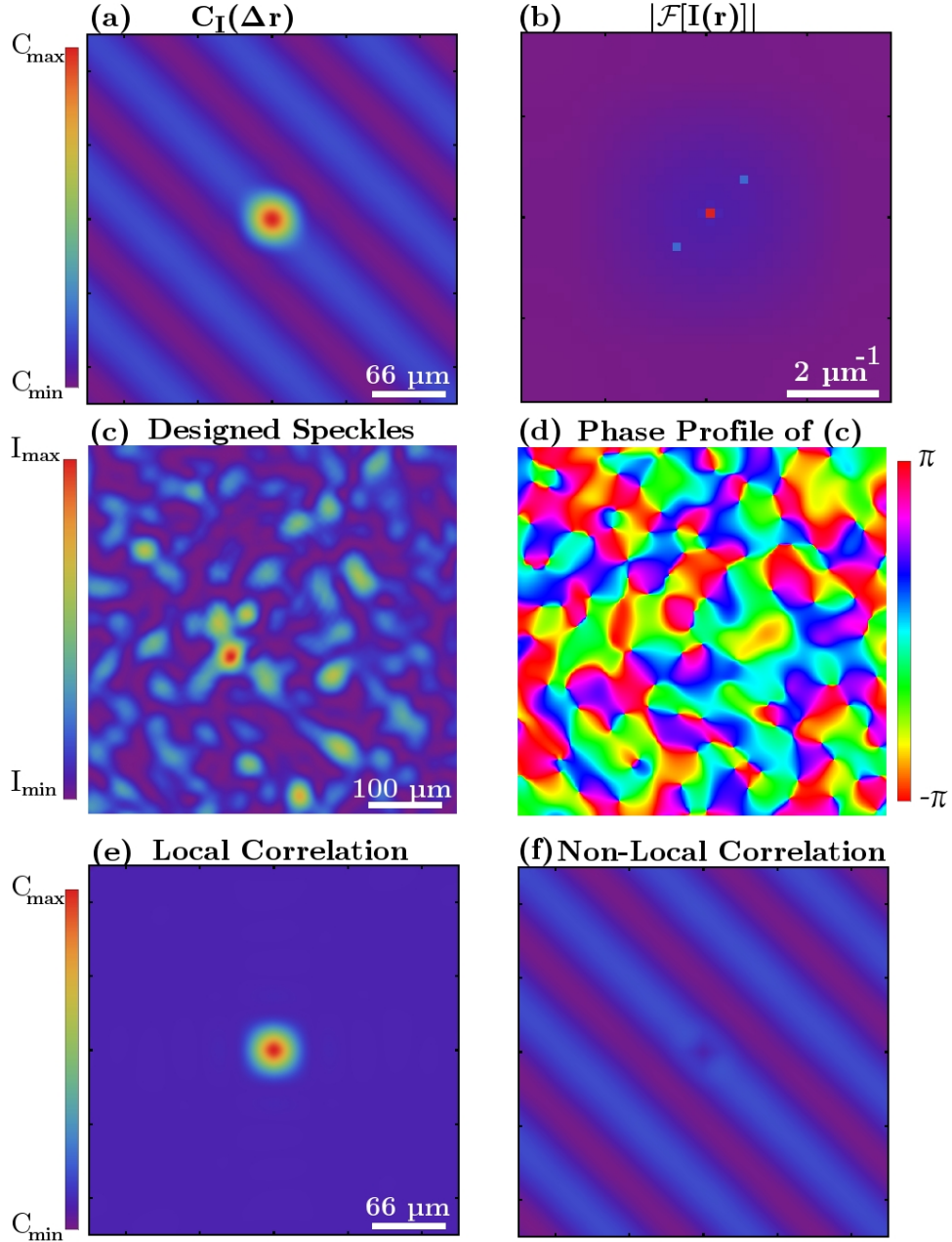


Figure 3.2: **Creating speckle patterns with spatially oscillating, anisotropic long-range intensity correlations.** The intensity correlation function  $C_I(\Delta\mathbf{r})$  (a), determines the Fourier amplitude profile of  $I(\mathbf{r})$  (b). An experimentally generated speckle intensity-pattern  $I(\mathbf{r})$  (c) possessing the correlations given in (a), and the corresponding phase profile  $\theta(\mathbf{r})$  (d).  $\theta$  is uniformly distributed between 0 and  $2\pi$ , confirming that the speckle pattern is fully developed. The local intensity correlation function  $C_L(\Delta\mathbf{r})$  (e) has a maximum value of 1, while the non-local intensity correlation function  $C_L(\Delta\mathbf{r})$  (f) has a maximum/minimum value of  $\pm 0.1$ . The correlation functions in (a,e,f) are obtained by averaging over 100 speckle patterns. The origins in (a,b,e,f) are located at the plots' centers.

Cyclical repetition of this process will eventually result in an intensity pattern which adheres to the desired correlation function. Starting with different initial Rayleigh speckle patterns will produce uncorrelated intensity patterns that satisfy the same  $C_I(\Delta\mathbf{r})$ . Using the nonlinear optimization algorithm discussed previously, we obtain the SLM phase patterns to create the desired intensity patterns on the camera. Figure 3.2(c) presents one such intensity pattern recorded experimentally. Its phase profile is predicted by the measured transmission matrix and shown in Fig. 3.2(d). The local intensity correlation function  $C_L(\Delta\mathbf{r}) = |C_E(\Delta\mathbf{r})|^2$ , shown in Fig. 3.2(e), remains isotropic and identical to that of the original Rayleigh speckles. However, the non-local correlation function  $C_{NL}(\Delta\mathbf{r})$ , plotted in Fig. 3.2(f), oscillates along the diagonal direction.

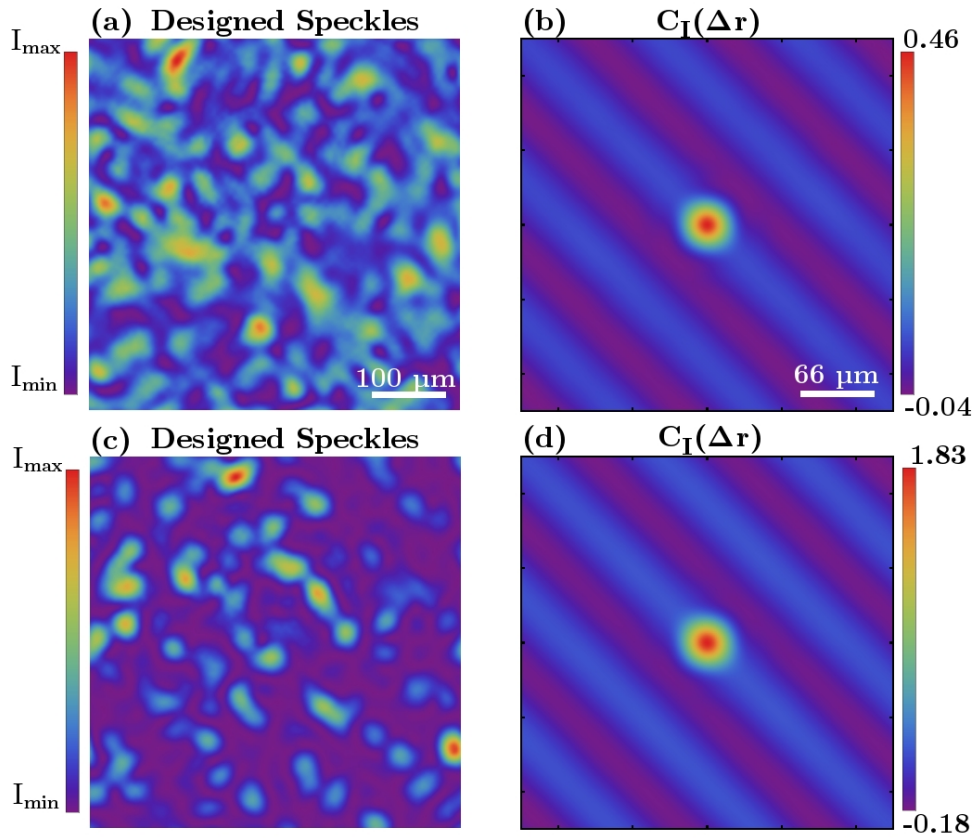


Figure 3.3: **Tuning the speckle contrast independently from the spatial intensity correlation function.** Two experimentally generated speckle patterns (a,c) with congruent intensity correlation functions (b,d). The intensity contrast is 0.68 in (a) and 1.35 in (c). The origin for (b) and (d) is located at the center of the plots.

A useful feature of our method is its ability to vary the contrast of the speckled intensity without altering the functional form of the long-range intensity correlation function. For the example given in Fig. 3.2(b), we can adjust the magnitude of the zeroth-order spatial frequency component, in order to change the constant background of the speckle intensity-pattern in real space and thus modify the speckle contrast. Speckle patterns with identically shaped, i.e. congruent,  $C_{NL}$  but different intensity contrasts are presented in Fig. 3.3(a) and 3.3(c). Given that the speckle contrast is directly related to the second moment of the intensity probability density function, this property illustrates the relative independence of the non-local correlations with respect to the intensity probability density function. We will explore this relation in greater detail in the next chapter.

Although the above method excels at generating speckle patterns when the desired non-local correlation function has sparse Fourier components, it fails to converge to a speckle pattern when the desired non-local correlation function is sparse in real space, such as the one shown in Fig. 3.4(a). While the correlations are positive at  $(0, 100 \mu\text{m})$  and  $(0, -100 \mu\text{m})$ , they become negative at  $(100 \mu\text{m}, 0)$  and  $(-100 \mu\text{m}, 0)$ . Rather than producing a random intensity pattern, the Gerchberg-Saxton algorithm converges to an ordered pattern,  $g(\mathbf{r})$  in Fig. 3.4(d), which adheres to the desired  $C_I(\Delta\mathbf{r})$  in Fig. 3.4(a). To produce a speckle intensity-pattern, we simply convolve  $g(\mathbf{r})$  with a speckle pattern without non-local correlations, such as  $J(\mathbf{r})$  in Fig. 3.4(e), and obtain  $I(\mathbf{r}) = g(\mathbf{r}) \otimes J(\mathbf{r})$ . This results in a speckle pattern with  $\mathcal{F}[I(\mathbf{r})] = \mathcal{F}[J(\mathbf{r})]\mathcal{F}[g(\mathbf{r})]$ , and  $\mathcal{F}[C_I(\Delta\mathbf{r})] \cong \mathcal{F}[C_J(\mathbf{r})]\mathcal{F}[C_g(\mathbf{r})]$ . Since the local correlation length of the convolving speckle pattern is set by the diffraction limit, its correlation function can be approximated by a  $\delta$  function [139]. Consequently,  $\mathcal{F}[C_I(\Delta\mathbf{r})] \approx \mathcal{F}[C_g(\mathbf{r})]$ , and  $I(\mathbf{r})$  possesses the same intensity correlations as  $g(\mathbf{r})$ . Once the target intensity-pattern  $I(\mathbf{r})$  is obtained, a corresponding speckle-pattern can be created experimentally using our nonlinear optimization algorithm: for example Fig. 3.4(f). Here the corresponding local and non-local intensity correlation

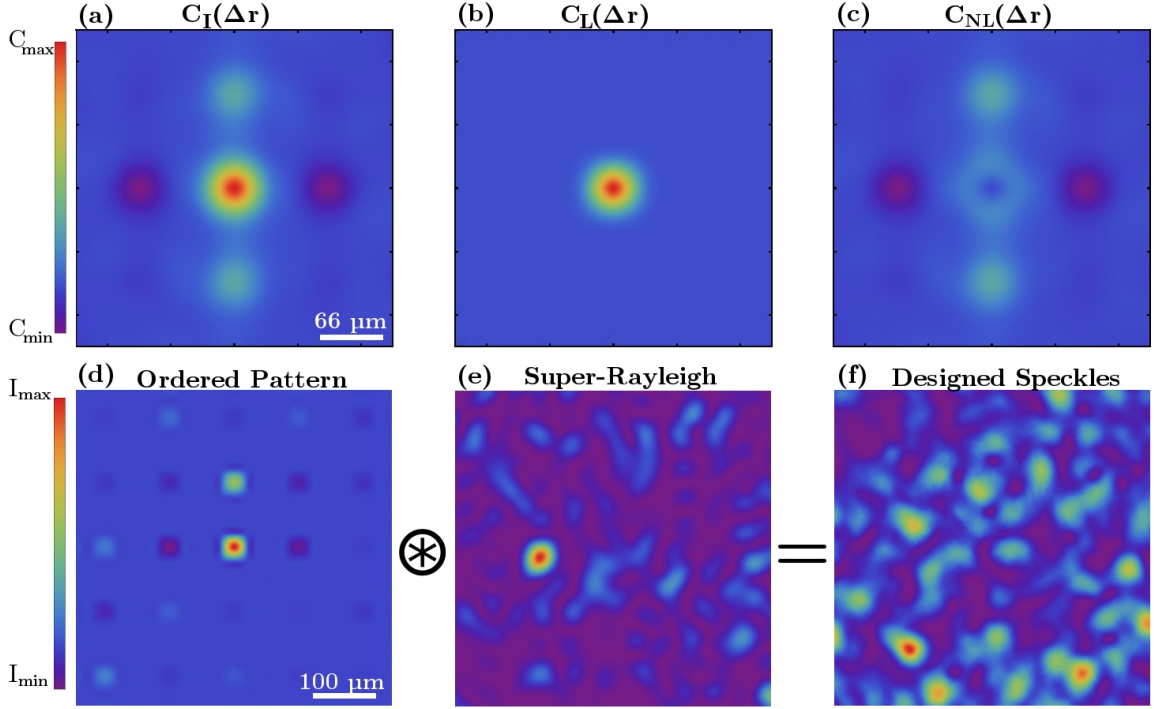


Figure 3.4: **Introducing spatially simple anisotropic non-local correlations into speckles.** The spatial intensity correlation function (a) is sparse. The local correlation function (b) has a maximum amplitude of 1, while the non-local correlation function (c) has a maximum/minimum amplitude of  $\pm 0.2$ . An ordered intensity pattern  $g(\mathbf{r})$  (d), produced by the Gerchberg Saxton algorithm, is convolved with super-Rayleigh speckle pattern  $J(\mathbf{r})$  (e) to generate a speckle intensity-pattern  $I(\mathbf{r})$  (f) with the desired non-local correlations given in (c). The correlation functions in (a,b,c) are obtained by averaging over 100 speckle patterns and the origins are located at the plots' centers.

functions are shown in Figs. 3.4(b & c). Just as before, one has the freedom to increase or decrease the speckle contrast of the target pattern, by convolving  $g(\mathbf{r})$  with either a super-Rayleigh or sub-Rayleigh speckled intensity pattern [33].

### 3.4 Origins Of Non-Local Correlations

Next, we illustrate that the non-local intensity correlations introduced into the speckle patterns,  $C_{NL}(\Delta\mathbf{r}) = C_I(\Delta\mathbf{r}) - |C_E(\Delta\mathbf{r})|^2$ , originate from high-order correlations encoded in the phase patterns on the SLM. As in the previous chapter, we consider a 1D speckled

field  $E(r)$ , of length  $L$ , and its spatial Fourier components,  $\varepsilon(\rho)$ , where  $\rho$  corresponds to the spatial position on the SLM plane.

$$E(r) = \frac{1}{\sqrt{L}} \sum_{\rho=0}^{L-1} \varepsilon(\rho) e^{i \frac{2\pi}{L} r \rho} \quad (3.2)$$

After simplification, the spatial field correlation function is given by:

$$C_E(\Delta r) = \frac{1}{L} \sum_{\rho=0}^{L-1} |\varepsilon(\rho)|^2 e^{-i \frac{2\pi}{L} \Delta r \rho}. \quad (3.3)$$

Taking the absolute-value squared of this expression gives the local intensity correlation function  $C_L(\Delta r)$ :

$$C_L(\Delta r) = \frac{1}{L^2} \sum_{\rho_1, \rho_2=0}^{L-1} |\varepsilon(\rho_1)|^2 |\varepsilon(\rho_2)|^2 e^{i \frac{2\pi}{L} \Delta r (\rho_2 - \rho_1)}.$$

With an expression for the local correlations in hand, we turn to the spatial intensity correlations:

$$I(r)I(r + \Delta \mathbf{r}) = \frac{1}{L^2} \sum_{\rho_1, \rho_2, \rho_3, \rho_4=0}^{L-1} \varepsilon(\rho_1) \varepsilon^*(\rho_2) \varepsilon(\rho_3) \varepsilon^*(\rho_4) e^{i \frac{2\pi}{L} [r(\rho_1 - \rho_2) + (r + \Delta r)(\rho_3 - \rho_4)]}. \quad (3.4)$$

Along the lines of the calculation in the previous chapter, grouping the summation into four terms according to the number of different  $\rho$ 's summed over and spatial averaging gives:

$$C_I(\Delta r) = C_1(\Delta r) + C_2(\Delta r) + C_3(\Delta r) + C_4(\Delta r) - 1 \quad (3.5)$$

where:

$$\begin{aligned}
C_1(\Delta r) &= \frac{1}{L^2} \sum_{\rho_1=0}^{L-1} |\varepsilon(\rho_1)|^4 \\
C_2(\Delta r) &= \frac{1}{L^2} \sum_{\substack{\rho_1, \rho_2=0 \\ \rho_1 \neq \rho_2}}^{L-1} |\varepsilon(\rho_1)|^2 |\varepsilon(\rho_2)|^2 (1 + e^{i\frac{2\pi}{L}\Delta r(\rho_2-\rho_1)}) \\
C_3(\Delta r) &= \frac{2}{L^2} \Re \left[ \sum_{\substack{\rho_1, \rho_2=0 \\ \rho_1 \neq \rho_2}}^{L-1} \varepsilon(\rho_1)^2 \varepsilon^*(\rho_2) \varepsilon^*(2\rho_1 - \rho_2) e^{i\frac{2\pi}{L}\Delta r(\rho_2-\rho_1)} \right] \\
C_4(\Delta r) &= \frac{1}{L^2} \sum_{\substack{\rho_1, \rho_2, \rho_3=0 \\ \rho_1 \neq \rho_2 \neq \rho_3}}^{L-1} \varepsilon(\rho_1) \varepsilon^*(\rho_2) \varepsilon(\rho_3) \varepsilon^*(\rho_1 - \rho_2 + \rho_3) e^{i\frac{2\pi}{L}\Delta r(\rho_2-\rho_1)}. \quad (3.6)
\end{aligned}$$

Since  $C_1$  and  $C_3$  are on the order of  $1/L$ , they are negligible for large  $L$ , and  $C_I$  is dominated by  $C_2$  and  $C_4$ :

$$C_I(\Delta r) \simeq C_2(\Delta r) + C_4(\Delta r) - 1. \quad (3.7)$$

Comparing the expression of  $C_L(\Delta r)$  to that of  $C_2(\Delta r) - 1$ , we notice their difference scales as  $1/L$ . When  $L$  is large,  $C_L(\Delta r) \simeq C_2(\Delta r) - 1$ , and

$$C_I(\Delta r) = C_L(\Delta r) + C_4(\Delta r) \quad (3.8)$$

Therefore, the non-local correlation function  $C_{NL}(\Delta r) \simeq C_4(\Delta r)$ . The expression for  $C_4(\Delta r)$  reveals that the non-local correlations originate from *only* the fourth-order correlations between different Fourier components of the speckled fields. Furthermore, the correlations for  $\Delta r \neq 0$  are different than those in the second moment of the intensity PDF in Eq. 2.13.

### 3.5 Axial Evolution Of Speckle Correlations

As in the last chapter, the tailored speckles will lose their customized properties as they axially propagate away from the Fourier plane of the SLM. Because the non-local intensity correlations result from fourth-order correlations encoded into the Fourier components; the phase parabola accompanying axial-propagation erodes away such correlations as the tailored speckles propagate (along the  $z$ -axis). Eventually only the local intensity correlations remain in the speckle pattern.

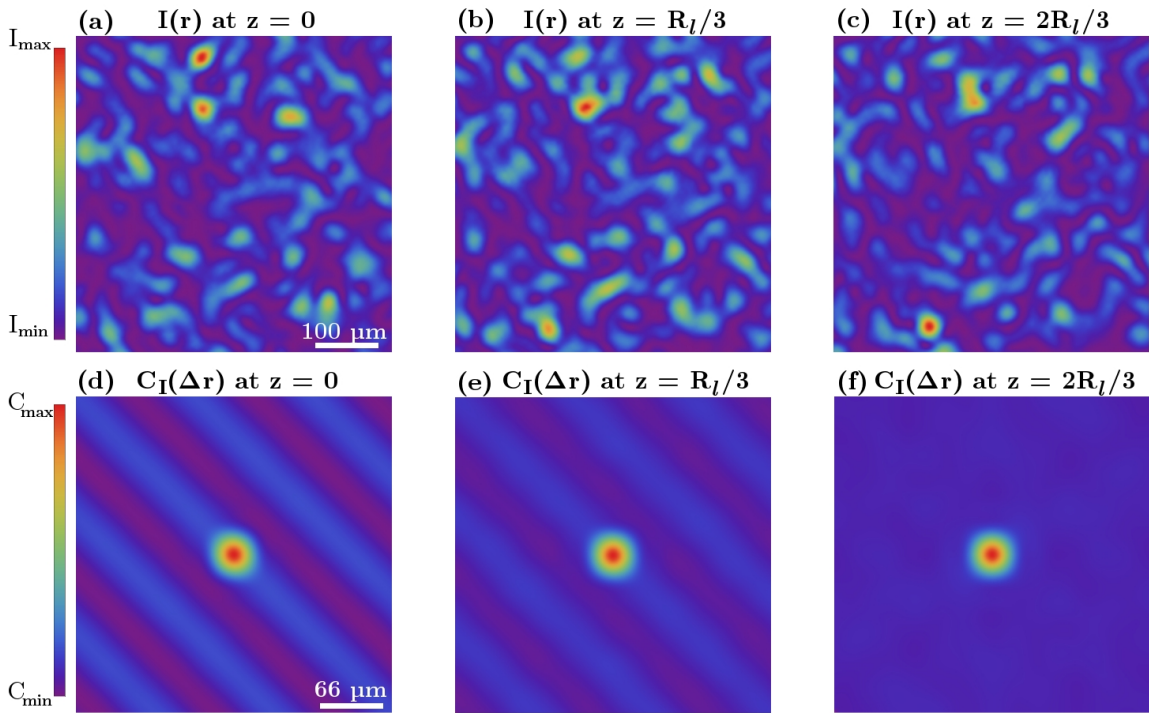


**Figure 3.5: Axial evolution of a customized speckle pattern.** An example customized speckle pattern (a), on the plane of customization  $z = 0$ , is juxtaposed with its corresponding spatial intensity correlation function (d). The speckle pattern (b) and its intensity correlation function (e), after axially propagating to  $z = R_l/3$ , are presented. At this distance, the magnitude of the non-local correlations has reduced by half. The speckle pattern (c) and its intensity correlation function (f) are shown after further propagation to  $z = 2R_l/3$ . At this point, the non-local correlations are completely erased and only the local correlations remain. The correlation functions in (d,e,f) are obtained by averaging over 100 different speckle patterns, and the origins are located at the center of the plots.

In Fig. 3.5 we experimentally demonstrate the attenuation of non-local correlations in the customized speckles, as a function of axial propagation. Again, we define  $R_l$  as the axial correlation length of a speckle intensity-pattern. Figure 3.5(a) shows an example speckle pattern which is customized to have the oscillatory intensity-correlation function shown in Fig. 3.5(d) at  $z = 0$ . After the speckle pattern propagates a fraction of the Rayleigh-range to  $z = R_l/3$ , Figs. 3.5(b), the non-local correlations attenuate to nearly half of their original magnitude, Fig. 3.5(d). Further propagation away from the plane of customization removes the remaining non-local correlations from the speckle pattern entirely, as can be seen in Figs. 3.5(c & f) for  $z = 2R_l/3$ . Beyond this point, the statistical properties of the customized speckles revert back to those of Rayleigh speckles.

### 3.6 Discussion & Conclusion

In conclusion, we presented a general approach for introducing strong non-local intensity-correlations into fully-developed speckle patterns using classical light in conjunction with a single scattering surface (SLM). By encoding fourth-order correlations into the phase of light reflected from the SLM, the second-order coherence function of the far-field speckles can be arbitrarily tailored without altering the respective first-order coherence function. Doing so, we drastically violate the Siegert relation: a fundamental principle in optical coherence theory.

Our method of encoding speckle correlations using the transmission matrix of an optical system is simple, yet versatile, and therefore can readily be incorporated into a broad range of optical experiments. For example, it would benefit studies of cold atom transport in correlated potentials [140–142], because the spatial correlations of the speckled optical potentials could be arbitrarily customizable and re-configurable without the need for mechanical motion. Furthermore, our method can generate speckle patterns with de-

sired correlations for illumination in compressive correlation imaging and stochastic optical sensing [130]. Since the spatial intensity correlation function determines the photon coincidence counting rate, it is possible to create spatially correlated photon sources with tailored speckle patterns and engineer the coincidence counting rate for photon pairs as a function of their spatial separation.

Finally, it is worth mentioning the advantage of breaking the Siegert relation when controlling the intensity correlations of speckles. Methods relying on the Siegert relation modify the amplitude of light in the near field to control the spatial field correlations in the far field. Therefore, the total power of the far-field speckle pattern can be drastically reduced, which will degrade the sensitivity of imaging/sensing modalities using speckle illumination. Our method only requires phase modulation of the near field light; thus, the total energy of the far-field speckle pattern is conserved.

# Chapter 4

## Creating And Controlling Complex Light

### 4.1 Introduction

<sup>1</sup>In this chapter, we experimentally demonstrate a method of *simultaneously* customizing the intensity PDF of speckle patterns and introducing long-range spatial correlations among the speckle grains. Various families of speckles are created by encoding high-order correlations into the phase front of a monochromatic laser beam with a spatial light modulator (SLM): using a two-stage method. In addition to our experimental demonstration, we explore both the theoretical and practical limitations on the extent to which the intensity PDF and the spatial intensity correlations can be manipulated simultaneously in a speckle pattern without modifying the spatial field correlation function.

As discussed previously, the ability to independently control the intensity PDF and correlations of speckles –arbitrarily– has many potential applications. For example they can be used as a form of ‘smart’ illumination in high-order ghost imaging [44–46], dynamic speckle illumination microscopy [40, 41], super-resolution imaging [42, 43, 143–145],

---

<sup>1</sup>The chapter material is primarily taken from reference [3]: Nicholas Bender, Hasan Yilmaz, Yaron Bromberg, and Hui Cao, “Creating and controlling complex light”, *APL Photonics*, vol. 4, 110806, (2019).

compressive sensing [130, 146], and optical sectioning microscopy [132]. Furthermore, using speckle patterns with customized intensity statistics as bespoke disordered optical potentials in transport studies of cold atoms [133], colloidal particles [134], and active media [53] could induce novel transport behaviors.

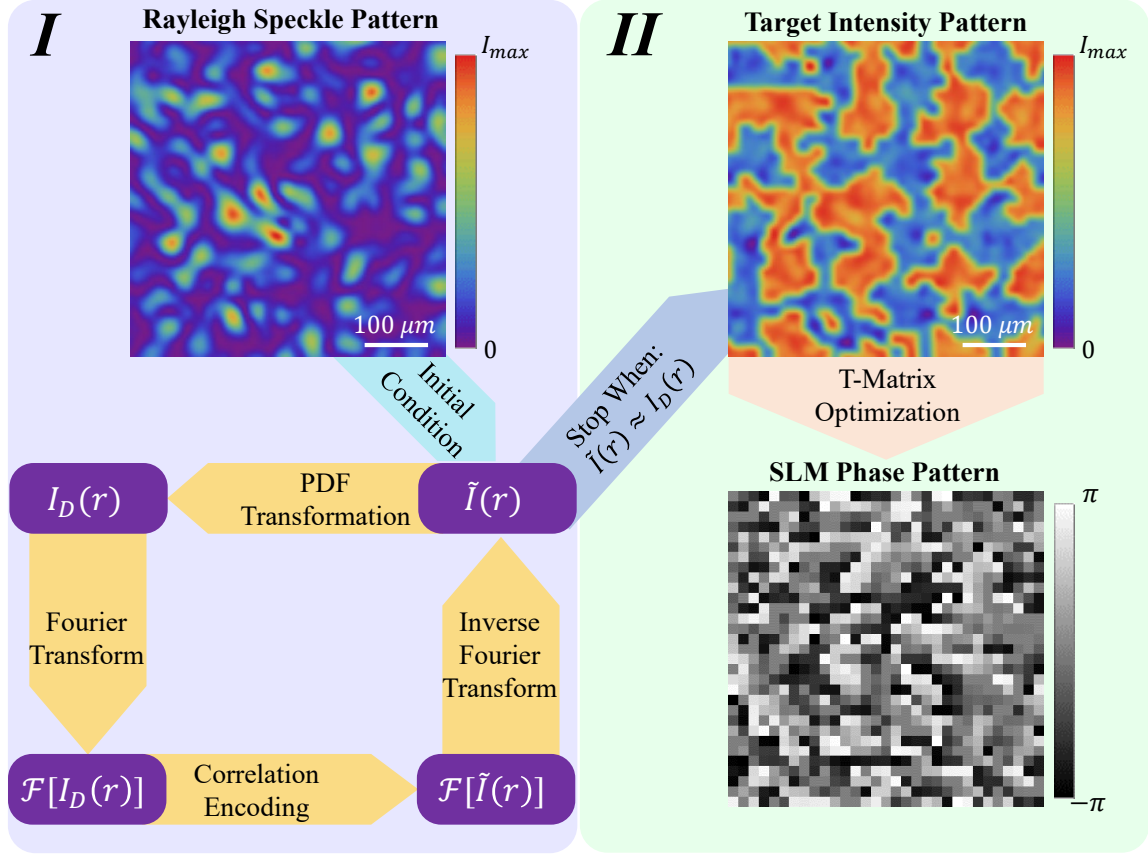


Figure 4.1: **Speckle customization method.** We show a flowchart visualization of our speckle customization method.  $I_D(\mathbf{r})$  represents an intensity pattern obeying the desired PDF and  $\tilde{I}(\mathbf{r})$  is an intensity pattern with the desired correlations.

## 4.2 Method

Our method of creating and controlling complex light, by simultaneously controlling the intensity PDF,  $P(I)$ , and the spatial intensity correlation function,  $C_I(\Delta\mathbf{r})$ , in a speckle pattern has two fundamental stages as depicted in Figure 4.1. Along the lines of the pre-

vious chapters, first, a target speckle intensity-pattern which obeys the desired intensity statistics –both  $P(I)$  and  $C_I(\Delta\mathbf{r})$ – is numerically generated by transforming a Rayleigh speckle pattern. Once a target intensity pattern is known, the next stage is using the field-transmission-matrix based nonlinear optimization algorithm to obtain a corresponding speckled field –possessing the desired target intensity profile– which can be created in our experimental setup using a phase-only SLM. Repeating our method with different/uncorrelated initial Rayleigh speckle patterns enables us to create a stationary and ergodic ensemble of speckle patterns obeying the desired custom statistics.

To complete the first stage of our method we generate a speckle intensity-pattern,  $I(\mathbf{r})$ , which adheres to a desired intensity probability density function,  $P(I)$ , and has a spatial intensity correlation function,  $C_I(\Delta\mathbf{r})$ , with a tailored functional form: by transforming an experimentally measured Rayleigh speckle pattern. In order to successfully encode both desired statistical properties into our target intensity pattern, we use an individual transformation for each property using our previously developed methods for customizing either  $P(I)$  or  $C_I(\Delta\mathbf{r})$ . To begin with, we can modify the intensity PDF of a speckle intensity-pattern by performing a local intensity transformation on it. To recap, a local intensity transformation is defined such that if  $I_0(\mathbf{r})$  is an initial speckle intensity-pattern adhering to the intensity PDF,  $P_0(I)$ , then the scalar transformation  $f(I_0(\mathbf{r})) = I_D(\mathbf{r})$  will produce a new intensity pattern  $I_D(\mathbf{r})$  which adheres to the desired intensity PDF,  $P_D(I)$ . The specific local intensity transformation associated with the target PDF,  $P_D(I)$ , can be found from the integral

$$\int_0^{I_0} P_0(I')dI' = \int_0^{I_D} P_D(I')dI'. \quad (4.1)$$

By expressing  $I_D$  as a function of  $I_0$ , we obtain the local intensity transformation  $f(I_0) = I_D$  as shown in Chapter 2. While this enables us to customize the intensity PDF of a

speckle pattern, long-range spatial intensity correlations are not modified by this operation. To introduce the desired  $C_I(\Delta\mathbf{r})$  into a speckle intensity-pattern, we employ the relation between the Fourier transform of a speckle intensity-pattern  $\mathcal{F}[I(\mathbf{r})]$  and its spatial intensity-correlation function  $C_I(\Delta\mathbf{r})$ :  $\mathcal{F}[C_I(\Delta\mathbf{r}) + 1] = |\mathcal{F}[I(\mathbf{r})]|^2$  shown in Chapter 3. Therefore by modifying a speckle intensity-pattern's Fourier amplitude according to  $|\mathcal{F}[I(\mathbf{r})]| = |\sqrt{\mathcal{F}[C_I(\Delta\mathbf{r}) + 1]}|$ , we can create a speckled intensity pattern,  $\tilde{I}(\mathbf{r})$ , which obeys the desired intensity correlation function: as shown in Chapter 3. Because information related to customizing the intensity PDF is encoded into the spatial representation of a speckle pattern –via the local intensity transformation of  $I(\mathbf{r})$ – and the desired intensity correlation function information is encoded in the Fourier representation of the speckled intensity pattern –by imposing  $|\sqrt{\mathcal{F}[C_I(\Delta\mathbf{r}) + 1]}|$ – we can merge both customization methods into a single Gerchberg-Saxton algorithm as illustrated in Figure 4.1(b). In this process, the only constraint on the statistical properties encoded into the speckle pattern is the fundamental relationship between the speckle correlation function and the intensity PDF:  $C_I(0) = C_0 = \langle I^2 \rangle / \langle I \rangle^2 - 1$ . Beyond this, however, the functional form of  $C_I(\Delta\mathbf{r})$  may be chosen independently from  $P(I)$ .

The first step of our Gerchberg-Saxton algorithm is to perform a local intensity transformation on a Rayleigh speckle pattern which converts it into a speckle intensity-pattern,  $I_D(\mathbf{r})$ , governed by the desired PDF. Next, we modify the amplitude of its Fourier components, such that  $|\mathcal{F}[I_D(\mathbf{r})]|$  is equal to the desired  $|\sqrt{\mathcal{F}[C_I(\Delta\mathbf{r}) + 1]}|$ , without altering the phase values. The inverse Fourier transform of the modified Fourier spectrum gives a complex valued function for the intensity pattern,  $\tilde{I}(\mathbf{r})$ , which obeys the desired correlation function. Since the intensity values must be positive real numbers, we ignore the phase values and set  $\tilde{I}(\mathbf{r}) = |\tilde{I}(\mathbf{r})|$ . In the process of encoding correlations into  $I_D(\mathbf{r})$ , the intensity PDF that the resulting pattern,  $\tilde{I}(\mathbf{r})$ , obeys is altered slightly relative to that of  $I_D(\mathbf{r})$ . This deviation from the desired PDF is corrected for by applying an appropriate

local intensity transformation to  $\tilde{I}(\mathbf{r})$ . While the modified intensity pattern now obeys the desired speckle intensity-PDF, the application of a local intensity transformation to  $\tilde{I}(\mathbf{r})$  has slightly altered the spatial intensity correlations previously encoded into the speckle pattern. The small deviation from the desired  $C_I(\Delta\mathbf{r})$  can be corrected by resetting the Fourier amplitude of the intensity pattern to  $|\sqrt{\mathcal{F}[C_I(\Delta\mathbf{r}) + 1]}|$ . Cyclical repetition of this process results in an intensity pattern which adheres to both the desired correlation function and the desired PDF: therefore, we have  $I_D(\mathbf{r}) = \tilde{I}(\mathbf{r})$ . Starting with different initial Rayleigh speckle patterns produces uncorrelated intensity patterns that satisfy the same  $C_I(\Delta\mathbf{r})$  and  $P_D(I)$ , and therefore by using a stationary and ergodic ensemble of uncorrelated Rayleigh speckle patterns we can create a stationary and ergodic ensemble of uncorrelated customized speckle patterns.

As discussed in Chapter 3, this method excels at generating speckle patterns when the desired non-local correlation function has sparse Fourier components, it may converge to an ordered –as opposed to speckled– intensity pattern when the desired non-local correlation function is sparse in real space –therefore dense in Fourier space– such as the example shown in Figure 4.2. In this case, rather than producing a random intensity pattern, the Gerchberg-Saxton algorithm converges to an ordered pattern which adheres to the desired intensity PDF and  $C_I(\Delta\mathbf{r})$ . In this algorithm, we can still rectify this absence of disorder by convolving the ordered intensity pattern with a speckle pattern which does not possess any long-range intensity correlations, such as a Rayleigh speckle pattern. This convolution does not alter the functional form of  $C_I(\Delta\mathbf{r})$  since Rayleigh speckles only have short-ranged correlations, however, it may alter the speckles’ intensity PDF. In general, this alteration can be removed by using the convolved speckle pattern as the initial speckle pattern of a second Gerchberg-Saxton algorithm, which follows the same procedure as the first Gerchberg-Saxton algorithm. In the event that  $P(I)$  is smooth the alteration of  $P(I)$  is minor [1] and to a good approximation only the value of  $C_I(0)$  changes: *i.e.* the vari-

ance of the encoded PDF. In this case, we can use either a super-Rayleigh or sub-Rayleigh speckle pattern in the convolution to adjust the value of  $C_I(0)$ : as was done for the case shown in Figure 4.2.

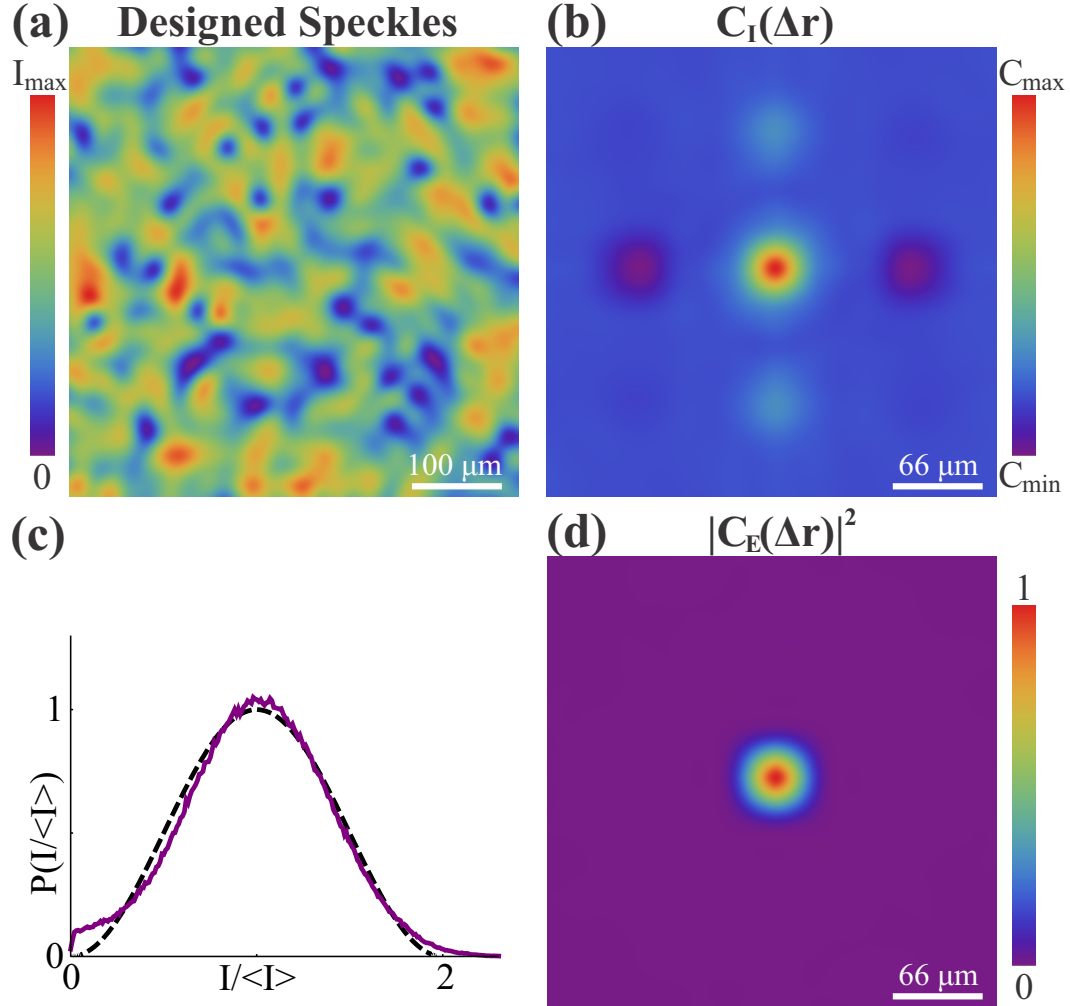


Figure 4.2: **Example customized speckle pattern.** A customized speckle pattern is shown in (a) with a spatially sparse intensity correlation function (b) and a unimodal intensity PDF (c). In (b)  $C_{\max} = 0.15$  and  $C_{\min} = -0.03$ . In (c) the intensity PDF of the experimentally created speckles (purple solid line) closely follows the target intensity PDF (black dashed line). The local intensity correlation function (d) remains the same as that of a Rayleigh speckle pattern, indicating that the modification of the spatial intensity correlation function is the result of introducing non-local correlations into the speckle pattern. To obtain (b-d) we ensemble average over 100 independent speckle patterns to obtain the PDF and the correlation functions. The origin of (b) and (d) is located at the center of each plot.

### 4.3 Example Customized Speckles

In Figure 4.2(a) we present an example of an experimentally measured speckle pattern which is customized to simultaneously possess the spatial intensity correlation function shown in (b) and adhere to the intensity PDF shown in (c). The experimentally obtained intensity PDF (purple line) in (c) was tailored to have the form,  $P(\hat{I}) = \sin^2[\pi\hat{I}/2]$ , over the range,  $0 \leq \hat{I} \equiv I/\langle I \rangle \leq 2$ , and  $P(\hat{I}) = 0$  for values of  $\hat{I} > 2$  (black dashed line). The two curves closely follow one another, except around  $\hat{I} = 0$ . This deviation occurs because optical vortices are inherently present in the experimentally-generated speckle patterns, and therefore the measured probability around  $\hat{I} = 0$  must be nonzero. The intensity correlation function shown in (b) was designed to have positive correlations,  $C_I(\Delta\mathbf{r}) = 0.03$ , at  $\Delta\mathbf{r} = (0, \pm 100 \mu\text{m})$  and negative correlations,  $C_I(\Delta\mathbf{r}) = -0.03$ , at  $\Delta\mathbf{r} = (\pm 100 \mu\text{m}, 0)$ . Again, because our method is based on the use of a phase-only SLM, which is in the Fourier plane of our camera, the Fourier amplitude profile of the speckled fields generated in the CCD camera plane is fixed. Therefore, due to the Wiener-Khinchin theorem, the spatial field correlation function of a customized speckle pattern in the camera plane remains identical to that of the initial Rayleigh speckle pattern (created by a random phase array on the SLM): as demonstrated in (d). Therefore, as discussed in the previous chapter, the modified intensity correlations are non-local.

### 4.4 Higher-Order Statistics Analysis

Often, complex-light patterns are classified in terms of a defining statistical property, such as the intensity PDF: the most common example would be a *Rayleigh* speckle pattern. Such a characterization requires the existence of an ensemble/family of independent speckle patterns which individually adhere to the stated statistical property. The speckle

patterns generated using our combined method are no exception; while we present the intensity PDF and spatial correlation function calculated using the entire ensemble of speckle patterns –in Figure 4.2– each speckle pattern adheres to the stated statistical properties individually and therefore is part of a statistically stationary and ergodic ensemble. We can verify that the intensity PDFs of the speckle patterns are stationary by calculating the average deviation of the PDF of a single speckle intensity-pattern,  $P_S(I)$ , from the intensity PDF constructed using the ensemble of speckle patterns,  $P_E(I)$ . We quantify the difference between the PDFs using the formula:  $\Delta P_S = [|\langle P_E(I) - P_S(I) \rangle_I|] / \left[ \sqrt{\langle P_E(I) \rangle_I \langle P_S(I) \rangle_I} \right]$ . The average deviation between the PDF of a single speckle pattern and the ensemble PDF is  $\approx 0.06$  for the family of speckle patterns presented in Figure 4.2. Because this average deviation is the same as what is obtained from an equivalent calculation using Rayleigh speckles, we conclude that our speckle intensity-PDFs are statistically stationary. To verify that the intensity PDFs are ergodic, we compare the intensity PDFs of different spatial locations  $P_x(I)$ , with respect to the ensemble PDF  $P_E(I)$ , using  $\Delta P_x = [|\langle P_E(I) - P_x(I) \rangle_I|] / \left[ \sqrt{\langle P_E(I) \rangle_I \langle P_x(I) \rangle_I} \right]$ . To calculate  $P_x(I)$  we use the ensemble of intensity values at a given position  $x$ . For the family of speckles in Figure 4.2, the average deviation between the PDF of a single spatial location and the ensemble PDF is  $\approx 0.06$ . Again, since this is equal to the value obtained from an equivalent ensemble of Rayleigh speckles, we can conclude that our intensity PDFs are ergodic in addition to being stationary.

Similarly for the encoded non-local correlations, one can perform an analogous calculation comparing the spatial intensity correlation function obtained from averaging over all positions in each customized speckle pattern to that obtained from sampling over the ensemble of speckle patterns: to verify that the encoded correlations are stationary. Additionally, one can compare the average spatial intensity correlation function of each spatial position to that obtained from sampling all positions: to verify that the encoded correla-

tions are ergodic. We have checked both cases and for each the average deviation was the same as the value obtained from an equivalent ensemble of Rayleigh speckle patterns. Thus, the intensity correlations encoded into the speckle patterns are both stationary and ergodic. In general therefore, our customized speckle patterns are represented by a statistically stationary and ergodic random process.

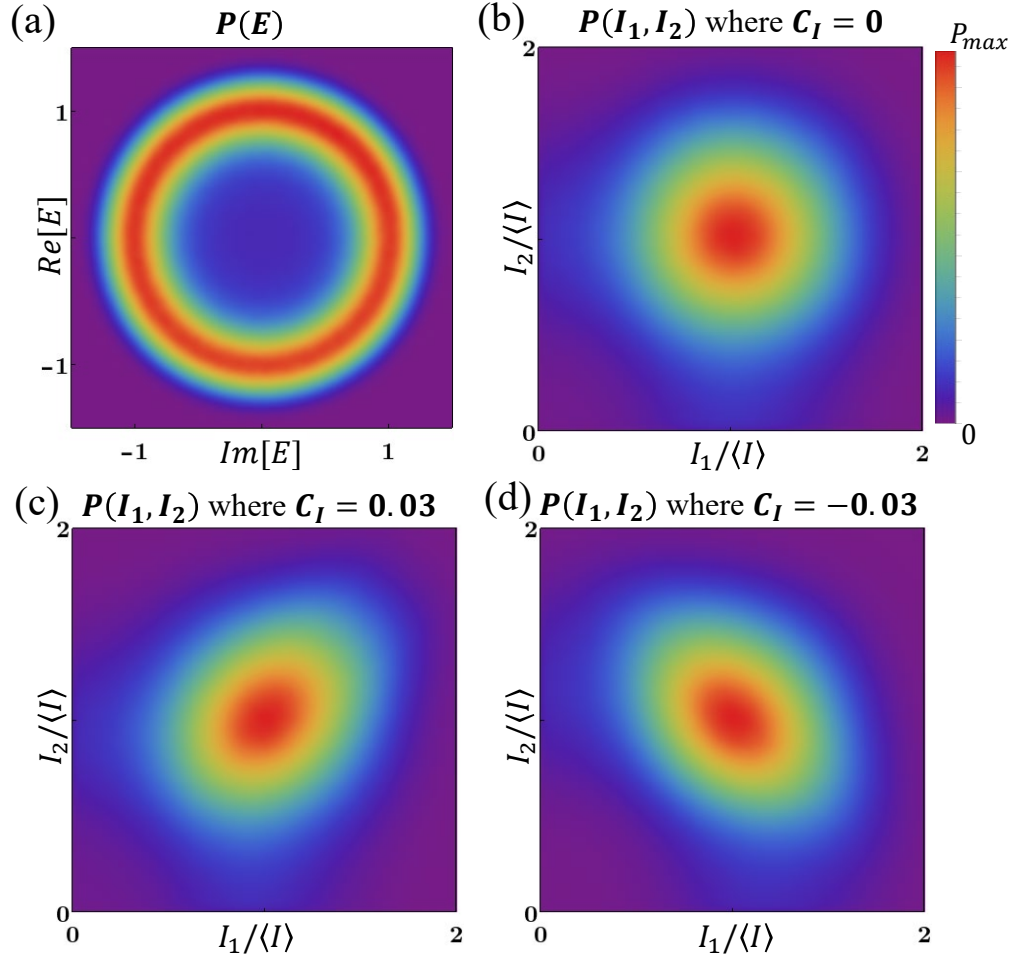


Figure 4.3: **Higher-order statistics.** Some high-order statistical properties of the family of customized speckle patterns in Fig. 4.2 are presented. In (a) the complex joint PDF of the speckled field reveals that the speckle patterns are circular non-Gaussian and therefore fully developed. In (b-d) we show the joint intensity PDF,  $P(I_1, I_2)$ , of  $I_1$  and  $I_2$  sampled at spatial locations separated by  $\Delta\mathbf{R} = (60 \mu\text{m}, 60 \mu\text{m})$ ,  $(0, 100 \mu\text{m})$ , and  $(100 \mu\text{m}, 0)$  respectively. In (b) the intensity values are uncorrelated and thus the joint intensity PDF is independent, while in (c,d) the encoded non-local correlations result in a dependent joint PDF. To obtain these results we use an ensemble of 5000 customized speckle patterns.

In Figure 4.3, we present some of the high-order statistical properties of the family of customized speckle patterns presented in Figure 4.2. We show the complex joint PDF of the speckled field,  $P(\text{Re}[E], \text{Im}[E])$ , in Figure 4.3(a). Because the complex field PDF is circular non-Gaussian, we know that the customized speckle patterns are fully developed. Therefore, this indicates that (i) the phases of the speckled fields are uniformly distributed from 0 to  $2\pi$ ; (ii) the amplitude and phase values in the complex field are uncorrelated. In (b-d) we show the joint intensity PDF,  $P(I_1, I_2)$ , of two intensity values,  $I_1$  and  $I_2$ , separated by a distance,  $\Delta\mathbf{R}$ . In (b) we choose the spatial separation,  $\Delta\mathbf{R} = (60 \mu\text{m}, 60 \mu\text{m})$ , at which the spatial intensity correlation function is zero. Because the intensity values are uncorrelated, the joint intensity PDF is independent,  $P(I_1, I_2) = P(I_1)P(I_2)$ . Conversely, when the spatial separation of  $I_1$  and  $I_2$  is chosen such that the intensity values are either positively correlated,  $\Delta\mathbf{R} = (0, 100 \mu\text{m})$ , or negatively correlated,  $\Delta\mathbf{R} = (100 \mu\text{m}, 0)$ , the joint intensity PDF is dependent,  $P(I_1, I_2) \neq P(I_1)P(I_2)$ , as shown in Figures 4.3(c & d).

While the method presented in this section, to customize the speckle patterns, provides a prescription for creating complex-light fields and controlling their statistical properties, it does not provide theoretical limitations on what intensity PDFs and spatial correlations can be realized, which will be addressed in the next section.

## 4.5 Theoretical Limitations

In this section, we discuss the degree to which  $C_I(\Delta\mathbf{r})$  and  $P(I)$  can be controlled simultaneously and independently in a speckle pattern. To study this, we switch to the Fourier basis of the speckle *intensity*  $I(\mathbf{r})$ ; which is distinct from the Fourier transform relationship between the *fields* on the SLM and CCD camera planes discussed in Chapters 2 & 3. Therefore, our analysis is general and independent of the precise mapping between the

fields on the SLM and camera planes.

For simplicity, we restrict our theoretical calculation to one dimension and consider the speckle intensity-pattern consisting of  $N$  speckle grains, which can be described by a discrete array with length  $L$ . We require that  $I(r)$  is statistically stationary and ergodic; therefore, spatial averaging over  $I(r)$  and ensemble averaging over different  $I(r)$  are equivalent processes. Additionally, we normalize our speckle patterns such that  $\langle I(r) \rangle = 1$ . Finally, under our conventions the discrete Fourier transform of the speckle pattern can be defined according to:

$$\begin{aligned}\mathcal{F}[I(r)] &= J(\rho) = \frac{1}{\sqrt{L}} \sum_{r=0}^{L-1} I(r) e^{-i\frac{2\pi r\rho}{L}}, \\ \mathcal{F}^{-1}[J(\rho)] &= I(r) = \frac{1}{\sqrt{L}} \sum_{\rho=0}^{L-1} J(\rho) e^{i\frac{2\pi r\rho}{L}}.\end{aligned}\tag{4.2}$$

In our method of customizing speckle intensity-statistics, the spatial correlations are encoded into the speckle pattern,  $I(r)$ , via modification of the Fourier amplitude of the intensity pattern,  $|J(\rho)|$ . According to the discrete Wiener-Khinchin theorem, this relationship can equivalently be written as

$$\begin{aligned}\langle I(r)I(r + \Delta r) \rangle &= \frac{1}{L} \sum_{\rho=0}^{L-1} |J(\rho)|^2 \cos\left(\frac{2\pi\Delta r\rho}{L}\right), \\ |J(\rho)|^2 &= \sum_{\Delta r=0}^{L-1} \langle I(r)I(r + \Delta r) \rangle \cos\left(\frac{2\pi\Delta r\rho}{L}\right).\end{aligned}\tag{4.3}$$

The above equations demonstrate that in a speckle intensity-pattern, there is a uniquely determined relationship between the Fourier amplitudes,  $|J(\rho)|$  and the intensity correlations  $\langle I(r)I(r + \Delta r) \rangle$ . Specifically, we know that  $\langle I(r)I(r + \Delta r) \rangle$  is what sets  $|J(\rho)|$ . Therefore for a given desired/arbitrary correlation function,  $\langle I(r)I(r + \Delta r) \rangle$ , there is a corresponding Fourier amplitude profile,  $|J(\rho)|$ , which is well defined and can be used to

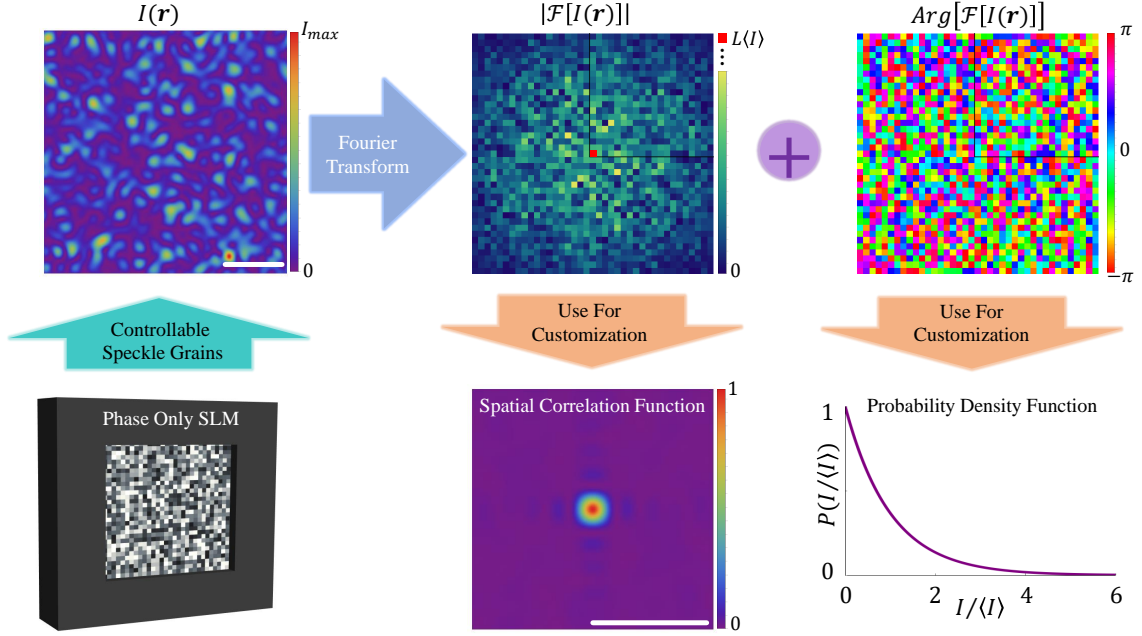


Figure 4.4: **A flowchart illustration of separate control over the speckle correlations and intensity PDF.** The phase-only SLM generates the speckle pattern  $I(r)$ , whose Fourier transform is  $J(\rho) = \mathcal{F}[I(\mathbf{r})]$ . The Fourier amplitude,  $|J(\rho)|$ , is modulated to manipulate  $C_I(\Delta\mathbf{r})$  and the phase,  $\text{Arg}[J(\rho)]$ , can be used to tailor the intensity PDF.

encode the desired/arbitrary correlations into a speckle pattern.

While we cannot directly write the intensity PDF,  $P(I)$ , as a function of  $I(r)$ ; we can use the relationship between  $P(I)$  and its intensity moments,  $\langle I^n(r) \rangle = \int P(I) I^n dI$  where  $n$  is a positive integer. We relate  $\langle I^n(r) \rangle$  to the Fourier amplitudes of  $I(r)$ , using the Fourier transformation relation in Eq. 4.2:

$$\langle I^n(r) \rangle = \left\langle \prod_{k=1}^n \left[ \sum_{\rho_k=0}^{L-1} \frac{J(\rho_k)}{\sqrt{L}} e^{i\frac{2\pi r \rho_k}{L}} \right] \right\rangle_r. \quad (4.4)$$

This expression can be simplified by using the delta function identity  $\langle e^{i\frac{2\pi r}{L}(\rho-\rho')} \rangle_r = \delta(\rho, \rho')$ , and written as

$$\langle I^n(r) \rangle = \frac{1}{L^{n/2}} \sum_{\rho_1 \dots \rho_{n-1}=0}^{L-1} J(\rho_1) \dots J(\rho_{n-1}) J^*(\rho_1 + \dots + \rho_{n-1}) \quad (4.5)$$

which is valid for  $n \geq 2$ . For the first moment  $n = 1$ , it can be shown  $\langle I(r) \rangle = J(0)/\sqrt{L}$ . Eq. 4.5 shows that the  $n^{\text{th}}$  moment of a speckle pattern is related to the  $n - 1$  order correlations among the elements of  $J(\rho)$ . Comparison between Eqs. 4.5 and 4.3 reveals that while  $C_I(\Delta r)$ ,  $\langle I \rangle$ , and  $\langle I^2 \rangle$  are determined by the amplitude profile of  $J(\rho)$ , the higher-order intensity moments  $n > 2$  can be manipulated separately using the phase values of  $J(\rho)$ . Since the only relationship between the intensity moment and spatial correlation function is  $\langle I^2 \rangle = C_I(0) + 1$ , the  $\Delta r$  dependence of the spatial intensity correlation function and the intensity PDF of a speckle pattern can be controlled independently in a speckle pattern, as we illustrate in Figure 4.4.

While we have established a relative independence between  $P(I)$  and  $C_I(\Delta r)$ , this does not necessitate that both can be arbitrarily customized. Next, we identify the limitations on our ability to manipulate  $P(I)$  in a speckle pattern. The ability to arbitrarily control the intensity profile of a speckle pattern with  $N$  speckle grains is equivalent to controlling the moments of the speckles' intensity PDF according to Eq. 4.5 wherein the highest moment one can control is on the order of the number of speckle grains  $N$ .

The next question is “how many moments are required to uniquely define a PDF?” To answer this question in the context of realistic speckle intensity-patterns, it is useful to take certain experimental facts into consideration. For example, all speckle patterns have a finite valued total power (spatially integrated intensity), which imposes a limit on the maximum intensity that a speckle pattern can have,  $I_M$ . Hence, the intensity PDF is bounded by the maximal intensity value  $I_M$ . Furthermore, a measured speckle pattern inherently has discrete intensity values, with the discretization step determined by either the dynamic range of the camera or the measurement noise, and therefore the intensity PDF of the speckle pattern must also have discrete intensity values. Consequently, we define  $\Delta I$  as the intensity discretization step,  $\Delta I = I_{m+1} - I_m$ , and as a result the intensity PDF is given by a set of values  $P(I_m)$ , where  $m = 1, 2, \dots, M$ . The integral equation relating

the intensity moments to the PDF can therefore be written in discrete form as  $\langle I^n \rangle = \Delta I \sum_{m=1}^M I_m^n P(I_m)$ . This relationship is expressed as the following matrix operation:

$$\begin{pmatrix} \langle I \rangle \\ \langle I^2 \rangle \\ \vdots \\ \langle I^N \rangle \end{pmatrix} = \Delta I \begin{pmatrix} I_1 & I_2 & \dots & I_M \\ I_1^2 & I_2^2 & \dots & I_M^2 \\ \vdots & \vdots & \ddots & \vdots \\ I_1^N & I_2^N & \dots & I_M^N \end{pmatrix} \begin{pmatrix} P(I_1) \\ P(I_2) \\ \vdots \\ P(I_M) \end{pmatrix}. \quad (4.6)$$

From this relation, reconstructing  $P(I)$  from a given number of moments becomes a matrix inversion problem. For the case where  $N = M$ , the matrix inverse in Eq. 4.6 is well defined and can be directly calculated. Therefore, any continuous intensity PDF which can be perfectly represented by  $M$  discrete data points is uniquely defined by its first  $M$  intensity moments. We can further this line of reasoning beyond the case where  $\Delta I$  is dictated by the effective dynamic range of the measurement, and consider the case where  $\Delta I$  is the minimum sampling rate required to accurately represent an intensity PDF. The Nyquist-Shannon sampling theorem –which establishes the minimum number of evenly spaced data points required to represent a continuous bandlimited-function without loss of information– tells us that if  $P(I)$  can be represented by a continuous bandlimited-function between  $I_0$  and  $I_M$ , we need to sample  $P(I)$  with at least two data points per period of its highest frequency component between  $I_0$  and  $I_M$ ; in order to represent it with a discrete array,  $P(I_m)$ , without losing any information. This means that if  $P(I)$  can be represented by a band limited and Nyquist-sampled array of  $M$  data points, then  $P(I)$  is uniquely defined by its first  $M$  intensity moments. In other words, if in a speckle pattern we can uniquely control  $M$  intensity moments, then the speckle pattern can possess any intensity PDF which: is represented by a band limited function over a finite intensity range, and satisfies the Nyquist sampling theorem when discretized into  $M$  data points.

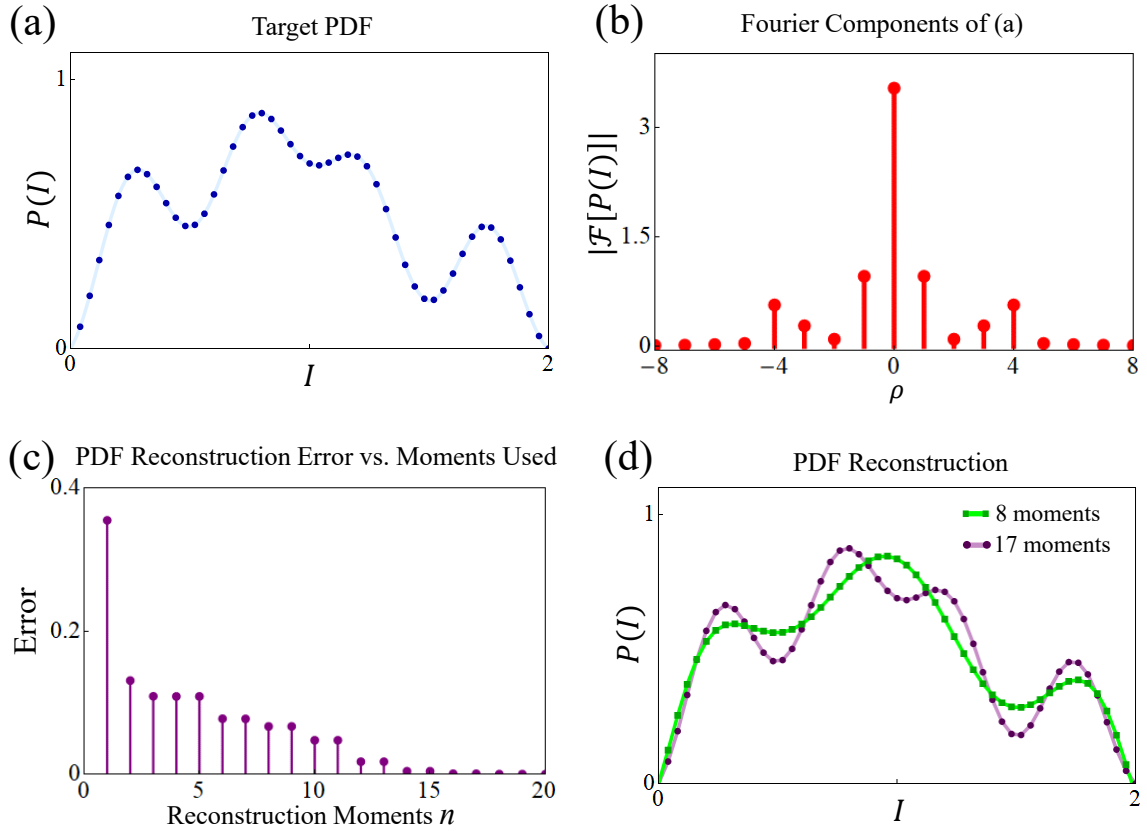


Figure 4.5: **The effect of reconstructing an intensity PDF from different numbers of its moments.** An example PDF,  $P(I)$ , with a finite range of intensity is shown in (a). The Fourier spectrum of  $P(I)$  is plotted in (b), demonstrating that the PDF has a limited number of non-zero Fourier components. (c) shows the PDF reconstruction error of (a) as a function of the number of intensity moments used for reconstruction. Two examples of reconstructed PDFs are shown in (d); they are created using 8 intensity moments and 17 intensity moments.

In Figure 4.5 we demonstrate this principle using the example PDF shown in (a). In this example we set  $I_M = 2$  and  $\Delta I = 1/25$ , thus  $M = 50$ , as seen in (a). In (b) the amplitude of the bandlimited Fourier spectrum of  $P(I)$  is shown, after  $P(I)$  has been Nyquist sampled. In this case the Fourier amplitudes are non-zero between  $-4 \leq \rho \leq 4$  and zero for  $4 < |\rho| \leq 8$ . Hence, at least 17 intensity moments are required to uniquely define the  $P(I)$  shown in (a): in term of its intensity moments. We can verify this by applying the pseudo-inverse of the  $M \times N$  matrix in Eq. 4.6 to different numbers of

moments of the PDF: under the condition that the number of moments used is less than the number of data points  $N < M$ . In this case, when we have a sufficient number of moments to uniquely define the PDF in (a), at least 17 moments, the PDF reconstructed from its moments is identical to the original. In (c) we plot the PDF reconstruction error of (a) as a function of the number of intensity moments  $N$  used in the reconstruction. Around when the number of moments reaches the critical number to uniquely define the PDF, the error vanishes. In (d), we plot two example PDFs reconstructed from  $N = 8$  and  $N = 17$  moments. While the reconstruction using  $N = 8$  intensity moments fails to reproduce the correct PDF, increasing  $N$  to  $N = 17$  results in a faithful reproduction of the original PDF.

In the context of using a phase-only SLM with our technique in 1D, if we modulate  $2N$  independent phase-values on the SLM, we can control the intensity profile of  $N$  speckle grains, and therefore the total degree of control we have on the complex  $J(\rho)$  values is  $N$ . Half of it,  $N/2$ , lies in the amplitude of  $J(\rho)$  which is used to manipulate spatial correlations  $C_I(\Delta\mathbf{r})$ . The other half, lies in the phase of  $J(\rho)$  and translates to the ability to control  $N/2$  intensity moments. As long as a desired intensity PDF can be Nyquist-sampled and represented in bandlimited form by less than  $N/2$  data points, a speckle pattern adhering to it can be generated. In 2D, the only practical difference is that we require  $4N$  independent phase values to control a speckle pattern with  $N$  speckle grains. At this point, it is important to recall that we require speckle patterns to be stationary and ergodic. In order to satisfy these conditions, the speckle patterns must consist of a large number of speckle grains, because the average difference between the ensemble PDF of a family of speckle patterns and a single realization scales as  $1/\sqrt{N}$ . Therefore,  $N$  is always large in practice, *e.g.*,  $N \approx 250$  in our experiments. For realistic intensity PDFs, however, the number of non-zero Fourier components is much less than  $N/2$  due to noise limitations [1], and therefore they can be reconstructed with significantly less than the available  $N/2$  intensity moments. To summarize, we have found that in a speckle

intensity-pattern the intensity PDF and the functional form of  $C_I(\Delta r)$  can be controlled independently and arbitrarily except for the constraint  $C_I(0) = \langle I^2 \rangle - 1$ .

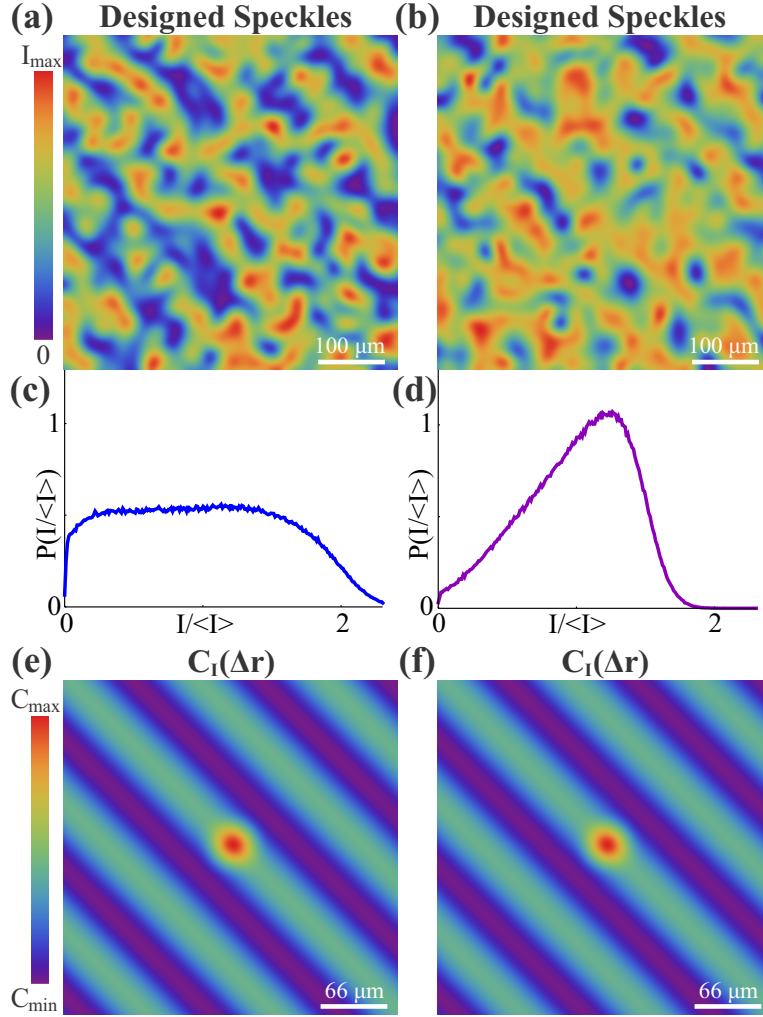


Figure 4.6: **Two customized speckle patterns (a,b) with different intensity PDFs (c,d) but identically shaped spatial intensity correlation functions are shown in (e,f).** In (a) we present a measured speckle pattern adhering to both the PDF shown in (c), which is flat over a pre-defined range of  $I/\langle I \rangle$ , and the diagonally oscillating spatial intensity correlation function shown in (e). In (b) we present a measured speckle pattern with the same shaped intensity correlation function (f), but obeying a different intensity PDF (d), which increases linearly over a pre-defined  $I/\langle I \rangle$  range. In (e)  $C_{\max} = 0.32$  and  $C_{\min} = -0.09$  while in (f)  $C_{\max} = 0.14$  and  $C_{\min} = -0.04$  due to the different PDFs. We ensemble average over 100 independent speckle patterns to obtain the PDF and correlation functions in (c-f). The origin of (e) and (f) is located at the center of each plot.

## 4.6 Experimental Realizations

Next, we experimentally demonstrate an independent control over the intensity PDF and the spatial intensity correlations of a speckle pattern. In Figure 4.6 we show two examples of speckle patterns that obey different  $P(I)$ , but have congruent  $C_I(\Delta\mathbf{r})$ . The intensity correlation function is designed to have non-local correlations of the form,  $C_{NL}(\Delta\mathbf{r}) = (2C_I(0)/7) \cos[(\Delta\mathbf{x} + \Delta\mathbf{y})/20]$ , where  $x$  and  $y$  are spatial coordinates. For the example customized speckle pattern in (a), the intensity PDF is designed to be constant,  $P(\hat{I}) = 1/2$ , over the intensity range  $0 \leq \hat{I} \equiv I/\langle I \rangle \leq 2$  and zero elsewhere. The second example speckle pattern, shown in (b), is designed to obey a different intensity PDF which linearly increases,  $P(\hat{I}) = \hat{I}$ , over the intensity range  $0 \leq \hat{I} \leq \sqrt{2}$ . As a result of obeying different intensity PDFs,  $\langle \hat{I}^2 \rangle$  differs between the two speckle patterns and therefore  $C_I(0) = 0.32$  in (e) while  $C_I(0) = 0.14$  in (f). While there is a visible difference in the speckle contrast between (a) and (b) due to the different intensity PDFs, as can be seen in (e) and (f), the spatial intensity correlations in both speckle patterns have the same functional form. Comparison between (a) and (b) illustrates how the topology of the customized speckle patterns changes in accordance with the PDF, while the overarching spatial order is dictated by the non-local correlations. Both speckle patterns in (a,b) have an overarching diagonal oscillation. Nevertheless, for the speckles with a linearly increasing PDF in (b), the spatial intensity profile has the appearance of an interwoven web of bright channels with randomly dispersed dark islands, while the speckles with a uniform PDF lack any definite channel structure beyond the diagonal oscillations.

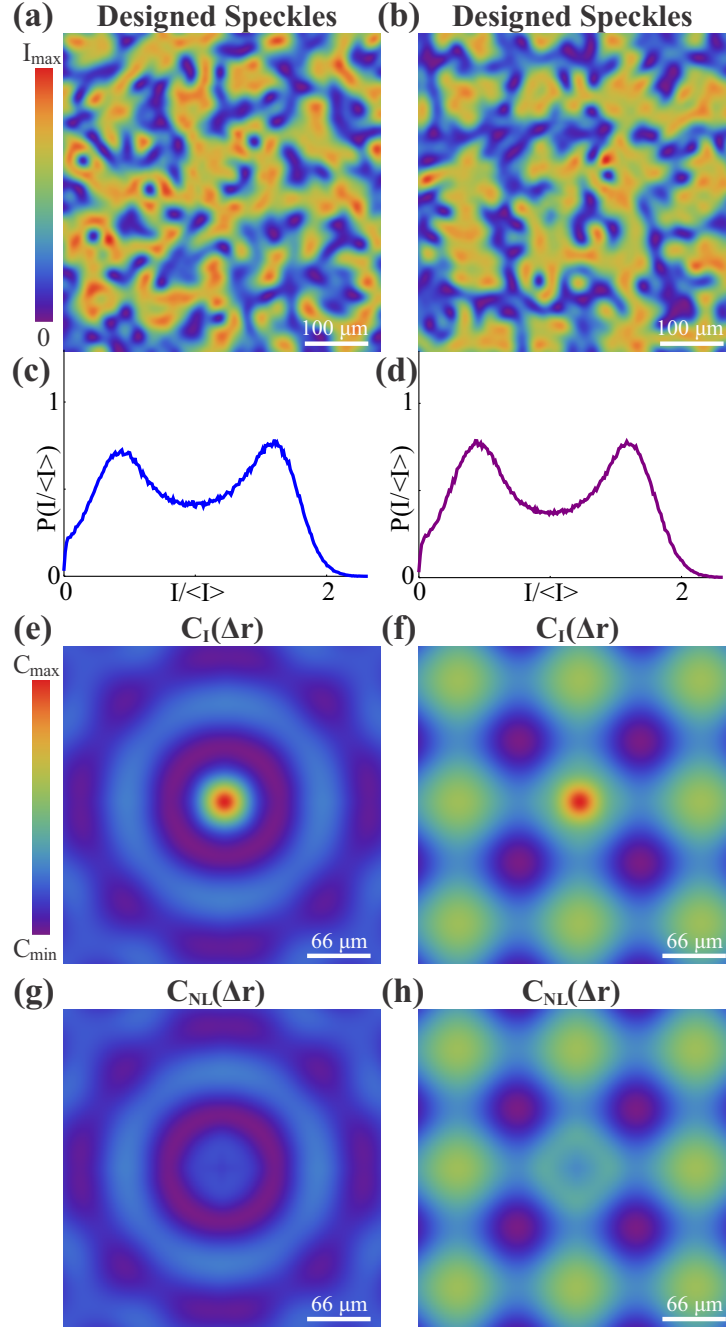


Figure 4.7: **Two customized speckle patterns with the same intensity PDF but different spatial intensity correlation functions are shown.** In (a) we present a measured speckle pattern adhering to both the bimodal intensity PDF shown in (c) and the isotropic oscillating correlation function shown in (e). In (b) we present a measured speckle pattern also adhering to a bimodal PDF (d) but possessing anisotropic ‘checkerboard’ correlations shown in (f). In (g,h) we show the corresponding non-local correlations. In (e)  $C_{\max} = 0.29$  and  $C_{\min} = -0.05$  while in (f)  $C_{\max} = 0.30$  and  $C_{\min} = -0.12$ . We ensemble average over 100 independent speckle patterns, to obtain the PDFs and correlation functions in (c-h). The origins of (e-h) are located at the center of each plot.

In Figure 4.7 we show two examples of speckle patterns that have the same intensity PDF; however, their spatial intensity correlation functions differ. The speckle patterns in both (a) and (b) adhere to a bimodal intensity PDF, as shown in (c) and (d). The local intensity transformation which generates speckles with the PDF,  $P(\hat{I}) = \sin^2(\pi\hat{I})$  over the intensity range  $0 \leq \hat{I} \equiv I/\langle I \rangle \leq 2$  and zero elsewhere, is used to create these speckle patterns. However, because optical fields must be continuous functions,  $P(\hat{I}) \neq 0$  over  $0 < \hat{I} < I_M$ , and therefore the experimental PDFs deviate from  $P(\hat{I}) = \sin^2(\pi\hat{I})$  around  $\hat{I} = 1$  as shown in Chapter 2. Despite having the same intensity PDF, the non-local intensity correlation functions of (a) and (b) are designed to have different spatial variations. In (e) the spatial intensity correlation function  $C_I(\Delta\mathbf{r})$  is an azimuthally-symmetric radially-oscillating function with the appearance of a ‘bullseye’. The non-local correlation function, shown in (g), is designed to have the form:  $C_{NL}(\Delta\mathbf{r}) = (C_I(0)/6) \sin[(\Delta r)/14]$ . In contrast, in (f)  $C_I(\Delta\mathbf{r})$  is designed to be an anisotropic function having a ‘checkerboard’ form with non-local correlations, (h), of the form:  $C_{NL}(\Delta\mathbf{r}) = [4C_I(0)/10] \cos[(\Delta\mathbf{x} + \Delta\mathbf{y})/40] \cos[(\Delta\mathbf{x} - \Delta\mathbf{y})/40]$ . While both speckle patterns in (a, b) share a similar topology, consisting of two interlaced bright and dim channels, the overarching structure differs in both its shape and orientation. In (b) the checkerboard correlations induce the formation of multi-speckle islands with a grid-like orientation. In (a), the bullseye correlations result in an interwoven web-like structure.

## 4.7 Discussion & Conclusion

In conclusion, we have experimentally demonstrated a method of customizing the intensity probability density functions of speckle patterns while simultaneously introducing long-range spatial correlations among the speckle grains. The customized speckle patterns exhibit radically different topologies and varying degrees of spatial order. In addition to

our experimental demonstration, we have explored both the theoretical and practical limitations on the extent to which the intensity probability density function and the spatial intensity correlations can be manipulated separately and arbitrarily in a speckle pattern.

Although the camera is placed on the Fourier plane of the SLM in our experiment this is not a necessity. Our method can easily be adapted to customize the statistical properties of speckle patterns on other  $2D$  planes, or even when a random scattering medium is placed in between the SLM and camera. To accomplish this, we simply need to measure the field-transmission matrix which maps the field on the SLM surface to the field incident on our camera. Therefore, our method and theoretical description provide a systematic approach for creating complex light fields and controlling their statistical properties with a phase-only spatial light modulator, while also providing the upper bounds on what is possible.

There are numerous avenues of research, related to customizing speckle patterns, that are worth further exploration. For example, our method tailors the speckle patterns at a specific plane defined by the camera. Such patterns, similar to Rayleigh speckle patterns, exhibit a rapid axial-decorrelation: occurring within the Rayleigh range of an optical system. In addition to decorrelating within one Rayleigh range, our customized speckles lose both their tailored intensity PDFs as well as their non-local correlations as they axially propagate away from the target plane. Whether or not it is possible to control the statistical properties of speckle patterns simultaneously on multiple planes –or even in a 3D volume– remains an open question [147].

Finally, we will discuss some of the potential applications of our customized speckle patterns. Because our method of creating and controlling complex light is versatile –yet simple– it can readily be incorporated into an extensive range of optical applications and experiments. For example, the ability to arbitrarily control the non-local correlations and intensity PDFs of speckle patterns could enhance many structured-illumination applica-

tions like speckle illumination microscopy [40,41,146], super-resolution imaging [42,43], and high-order ghost imaging [44–46]. Similarly, it could also benefit studies of cold atom [133], active media [53], and microparticle [134] transport in correlated optical potentials. Our method is advantageous because both the topology and the degree of spatial order in the speckled optical potentials are arbitrarily customizable and reconfigurable without any mechanical motion.

# Chapter 5

## Circumventing The Optical Diffraction Limit With Customized Speckles

### 5.1 Introduction

<sup>1</sup>In fluorescence microscopy, a sub-diffraction-limited resolution can be obtained with saturable structured illumination techniques. Examples include stimulated emission depletion (STED) microscopy [148, 149], ground state depletion (GSD) microscopy [150], and reversible saturable optical fluorescence transitions (RESOLFT) [151–153]. Generally, these techniques rely on spatially modulating the illumination intensity to toggle fluorescence on and off in a spatially selective manner. For example, in RESOLFT, a doughnut-shaped optical beam photoconverts all fluorophores in a region of a sample except those close to the vortex center, and therefore fluorescence is only emitted from a sub-diffraction-sized region. Usually, point scanning of the doughnut beam is required to construct an image which can be very time consuming. Recently, this process has been parallelized using either a one-dimensional (1D) standing wave pattern [154] or a two-dimensional (2D) lattice of doughnuts [153]. The first method involves rotating or trans-

---

<sup>1</sup>The chapter material is primarily taken from reference [4]: Nicholas Bender, Mengyuan Sun, Hasan Yilmaz, Joerg Bewersdorf, and Hui Cao, “Circumventing the optical diffraction limit with customized speckles”, *Optica*, vol. 8, 122-129, (2021).

lating the illumination pattern, and as a result, post-processing is required for 2D super-resolution since each individual pattern will only improve the resolution in one direction. In the second method, two incoherently-superimposed orthogonal standing waves create a square lattice of intensity minima, but axial uniformity of the intensity pattern hinders optical sectioning. One way to circumvent this issue is to use the optical vortices in a speckle pattern as the nonlinear structured illumination pattern [155]. Because fully-developed speckle patterns rapidly and non-repeatably change along the axial direction, they can be used to obtain a three-dimensional super-resolution image [146]. In this context, speckles are advantageous because they are robust to optical distortions/aberrations while simultaneously enabling three-dimensional super-resolution [40–42, 132, 143–146, 156–162]. The problem with using Rayleigh speckles, however, is that the anisotropic and strongly fluctuating shapes of their optical vortices leads to non-isotropic and non-uniform improvements in the spatial resolution.

In this chapter, we introduce and use an ideal family of tailored speckle-patterns for nonlinear pattern-illumination microscopy. The speckle patterns we design need to possess the following properties in order to produce isotropic and uniform super-resolution. All of the vortices in the speckles must have a circular shape and an identical high-intensity halo surrounding each vortex core. Away from the randomly distributed optical vortices, however, the spatial intensity profile of the speckles should be uniform with minor fluctuations. When this is the case, the speckles' intensity PDF is a narrow peak that can be approximated as a delta function. We thus refer to this family of tailored speckles as “delta” speckles. To enable optical sectioning, the delta speckles' field must be fully developed and as a result the speckles' intensity pattern will rapidly and non-repeatably evolve upon axial propagation. Experimentally, we generate delta speckle patterns by modulating the phase-front of a monochromatic laser beam with a spatial light modulator using the technique described in the last chapter. Using delta speckle patterns, we photoconvert a planar

fluorescent gel sample and measure the fluorescence signal from the unconverted regions in the vicinity of optical vortices. Not only do we demonstrate a  $3\times$  enhanced spatial resolution relative to the optical diffraction limit of the illumination optics, but also, we show the significant advantages of using customized speckles over Rayleigh speckles in fluorescence microscopy.

## 5.2 Experimental Setup

### 5.2.1 Optical Setup

In our demonstration, the fluorescent sample is a  $25\text{-}\mu\text{m}$  thick layer of the photoconvertible protein mEos3.2, which is uniformly distributed and suspended in a gel [163] (see the next subsection for details). A continuous-wave (CW) laser beam with a wavelength of  $\lambda = 405$  nm is used to photoconvert the protein. The laser's wavefront is modulated by a phase-only spatial light modulator (SLM), which generates a speckle pattern in its far-field (Fourier plane). The polarization of the far-field speckles' field is converted from linear to circular by a quarter-waveplate. The far-field speckle pattern illuminates and photoconverts the sample.

A schematic of the detailed experimental setup for photoconverting a fluorescent sample with customized speckle patterns and imaging the unconverted fluorescence is shown in Fig. 5.1. The  $\lambda = 405$  nm CW laser beam is expanded and linearly polarized before it is incident on the phase-only SLM (Meadowlark Optics). The pixels on the SLM can modulate the phase of the incident field between 0 and  $2\pi$ : in increments of  $2\pi/90$ . Because a small portion of light reflected from the SLM is unmodulated, we write a binary phase diffraction grating on the SLM and use the light diffracted to the first order for photoconversion. In order to avoid cross-talk between the neighboring SLM pixels,  $32 \times 32$  pixels

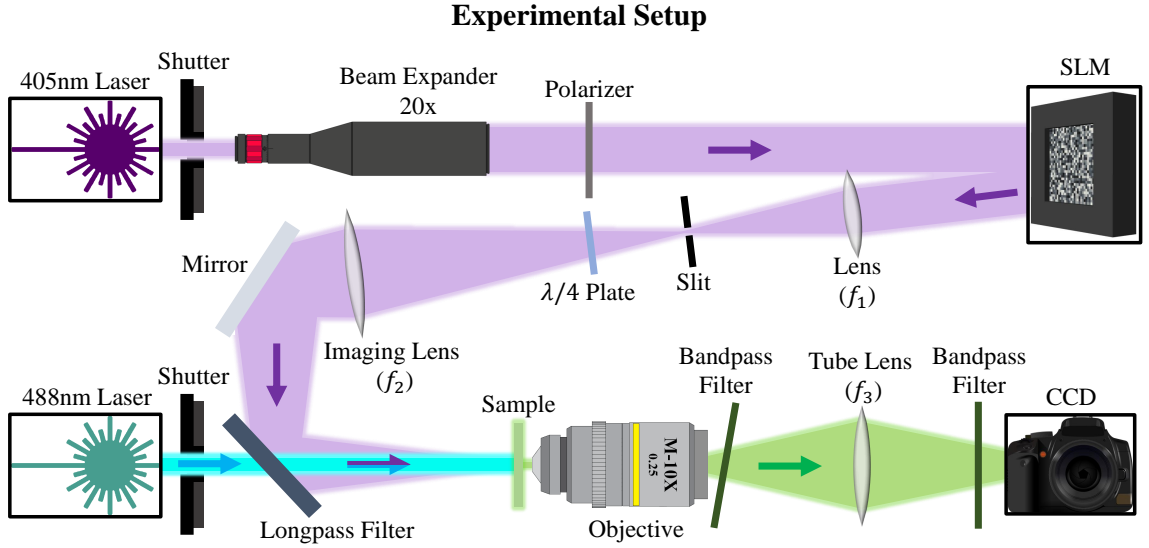


Figure 5.1: **Experimental setup.** The experimental setup used for nonlinear speckle-illumination microscopy is shown. We use a phase-only SLM to generate a customized speckle pattern which illuminates and photoconverts a fluorescent sample.

are grouped to form one macropixel, and the binary diffraction grating is written within each macropixel with a period of 8 pixels. We use a square array of  $32 \times 32$  macropixels in the central part of the phase modulating region of the SLM to shape the photoconverting laser light. The light modulated by our SLM is Fourier transformed by a lens with a focal length of  $f_1 = 500$  mm and cropped in the Fourier plane with a slit to keep only the first-order diffraction. The complex field on the Fourier plane of the SLM is imaged onto the surface of the sample by a second lens, with a focal length of  $f_2 = 500$  mm. Using a  $\lambda/4$  plate, we convert the linearly polarized photoconverting beam into a circularly polarized beam before it is incident upon the sample. In this setup, the full width at half-maximum of a diffraction-limited focal spot is  $17 \mu\text{m}$ .

After the photoconversion process, a second laser, operating at a wavelength of  $\lambda = 488$  nm, uniformly illuminates the sample and excites the non-photoconverted mEos3.2 proteins. The unconverted protein fluorescence has a wavelength centered around  $\lambda = 532$

nm [163]. To collect the fluorescence, we use a  $10\times$  objective of  $NA = 0.25$  and a tube lens with a focal length of  $f_3 = 150$  mm. The 2D fluorescence image is recorded by a CCD camera (Allied Vision Manta G-235B). The spatial resolution of the detection system is estimated to be  $1.1\ \mu\text{m}$ , which allows us to resolve features in the sample that are smaller than the diffraction limit of our illumination optics. The remaining excitation laser light, which is not absorbed by the sample, is subsequently removed by two Chroma ET 535/70 bandpass filters. One filter is placed after the objective lens and reflects the excitation beam off the optical axis of our system. The second one is placed directly in front of the camera.

## 5.2.2 Purified Protein Sample Preparation

The plasmid for mEos3.2 expression is cloned with PCR and NEBuilder assembly, and transformed into BL21-CondonPlus (DE3) competent cells. The mEos3.2 protein is purified using Ni-NTA His-Bind resin and dialyzed in dialysis buffer (20 mM Tris, pH 7.5/ 10 mM NaCl/ 1mM EDTA/ 10 mM BME). To immobilize mEos3.2, a mixture containing  $42\ \mu\text{L}$  purified mEos3.2 (0.1 mM),  $30\ \mu\text{L}$  30.8 % Acrylamide/bis-acrylamide,  $0.5\ \mu\text{L}$  10 % APS, and  $0.5\ \mu\text{L}$  TEMED is sandwiched between a clean coverslip and a slide to make a 25- $\mu\text{m}$ -thick gel.

## 5.3 Photoconversion Fluorescence Microscopy

Fig. 5.2(a) shows part of an example speckle pattern used to photoconvert the fluorescent sample. The lateral dimension of the entire speckle pattern is  $600\ \mu\text{m}$ . The speckle pattern consists of two regions. Within the central region marked by the white dashed square,  $300\ \mu\text{m} \times 300\ \mu\text{m}$  in size, the speckle pattern obeys delta intensity statistics, i.e. a random array of circular vortices embedded in a nearly uniform intensity background. Outside the

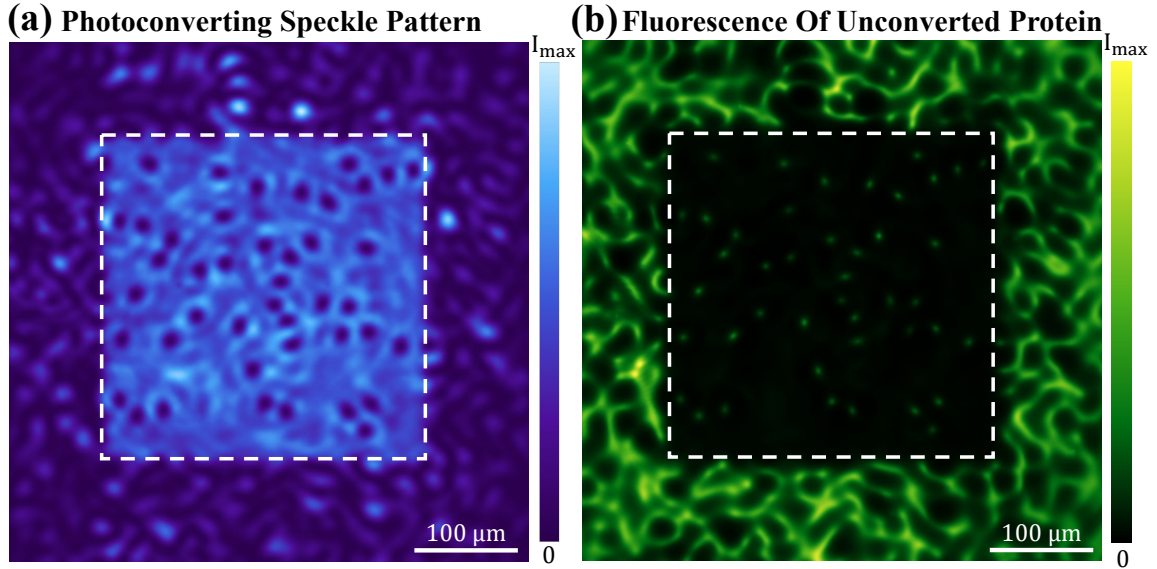


Figure 5.2: **Customizing speckles for nonlinear pattern illumination.** An experimentally recorded speckle pattern that illuminates and photoconverts a uniform fluorescent protein sample is shown in (a). Within the white box the speckles obey delta statistics and outside they obey Rayleigh statistics. In (b), an experimentally recorded image of the fluorescence from the unconverted regions shows isometric and isotropic spots produced by the vortices in the delta speckles; while the region photoconverted by the Rayleigh speckles features large, irregular, and interconnected fluorescent grains.

square, the speckles adhere to Rayleigh statistics, featuring sparse, nearly circular islands of high intensity, randomly distributed in a dark sea. The average speckle grain size is 17  $\mu\text{m}$ .

Fig. 5.2(b) shows the fluorescence from the uniform protein gel sample after being photoconverted by the speckle pattern presented in Fig. 5.2(a). Outside the central square, the sample is photoconverted by the Rayleigh speckle pattern. The fluorescent pattern consists of a sprawling anisotropic web, which reflects the topology of the low-intensity regions surrounding the optical vortices. In stark contrast, the fluorescence pattern within the central square, which is photoconverted by delta speckles, features isolated fluorescent spots of a much smaller size. They are all created by the optical vortices in the central square of Fig. 5.2(a). The high level of isotropy exhibited by the fluorescent spots originates from the high degree of rotational symmetry that is present in the vortices generating

them. Apart from these spots, the fluorescent intensity is uniformly low. This dark background arises from the homogeneity of the delta speckle pattern's intensity away from optical vortices. A qualitative comparison between the distinct fluorescence patterns inside and outside the central square illustrates how customizing the intensity statistics of speckles can significantly enhance the performance of speckle-based pattern illumination microscopy.

## 5.4 Quantitative Analysis

Next, in Fig. 5.3, we quantitatively assess the performance of delta speckles in our application. We compare a diffraction-limited spot, shown in Fig. 5.3(a), with the fluorescent spots produced in the central region of Fig. 5.2(b) to quantitatively determine the resolution enhancement. The diffraction-limited spot is created using the experimentally measured field-transmission matrix of the 405 nm light, from the SLM to the sample, and it gives the 2D point spread function (PSF) of our illumination optics. The full width at half maximum (FWHM) of the spot is  $17\ \mu\text{m}$ , which is in agreement with the estimated value of  $18\ \mu\text{m}$  from the diffraction limit  $\lambda/(2\text{NA})$ , where  $\text{NA} \cong 0.011$  is the numerical aperture of the illumination optics. Fig. 5.3(b) shows an example fluorescent spot created by one of the vortices in the illuminating delta speckle pattern. Its shape is close to circular. We determine the full width at half maximum (FWHM) along both the major axis  $a = 6.1\ \mu\text{m}$  and the minor axis  $b = 5.0\ \mu\text{m}$  by fitting. The average spot size,  $(a + b)/2 \cong 5.6\ \mu\text{m}$ , is three times below the diffraction limit ( $17\ \mu\text{m}$ ).

### 5.4.1 Fluorescent Spot Measurement

We use the following procedure to quantitatively analyze the size and shape of the fluorescent spots created by the optical vortices in a photoconverting delta speckle pattern. First,

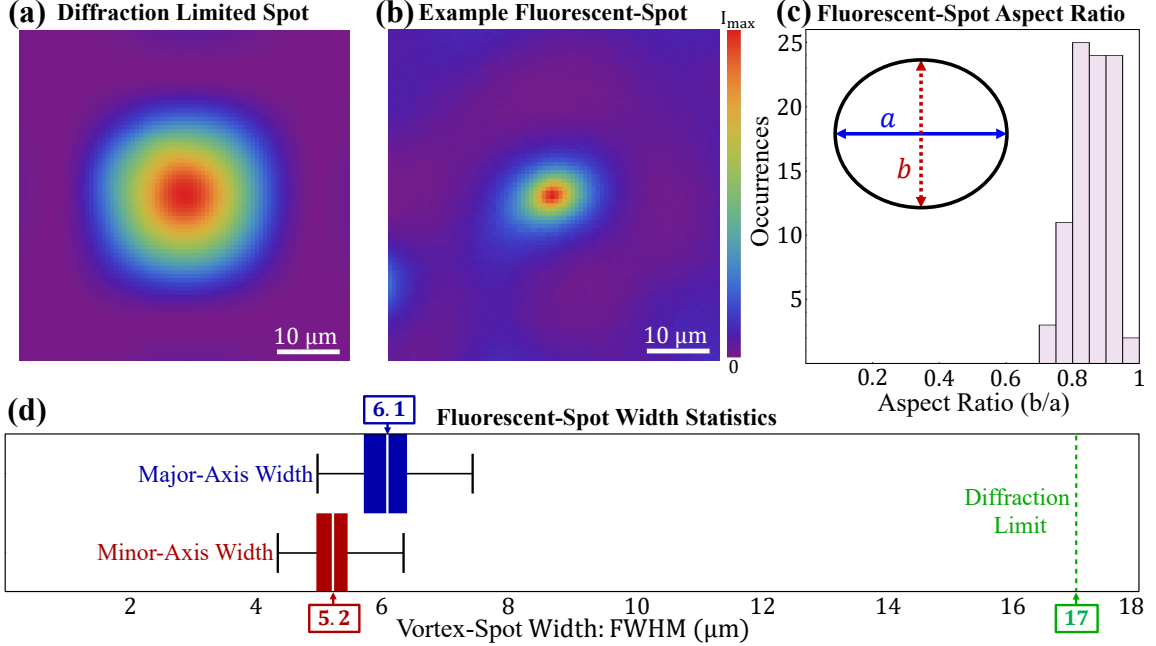


Figure 5.3: **Circumventing the diffraction limit.** A diffraction-limited spot of the 405 nm illumination/photoconversion optics is presented in (a). In (b), an example fluorescent spot produced by a vortex in the delta speckle pattern is illustrated. Its size is much smaller than the diffraction-limited spot. Its shape can be fit by an ellipse of major axis width  $a = 6.1 \mu\text{m}$  and minor axis width  $b = 5 \mu\text{m}$ . The aspect-ratio,  $b/a$ , histogram of all fluorescent spots produced by the delta speckles is shown in (c). The inset illustrates an ellipse with the average aspect ratio  $\langle b/a \rangle = 0.86$ . In (d), the box-plot analysis of the major and minor axes widths is shown. The white line marks the mean value, and the black whiskers represent the upper and lower bounds of the data. The edges of the blue and red shaded regions mark the upper and lower quartiles (25%, 75%) of the ensemble. The green dashed line indicates the FWHM of the diffraction-limited spot in (a).

we locate the center of each fluorescent spot:  $\mathbf{r}_c = \int \mathbf{r} I(\mathbf{r}) d\mathbf{r} / \int I(\mathbf{r}) d\mathbf{r}$ . Using the  $38 \mu\text{m} \times 38 \mu\text{m}$  region surrounding each fluorescent spot, which corresponds to  $61 \times 61$  pixels on the CCD camera, we numerically construct a 2D interpolation of every fluorescent spot. Next, we rotate each interpolated grid around the center  $\mathbf{r}_c$  in increments of  $1^\circ$ , over a total of  $180^\circ$ , and record the 1D profile along the horizontal axis for each rotation. Then we fit each of these 1D profiles to a Gaussian function,  $I_a \times \exp[-(x - x_0)^2 / (2\sigma^2)] + I_c$ , with  $I_a$ ,  $x_0$ ,  $\sigma$ ,  $I_c$  as the fitting parameters. After determining the maximum and minimum values of  $\sigma$  from all rotation angles, for each fluorescent spot, we extract both the major and minor

axis widths from the full width at half maximum (FWHM)  $2\sigma\sqrt{2\ln(2)}$ . For the results shown in Fig. 5.3, the average  $R^2$  fitting coefficient is 0.996. Generally the rotation angles corresponding to the maximum and the minimum widths are offset by  $90^\circ$ , reflecting the elliptical shape of the fluorescent spots.

### 5.4.2 Fluorescent Spot Properties

To determine the isotropy of the spatial resolution enhancement produced by the delta speckles, we measure the major axis  $a$  and minor axis  $b$  of all fluorescent spots in the central region. The aspect ratio  $b/a$  is a measure of isotropy. Using measurements from a total of 89 fluorescent spots stemming from two independent delta speckle patterns, we calculate a histogram of the ratio ( $b/a$ ) which is shown in Fig. 5.3(c). All of the spots are close to circular. The mean value of  $b/a$  is 0.86. The most circular fluorescent spot has  $b/a = 0.95$ , and the least circular spot  $b/a = 0.72$ .

The size uniformity of the fluorescent spots is reflected in the box-plot analysis of the major and minor axis widths in Fig. 5.3(d). The mean value of major and minor axis widths, marked by white lines, are  $\langle a \rangle = 6.1 \mu\text{m}$  and  $\langle b \rangle = 5.2 \mu\text{m}$ . The black whiskers show the maximum and minimum of the ensemble. The edges of the blue and red shaded regions denote the upper and lower quartile (25% and 75%) of the data, which are  $5.7 \mu\text{m}$  and  $6.4 \mu\text{m}$  for the major axis  $a$ ,  $4.9 \mu\text{m}$  and  $5.4 \mu\text{m}$  for the minor axis  $b$ . The green dashed line indicates the diffraction limit, i.e., the width of the PSF in (a). Not only do all of the fluorescent spots have a uniform size, but they are also significantly smaller than the diffraction-limited spot size. Therefore, the spatial resolution enhancement provided by delta speckles is homogeneous.

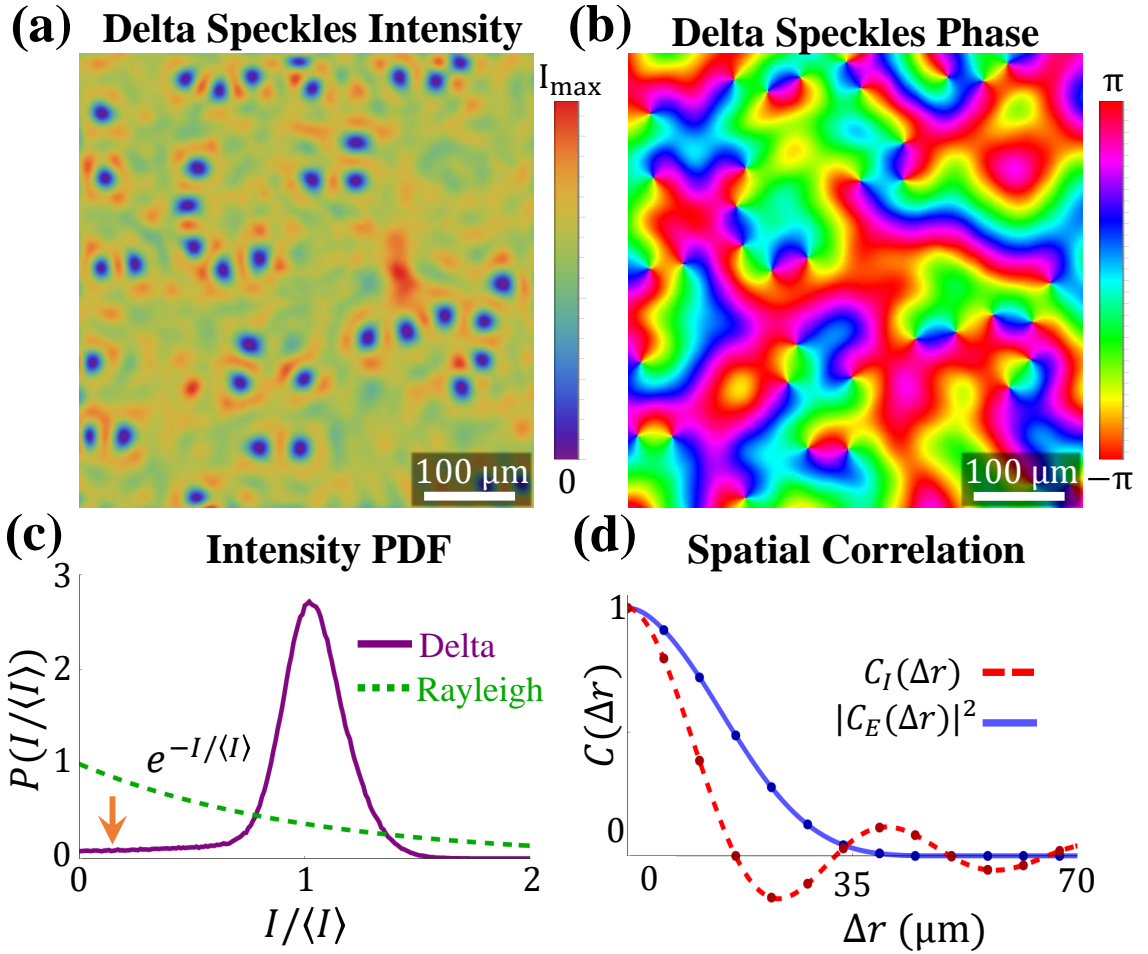


Figure 5.4: **Customized Speckle Statistics.** An example delta speckle pattern is presented in (a) and the corresponding phase distribution of its complex field is shown in (b). The phase is randomly distributed between  $-\pi$  and  $\pi$ , indicating that the speckle pattern is fully developed. The intensity PDF (purple solid line) of the delta speckle pattern is shown in (c) and compared with a Rayleigh PDF (green dashed line). The spatial correlation functions of the intensity (red dashed line) and the field (blue solid line) in the delta speckle pattern are shown in (d). The spatial fluctuations of the intensity are faster than those of the field. The anti-correlation ( $C_I < 0$ ) originates from the bright ring surrounding each vortex core. The plots both in (c) and (d) are obtained from an ensemble of 100 speckle patterns.

## 5.5 Customized Speckle Statistics

In the previous section, we established the significant advantages of creating isotropic and isomeric vortices in the photoconverting speckle patterns used in fluorescence microscopy. Here we characterize the customized speckles' properties in detail and show how their vortex characteristics are transferred to the fluorescent spots. To this end, we use the simpler experimental setup described in the previous chapters to generate the speckles.

An example of an experimentally measured delta speckle pattern is shown in Fig. 5.4(a). The corresponding 2D phase profile of the speckle pattern is shown in (b). While the 2D intensity profile of the speckle pattern is relatively homogeneous apart from the vortices, the corresponding phase profile is random and irregular everywhere. This reflects the fact that the complex field of the delta speckles adheres to a circular non-Gaussian PDF. The phase has a uniform probability distribution within the range of  $-\pi$  to  $\pi$  and the intensity is independent of the phase, thus the speckles' field is fully developed.

In Fig. 5.4(c), we compare the intensity PDF of an ensemble of 100 delta speckle patterns like the one shown in (a) (purple line) to a Rayleigh PDF (green dashed line). Because the Rayleigh intensity PDF exhibits an exponential decay, the most probable intensity values in a Rayleigh speckle pattern are close to 0. Therefore, the spatial profile of a Rayleigh speckle pattern is dominated by the low-intensity regions surrounding the optical vortices. The high-intensity regions, which are the bright speckle grains, are sparse, well separated, and isotropic. In many ways the spatial profile of a delta speckle pattern is the inverse of a Rayleigh speckle pattern. Because the spatially uniform regions of high intensity dominate the spatial profile of a delta speckle pattern, the intensity PDF is narrowly peaked and centered around the mean value  $\langle I \rangle$ . The peak's width is a reflection of the intensity fluctuations associated with the speckle grains. The presence of optical vortices, and the surrounding dark regions, in the speckle patterns result in a low-intensity tail in

the PDF extending to  $I = 0$  (marked by the orange arrow in (c)). Because the probability density in this tail is low, the vortices are sparse and spatially isolated.

Using the spatial field correlation function,  $C_E(\Delta r)$ , and the spatial intensity correlation function,  $C_I(\Delta r)$ , we can identify the characteristic length scales in the speckle patterns. Here, for simplicity, the spatial correlation function of the speckles' field is defined according to the Pearson correlation function as:

$$C_E(\Delta \mathbf{r}) \equiv \frac{\langle E(\mathbf{r})E^*(\mathbf{r} + \Delta \mathbf{r}) \rangle}{\sqrt{\langle |E(\mathbf{r})|^2 \rangle} \sqrt{\langle |E(\mathbf{r} + \Delta \mathbf{r})|^2 \rangle}} \quad (5.1)$$

where  $\langle \dots \rangle$  denotes spatial averaging over  $\mathbf{r}$ . Similarly, the spatial correlation function of the speckles' intensity is defined as:

$$C_I(\Delta \mathbf{r}) \equiv \frac{\langle \delta I(\mathbf{r})\delta I(\mathbf{r} + \Delta \mathbf{r}) \rangle}{\sqrt{\langle [\delta I(\mathbf{r})]^2 \rangle} \sqrt{\langle [\delta I(\mathbf{r} + \Delta \mathbf{r})]^2 \rangle}} \quad (5.2)$$

where  $\delta I(\mathbf{r}) = I(\mathbf{r}) - \langle I(\mathbf{r}) \rangle$  denotes intensity fluctuations around the mean. Because the spatial correlation function of the speckle patterns under consideration are azimuthally symmetric and depend only on the distance  $\Delta r = |\Delta \mathbf{r}|$ ;  $|C_E(\Delta \mathbf{r})|^2$  and  $C_I(\Delta \mathbf{r})$  can be represented by  $|C_E(\Delta r)|^2$  and  $C_I(\Delta r)$ .

As discussed previously, for a Rayleigh speckle pattern,  $C_I(\Delta r) = |C_E(\Delta r)|^2$ , and therefore both the field and the intensity fluctuate on the same length scale. The spatial correlation length, defined as the full width at half maximum (FWHM) of  $C_I(\Delta r)$ , is determined by the diffraction limit. For a delta speckle pattern,  $C_I(\Delta r)$  is narrower than  $|C_E(\Delta r)|^2$ , as can be seen in Fig. 5.4(d). In the delta speckles,  $|C_E(\Delta r)|^2$  remains the same as in Rayleigh speckles, because both patterns are generated by a phase-only SLM and their spatial frequency spectra are identical. Because  $C_I(\Delta r)$  is narrower than  $|C_E(\Delta r)|^2$  in a delta speckle pattern, it indicates that the intensity varies faster than the field, spatially. Another difference is that with increasing  $\Delta r$ , the delta speckles'  $C_I(\Delta r)$

exhibits a damped oscillation instead of a monotonic decay. These results can be understood as follows: according to the definition of  $C_I(\Delta r)$ , the features in the speckle patterns that contribute the most to the intensity correlation function are those where the intensity deviates the most from the mean value. In a Rayleigh speckle pattern, the bright speckle grains have the greatest difference in intensity relative to the mean value. As a result, the speckle grain size determines the FWHM of  $C_I(\Delta r)$  in a Rayleigh speckle pattern. Conversely, in a delta speckle pattern, the vortices differ from the mean intensity value more than any other element in the pattern. Therefore, the characteristic features of the optical vortices dictate  $C_I(\Delta r)$ . For example, the high-intensity halo surrounding each vortex core is reflected in the negative correlation  $C_I(\Delta r) < 0$  around  $\Delta r = 20 \mu\text{m}$ , which corresponds to the distance from the vortex center to the high-intensity halo.

## 5.6 Vortex Characteristics

In our photoconversion experiment, effectively, the inverse of the  $\lambda = 405 \text{ nm}$  speckle pattern is imprinted onto the uniform fluorescent sample. Therefore after photoconversion, the measured fluorescence originates from the regions of the sample in the vicinity of the optical vortices in the speckle pattern. Here, we investigate the shape and intensity fluctuations of such regions in both delta speckles and Rayleigh speckles. In Fig. 5.5(a,b), we magnify two representative vortex-centered regions in a delta speckle pattern and in a Rayleigh speckle pattern. While the dark region surrounding the vortex cores in the delta speckle pattern is relatively circular, it is elongated and irregular in the Rayleigh speckle pattern. These properties are general and occur within one spatial correlation length from the vortex center. In Fig. 5.5(c), we plot the radial intensity profiles averaged over all vortices in ensembles of delta (purple line) and Rayleigh (green line) speckle patterns. The intensity rises faster with distance from the vortex center in delta speckles,

leading to a smaller region of low intensity than found in Rayleigh speckles. In (c) the intensity fluctuations about the average profile are described by the shaded area, whose edges represent one standard deviation from the mean. Relative to Rayleigh speckles, the dramatically reduced intensity fluctuations in the neighborhood of the delta speckles' vortices leads to more consistent vortex profiles.

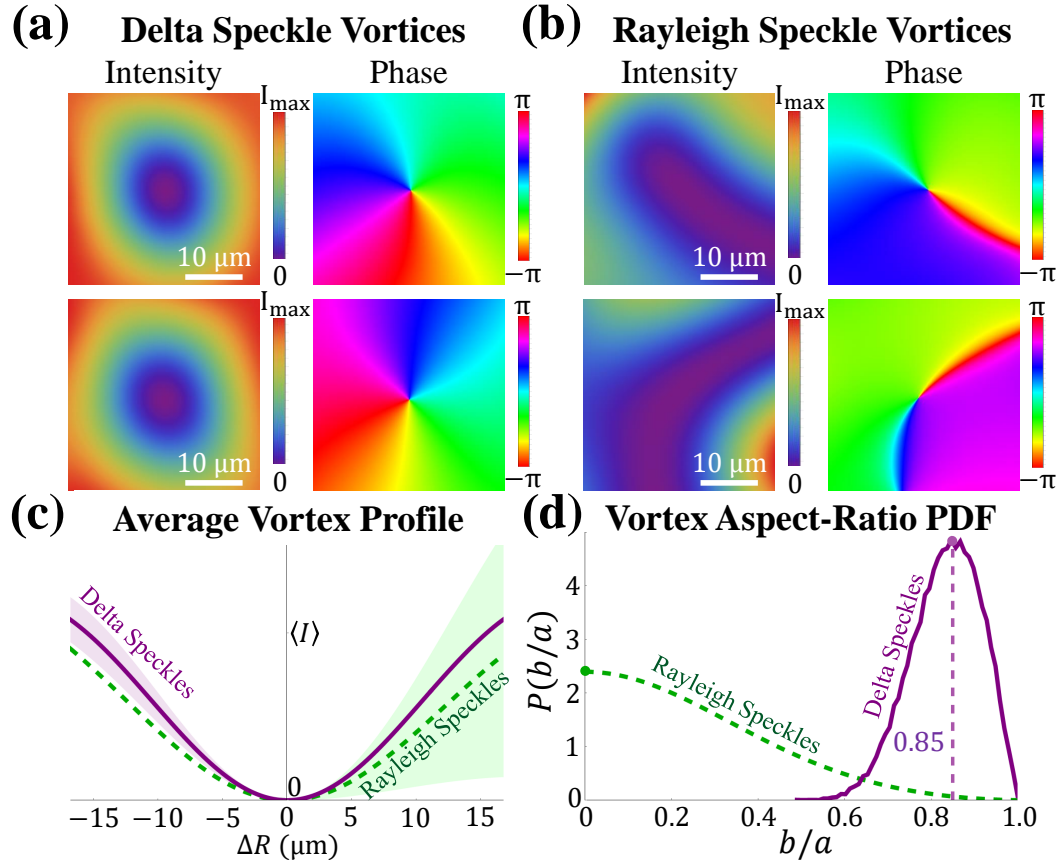


Figure 5.5: **Optical Vortex Characteristics.** Two example vortices from a delta speckle pattern, (a), and from a Rayleigh speckle pattern, (b), are shown. While the vortices in the delta speckles are nearly circular, the Rayleigh speckles' vortices have highly irregular shapes. This property is reflected in (c) where we plot the average intensity profile of light around vortices in 1,000 delta speckle patterns (purple solid line) and around vortices in 1,000 Rayleigh speckle patterns (green dashed line). The edge of the purple and green shaded regions indicates one standard deviation away from the corresponding mean profile. In (d), we plot the probability density of the equal-intensity contours' aspect-ratio around the vortices in 1,000 delta speckle patterns (purple) next to the theoretical prediction for Rayleigh speckle patterns (green).

The core structure of a vortex is characterized by the equal-intensity contour immediately surrounding the phase singularity. As with the fluorescent spots analyzed previously, this structure can be described by an ellipse whose major and minor axis lengths are  $a$  and  $b$ . The aspect ratio  $b/a$  reflects the degree of isotropy of the vortex core structure. In Fig. 5.5(d), we plot the PDF of  $b/a$ ,  $P(b/a)$ , obtained from 1,000 independent delta speckle patterns and compare it with that of Rayleigh speckles. For Rayleigh speckles,  $P(b/a)$  has a maximum at  $b/a = 0$ , indicating the most probable shape of the intensity contour around a vortex is a line [164–166]. Furthermore, the probability of a circular contour,  $b/a = 1$ , vanishes, confirming the absence of isotropic vortices in a Rayleigh speckle pattern. Contrarily,  $P(b/a)$  for the delta speckles features a narrow peak centered at  $b/a = 0.85$ , meaning all vortices are nearly circular. For comparison, the probability that a vortex will have  $b/a > 0.6$  is 99.7% in a delta speckle pattern, while the probability is only 6% in a Rayleigh speckle pattern. Due to the circular symmetry exhibited by the optical vortices [167] in delta speckles, the nearest-neighbor vortex spacing,  $\cong 45 \mu\text{m}$ , is larger than that in Rayleigh speckles,  $\cong 27 \mu\text{m}$ . Therefore, the average vortex density is lower in a delta speckle pattern, when compared to a Rayleigh speckle pattern.

## 5.7 Protein Photoconversion Simulation

In this section, we simulate the photoconversion process with a customized speckle pattern. We consider the case of a uniform sample photoconverted by an intensity pattern  $I_p(\mathbf{r})$ , starting from  $t = 0$ . The unconverted protein density  $\rho(\mathbf{r}, t)$  satisfies the rate equation:

$$\frac{d\rho(\mathbf{r}, t)}{dt} = -qI_p(\mathbf{r})\rho(\mathbf{r}, t) \quad (5.3)$$

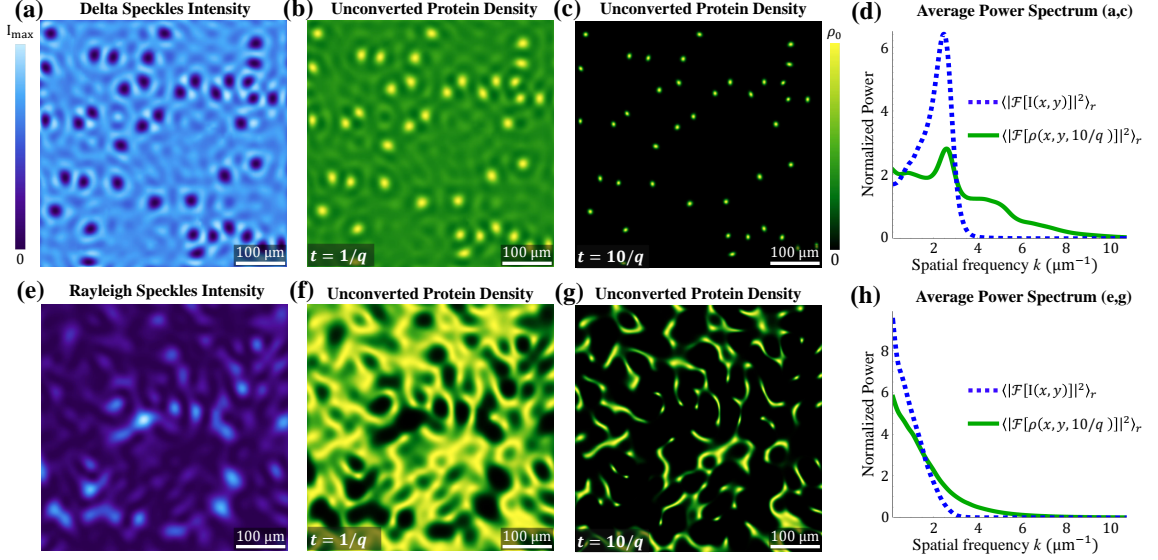


Figure 5.6: **Photoconversion simulation.** When a delta speckle pattern is used for photoconversion (a), the unconverted regions near the vortices quickly evolve into isotropic and isomeric islands as seen in (b) at  $t = 1/q$ . At long timescales the islands remain, as shown in (c) where  $t = 10/q$ , yet they have considerably smaller size and higher spatial frequencies (d). When a Rayleigh speckle pattern is used for photoconversion (e), an interconnected web forms instead of isolated islands at  $t = 1/q$  as shown in (f). Even at long time scales isolated and isotropic islands are rarely seen in (g) and fewer high-spatial frequencies are present when compared to (c), as shown in (h). The power spectra in (d,h) are ensemble-averaged over 100 realizations, and normalized to have a mean value of 1 over the spatial frequencies plotted. Note, the values at  $k = 0$  are not plotted.

where  $q$  is a coefficient describing the photoconversion strength. The solution to this equation is given by

$$\rho(\mathbf{r}, t) = \rho_0 e^{-q I_p(\mathbf{r}) t}, \quad (5.4)$$

where  $\rho_0 = \rho(\mathbf{r}, 0)$  is the initial uniform protein density.

The fluorescence intensity from the unconverted proteins  $I_e(\mathbf{r}, t)$  is proportional to  $\rho(\mathbf{r}, t)$ . Thus the negative of the photoconverting intensity  $I_p(\mathbf{r}, t)$  is nonlinearly (exponentially) imprinted onto the fluorescence image  $I_e(\mathbf{r}, t)$ . In Fig. 5.6, we plot  $\rho(\mathbf{r}, t)$  for both delta speckles (Fig. 5.6(a)) and Rayleigh speckles (Fig. 5.6(e)). With increasing photoconversion time the unconverted regions shrink. As can be seen in Fig. 5.6(b,c), for

delta speckles the unconverted regions evolve to isolated circular spots of homogeneous size. For Rayleigh speckles, the unconverted regions have irregular shapes and highly inhomogeneous sizes (Fig. 5.6(f,g)). We compute the power spectra by Fourier transforming the speckled intensity patterns in (a,e) and the unconverted protein density distributions in (c,g). The azimuthally-averaged power spectra are shown in (d,h). Because delta speckles possess non-local correlations, which shorten the spatial intensity correlation length, the speckles' intensity power spectrum contains higher spatial frequencies than those present in Rayleigh speckles: this can be seen by comparing the blue dashed lines in (d,h). As a result, the delta speckles produce higher spatial frequencies in the unconverted protein density patterns, especially at long photoconversion time scales, as shown by the green solid lines in (d,h).

Our model demonstrates that the circularity of the low-intensity region surrounding each vortex, in a delta speckle pattern, directly translates to the circularity of the corresponding fluorescent spots in the photoconverted sample. This supports our experimental findings, where the aspect ratio of the fluorescent spots has a mean value of  $\langle b/a \rangle = 0.86$ , which agrees with the mean aspect ratio of the optical vortices,  $\langle b/a \rangle = 0.85$ . Similarly, this model explains the homogeneity in size and shape of the fluorescent spots when a delta speckle pattern is used for photoconversion. When a Rayleigh speckle pattern is used for photoconversion, the vanishing likelihood of having circular vortices coupled with the irregular shape of the surrounding low intensity regions results in the scarcity of isotropic fluorescent spots.

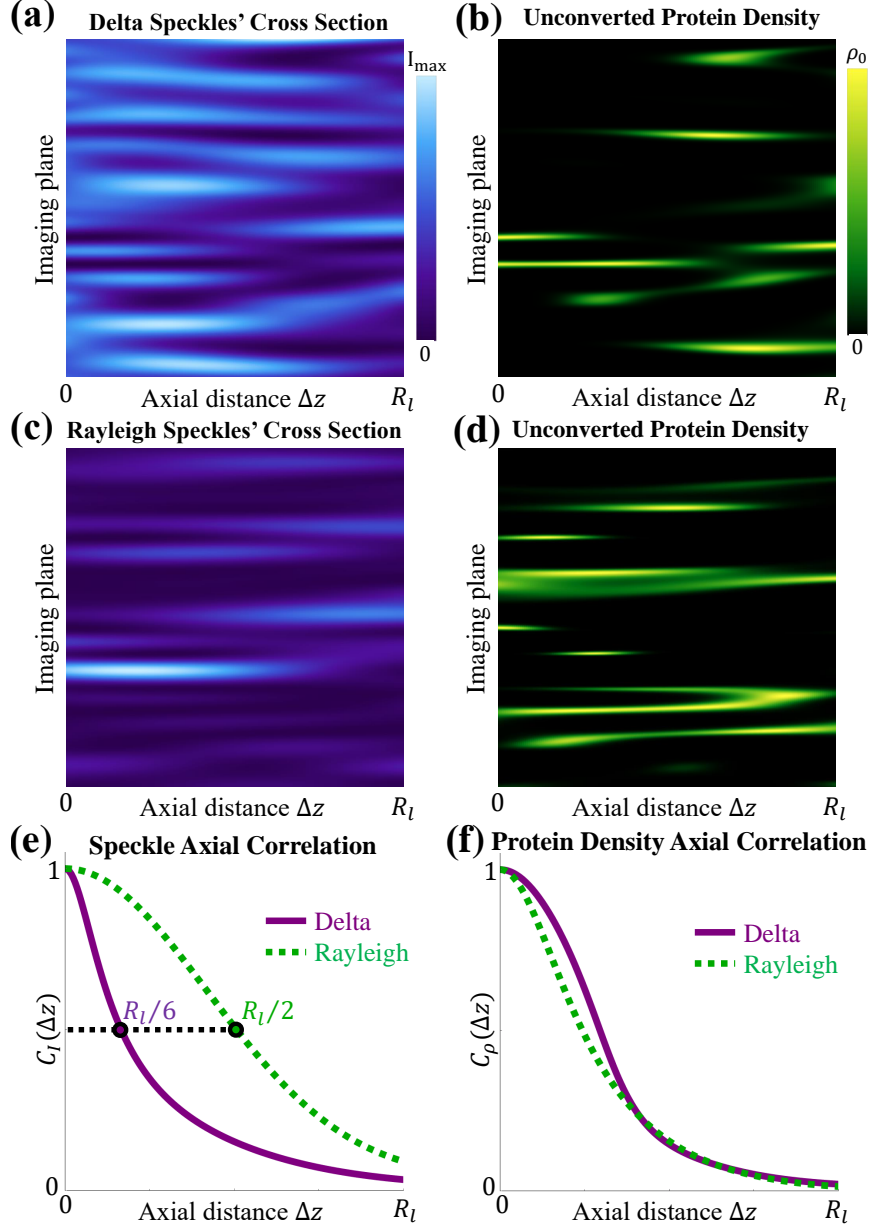


Figure 5.7: **Axial Propagation.** Axial intensity cross-sections,  $I(x = x_0, y, \Delta z)$ , of both delta (a) and Rayleigh (c) speckles are juxtaposed with a simulation of the corresponding unconverted protein density in a uniform sample,  $\rho(x = x_0, y, \Delta z, 10/q)$ , (b,d) over one Rayleigh axial-decorrelation length  $R_l$ . In (e), the axial intensity correlation function  $C_I(\Delta z)$  of the delta speckles (purple line) is three times narrower than that of the Rayleigh speckles (green dashed line). In (f), the axial correlation function of the unconverted protein density  $C_\rho(\Delta z)$  generated by delta speckles (purple line) has almost same width as that generated by Rayleigh speckles (green dashed line). We ensemble average over the propagation of 100 speckle patterns to create the curves in (e,f).

## 5.8 Optical Sectioning

The rapid axial-decorrelation of a speckled intensity pattern, which enables parallel 3D nonlinear patterned-illumination microscopy, is the result of the field's uniform phase distribution. The axial decorrelation length of a speckle pattern is defined as the FWHM of the axial intensity correlation function  $C_I(\Delta z)$ . For a Rayleigh speckle pattern, the axial decorrelation length  $R_l$  is proportional to the Rayleigh range, which is determined by the axial diffraction limit  $2\lambda/\text{NA}^2$ . With axial propagation, a delta speckle pattern evolves into Rayleigh speckles over one  $R_l$ . In Fig. 5.7(a), an example axial intensity cross-section,  $I(x = x_0, y, \Delta z)$ , of a delta speckle pattern over one  $R_l$  is juxtaposed with a numerical simulation of the corresponding unconverted protein density in a uniform sample,  $\rho(x = x_0, y, \Delta z, t = 10/q)$ . For comparison, the simulation results for a Rayleigh speckle pattern are shown in (c,d). As the illuminating speckle patterns decorrelate axially, the fluorescent spots (corresponding to optical vortices) move laterally, enabling parallel 3D nonlinear patterned-illumination microscopy.

As shown in Fig. 5.7(e), the axial intensity correlation function  $C_I(\Delta z)$  of the delta speckles has a notably narrower width than that of the Rayleigh speckles. Consequently, the axial decorrelation length of the delta speckles (FWHM of the axial intensity correlation function) is  $R_l/3$ , which is three times shorter than that of the Rayleigh speckles. This behavior can be attributed to the rapid axial evolution of a delta speckle pattern into a Rayleigh speckle pattern, a general feature of customized speckles created with our methods, as discussed in the previous chapters. However, the axial decorrelation lengths of the unconverted protein density in uniform samples,  $\rho(\mathbf{r}, t)$ , remains nearly identical for long exposure times (Fig. 5.7(f)). This is because the axial decorrelation of  $\rho(\mathbf{r}, t)$  is dictated by the lateral movement of optical vortices, when propagating axially, which is almost the same for both families of speckles. Since optical vortices in a delta speckle

pattern are farther apart than those in a Rayleigh speckle pattern, their transverse motion is slightly slower, leading to a minor broadening of  $C_\rho(\Delta z)$ . Nevertheless, the delta speckle illumination provides approximately the same optical sectioning as the Rayleigh speckle illumination.

## 5.9 Live Sample Demonstration

In our experiment, a uniform film of purified protein is photoconverted by a speckle pattern. This technique is also compatible with live yeast cells, which are nonuniformly distributed in space.

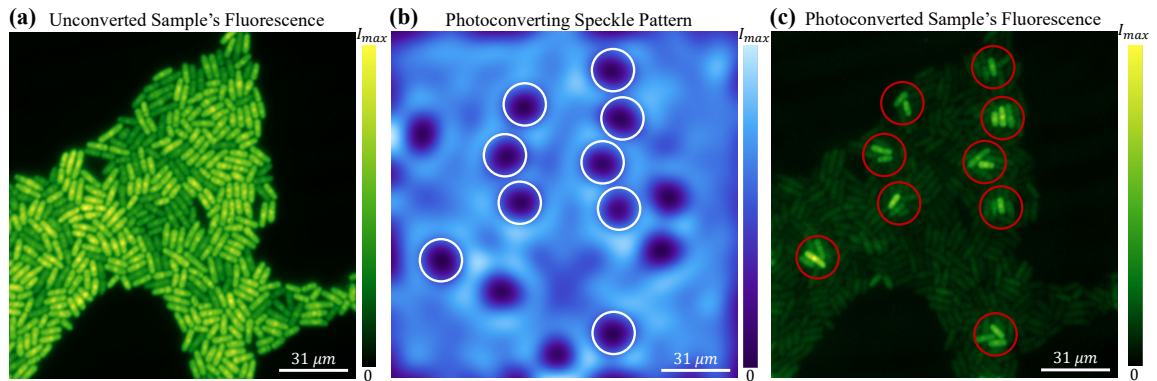


Figure 5.8: **Photoconversion of live yeast cells with a customized speckle pattern.** In (a), we present an optical image of the fluorescent light emitted from a sample of live yeast cells before they are photoconverted by the delta speckle pattern shown in (b). The white circles in (b) indicate the vortices which overlap with the yeast cells. An image of the fluorescent light emitted by the live-cell sample after photoconversion is shown in (c). The red circles in (c) correspond to the white circles in (b).

### 5.9.1 Photonconverting Live Yeast Cells With Customized Speckles

We illuminate the collection of nonuniformly distributed yeast cells shown in Fig. 5.8(a) with the photoconverting speckle pattern presented in (b). The optical vortices of the delta speckle pattern do not photoconvert the yeast cells in their direct vicinity. Consequently,

after photoconversion, multiple isolated groups of cells will emit fluorescence when illuminated by 488 nm light. In the fluorescence image taken after photoconversion, the fluorescent regions (marked by red circles in (c)) have a one-to-one correspondence to the optical vortices –in the delta speckle pattern– that overlap with the yeast cells (marked by white circles in (b)). Because the mEos3.2 protein is cytosolic, it is impossible to obtain fluorescence from a sub-cellular region, even if we shrink the dark region surrounding each vortex core using high-NA optics. Nevertheless, we are able to select individual groupings of live cells located near the vortices.

### **5.9.2 Live Yeast Cell Culture & Preparation**

The *S. Pombe* strain *Leu1::Leu1+ pAct1 mEos3.2 nmt1Term ade6-M216 his3-Δ1 leu1-32 ura4-Δ18* is generated from NruI digested plasmid pJK148-pAct1-mEos3.2-nmt1Term through homologous recombination. Cytosolic mEos3.2 is expressed from the act1 promoter in the endogenous Leu1 locus. Cells are grown in exponential phase at 25 °C in YE5S-rich liquid medium in 50 mL flasks in the dark before switching to EMM5S-synthetic medium for 12-18 hours, to reduce the cellular autofluorescence background. Live cells are concentrated 10- to 20-fold by centrifugation at 3,000 rpm for 30 s and re-suspended in EMM5S for imaging. Concentrated cells in 10 uL are mounted on a thin layer consisting of 35 μL 25 % gelatin (Sigma-Aldrich; G-2500) in EMM5S.

## **5.10 Discussion & Conclusion**

In summary, we have presented a proof-of-principle demonstration of parallel pattern illumination with a family of tailored speckle patterns. By customizing the statistical properties of speckle patterns for photoconversion, we obtain a spatial resolution that is three times higher than the diffraction limit of the illumination optics. The isometric and circu-

lar vortices in the tailored speckle patterns provide a homogeneous and isotropic spatial resolution enhancement: which cannot be obtained from standard Rayleigh speckles.

Since the photoconversion process is nonlinear, in principle, there is no limit on the spatial resolution that can be reached. In reality, because the intensity of our photoconverting laser beam is relatively low, the photoconversion process takes a long time ( $\sim 12$  hours). During this time, sample drift and protein motion limit the spatial resolution that can be achieved with fluorescence from the unconverted regions. A further increase in spatial resolution is possible using a higher-powered laser with dilute samples of immobile proteins.

In the photoconversion experiment, the illumination optics has a relatively low NA so that the fluorescence spots of size exceeding  $4 \mu\text{m}$  can be well resolved with the detection optics of  $1.1 \mu\text{m}$  resolution. To reach nanoscale resolution, high-NA optics are required to create the photoconverting speckle pattern. In this case, the vector nature of the light field must be considered. It is known that the axial field at a vortex center can be canceled by manipulating the polarization state of light [168, 169]. In a Rayleigh speckle pattern, the intensity contours around a vortex core are elliptical, and the polarization state must be an ellipse with an identical aspect ratio and an identical handedness in order to cancel the axial field [146, 155]. Since the elliptical contours vary in aspect ratio from one vortex to the next in a Rayleigh speckle pattern, it would be challenging, if not impossible, to set the polarization state of a speckle pattern to cancel the axial fields at all of its vortices. In a delta speckle pattern, in contrast, the vortices are almost circular, and half of them have the same handedness. With circularly polarized light, the axial fields will vanish at half of the vortices: specifically, those with the same handedness. To be consistent with high-NA applications, delta speckles with circular polarization are generated in our experiment.

Finally, 2D raster scanning delta speckles over a fluorescent sample enables 3D super-resolution imaging of the sample, via the same technique demonstrated with Rayleigh

speckles in [146]. Alternatively, it is possible to eliminate scanning from this process by illuminating the entire sample with multiple, distinct, delta speckle patterns which cover the field of view. While the axial resolution obtained using delta speckles for illumination is comparable to that of Rayleigh speckles, further improvements can be made. Specifically, accelerating the transverse motion of optical vortices in delta speckles can enhance their optical sectioning capabilities.

# Chapter 6

## Fluctuations And Correlations Of Transmission Eigenchannels In Diffusive Media

### 6.1 Introduction

<sup>1</sup>In recent years, extensive studies of coherent wave transport in multiple-scattering media have been conducted with light, microwaves, and acoustic waves [56, 170]. The overarching goal of this research is overcoming the limitations imposed by incoherent diffusion: thereby, enabling energy delivery deep inside a turbid medium. While multiple scattering persistently randomizes waves traveling in a linear system with static disorder, the coherent wave transport is ultimately a deterministic process. Therefore, it can be described by a field transmission matrix  $t$ , which maps the incident waves to the transmitted waves [86]. As discussed in the introduction, the eigenvectors of  $t^\dagger t$  provide the input wavefronts which excite a set of disorder-specific wavefunctions –spanning the system– known as the transmission eigenchannels. Any incoming wave can be decomposed into

---

<sup>1</sup>The chapter material is primarily taken from reference [5]: Nicholas Bender, Alexey Yamilov, Hasan Yilmaz, and Hui Cao, “Fluctuations and Correlations of Transmission Eigenchannels in Diffusive Media”, *Phys. Rev. Lett.*, vol. 125, 165901, (2020).

a linear combination of eigenchannels, each propagating independently through the system with a transmittance given by the corresponding eigenvalue  $\tau$ . One of the striking theoretical predictions of diffusive systems is the bimodal distribution of the transmission eigenvalues: with maxima at  $\tau = 0$  and  $\tau = 1$  [81–85]. The corresponding eigenchannels are referred to as closed and open channels.

Both the fluctuations of, and the correlations between transmission eigenvalues are intensely studied topics [56, 86, 171, 172]. This fundamental research area has provided explanations for prominent physical phenomena like universal conductance fluctuations and quantum shot noise [82, 85, 86, 127, 173–177]. However, the statistical properties of individual eigenchannels, such as the fluctuations of eigenchannel profiles and correlations between them, have not been studied before. In electronic systems, this is because input states cannot be easily controlled and therefore systematically exciting individual eigenchannels is unfeasible. Thanks to the recent developments of optical wavefront shaping techniques, photonic systems offer a unique opportunity for studying the second-order statistics of transmission eigenchannels.

The ability to manipulate input states in optics and acoustics has spurred a renewed interest in using transmission eigenchannels for imaging and sensing applications [56, 57, 65, 170]. Coupling waves into an open channel, not only enhances the transmitted power through a diffusive system [74–76, 79, 93, 178, 179], but also enhances the energy density inside the system [71, 73, 77, 78, 180–184]. The latter has a tremendous impact on enhancing light-matter interactions and manipulating nonlinear processes in turbid media [62, 185]. So far, however, the potential energy density enhancement is only known after ensemble averaging over many disorder realizations. Thus, it is still an open question if coupling energy into an open channel guarantees a significant enhancement of the energy density inside a single diffusive sample as well as an intensity depth profile with a specific shape.

In this chapter, we experimentally and numerically investigate both the fluctuations and correlations of transmission eigenchannel depth profiles in optical diffusive systems. We develop novel experimental techniques for measuring the transmission matrix of an on-chip diffusive waveguide, exciting its individual transmission eigenchannels, and performing an interferometric measurement of the light field everywhere inside the waveguide. We find that high-transmission eigenchannels exhibit small realization-to-realization fluctuations in their depth profiles; demonstrating a robustness when compared to either low-transmission eigenchannels or random inputs. Furthermore, different eigenchannels are correlated in their depth profile fluctuations from realization-to-realization. The correlations are weaker for higher-transmission eigenchannels, indicating they are more independent than lower-transmission eigenchannels.

## 6.2 Experimental Setup

To directly observe the depth profiles of transmission eigenchannels *within* a diffusive system, we fabricate two-dimensional (2D) waveguide structures on a silicon-on-insulator wafer with electron beam lithography and plasma etching. As shown in Fig. 6.1(a), 100 nm-diameter holes are randomly etched into the waveguides, which have photonic crystal sidewalls to reflect light [186]. At the wavelength of our probe light,  $\lambda = 1.55 \mu\text{m}$ , the transport mean free path,  $\ell_t = 3.2 \mu\text{m}$ , is much shorter than the disordered region length,  $L = 50 \mu\text{m}$ , in each waveguide. Therefore, the light undergoes multiple scattering and diffusive transport through each waveguide. Light scatters out-of-plane from the random holes, providing a direct probe of the light inside the disordered region. This process can be modeled as an effective loss, and accounted for in the diffusive dissipation length:  $\xi_a = 28 \mu\text{m}$ . The waveguides are each  $15 \mu\text{m}$  wide, supporting  $N = 55$  propagating modes at  $\lambda = 1.55 \mu\text{m}$ . Before entering one of the diffusive waveguides, light is injected via

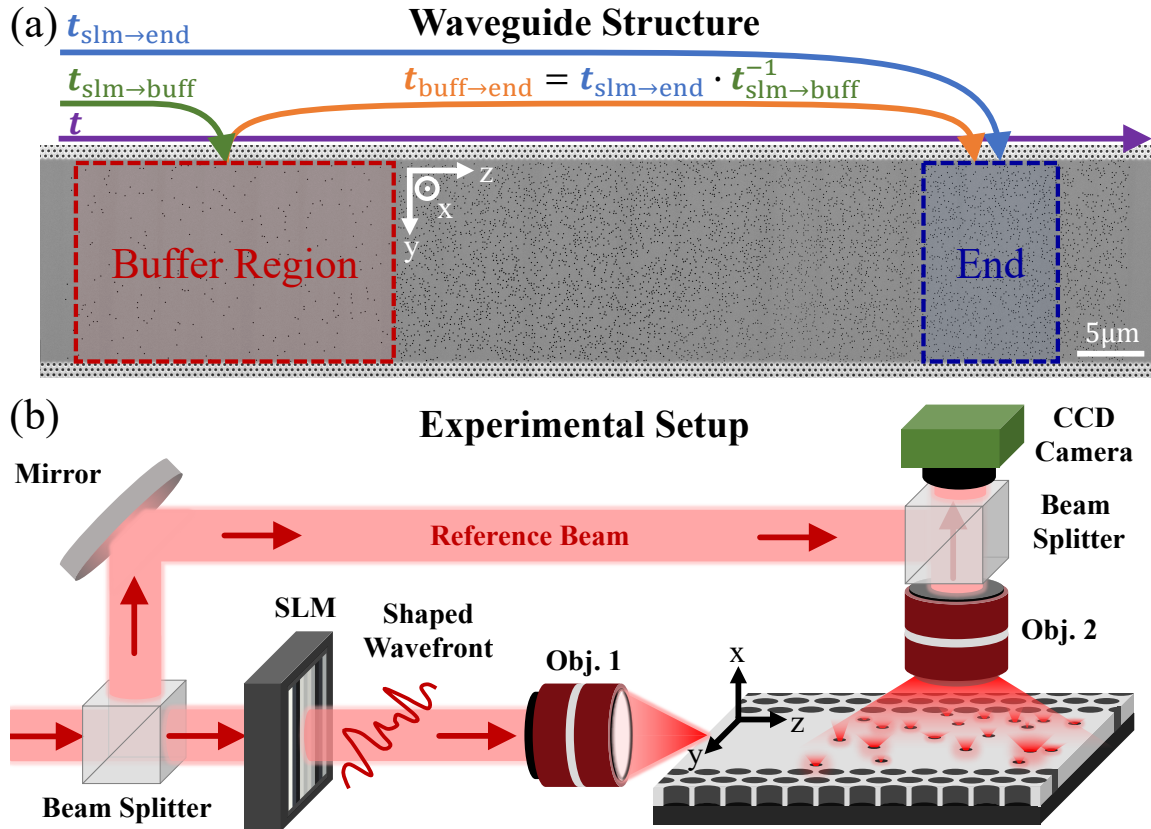


Figure 6.1: **Waveguide structure and optical setup.** A composite SEM image of a diffractive waveguide is shown in (a). The matrix mapping the field in the buffer region to the end region,  $t_{\text{buff} \rightarrow \text{end}}$ , is related to the matrices  $t_{\text{slm} \rightarrow \text{buff}}$  and  $t_{\text{slm} \rightarrow \text{end}}$ . In (b) the simplified sketch of the experimental setup illustrates how we wavefront shape a laser beam with a spatial light modulator (SLM) while performing an interferometric measurement of the light scattered out of the waveguide.

the edge of the wafer into a ridge waveguide. Due to the large refractive index mismatch between silicon and air, only low-order waveguide modes are excited at the interface. Before the disordered region, the waveguide width is tapered from 300  $\mu\text{m}$  to 15  $\mu\text{m}$  in order to convert the lower-order modes to higher-order ones. The taper enables us to access all waveguide modes incident on the disordered region [183]. For more details on the sample fabrication and design, consult Appendix B.

To measure the light field inside individual diffusive waveguides, we use an interferometric setup, as sketched in Fig. 6.1(b). In our setup, the monochromatic light from a wavelength-tunable laser source is split into two beams. One beam is modulated by a spatial light modulator (SLM) and then injected into one of the waveguides via the edge of the wafer. The other beam is used as a reference beam. It is spatially overlapped with the out-of-plane scattered light from the diffusive waveguide, on the CCD camera chip. The CCD camera records the resulting interference pattern, from which the complex field profile across the diffusive waveguide is obtained. For more details on the experimental setup, consult Appendix B.

### 6.3 Determination Of Sample Transport Parameters

Diffusive wave propagation in a scattering medium with loss is determined by two parameters: the transport mean free path  $\ell_t$  and the diffusive dissipation length  $\xi_a$ . In a 2D system, the latter can be expressed as  $\xi_a = \sqrt{\ell_t \ell_a / 2}$ , where  $\ell_a$  is the ballistic dissipation length.

To determine  $\xi_a$  and  $\ell_t$  in the diffusive region of the 2D waveguide, we first measure the cross-section-averaged intensity  $I(z)$  as a function of depth  $z$  for multiple random input wavefronts. We then ensemble average the data,  $\langle I(z) \rangle$ , and fit the theoretically-predicted depth profile –based on the diffusive equation– to it. The theoretical  $\langle I(z) \rangle$  is found by

convolving the incident ballistic intensity  $I_0 \exp[-z/\ell_s]$  ( $\ell_s$  represents the scattering mean free path, and  $\ell_s \approx \ell_t$  in our case), which acts as the source, and the Green's function of the diffusion equation [187]:

$$G(z, z') = \begin{cases} P(z)P(L - z'), & z < z' \\ P(z')P(L - z), & z > z' \end{cases} \quad (6.1)$$

where  $P(z) = \sinh(z/\xi_a) + z_0/\xi_a \cosh(z/\xi_a)$ , and  $z_0 = (\pi/4) \times \ell_t$  is the so-called extrapolation length.

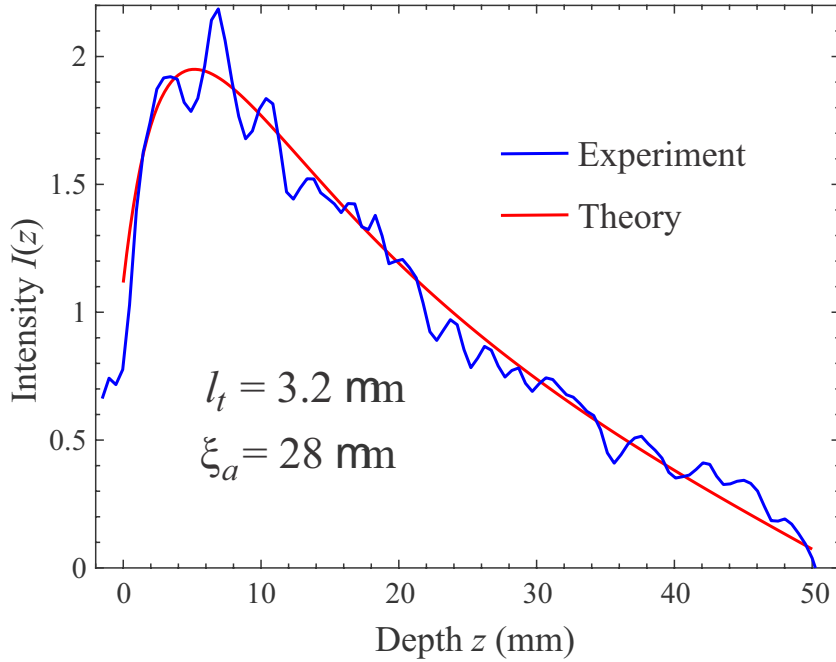


Figure 6.2: **Determining the sample transport parameters.** Determining the transport mean free path  $\ell_t$  and the diffusive dissipation length  $\xi_a$  of the diffusive waveguides by fitting the experimentally-measured average depth profile for random incident wavefronts,  $\langle I(z) \rangle$ , (blue) to theoretical predictions from the diffusion equation (red).

We compute the difference between the experimental and theoretical  $\langle I(z) \rangle$  for different values of  $\xi_a$  and  $\ell_t$ , and identify the minimum difference at  $\xi_a = 28 \mu\text{m}$  and  $\ell_t = 3.2 \mu\text{m}$ . Fig. 6.2 shows an excellent agreement between the measured  $\langle I(z) \rangle$  and the theoret-

cal prediction.

In the buffer region, the air hole density is 10 times lower than in the diffusive region. Thus, the transport mean free path is 10 times longer,  $\ell_t^{\text{buff}} = 32 \mu\text{m}$ . The loss, caused by out-of-plane scattering from the air holes, is also 10 times weaker, thus the ballistic dissipation length  $\ell_a$  is 10 times longer. This leads to a tenfold increase in the diffusive dissipation length:  $\xi_a^{\text{buff}} = 280 \mu\text{m}$ .

## 6.4 Measurement Procedure

By sequentially applying an orthogonal set of phase patterns to the 128 SLM macropixels, and measuring the field within the sample, we acquire a field reconstruction matrix that maps the field from the SLM to the field anywhere inside the disordered waveguide  $t_{\text{slm} \rightarrow \text{int}}$ . This matrix encompasses information about the light transport inside the waveguide and the light propagation from the SLM to the waveguide. To separate these, we need access to the field incident on the disordered region of the waveguide. We obtain this information by adding an auxiliary weakly-scattering region in front of the diffusive region called the “buffer” region, as shown in Fig. 6.1(a). From the light scattered out-of-plane from the buffer, we recover the field right in front of the strongly-scattering region. The length of the buffer region is  $25 \mu\text{m}$ , which is shorter than its  $32 \mu\text{m}$ -length transport mean free path. Therefore, light only experiences single scattering in the buffer, and as a result, the diffusive wave transport in the original disordered region is not appreciably altered.

With access to the field inside the buffer, we can construct the matrix relating the field on the SLM to the buffer,  $t_{\text{slm} \rightarrow \text{buff}}$ . From  $t_{\text{slm} \rightarrow \text{int}}$ , we can also construct the matrix,  $t_{\text{slm} \rightarrow \text{end}}$ , which maps the field from the SLM to a region near the end of the diffusive waveguide. With these we calculate the matrix which maps the field from the buffer to the end,  $t_{\text{buff} \rightarrow \text{end}} = t_{\text{slm} \rightarrow \text{end}} t_{\text{slm} \rightarrow \text{buff}}^{-1}$ , using Moore-Penrose matrix inversion. Although

$t_{\text{buff} \rightarrow \text{end}}$  is not the field transmission matrix  $t$ , the depth profiles of its eigenchannels match those of transmission eigenchannels in our numerical simulation (see Fig. 6.3 and discussion below). Therefore,  $t_{\text{buff} \rightarrow \text{end}}$  can be used as an experimental proxy for the field transmission matrix,  $t$ , of the diffusive waveguide.

To excite a single eigenchannel, we first perform a singular value decomposition on  $t_{\text{buff} \rightarrow \text{end}}$  to obtain the field distribution in the buffer corresponding to one eigenchannel. Then we multiply the field profile in the buffer with  $t_{\text{slm} \rightarrow \text{buff}}^{-1}$  to calculate the SLM phase-modulation pattern. By displaying this pattern on the SLM, we excite a single eigenchannel of the diffusive waveguide. We record the spatial intensity profile of each eigenchannel within the diffusive waveguide. From this measurement, we obtain the eigenchannel depth profile  $\tilde{I}(z)$  associated with each measurement by summing the intensity over the waveguide cross-section. For each depth profile, the measured intensity profile  $\tilde{I}(z)$  is normalized to

$$I(z) = \tilde{I}(z) / [(1/L) \int_0^L \tilde{I}(z') dz']. \quad (6.2)$$

## 6.5 Transmission Eigenchannel Depth-Profiles

In Figures 6.3(a & b), the experimentally-measured depth profiles of a high-transmission and a low-transmission eigenchannel are juxtaposed. The high-transmission eigenchannel in (a) has an arch-shaped energy-density distribution which spans the depth of the diffusive region. In (b), the energy-density distribution of the low-transmission eigenchannel rapidly decays with depth. We numerically calculate the transmission eigenchannels with the Kwant simulation package [188]. The experimentally measured profiles match the corresponding depth profiles generated from numerical simulations of both  $t$  and  $t_{\text{buff} \rightarrow \text{end}}$ ; confirming that we excite individual eigenchannels in our measurements. Furthermore, the agreement between the eigenchannels of  $t_{\text{buff} \rightarrow \text{end}}$  and  $t$ , confirms that the depth pro-

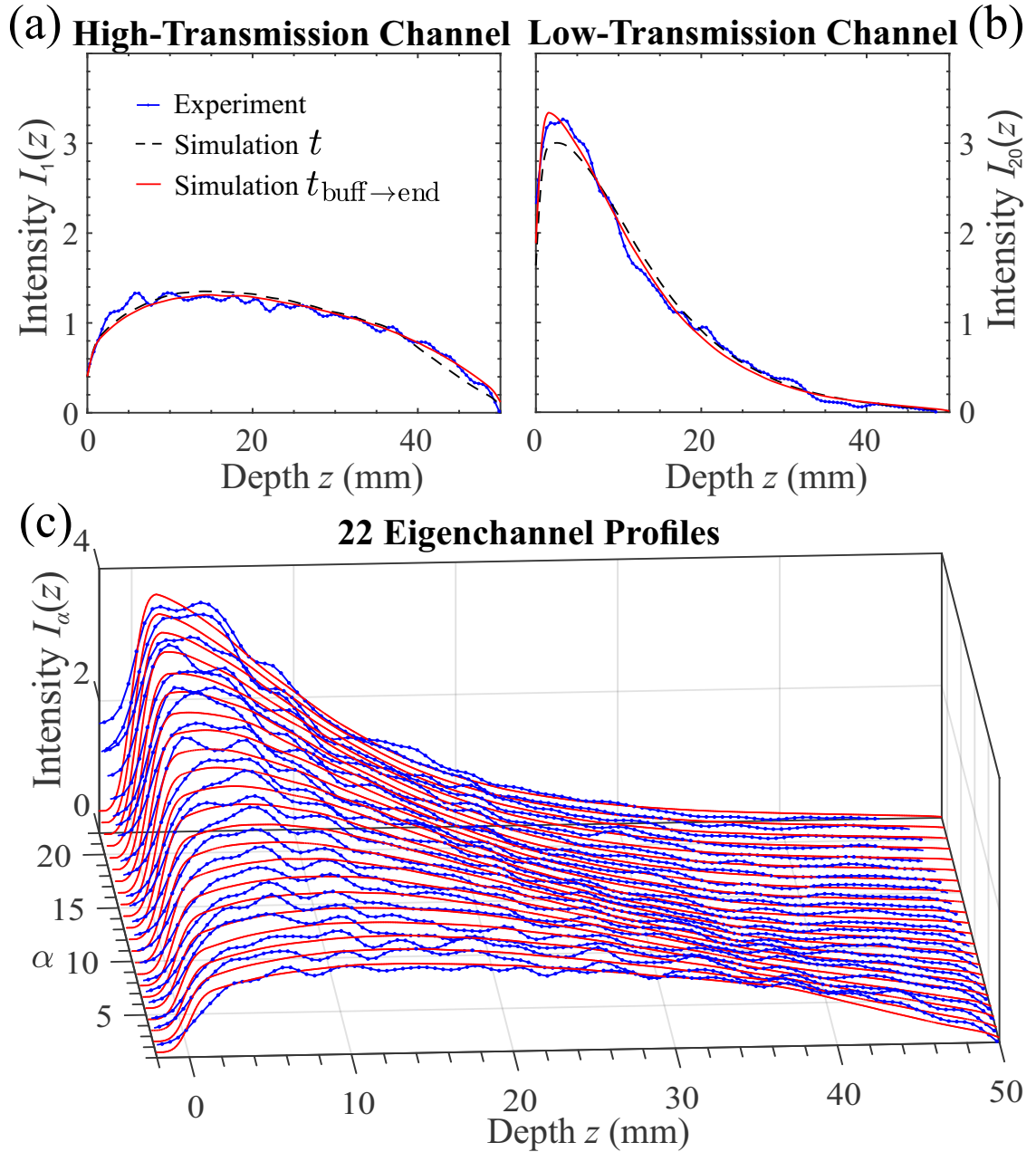


Figure 6.3: **Depth profiles of transmission eigenchannels.** High ( $\alpha = 1$ ) and low ( $\alpha = 20$ ) transmission eigenchannel profiles are presented in (a,b) while the 22 measured eigenchannel profiles are juxtaposed in (c). The experimentally measured profiles (blue lines) agree well with the profiles calculated from numerical simulations using the transmission matrix  $t$  (black dashed lines) and the matrix  $t_{\text{buff} \rightarrow \text{end}}$  (red lines).

files of  $t_{\text{buff} \rightarrow \text{end}}$  have a one-to-one correspondence with the eigenchannels of  $t$ . For more details on the numerical analysis, consult Appendix B.

In total, we measure 50 eigenchannel profiles for a single experimental system realization. Each profile matches one of the ensemble-averaged profiles of  $t_{\text{buff} \rightarrow \text{end}}$  generated numerically without any fitting parameters. Measurement noise causes multiple experimental profiles to be mapped to a single numerical profile, and this limits the total number of recovered eigenchannels to 22. Fig. 6.3(c) shows the depth profiles for all 22 eigenchannels, which agree well with the numerical simulations. The transmittance of the measured eigenchannels varies from  $\tau_1 \simeq 0.43$  to  $\tau_{22} \simeq 7.9 \times 10^{-4}$ , with a mean value of  $\langle \tau_\alpha \rangle = 0.041$ .

## 6.6 Transmission Eigenchannel Fluctuations

Next, we study the realization-to-realization fluctuations of eigenchannel profiles. From measurements of 13 system realizations, we compute the mean depth profile of each eigenchannel,  $\langle I_\alpha(z) \rangle$ , and the realization-specific deviation,  $\delta I_\alpha(z) = I_\alpha(z) - \langle I_\alpha(z) \rangle$ . From this, the total fluctuation of each eigenchannel profile is quantified by

$$\tilde{C}_\alpha = (1/L) \int_0^L \langle [\delta I_\alpha(z)]^2 \rangle dz, \quad (6.3)$$

where  $\langle \dots \rangle$  represents ensemble averaging. Fig. 6.4(a) shows that the total fluctuation of each eigenchannel profile increases monotonically as a function of eigenchannel index. The uncertainty of  $\tilde{C}_\alpha$ —due to the finite number of ensembles in our experiment—is estimated from simulations to be  $\pm 25\%$  the value of  $\tilde{C}_\alpha$ , which is smaller than the overall change of  $\tilde{C}_\alpha$  with  $\alpha$ . Hence, the depth profiles of high-transmission eigenchannels fluctuate less than the profiles generated by random illumination patterns (indicated by the green

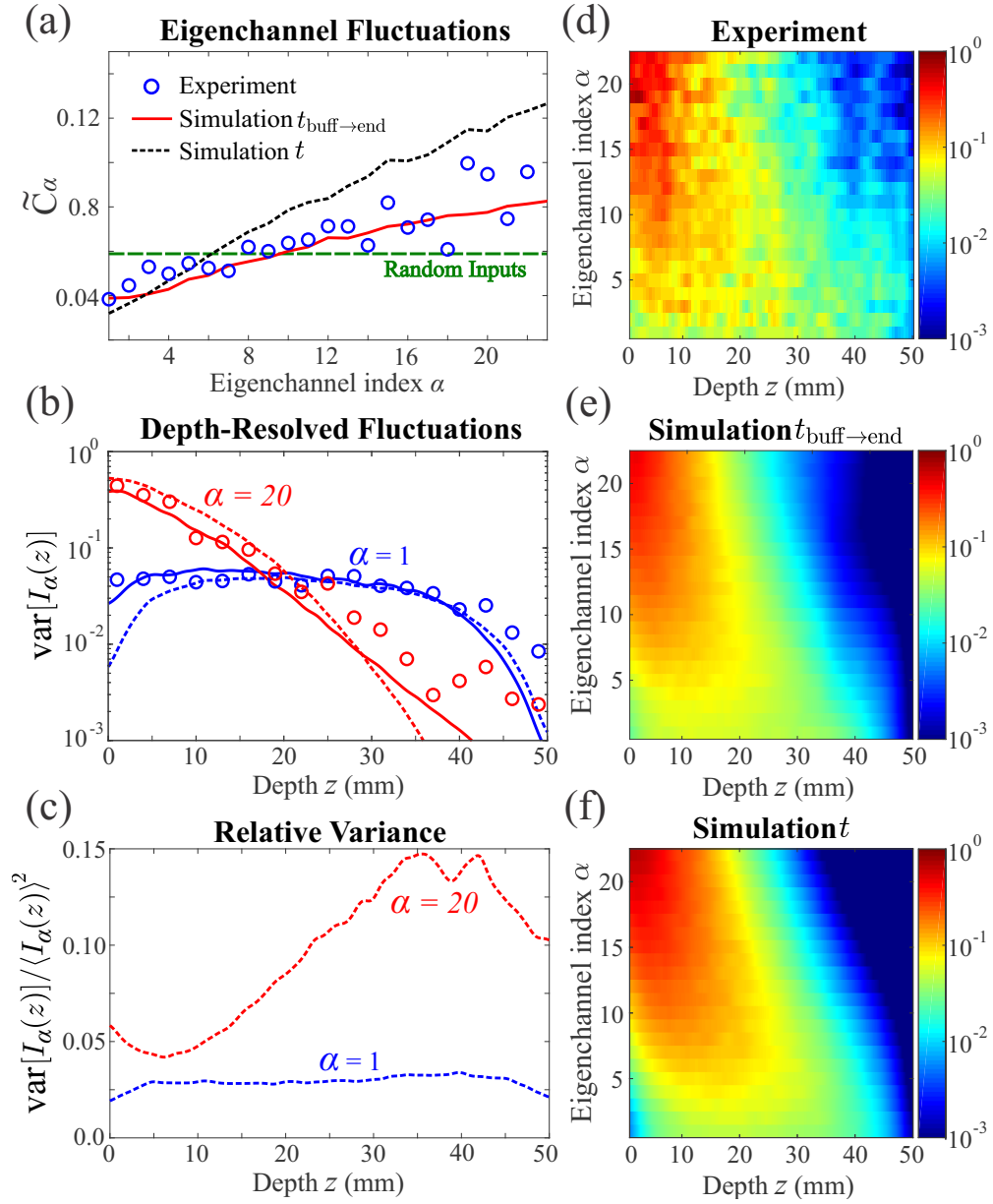


Figure 6.4: **Eigenchannel fluctuations.** In (a), the spatially-averaged depth-profile fluctuations of the eigenchannels,  $\tilde{C}_\alpha$ , increase monotonically with the channel index  $\alpha$ . The green dashed line indicates the experimentally observed fluctuations for random incident wavefronts: 0.59. In (b), experimentally observed depth-resolved intensity fluctuations,  $\text{var}[I_\alpha(z)]$ , of high ( $\alpha = 1$ ) and low ( $\alpha = 20$ ) transmission eigenchannels (circles) are closely reproduced by the numerical simulations of transmission eigenchannels from  $t_{\text{buff} \rightarrow \text{end}}$  (solid lines) and  $t$  (dashed lines). In (c),  $\text{var}[I_\alpha(z)]$  is divided by  $\langle I_\alpha(z) \rangle^2$  for the high/low-transmission eigenchannels of  $t$ . In (d-e), the experimentally-observed and numerically-calculated depth-resolved intensity fluctuations for individual eigenchannels show how  $\text{var}[I_\alpha(z)]$  evolves with  $\alpha$ .

dashed line); while lower-transmission eigenchannels fluctuate more.

Now we look into the position-dependent fluctuation of individual eigenchannel profiles about their ensemble average,  $\text{var}[I_\alpha(z)] = \langle [\delta I_\alpha(z)]^2 \rangle$  as a function of depth,  $z$ . Fig. 6.4(b) reveals distinct differences in the depth dependence of high and low-transmission eigenchannels. While  $\text{var}[I_\alpha(z)]$  is nearly flat for the high-transmission eigenchannel, it features a fast drop with  $z$  for the low-transmission eigenchannel. Figs. 6.4(d-f) are 2D plots of  $\text{var}[I_\alpha(z)]$  for all 22 eigenchannels calculated using: experimental data, as well as simulations of  $t_{\text{buff} \rightarrow \text{end}}$ , and  $t$ . As the transmittance decreases, the maximum of  $\text{var}[I_\alpha(z)]$  moves towards the front surface of the diffusive region. The decrease in the variance with depth results from the decay of the mean intensity with depth:  $\langle I_\alpha(z) \rangle$ . However, the relative intensity fluctuation of the low-transmission eigenchannels, characterized by  $\text{var}[I_\alpha(z)]/\langle I_\alpha(z) \rangle^2$ , actually increase with depth as shown in Fig. 6.4(c) for  $\alpha = 20$ . In contrast, the relative intensity fluctuation of high-transmission eigenchannels is uniform with depth and small: for example,  $\text{var}[I_1(z)]/\langle I_1(z) \rangle^2 < 0.04$  for all  $z$ . Moreover, the fluctuation of a transmission eigenchannel's intensity at the sample output reflects the fluctuation of the corresponding transmission eigenvalue. Therefore, the stronger fluctuation of a low-transmission eigenchannel, relative to a high-transmission eigenchannel, at the output end  $z = L$  indicates the fluctuation of its eigenvalue is similarly higher. This result, which we confirmed in our numerical simulations, is consistent with the theoretical prediction in Ref. [171].

The experimentally observed fluctuations of individual transmission eigenchannels are quantitatively reproduced by the numerical simulations of  $t_{\text{buff} \rightarrow \text{end}}$  and  $t$  in Figs. 6.4(a,b,d-f). The excellent agreement between experimental and numerical results confirms that eigenchannel fluctuations depend on their transmittance. The higher the transmittance, the lower the fluctuations. This means that high-transmission eigenchannels have a robust and consistent depth profile, irrespective of the disorder configuration of a system.

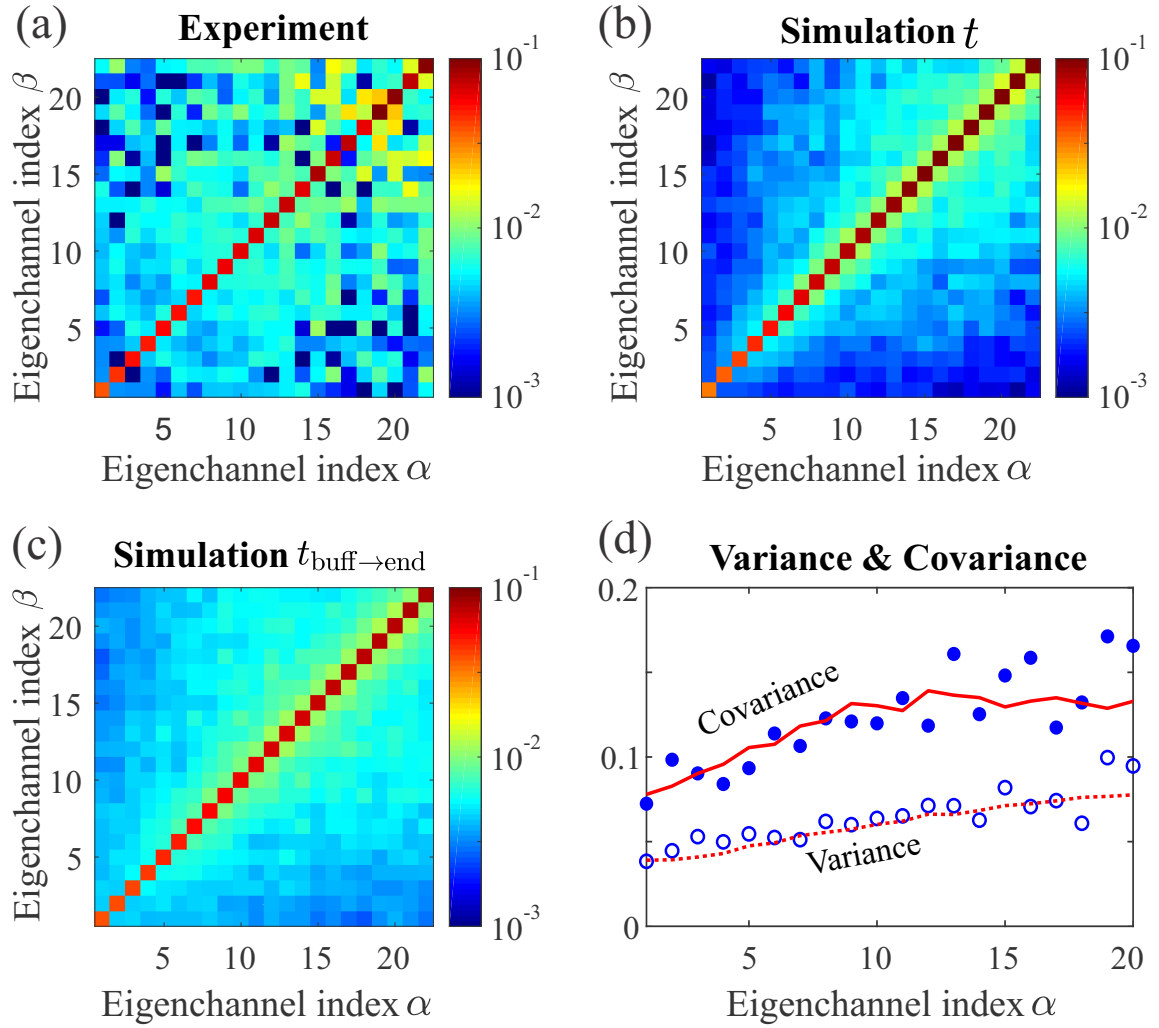


Figure 6.5: **Inter-channel correlations.** The covariance  $\tilde{C}_{\alpha\beta}$  between any two pairs of eigenchannels,  $\alpha$  and  $\beta$ , is calculated from experimental data (a) and numerical simulations (b,c). The cumulative covariance  $\sum_{\beta \neq \alpha} \tilde{C}_{\alpha\beta}$  exceeds the variance  $\tilde{C}_{\alpha\alpha}$  in (d). The blue symbols represent experimental data and red lines represent numerical simulations based on  $t_{\text{buff} \rightarrow \text{end}}$ .

## 6.7 Transmission Eigenchannel Correlations

Finally, we investigate the cross-correlations between different transmission eigenchannels. For any given disorder realization, eigenchannels are an orthogonal set of functions at the front and back surfaces of the medium. While eigenchannels differ from realization-to-realization, their orthogonality implies that the differences in their field profiles must be correlated from realization-to-realization. This does not mean, however, that the *intensity* fluctuations of their profiles *inside* the sample should be correlated. To study cross-correlations in the eigenchannels' intensity fluctuations across the sample, we introduce the covariance  $\tilde{C}_{\alpha\beta} = \langle \delta I_\alpha(z) \delta I_\beta(z) \rangle_z$ , where  $\langle \dots \rangle_z$  describes both ensemble averaging and depth averaging. For  $\alpha = \beta$ ,  $\tilde{C}_{\alpha\alpha}$  reduces to the variance  $\tilde{C}_\alpha$  which describes the eigenchannel fluctuations.

Fig. 6.5(a-c) shows the experimental and numerical results of  $\tilde{C}_{\alpha\beta}$  for all  $\alpha$  and  $\beta$ . The non-vanishing off-diagonal elements of  $\tilde{C}_{\alpha\beta}$  ( $\alpha \neq \beta$ ) reveal coordinated changes in the eigenchannels' depth profiles. Between different pairings of eigenchannels, the correlations differ. The larger the difference in the transmittances of a pair, the weaker the correlation of their depth profile fluctuations. Furthermore, lower-transmission eigenchannels tend to correlate more with other low-transmission eigenchannels than higher-transmission eigenchannels do with other high-transmission eigenchannels. Quantitatively we can describe the correlation of a single eigenchannel to all others by the cumulative covariance  $\sum_{\beta \neq \alpha} \tilde{C}_{\alpha\beta}$ . As shown in Fig. 6.5(d), the cumulative covariance increases with  $\alpha$ , indicating higher-transmission eigenchannels are more independent from other eigenchannels than lower-transmission eigenchannels are. Moreover, the cumulative covariance exceeds the variance  $\tilde{C}_{\alpha\alpha} = \tilde{C}_\alpha$  by a factor of 2. Hence, the total cross-correlation for a single eigenchannel is stronger than its own fluctuation.

## 6.8 Discussion & Conclusion

To provide a plausible explanation for the observed phenomena, we resort to the modal description of transmission eigenchannels [189]. A transmission eigenchannel can be decomposed by the quasi-normal modes of the disordered system. Previous research [189] has revealed that high-transmission eigenchannels are composed of only a few on-resonance modes, while low-transmission eigenchannels are composed of many off-resonance modes that destructively interfere. Since the destructive interference is sensitive to changes in the scattering configuration, the low-transmission eigenchannels exhibit strong fluctuations. Moreover, because individual low-transmission eigenchannels share many of the same off-resonant modes, their fluctuations are correlated. Since high-transmission eigenchannels are composed of a different set of modes than low-transmission eigenchannels, the correlations between high and low-transmission eigenchannels are weak.

Our findings regarding the second-order statistical properties of transmission eigenchannels are general and applicable to other types of waves such as microwaves, acoustic waves, and matter waves. In practical applications, the consistent and robust depth profiles of open channels guarantee that they can deliver energy through *any* diffusive system regardless of the disorder configuration. Such *reliable* energy delivery has major implications in applications ranging from multi-photon imaging to photothermal therapy, and shock wave treatment. Since our on-chip experimental platform allows for both direct measurement of the complex field inside a random structure and near-complete control over the incident field, we can investigate how to shape an incident wavefront to control the spatial distribution of light across the entire disordered sample. Furthermore, this setup can be used to experimentally study the spatial structure and statistics of the time-delay eigenchannels of a diffusive medium, and the time-gated transmission and reflection eigenchannels of a diffusive system.

# Chapter 7

## Depth-Targeted Energy Deposition Deep Inside Scattering Media

### 7.1 Introduction

<sup>1</sup>Depositing energy into a target region *deep inside* an opaque diffusive system –by controlling random wave scattering– is essential in a wide range of applications involving light, microwaves, and acoustic waves [55,56]: such as deep-tissue imaging [57,58], optogenetically controlling neurons [59,60], non-invasive ultrasound surgery [61], and optimization of photoelectrochemical processes in strongly-scattering systems [62]. As discussed in Chapter 6, controlling the incident wavefront of a coherent beam enables the suppression of wave diffusion; which, has been used to *focus* light either inside or through a scattering medium [64,65,87–91]. The appropriate incident wavefront can be obtained via the time-reversal principle [92]; the phase conjugate of an output field generated by a point source will focus back to that point [64]. Targets in many applications like neurons or early-stage tumors, however, are much larger than an optical-diffraction-limited focal spot and therefore wavelength-scaled light focusing does not corresponds to maximal energy deposition

---

<sup>1</sup>The chapter material is primarily taken from reference [6]: Nicholas Bender, Alexey Yamilov, Arthur Goetschy, Hasan Yilmaz, Chia Wei Hsu, and Hui Cao, “Depth-Targeted Energy Deposition Deep Inside Scattering Media”, *Arxiv*, 2105.13417, (2021).

into an extended target. Since the optimal spatial field distribution across the target is not known *a priori*, neither time reversal nor phase conjugation can be used to find the optimal incident wavefront. Furthermore, while feedback-based iterative optimization of the input wavefront [65] is efficient at reaching the global maximum when focusing light [93]; currently, this is not the case for energy delivery into a target of arbitrary size and shape.

Over the years, various operators and matrices related to physical quantities of interest in disordered systems have been introduced –and their eigenstates studied– in the search for the global optima of the quantities. Examples include the field transmission matrix [5, 71–80] discussed in Chapter 6, the energy density matrix [190], the photoacoustic transmission matrix [191], the generalized Wigner-Smith operator [192, 193], the time-gated reflection matrix [194, 195], the acousto-optic transmission matrix [196], the dwell-time operator [197], the distortion matrix [198, 199], and the Fisher information operator [200]. None of them, however, provide the solution for maximal energy deposition in an arbitrary-sized region at an arbitrary depth in a scattering medium. Furthermore, a general framework for predicting and understanding the ultimate limit on targeted energy delivery into a diffusive system is missing. As such, the following scientifically and technologically important questions remain unanswered, “How can one systematically find the incident wavefront that optimally deposits energy into a target region of arbitrary size and shape, deep inside a diffusive medium?” and “What is the ultimate limit on the energy enhancement in a region?”

In this chapter, we address these questions by performing a comprehensive experimental, numerical and theoretical study. First, we define the deposition matrix  $\mathcal{Z}$  which relates input waves to the corresponding regional field distributions at an arbitrary depth within a diffusive system. The largest eigenvalue of  $\mathcal{Z}^\dagger \mathcal{Z}$  gives the maximal energy that can be deposited into the designated region, and the associated eigenvector provides the input wavefront. Next, we build a theoretical model which can analytically predict the

probability density function of the eigenvalues of  $\mathcal{Z}^\dagger \mathcal{Z}$ , and demonstrate how energy enhancement depends on the depth of the region and the system parameters such as the transport mean free path  $\ell_t$  and the sample thickness  $L$ . While the largest possible energy enhancement scales as  $L/\ell_t$ , it always occurs at depth  $(3/4)L$  in a lossless diffusive medium: independent of the scattering strength. Using the on-chip disordered-waveguide platform presented Chapter 6, we experimentally measure the deposition matrix  $\mathcal{Z}$  for regions at different depths inside a diffusive system, and directly excite individual eigenstates to observe their spatial structures across the entire system. Furthermore, we explore the relationship between deposition eigenchannels and transmission eigenchannels; revealing that the regional energy enhancement results from *both* selective excitation of high-transmission eigenchannels *and* constructive interference between them.

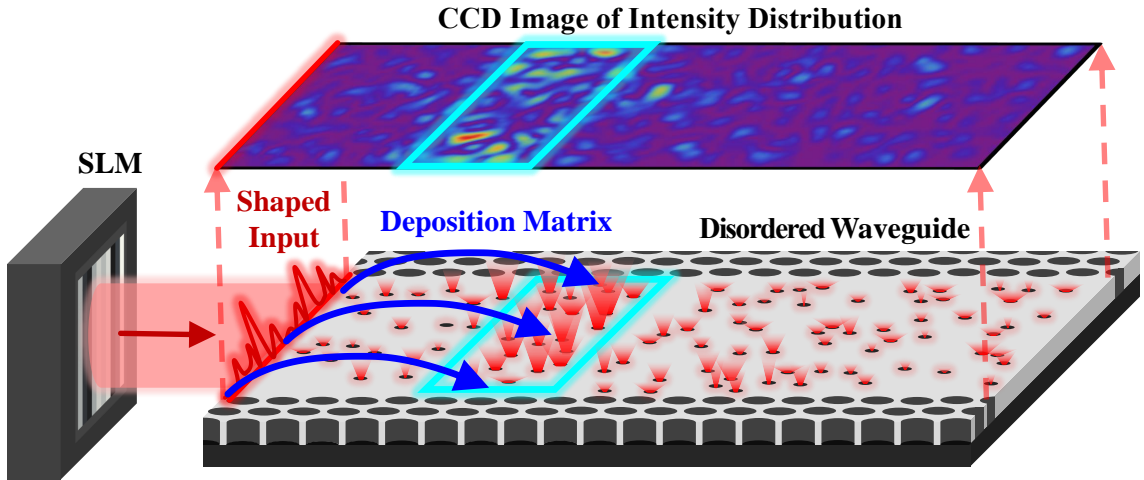


Figure 7.1: **Schematic of the experimental platform for investigating energy deposition in a diffusive system.** A spatial light modulator (SLM) shapes the incident wavefront of a monochromatic laser beam, and the field distribution inside a two-dimensional disordered waveguide is probed from above. This setup allows measurement of the deposition matrix that relates the incoming field pattern to the spatial field distribution inside a target region (marked by the cyan box). Selective coupling of light into the deposition eigenchannels can enhance or suppress energy inside the target region, as confirmed by the CCD camera image of the spatial intensity distribution.

## 7.2 Deposition Matrix

As illustrated in Fig. 7.1, controlling energy deposition inside a disordered system requires introducing the deposition matrix  $\mathcal{Z}$  of a target region that can have an arbitrary size, shape, and depth. The matrix relates an orthonormal set of input wavefronts to the corresponding spatial field distributions within the target region. The eigenvalues  $\zeta$  of  $\mathcal{Z}^\dagger \mathcal{Z}$  give the total energy inside the target region when sending the corresponding eigenvectors into the system, with proper normalization. Therefore, the eigenvector with the highest eigenvalue provides the input wavefront which deposits the most energy into the target region.

As an example case, we consider a target region that is a thin slice inside the disordered waveguide, at depth  $z_D$  [see inset of Fig. 7.2(a)]. The width  $W$  of the slice is equal to that of the waveguide, and the slice thickness  $\Delta z$  is small enough that the field variation along  $z$  (waveguide axis) is negligible. Therefore, only the field distribution along the  $y$  axis (waveguide cross-section) needs to be sampled, with  $M$  evenly spaced points. For this target region configuration, the elements of the deposition matrix are given by

$$\mathcal{Z}_{mn}(z_D) \equiv (W\Delta z/M)^{1/2} E_n(y_m, z_D), \quad (7.1)$$

where  $E_n(y_m, z_D)$  is the electric field at position  $(y_m, z_D)$  for an incoming wave (of unit flux) in the  $n$ -th mode of the empty waveguide (input). This definition for the elements of the deposition matrix can easily be generalized to higher dimensions; however, restricting ourselves to a cross-sectional target region facilitates comparison between the deposition matrix and the well-known transmission matrix. Switching to the waveguide-mode basis, the deposition matrix becomes  $\mathcal{Z}_{mn}(z_D) = \int_0^W \chi_m(y) E_n(y, z_D) dy$ , where  $\chi_m(y)$  is the normalized transverse profile of the  $m$ -th mode of a homogeneous waveguide with a refractive index equal to the average index of the disordered region. Note that the waveguide

modes include both propagating modes and evanescent modes. If the evanescent waves are negligible, only the propagating modes are kept and normalized by their propagation speed  $v_m$ , we get

$$\mathcal{Z}_{mn}(z_D) = \sqrt{v_m} \int_0^W \chi_m(y) E_n(y, z_D) dy. \quad (7.2)$$

In this form, the deposition matrix naturally reduces to the transmission matrix at the end of the disordered region  $z_D = L$ . In our disordered waveguides, the deposition matrices defined by Eqs. 7.1 and 7.2 have nearly identical eigenvalues and eigenvectors for most depths except when very close to the exit surface  $z_D = L$ . More details are given in Appendix B.

### 7.3 Numerical Simulation & Analytical Model

To reveal the full potential of the deposition matrix (DM) for energy deposition inside disordered systems, we first carry out numerical simulations of wave propagation in 2D disordered waveguides using the Kwant software package [188]: the simulations are along the same lines as in Chapter 6 and described in detail in Appendix B. For comparison with the transmission matrix (TM), we adopt the DM defined by Eq. 7.2 and calculate its eigenvalues  $\zeta$  for a thin slice at different depths  $z_D$  inside a lossless disordered waveguide. The probability density function (PDF)  $P(\zeta)$ , shown in Fig. 7.2(a), is very different from the celebrated bimodal PDF of transmission eigenvalues  $P(\tau)$  [86]. At depths  $z_D < L$ ,  $P(\zeta)$  has a single peak at  $\zeta = 0$ , but it develops a second peak at  $\zeta = 1$  near the exit surface  $L - z_d < \ell_t$  (shaded area). We normalize the eigenvalues  $\zeta$  by their mean  $\langle \zeta \rangle$ , which represents the typical energy within the slice at depth  $z_D$  under random illumination conditions. Despite the lack of a peak at the maximum eigenvalue  $\zeta_{\max}$ , for most depths  $P(\zeta / \langle \zeta \rangle)$  has a long tail extending beyond the range of  $P(\tau / \langle \tau \rangle)$ . Consequently, the maximal enhancement of energy inside the diffusive system, given by  $\zeta_{\max} / \langle \zeta \rangle$ , is noticeably larger

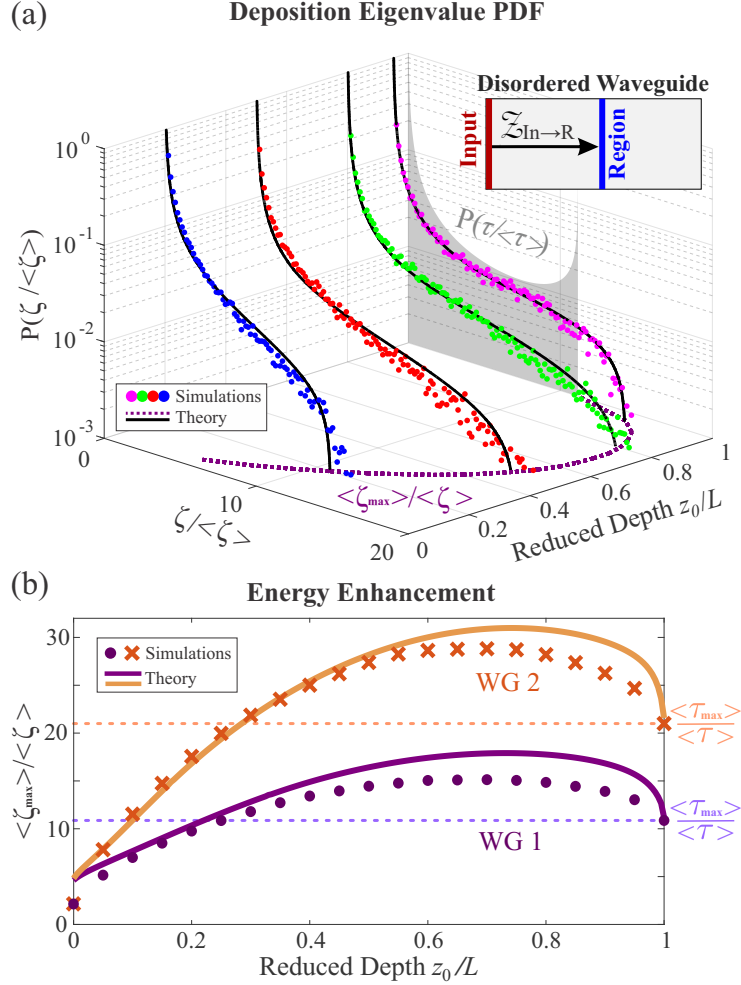


Figure 7.2: **Numerical simulation and analytic prediction of deposition eigenvalues.** (a) Probability density function of normalized deposition eigenvalues  $\zeta / \langle \zeta \rangle$  for a thin slice at varying depths  $z_D$  inside a diffusive waveguide (see inset). Analytical FRM predictions (solid lines) agree with numerical simulations (dots) averaged over 1000 disorder configurations. For most depths,  $P(\zeta / \langle \zeta \rangle)$  is very different from the bimodal distribution of the transmission eigenvalues  $P(\tau / \langle \tau \rangle)$ , although it converges to bimodal at the end (shaded area at  $z_D/L = 1$ ). The theoretical prediction for the upper edge of  $P(\zeta)$ , which sets the limit for energy enhancement  $\langle \zeta_{\max} \rangle / \langle \zeta \rangle$ , is marked by dashed purple line in the horizontal plane. (b) Energy enhancement in two diffusive waveguides (WG1, WG2), given by the ratio of the largest ensemble-averaged deposition-eigenvalue  $\langle \zeta_{\max} \rangle$  over the mean eigenvalue  $\langle \zeta \rangle$ , increases with depth  $z_D$  and reaches its maximum at  $z_D/L \sim 3/4$ . Analytical predictions for the upper edge of  $P(\zeta / \langle \zeta \rangle)$  (solid lines) are compared to numerical data (symbols). The energy enhancement  $\langle \tau_{\max} \rangle / \langle \tau \rangle$  exceeds the transmission enhancement  $\langle \zeta_{\max} \rangle / \langle \zeta \rangle$  (horizontal dotted line) at most depths. In (a), the waveguide (WG1) has a length  $L = 50 \mu\text{m}$ , width  $W = 15 \mu\text{m}$ , and transport mean free path  $\ell_t = 3.3 \mu\text{m}$ . (b) includes a second waveguide (WG2) of  $L = 50 \mu\text{m}$ ,  $W = 30 \mu\text{m}$ , and  $\ell_t = 1.6 \mu\text{m}$ .

than the maximum enhancement of the transmission  $\tau_{\max}/\langle\tau\rangle$  for open channels ( $\tau_{\max} = 1$ ,  $\langle\tau\rangle \sim \ell_t/L \ll 1$ ).

To interpret these results quantitatively, we develop an analytical model for the PDF of the deposition eigenvalues  $P(\zeta)$ . The DM  $\mathcal{Z}(z_D)$  cannot be treated as a random matrix with uncorrelated matrix elements, because the eigenvalue PDF in Fig. 7.2(a) drastically differs from the Marchenko-Pastur law [201]. In particular, the latter predicts  $\langle\zeta_{\max}\rangle/\langle\zeta\rangle = 4$ , whereas significantly larger values are obtained at almost all depths, indicating that correlations between elements of  $\mathcal{Z}(z_D)$  are beneficial for energy deposition. Since the DM and the TM coincide at the exit, we build a model that captures the continuous evolution from  $P(\zeta)$  at  $z_D < L$  to the bimodal PDF at  $z_D = L$ . This is realized by using a filtered random matrix (FRM) ensemble as initially introduced in Ref. [202]. This theory amounts to assuming that  $\mathcal{Z}(z_D)$  has the same spectrum as a filtered matrix drawn from a larger virtual TM (Appendix B). The advantage of this approach is that the full PDF  $P(\zeta)$  can be inferred from the first two moments  $\langle\zeta\rangle$  and  $\langle\zeta^2\rangle$ . Here we use the numerical values of these two moments as input parameters of the model. The good agreement between the numerical PDF and the FRM prediction in Fig. 7.2(a) validates our ansatz.

Combining the FRM model with analytic predictions for the first two moments of  $P(\zeta)$ , we get analytical expressions for the full PDF as well as the maximal enhancement. The first moment decays linearly with depth,

$$\langle\zeta(z_D)\rangle \simeq 2(1 - \langle\tau\rangle)(1 - z_D/L) + \langle\tau\rangle, \quad (7.3)$$

as given by diffusion theory [203]. The second moment is given by the variance  $\text{Var}[\zeta(z_D)]$ , which is related to the fluctuation of the cross-section integrated intensity at depth  $z_D$  gen-

erated by random wavefront illumination [76]:

$$\text{Var}[\zeta(z_D)] \simeq \langle \zeta \rangle^2 [1 + N C_2(z_D)]. \quad (7.4)$$

In this expression,  $N$  is the number of waveguide modes in the disordered region and  $C_2(z_D)$  stands for long-range contributions to the spatial intensity correlation function, whose analytic expressions are given in [204,205]. Combining these with the FRM model, in the limit  $N \gg 1$ , we predict a finite support for  $P(\zeta)$  and thus a maximal energy enhancement given by the upper edge of  $P(\zeta)$ . Fig. 7.2(b) shows a quantitative agreement between this prediction and  $\langle \zeta_{\max} \rangle / \langle \zeta \rangle$  evaluated numerically for disordered waveguides of different sizes and scattering strengths: without any adjustable parameter. The FRM predicts that  $\langle \zeta_{\max} \rangle / \langle \zeta \rangle$  depends only on  $C_2(z_D)$  for most depths  $z_D$ , confirming the crucial role of mesoscopic correlations in enhancing energy deposition. The general expression for the energy enhancement is derived and presented in Appendix B, below we present a simplified form in the limit of  $L \gg \ell_t$ :

$$\frac{\langle \zeta_{\max}(z_D) \rangle}{\langle \zeta(z_D) \rangle} \simeq \frac{3N C_2(z_D)}{2} \simeq \frac{3(z_D/L) - 2(z_D/L)^2}{\langle \tau \rangle}. \quad (7.5)$$

Two conclusions can be drawn from this result. First, the maximal energy enhancement is inversely proportional to  $\langle \tau \rangle$  and thus grows linearly with  $L/\ell_t$ . In particular, it is independent of the width  $W$  of the disordered waveguide as long as the dimensionless conductance  $g = N \langle \tau \rangle$  is sufficiently large. Second, apart from  $\langle \tau \rangle$ , the energy enhancement depends on the reduced depth  $z_D/L$  only; reaching a maximal value of  $9/8\langle \tau \rangle \sim L/\ell_t \gg 1$  at  $z_D^{(\max)}/L \sim 3/4$ . This result holds for different transport mean free paths, as confirmed in Fig. 7.2(b). Hence, the largest enhancement is *not* obtained at the output surface, but rather deep inside the diffusive medium at depth  $3L/4$ : independent of  $\ell_t$ .

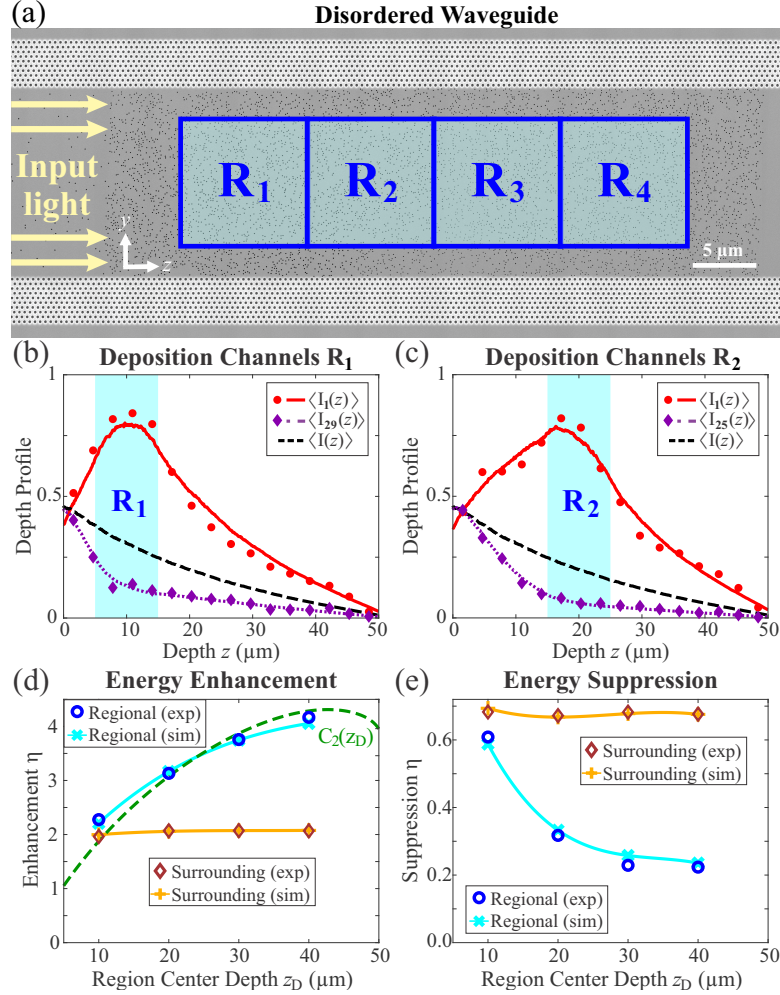


Figure 7.3: **Experimental measurement of deposition eigenchannels.** (a) A composite scanning electron microscope (SEM) image of a disordered waveguide of width  $W = 15 \mu\text{m}$ . Randomly distributed air holes (each  $100 \text{ nm}$  in diameter) are etched throughout a designated  $L = 50 \mu\text{m}$  long region. Superimposed are four target regions used for energy deposition; each is  $10 \mu\text{m} \times 10 \mu\text{m}$ . (b,c) The depth profiles (cross-section integrated intensities) of two deposition eigenchannels with enhanced and suppressed energies in the target region  $R_1$  centered at depth  $z_D = 10 \mu\text{m}$  (b), and  $R_2$  at  $z_D = 20 \mu\text{m}$  (c) are shown. The experimental data (red circle, purple diamond) agrees with the numerical simulations (red solid line, purple dotted line). The black dashed line is the averaged intensity profile generated by random input wavefronts. Each experimental data point is averaged over  $\Delta z = \ell_t$  to reduce fluctuations. (d,e) The experimentally measured energy enhancement in the target region  $\eta_t$  (blue-circles) and in the surrounding area  $\eta_s$  (brown-diamonds) of two deposition eigenchannels  $\alpha = 2$  (d) and  $\alpha = 24$  (e) are compared with numerical data (light-blue and orange lines): for the case of energy deposition into four target regions centered at  $10, 20, 30,$  and  $40 \mu\text{m}$ . In (d) the green line corresponds to  $35C_2(z_D)$ , and its agreement with the experimental/numerical results of  $\eta_t(z_D)$  confirms the essential contribution of long-range intensity correlations to energy deposition.

## 7.4 Measurement Of Deposition Eigenchannels

We experimentally measure different deposition matrices in the disordered waveguides presented in Chapter 6, shown in Fig. 7.3(a). We construct the deposition matrices associated with four target regions inside the disordered waveguide, each is  $10 \mu\text{m} \times 10 \mu\text{m}$ . They are centered at depths  $z_D = 10, 20, 30, 40 \mu\text{m}$ .

Following the experimental technique in Chapter 6, we use the SLM in our setup to modulate the monochromatic laser beam incident on the waveguide, and measure the field distribution within each target region (for details see Appendix B). From the data, we extract the DM and perform a singular value decomposition to obtain the deposition eigenchannels' input vectors. These vectors are the eigenvectors of  $\mathcal{Z}^\dagger \mathcal{Z}$ ; each is sorted by its corresponding eigenvalue, from high to low, and labeled by an index  $\alpha$ . We sequentially shape the incident wavefront into each of the eigenvectors, thereby exciting one eigenchannel at a time, and record the 2D intensity distribution over the entire disordered waveguide. The cross-section integrated intensity  $I_\alpha^{(D)}(z)$  depicts the depth profile of every eigenchannel. We repeat this measurement for multiple disorder realizations –generated at multiple wavelengths and with different hole configurations– and ensemble average the spatial profiles of the eigenchannels with the same index  $\alpha$ .

In Fig. 7.3(b,c), we show the depth profiles of example eigenchannels with enhanced or suppressed energy deposition, for two different target regions. Both strong energy enhancement and suppression are observed experimentally in the target region –when compared to the average depth profile  $\langle I(z) \rangle$  of random illumination patterns– and reproduced numerically. Simultaneously the energy outside the target region is enhanced or suppressed, reflecting the non-local effects in the energy deposition. Quantitatively, we compute the energy enhancement factor in the target region  $\eta_t = \int_{z \in R} I_\alpha(z) dz / \int_{z \in R} \langle I(z) \rangle dz$ , and in the surrounding area  $\eta_s = \int_{z \notin R} I_\alpha(z) dz / \int_{z \notin R} \langle I(z) \rangle dz$ . Figure 7.3(d) shows that

$\eta_t$  increases with depth  $z_D$ , while  $\eta_s$  remains nearly constant. The depth variation of the regional enhancement  $\eta_t(z_D)$  is captured by the long-range correlation function  $C_2(z_D)$ , in agreement with our theoretical model. Due to the presence of loss in the diffusive waveguide, the depth of the maximal energy enhancement –which coincides with the maximum of  $C_2(z_D)$ – is slightly shifted from  $z_D = (3/4)L$  towards the output end. Figure 7.3(e) shows that the suppression of energy within the target region gets stronger for larger depths, but the suppression in the surrounding area is independent of depth.

## 7.5 Two Mechanisms For Energy Deposition

To gain physical insight into the formation of deposition eigenchannels and how they enhance or suppress energy within local regions *inside* a diffusive system, we decompose them into the transmission eigenchannels, whose spatial profiles have been studied extensively [5, 73, 78, 183, 184, 206–208]. At the entrance of the system  $z = 0$ , the transmission eigenvectors form a complete basis, and the input wavefront of a deposition eigenchannel can be expressed as a linear superposition of the transmission eigenchannels. The linear mapping from the incident field to the internal field carries the decomposition to the entire field distribution inside the disordered waveguide:  $E_\alpha^{(D)}(y, z) = \sum_{\beta=1}^N d_{\alpha\beta} E_\beta^{(T)}(y, z)$ . In this expression  $E_\alpha^{(D)}(y, z)$  [ $E_\beta^{(T)}(y, z)$ ] denotes the field distribution of the  $\alpha$ -th deposition ( $\beta$ -th transmission) eigenchannel and  $N$  is the number of transmission eigenchannels (equal to the number of propagating modes in the input waveguide). The depth profile of a deposition channel, given by the cross-section integrated intensity  $I_\alpha^{(D)}(z) = \int_0^W |E_\alpha^{(D)}(y, z)|^2 dy$ , consists of two terms:

$$\begin{aligned} I_\alpha^{(D)}(z) &= I_\alpha^{(i)}(z) + I_\alpha^{(c)}(z) \\ &= \sum_{\beta=1}^N |d_{\alpha\beta}|^2 I_\beta^{(T)}(z) + \sum_{\beta \neq \beta'} d_{\alpha\beta} d_{\alpha\beta'}^* I_{\beta\beta'}^{(T)}(z). \end{aligned} \tag{7.6}$$

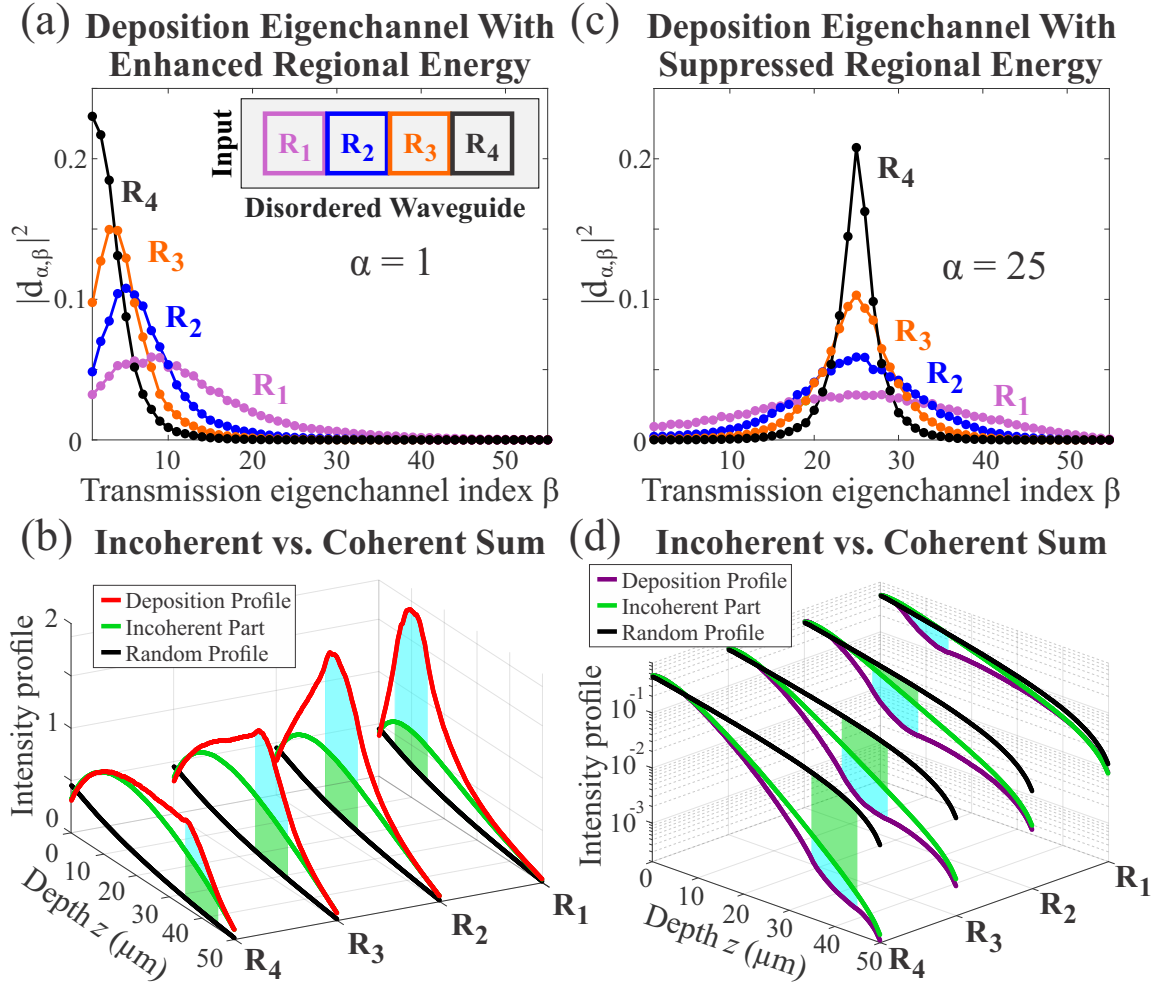


Figure 7.4: **Relation between deposition eigenchannels and transmission eigenchannels.** (a,c) The projection of a deposition eigenchannel with index  $\alpha = 1$  (a) or 25 (c) onto transmission eigenchannels with index  $\beta$  gives the coefficients  $d_{\alpha\beta}$ . Four curves denote  $|d_{\alpha\beta}|^2$  for four target regions  $R_1 - R_4$  [inset of (a)] in the same disordered waveguide as in Fig. 7.3. (b,d) Comparison between the coherent sum (red/purple) and incoherent (green) sum of the transmission eigenchannels describing deposition eigenchannel profiles, with coefficients given in (a,c). For each deposition region, the enhancement/suppression above/below the random input intensity profile (black dashed line) has two distinct contributions from selective excitation of transmission eigenchannels (green areas) and constructive/destructive interference between them (cyan areas).

The first term  $I_\alpha^{(i)}(z)$  is an incoherent sum of the constituent transmission eigenchannel depth profiles,  $I_\beta^{(T)}(z) = \int_0^W |E_\beta^{(T)}(y, z)|^2 dy$ , studied in [5, 73, 78, 183, 184, 206–208]. The second term  $I_\alpha^{(c)}(z)$  is the result of interference between different transmission eigenchannels inside the diffusive waveguide, which we observe for the first time. Although the transmission eigenchannels are orthogonal at  $z = 0$  and  $z = L$ , this is not the case inside:

$$I_{\beta\beta'}^{(T)}(z) = \int_0^W E_\beta^{(T)}(y, z) E_{\beta'}^{(T)*}(y, z) dy \neq 0 \quad (7.7)$$

for  $0 < z < L$ .

To find how much these two terms contribute to the energy enhancement, we numerically decompose the maximal energy deposition eigenchannels ( $\alpha = 1$ ) for the four target regions inside our disordered waveguide. As shown in Fig. 7.4(a), each is composed of multiple high-transmission eigenchannels (higher transmission corresponds to lower index  $\beta$ ). With increasing depth  $z_D$ , the number of constituent transmission eigenchannels decreases, and the maximal decomposition coefficient  $|d_{\alpha\beta}|^2$  shifts to  $\beta = 1$  (the highest-transmission eigenchannel). Figure 7.4(b) shows the incoherent contribution  $I_1^{(i)}(z)$  and coherent contribution  $I_1^{(c)}(z)$  to energy deposition in the target region. When the target region is located at a shallower depth, more transmission eigenchannels participate in constructing the deposition eigenchannel, and their constructive interference plays an important role in enhancing energy deposition in the target region. As the number of participating transmission eigenchannels becomes progressively smaller with increasing depth, the interference effect is weakened and the incoherent contribution from selective excitation of transmission eigenchannels becomes dominant.

We also investigate the deposition eigenchannels that reduce energy within the target regions. As shown in Fig. 7.4(c), the  $\alpha = 25$  deposition eigenchannels consist of multiple transmission eigenchannels with indices  $\beta$  close to 25. The suppression of energy within

the target region results from selective excitation of lower-transmission eigenchannels and their destructive interference [see Fig. 7.4(d)]. The deeper the target region, the lower the number of constituent transmission eigenchannels, the weaker their destructive interference effect. Thanks to the destructive interference, the total transmission can be greater than the total energy at a given depth inside the target region. Thus, when sending light through a diffusive system it is possible to avoid certain regions inside.

## 7.6 Discussion & Conclusions

In conclusion, we have delineated the fundamental limits on depositing energy into a finite region, located at any depth, inside a diffusive system. In contrast to the bimodal distribution of transmission eigenvalues, the PDF of deposition eigenvalues  $P(\zeta)$  has only one peak at  $\zeta = 0$  and a long tail for most depths:  $\zeta / \langle \zeta \rangle \gg 1$ . Our theoretical model, based on a filtered random matrix ensemble, can analytically predict  $P(\zeta)$  for regions anywhere inside a diffusive medium. The long-range correlations present in the intensity of the field, induced by the multiple scattering of light and characterized by  $C_2(z_D)$ , facilitate optical energy deposition. In a diffusive waveguide of length  $L$  much larger than the transport mean free path  $\ell_t$ , the largest possible energy enhancement  $\langle \zeta_{\max} \rangle / \langle \zeta \rangle$  at a depth  $z_D$  depends only on two parameters:  $L/\ell_t$  and  $z_D/L$ . With increasing depth  $z_D$ ,  $\langle \zeta_{\max} \rangle / \langle \zeta \rangle$  rises and reaches a global maximum  $\sim L/\ell_t$  at  $z_D^{(\max)}/L \sim 3/4$ . Because  $z_D^{(\max)}$  is dependent on  $L$  and independent of  $\ell_t$ , when  $L \gg \ell_t$ , the depth of the maximal enhancement is deep inside the sample rather than near the front or back surfaces. Although our experimental and numerical studies are conducted on 2D systems, the above scaling results follow from filtered matrix theory, e.g. Eq. 7.5, which also applies in three dimensions.

Additionally, we discovered the relationship between deposition eigenchannels and transmission eigenchannels. We found that it is impossible to construct the intensity profile

of a deposition eigenchannel from the intensity profiles of the transmission eigenchannels alone. Constructive or destructive interference between transmission eigenchannels inside the disordered system plays a prominent role in enhancing or suppressing energy within the target region. Therefore, our analysis reveals two distinct mechanisms for energy deposition: selective excitation of transmission eigenchannels and interference between them. Their contributions are characterized by the amplitudes and phases of the coefficients obtained when decomposing a deposition eigenchannel into a summation of transmission eigenchannels.

Although our studies are conducted on planar waveguides with narrow widths and transverse confinement, we believe the conclusions can be extended to wide slabs with open boundaries and to volumetric diffusive systems. They are also applicable to other types of waves such as microwaves and acoustic waves. Targeted energy delivery opens the door to numerous applications, e.g., optogenetic control of cells, photothermal therapy, as well as probing and manipulating photoelectrochemical processes deep inside nominally opaque media.

# Chapter 8

## Remission Eigenchannels Inside Diffusive Scattering Media

### 8.1 Introduction

Diffusive-waves have been used for sensing and imaging [94–103, 209] in a diverse variety of random media: ranging from the earth’s crust [104–106] to the human brain [101, 107–109]. Often, in theoretical investigations and lab-based experiments waves transmitted through diffusive media are utilized and studied for imaging and sensing. In many real-world applications, however, transmitted waves are unavailable and directly reflected waves cannot penetrate beyond one transport mean free path into the system; though, recent studies have attempted to push this boundary with adaptive optics [210–212] and matrix-based approaches [213–221]. Therefore, in many applications either re-mitted waves must be used –diffusive waves actively generated by an external source and emitted from the medium at a separate location on the same side– or passive imaging & sensing techniques –based on naturally occurring incoherent sources– must be used. Seismic interferometry is, perhaps, the most notable domain for passive diffusive-wave imaging & sensing techniques; relying on incoherent acoustic waves generated by earthquakes

and other seismic activity to map the Earth’s subsurface [222–236]. It is worth noting, however, that this technique has also been explored in the context of ultrasonic acoustic-waves [237, 238]. Nevertheless, in many applications outside the domain of acoustics, incoherent waves are not naturally generated by the random media investigated: requiring external sources. An exemplary application currently in development is wearable optics-based non-invasive brain-computer interfaces [103, 239–243]. In the context of this application, active-source diffusive-wave spectroscopy is used to monitor the temporal dynamics of cerebral blood flow, which is assumed to be a proxy for neural activity. While the optical source is external and in principle controllable, in practice, the light generated by the source is often effectively treated as a random input: with energy diffusing in all directions. The depth-penetration of the collected-light is controlled by varying the separation between the source and detector, due to the “banana” [244] shaped trajectory of randomly-generated remitted light in diffusive systems. Specifically, increasing the separation between source and detector increases the penetration-depth of the collected light. In this imaging paradigm, therefore, the increased depth-penetration of the measured light comes at the expense of the signal strength. It is reasonable to ask, therefore, “Is possible to coherently shape the input-light in order to optimized the output energy-density of remitted light which has traveled along a specific “banana” trajectory?”

In this chapter we perform an experimental study on diffusive-wave remission eigenchannels in open disordered systems, as illustrated in Fig. 8.1. First, we introduce the remission matrix,  $\mathcal{R}$ , of a diffusive system; which relates wavefronts input over a finite region of the surface to the resulting waves emitted from a finite-region arbitrarily-displaced from the injection site on the same surface. Using a modified version of the on-chip platform and the experimental setup presented in Chapters 6 & 7, we experimentally measure the remission matrix for output regions with different separations. Then, we directly excite the individual remission eigenstates, and observe their spatial structures as a func-

tion of separation between the input and output regions. We show that “open” remission eigenchannels enhance the output signal without sacrificing the penetration-depth of the collected light.

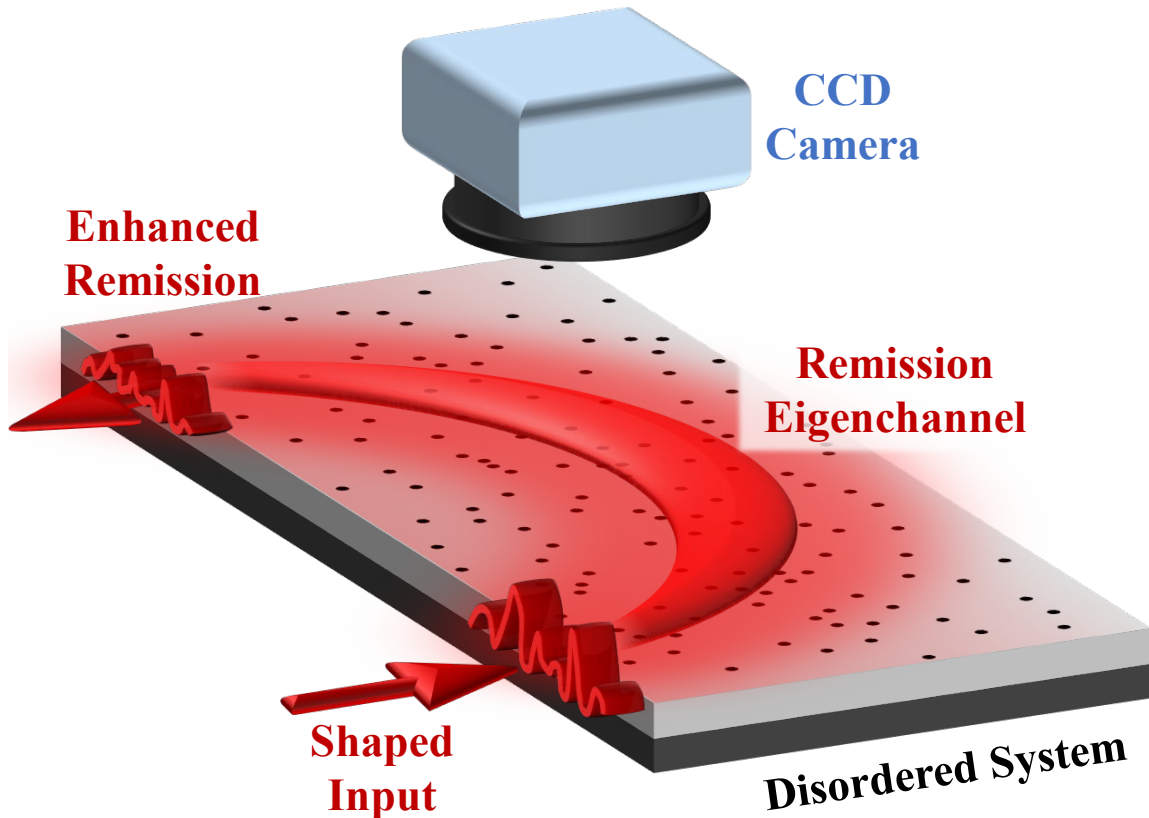


Figure 8.1: **Remission eigenchannel concept.** By coherently controlling the wavefront of light injected into a slab-geometry diffusive-medium with a spatial light modulator; we can couple into a remission-eigenchannel to enhance the signal of the emitted light, without sacrificing the penetration depth. We can directly observe the spatial profile of the remission-eigenchannel by capturing the light scattered out-of-plane with a CCD camera.

## 8.2 Experimental Samples

To directly observe the spatial distribution of remission eigenchannels *within* open diffusive systems, we fabricate on-chip two-dimensional diffusive structures on a silicon-on-insulator wafer with electron beam lithography and plasma etching (see Appendix B for

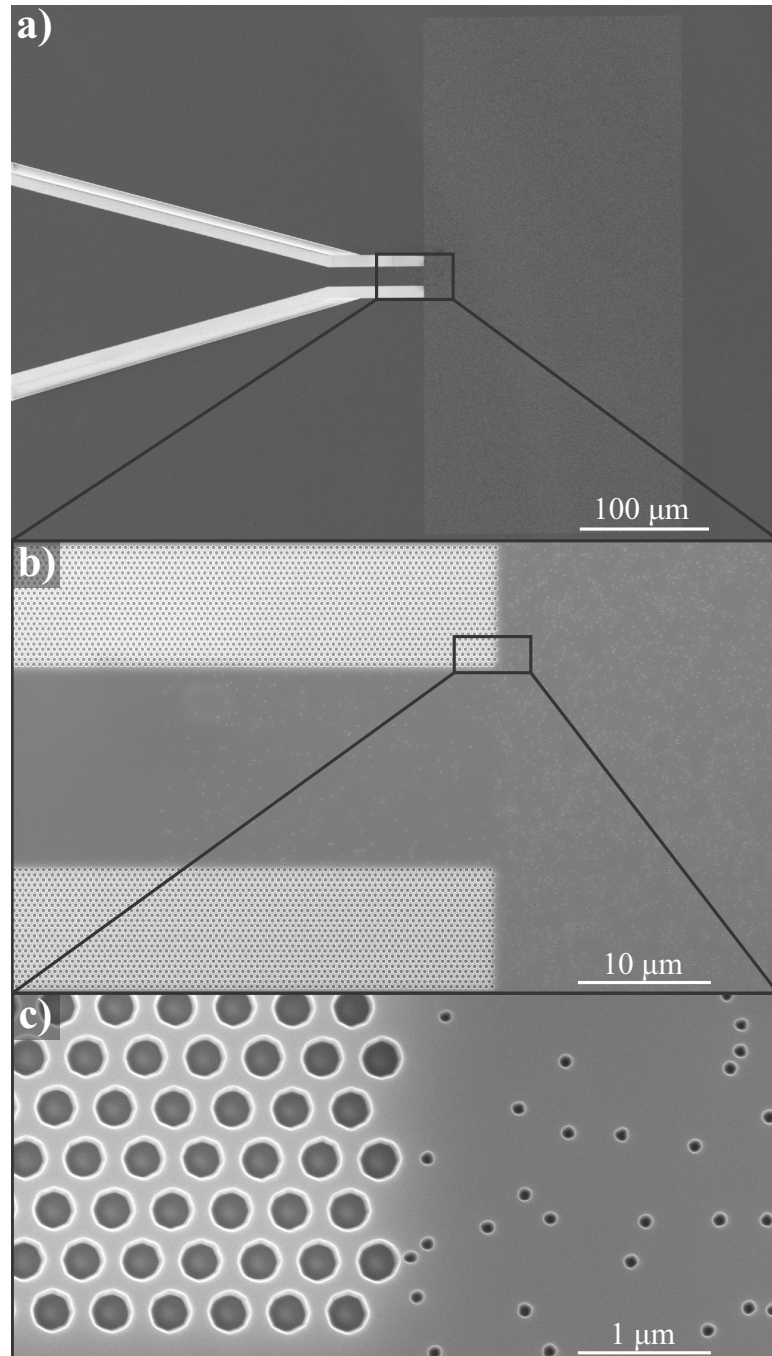


Figure 8.2: **On-chip diffusive-slab SEM images.** A SEM image of the full on-chip slab-geometry diffusive system used in our experiments is shown in (a). Magnifying by an order of magnitude, in (b) the 15  $\mu\text{m}$ -wide input waveguide is shown at the buffer-region diffusive-region interface. Further magnification shows the trigonal photonic-crystal lattice of air holes (radius = 155 nm, lattice constant = 440 nm) and examples of the randomly arranged 100-nm-diameter holes in the diffusive region.

details). An example of the overarching structure we fabricate is shown in Fig. 8.2(a). We inject light into a diffusive system configured in a slab-geometry with a width of 400  $\mu\text{m}$ , a depth of 200  $\mu\text{m}$ , and open boundaries. The on-chip optical structures we use to route light into the diffusive slab are equivalent to those used in our waveguide geometry, shown in Figs. 8.2(a,b). Light is injected via the edge of the wafer into a ridge waveguide and after  $\sim 1.5$  cm of propagation it enters a  $15^\circ$  optical taper. The taper reduces the waveguide width from 300  $\mu\text{m}$  to 15  $\mu\text{m}$ , in order to convert the lower-order modes to higher-order, enabling us to access all waveguide modes in the input region. The 15- $\mu\text{m}$ -wide injection waveguide prior to the slab supports  $N = 55$  propagating modes at the wavelength of our probe light,  $\lambda = 1.55$   $\mu\text{m}$ . As shown in Fig. 8.2(b), we include a “buffer” region in this waveguide to provide mode mixing and remove artifacts from the previous optical elements. The one notable difference, relative to the structures discussed in the previous chapters, is the addition of a 10  $\mu\text{m}$  trench on the outside surface of the photonic crystal taper. The trench is a loss-mechanism designed to prevent any light leaking through the photonic-crystal taper from reaching the open diffusive-slab. Because the intensity of the remitted light can be orders of magnitude lower than the incident wavefront, mitigating any stray light from the input is essential in our structures. The other notable difference in this chapter’s on-chip structure is the hole density of the diffusive slab. While we still use randomly arranged 100 nm-diameter holes to induce diffusive wave transport, as shown in Fig. 8.2(c), the air filling fraction is 2.75% instead of 5.5%. As a result, both the transport mean free path and diffusive absorption length are longer than in the previous chapters:  $\ell_t = 6.4$   $\mu\text{m}$  and  $\xi_a = 56$   $\mu\text{m}$ .

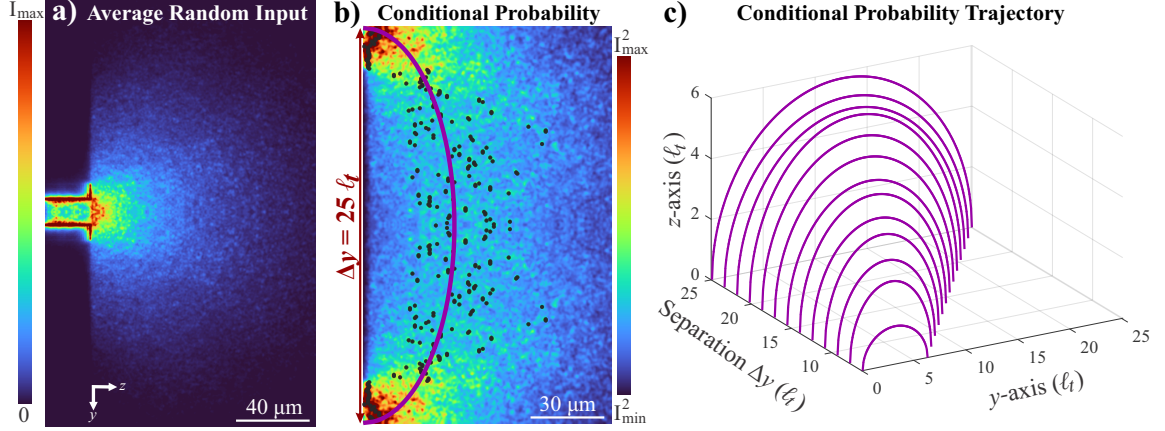


Figure 8.3: **Remission of random input wavefronts.** The average intensity pattern produced by random input wavefronts  $\langle I(y, z) \rangle$  is shown in (a). An example conditional probability distribution,  $\langle I(y, z) \rangle \langle I(y + \Delta y, z) \rangle$ , of remitted random light is presented in (b) for  $\Delta y = 25\ell_t$ . The black dots represent the maxima of  $\langle I(y, z) \rangle \langle I(y + \Delta y, z) \rangle$  along the  $z$ -axis, for each value of  $y$ , and the purple curve is the best fit of an ellipse to the data. The ellipse gives the trajectory of randomly-generated remitted-light traveling from the input to the displaced region. In (c) the trajectory of remitted light in the  $(y, z)$  plane is plotted as a function of separation  $\Delta y$ .

### 8.3 Remitted Random Light

When a finite region of a disordered-slab’s surface is illuminated with a random wavefront, the light diffuses throughout the medium in every direction. The experimentally measured and ensemble-averaged intensity distribution,  $\langle I(y, z) \rangle$ , generated by random illumination patterns in our setup is shown in Fig. 8.3(a). For reference, in the case of a large passive-system with a point-source at  $(y = 0, z = 0)$ , the ensemble-averaged random-input intensity distribution decreases quadratically  $\langle I(y, 0) \rangle \propto 1/y^2$  as a function of lateral separation from the source, and decreases linearly  $\langle I(0, z) \rangle \propto 1/z$  as a function of depth [245]. This scaling is why remitted light is significantly more difficult to detect than transmitted light, for the same separation from the source.

Based on the experimentally calculated  $\langle I(y, z) \rangle$  we can obtain the “banana” shaped trajectory of remitted light generated by random-inputs, for a specific separation between

the source and detector  $\Delta y$ . The statistically-likely pathway random remitted-light traverses within the diffusive system can be obtained from the conditional probability distribution,  $\langle I(y, z) \rangle \langle I(y + \Delta y, z) \rangle$ , shown in Fig. 8.3(b). For every value of  $y$  we can locate the maxima of the depth cross-section,  $\max[\langle I(y, z) \rangle \langle I(y + \Delta y, z) \rangle]_z$ , (black dots) and fit the  $z$ -dependent data to an ellipse (purple line) to obtain an estimate for the trajectory of the remitted light, for a given separation  $\Delta y$ . In Fig. 8.3(c) we plot the trajectory of the randomly-generated remitted-light as a function of separation. The penetration depth of the remitted light increases as a function of separation. This occurs because the likelihood that a photon will depart the system –and therefore not reach  $\Delta y$ – is highest near the surface:  $z = 0$  [244]. So while increased separation between a source and detector gives access to deeper-penetrating light, it is important to remember that it comes with the price of a  $\propto 1/\Delta y^2$  reduced signal-strength. Our goal is to use coherent wavefront shaping to manipulate the spatial degrees of freedom, in the input wavefront, to improve the remitted signal strength.

## 8.4 Remission Matrix

To help ameliorate the anemic signal-strength of remitted light generated by random inputs, we introduce the remission matrix,  $\mathcal{R}$ , and its associated eigenstates. As with the operators discussed in the previous chapters, the remission matrix relates an orthonormal set of input wavefronts to the corresponding spatial field distributions within a target region. For simplicity, we can consider the case of a target slice on the input surface of the diffusive medium ( $z = 0$ ) with a center-to-center displacement from the input of  $\Delta y$ , a width  $W$ , and a thickness  $\Delta z$  small enough that the field variation along  $z$  is negligible. Therefore, only the field distribution along the  $y$  axis of the slice needs to be sampled, which can be done with  $M$  evenly spaced points. If we index the remission region's points

by  $y_m$ , then  $y_{M/2} = \Delta y$  when the input is centered at  $y = 0$ . For this configuration, the elements of the remission matrix are given by

$$\mathcal{R}_{mn} \equiv (W\Delta z/M)^{1/2} E_n(y_m, z = 0), \quad (8.1)$$

where  $E_n(y_m, z = 0)$  is the electric field at position  $(y_m, z = 0)$  generated by an incoming wavefront of unit flux, specifically the  $n$ -th state of a chosen orthonormal basis of input wavefronts. As before, the chosen basis of input vectors can be the modes of the input waveguide, however, any orthonormal basis is sufficient. The eigenvalues of  $\mathcal{R}^\dagger \mathcal{R}$  determine the energy within the target slice when sending the corresponding eigenvectors into the system. As such, the eigenvector with the highest eigenvalue provides the input wavefront which emits the most light from the target slice.

## 8.5 Experimentally Measuring Remission Eigenchannels

We experimentally measure different remission matrices in the diffusive-slab shown in Fig. 8.2(a). We vary the wavelength of the input light—in increments of 1 nm between 1547 nm and 1558 nm—to create different system realizations. We construct the remission matrices associated with  $10 \mu\text{m} \times 10 \mu\text{m}$  target regions on the surface of the diffusive-slab with center-to-center separations from the input ranging from  $\Delta y = 20 \mu\text{m}$  ( $\Delta y \equiv 3.1\ell_t$ ) all the way to  $\Delta y = 160 \mu\text{m}$  ( $\Delta y \equiv 25\ell_t$ ). Note, that in our experimental measurements, target-regions are used as proxies for target-slices in order to mitigate out-of-plane scattering enhancements when calculating the eigenvalues of  $\mathcal{R}$ . To obtain the remission matrices, we use the SLM to modulate the monochromatic laser beam incident on the diffusive-slab, and measure the field-reconstruction matrix of the entire on-chip system. From the field-reconstruction matrix, we can extract any desired remission-matrix.

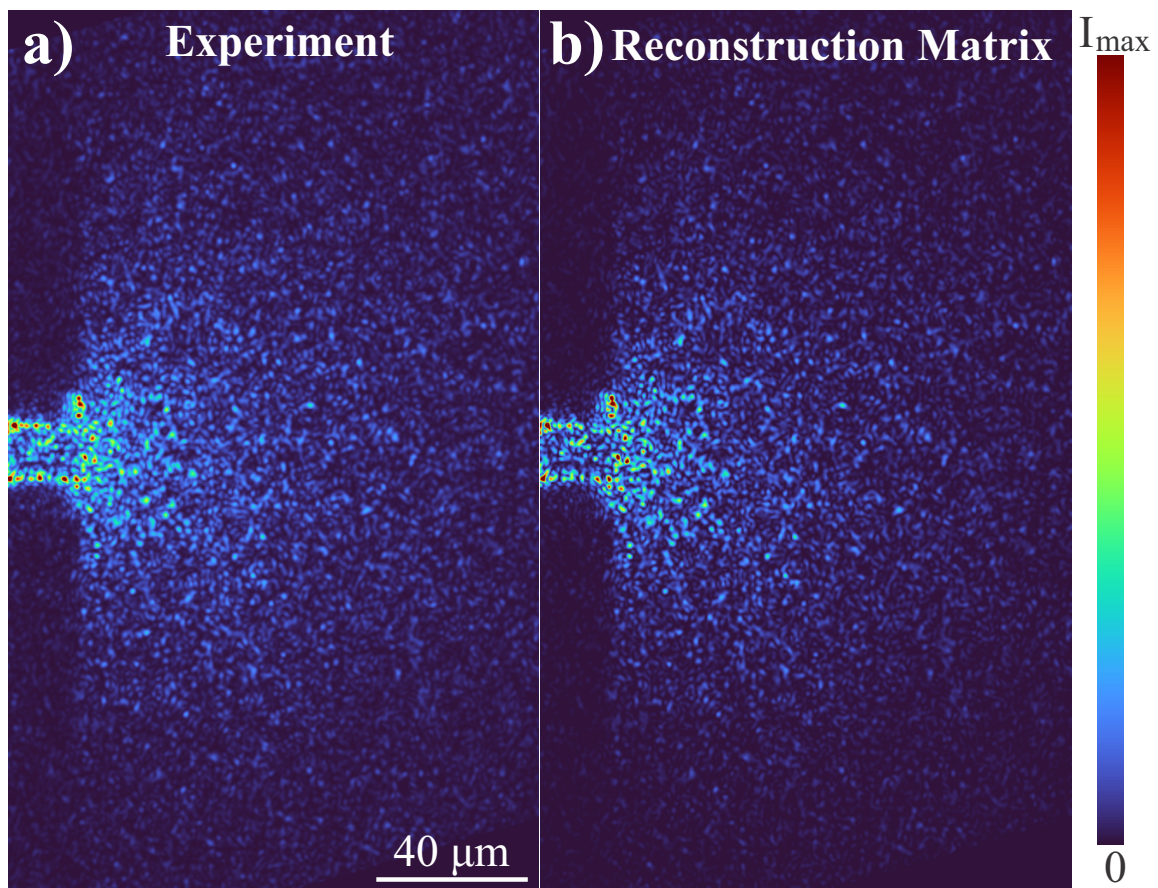


Figure 8.4: **Field-reconstruction matrix validation.** An experimentally measured intensity distribution within the diffusive slab –generated by a random phase pattern on the SLM– is presented in (a) next to the field-reconstruction matrix prediction (b). The intensity patterns have a Pearson correlation coefficient of 0.94 without any data manipulation or noise reduction.

Unlike in the previous chapters, we do not use the buffer region as a ‘launch pad’ when constructing the remission matrices. While the photonic crystal sidewalls in the diffusive waveguide-geometry prevents light from circumventing the buffer-region before reaching the target-regions; the open boundaries of the diffusive slab-geometry do not. In short, defects in the on-chip input-coupling structures –such as stitching errors in the taper– provide pathways for light to avoid the buffer region completely, and still reach the target region. Therefore, optimizing the ratio of the light in the buffer region relative to the light in the target region will prioritize these defect pathways in an open system instead of regulating the input. As such, we perform a singular value decomposition on the remission matrix between the SLM pixels and the target region,  $\mathcal{R}_{SLM \rightarrow \Delta y}$ , to obtain the remission eigenchannels’ input vectors. We can apply the calculated input vectors of the remission eigenchannels to the field-reconstruction matrix to generate the 2D intensity pattern of each eigenchannel; in addition to exciting them experimentally and directly observing the profiles. The average intensity correlation coefficient –across the entire slab region in the CCD field of view– between measured and reconstructed patterns is  $\langle C \rangle = 0.92$  (see Fig. 8.4 for an example), and therefore experimentally reconstructed patterns are effectively interchangeable with measured patterns. Using reconstructed patterns, however, is advantageous because it allows us to modulate both the amplitude and phase of the input wavefront. As such, we will proceed using the field-reconstruction matrix to generate the spatial profiles of the remission eigenchannels. After reconstructing the intensity pattern of a remission eigenchannel, we renormalize the average intensity in the buffer region  $\langle I_{Buf}(y, z) \rangle_{y,z}$  in order to account for variation in the coupling strength in the eigenstates of  $\mathcal{R}_{SLM \rightarrow \Delta y}$ . After renormalization, we calculate the remission-eigenchannel intensity distributions for different system realizations (averaging over wavelength) and ensemble average the corresponding 2D patterns.

In Fig. 8.5(a), we show an example ensemble-averaged “open” remission eigenchan-

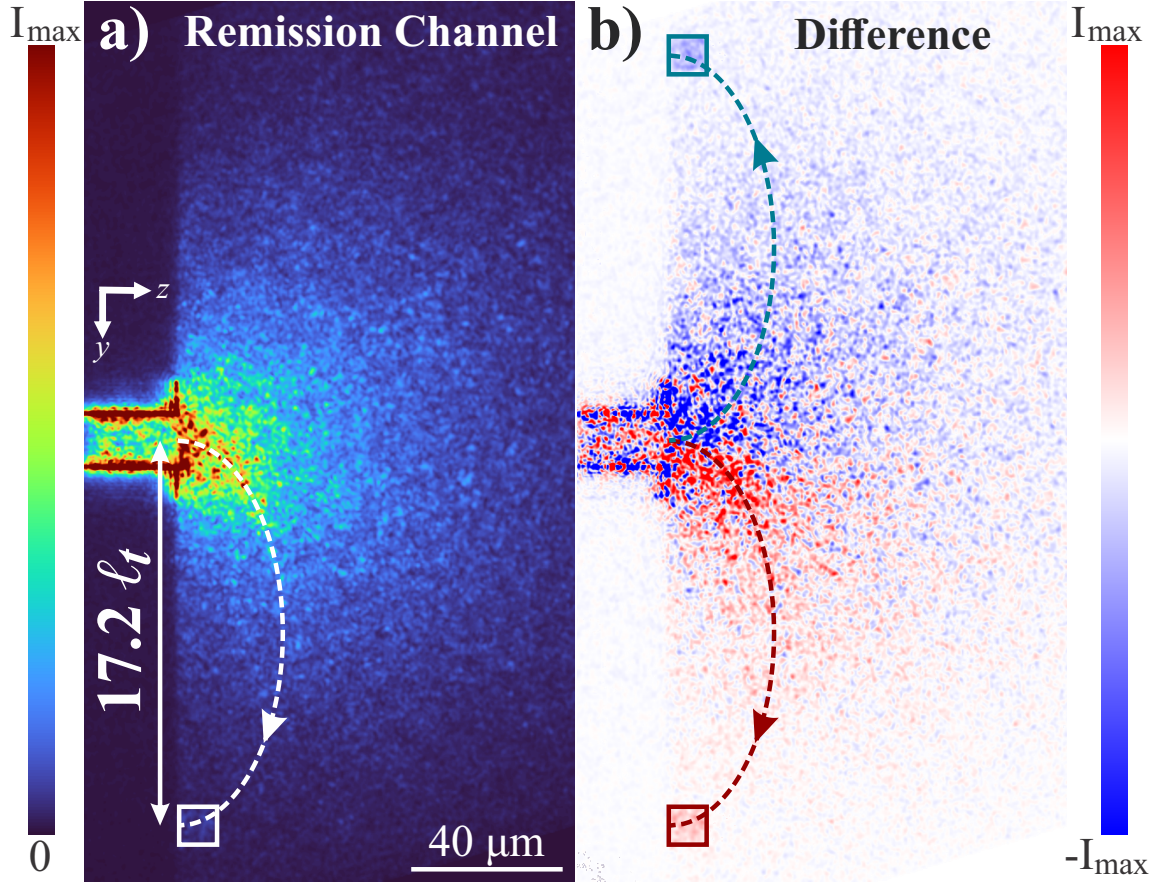


Figure 8.5: **Remission eigenchannel intensity distribution.** An example ensemble-averaged remission eigenchannel intensity distribution is shown in (a) for a remission region displaced  $\Delta y = 17.2\ell_t$  along the input surface. For reference, the trajectory of the random-light-generated conditional probability distribution from the input to the emission region (white dashed curve) is shown. To illustrate the directionality of remission eigenchannels, and their ability to redistribute energy *inside* the diffusive system, in (b) we show the difference between the lower and upper remission eigenchannel intensity distributions:  $\langle I_{+\Delta y}(y, z) \rangle - \langle I_{-\Delta y}(y, z) \rangle$ . For reference, the corresponding random-light conditional probability distributions are shown.

nel pattern  $\langle I_{\Delta y}(y, z) \rangle$ . The target region (white square) is located  $\Delta y = 17.2\ell_t$  away from the input source. The “banana” trajectory of the corresponding random-input conditional probability distribution is superimposed on top (white dashed line). The intensity distribution of the remission eigenchannel follows the “banana” trajectory, redistributing the energy inside the system towards the target region. The redistribution of energy is clearly illustrated in Fig. 8.5(b) where we calculate the difference between the lower and upper remission eigenchannel intensity distributions:  $\langle I_{+\Delta y}(y, z) \rangle - \langle I_{-\Delta y}(y, z) \rangle$ . The blue (red) shading corresponds to the intensity distribution of the remission eigenchannel directed towards the upper (lower) region. Both the upper and lower “open” remission pattern redistribute the optical energy in the system along the trajectory of the corresponding conditional probability distribution (dashed line) for random inputs. In (a,b) we use the intensity patterns of the first and second order eigenchannels from 12 different wavelengths, when calculating the ensemble-averaged “open” remission eigenchannel.

In Fig. 8.6(a-c), we plot the difference between the “open” remission eigenchannel patterns  $\langle I_{\Delta y}(y, z) \rangle$  and the ensemble-averaged random input pattern  $\langle I(y, z) \rangle$ . In (a-c) The target region (black square) is located at  $\Delta y = 12.5\ell_t$ ,  $18.8\ell_t$ , &  $25\ell_t$ , away from the input source respectively. The development of the lower (red) and upper (blue) regions in the intensity distribution demonstrate that remission eigenchannels significantly redistribute the optical energy in the system compared to random inputs. Furthermore, the red regions in (a-c) follow along the trajectory of the random-input conditional probability (green line) from the input to the target region. Additionally, the trajectory of the remission eigenchannels’ conditional probability distribution,  $\langle I_{+\Delta y}(y, z) \rangle \langle I_{-\Delta y}(y + 2\Delta y, z) \rangle$ , is plotted (black dashed line). Comparison between the curves shows that “open” remission eigenchannels have the same trajectory as the equivalent random-input generated “bananas”. Therefore, we can direct the flow of light through diffusive systems by coupling into remission eigenchannels to enhance the signal without sacrificing the penetration-depth. In

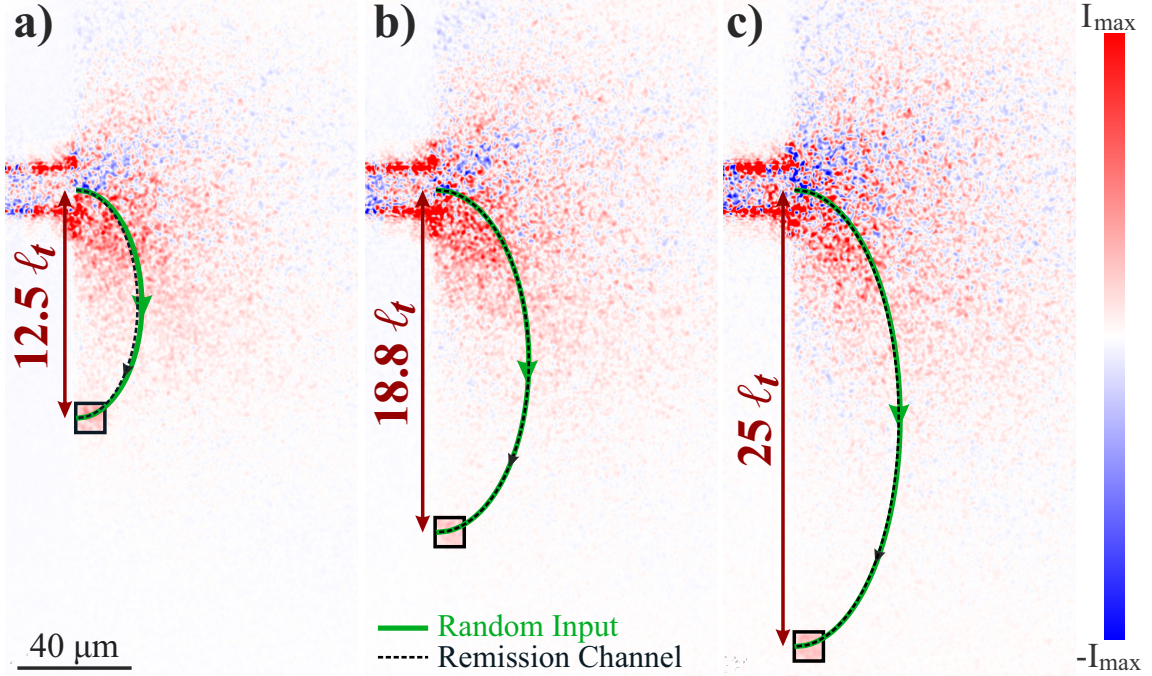


Figure 8.6: **Difference between remission eigenchannels and random illumination patterns.** In (a-c), the ensemble-averaged “open” remission eigenchannel pattern subtracted by the ensemble-averaged random input pattern  $\langle I_{\Delta y}(y, z) \rangle - \langle I(y, z) \rangle$  is shown for a target region (black square) located at  $\Delta y = 12.5l_t$ ,  $18.8l_t$ , &  $25l_t$  away from the input source. The solid-green lines show the trajectory of the conditional probability distribution generated by random light, in each panel, while the black dashed lines show the trajectory the remission eigenchannel’s conditional probability distribution.

our experimental setup, unfortunately, enhancements in the out-of-plane scattering can artificially inflate the eigenvalues of  $\mathcal{R}_{SLM \rightarrow \Delta y}$ . As such, numerical simulations of the realistic system are required to quantitatively estimate the eigenvalue enhancement remission eigenchannels provide. Kwant-based numerical simulations [188] of the realistic system show that for the separations shown, the “open” eigenchannels enhance the remitted signal strength by a factor of  $\approx 7$  across the entire target slice, when using a  $10 \mu\text{m}$  target slice on the surface<sup>1</sup>. Therefore, we can obtain a significant enhancement in the strength of the remitted light: over a finite area.

<sup>1</sup>These results are currently unpublished.

## 8.6 Discussion & Conclusion

In conclusion, we have conceptually introduced and experimentally investigated remission eigenchannels in open slab-geometry diffusive-systems. Using our on-chip interferometric platform, we can measure remission matrices and directly investigate the associated eigenchannels; for different realizations of statistically equivalent disordered systems. We show that exciting remission eigenchannels significantly enhances the signal strength of diffuse remitted-light, without altering the depth penetration. Our findings are relevant to many diffusive-wave imaging and sensing applications: ranging from seismology, to non-invasive photo-medical devices and computer-brain interfaces.

# Chapter 9

## Conclusion

In this dissertation, a methodology for experimentally creating and controlling random light in free space and in diffusive media was presented.

In free space, we demonstrated the ability to arbitrarily customize the intensity statistics and spatial-correlations of spatially-incoherent light. Because our method of creating and controlling complex light is simple –yet versatile– it can easily be adapted for use in a diverse range of optical experiments and applications. For example, the ability to arbitrarily control the non-local correlations and intensity PDFs of speckle patterns can be used to create exotic optical-potentials for studies on the transport of cold atoms, active media, and microparticles. Potentially, it can also enhance many structured-illumination applications like speckle illumination microscopy, super-resolution imaging and high-order ghost imaging. We demonstrated this in the case of super resolution imaging, where we created and used bespoke speckle patterns for parallelized nonlinear pattern-illumination microscopy. In our proof-of-principle experimental demonstration, we obtained a spatial resolution three times higher than the diffraction limit of the illumination optics in our setup. Furthermore, we demonstrated why intelligently tailoring speckles enables them to outperform Rayleigh speckles. While our demonstration was designed with a single imaging technique in mind, there are a myriad of random-light based imaging & sensing

techniques that can be similarly enhanced.

Beyond direct applications, it is worth speculating about the future of research on customizing random light. In this dissertation, all of the customized speckle patterns were generated within a 2D plane with spatially-coherent and monochromatic light. In principle, however, nothing prevents speckle customization in pulsed light, broadband light, or over a 3D volume. As such, the research presented in the first half of the dissertation is merely the beginning of a diverse and exciting branch of future research on creating and controlling random light.

In diffusive media, we have demonstrated the ability to coherently control wave transport through –and throughout– multiple scattering systems. We developed a unique experimental platform based on the synthesis of nanofabricated on-chip structures with interferometric wavefront-shaping. With it, we investigated the fluctuations and correlations of transmission eigenchannel depth profiles in diffusive media. Using our unparalleled access to the optical field inside on-chip diffusive structures; we introduced and experimentally investigated the deposition matrix  $\mathcal{Z}$ . In conjunction, we developed a theoretical formalism to predict the ultimate limitations on energy deposition at any depth inside a diffusive medium. Finally, we conceptually defined the remission matrix  $\mathcal{R}$  and experimentally demonstrated that “open” remission eigenchannels enhance the output signal strength without sacrificing the penetration-depth of the collected light.

Although our studies were conducted on planar diffusive structures, we believe, many of our findings can be extended to volumetric diffusive systems. Furthermore, they are applicable to other types of waves such as microwaves and acoustic waves. Therefore, the range of future applications of our work is quite diverse. In biology & medicine these deep tissue applications include cellular imaging/sensing, photothermal surgery/therapy, and optogenetic control over cells. In more day-to-day applications, our findings can be applied to enhance “wearable” optical sensors –like those found in a smartwatch– as well as aid

the development of non-invasive computer brain interfaces. Outside biology & medicine, applications include developing the ability to probe and manipulate photoelectrochemical processes deep inside nominally opaque media. In seismology, our results can enhance imaging and sensing deep below the earth's crust.

Beyond applications, there still are many fundamental-physics research-topics that our experimental platform is uniquely poised to explore. Since our on-chip experimental platform allows for both direct measurement of the complex field inside a random structure and near-complete control over the incident field, we can investigate how to shape an incident wavefront to control the spatial distribution of light across an entire disordered system: via a "Green's" matrix. Furthermore, this setup can be used to experimentally study the spatial structure and statistics of the time-delay eigenchannels of a diffusive system, as well as the time-gated transmission and reflection eigenchannels of a diffusive system.

# Appendix A

## Random Light In Free Space

### A.1 Transmission-Matrix Measurement

Wave propagation in any static, linear, scattering system is deterministic: no matter how complex. Therefore, such a system's response to an incident wavefront can be completely characterized by a linear operator. In this dissertation, predominantly two such operators are experimentally measured: the field-transmission matrix and the field-reconstruction matrix. The field-transmission matrix transforms any wavefront incident on a scattering-system into the corresponding wavefront transmitted by the system. As such, it is a subset of a system's scattering matrix. The field-reconstruction matrix transforms any input wavefront into the corresponding spatial field profile within the scattering-system. To measure either a transmission matrix or a field-reconstruction matrix, a simple *four-phase plus one-amplitude* technique is needed. The following section explores the measurement processes used in this dissertation.

### A.1.1 Four-Phase Plus One-Amplitude Measurement

The fundamental step of a transmission/field-reconstruction matrix measurement is recovering a complex field profile from a series of interferometric intensity measurements. To explain this technique, consider the case of two field patterns,  $E_R(\mathbf{r})$  &  $E_M(\mathbf{r})$ , interfering

$$I(\mathbf{r}) = |E_R(\mathbf{r}) + E_M(\mathbf{r})|^2 \quad (\text{A.1})$$

to produce the measurable intensity  $I(\mathbf{r})$ . Our goal is to recover the field pattern  $E_M(\mathbf{r})$ , up to a relative phase. To that end, we will allow ourselves the ability to apply a global phase modulation,  $\Delta\theta$ , to  $E_M(\mathbf{r})$ : of the form  $E_M(\mathbf{r})e^{i\Delta\theta}$ . With this our measured intensity pattern can be written as

$$I(\mathbf{r}, \Delta\theta) = |E_R(\mathbf{r}) + E_M(\mathbf{r})e^{i\Delta\theta}|^2 \quad (\text{A.2})$$

$$= |E_R(\mathbf{r})|^2 + |E_M(\mathbf{r})|^2 + 2\text{Re}[E_R^*(\mathbf{r})E_M(\mathbf{r})e^{i\Delta\theta}]. \quad (\text{A.3})$$

From this expression one can show that

$$I(\mathbf{r}, 0) - I(\mathbf{r}, \pi) = 4\text{Re}[E_R^*(\mathbf{r})E_M(\mathbf{r})] \quad (\text{A.4})$$

and

$$I(\mathbf{r}, \pi/2) - I(\mathbf{r}, 3\pi/2) = -4\text{Im}[E_R^*(\mathbf{r})E_M(\mathbf{r})]. \quad (\text{A.5})$$

Therefore, with four phase modulation measurements we can obtain

$$E_R^*(\mathbf{r})E_M(\mathbf{r}) = \frac{I(\mathbf{r}, 0) - I(\mathbf{r}, \pi)}{4} + i\frac{I(\mathbf{r}, 3\pi/2) - I(\mathbf{r}, \pi/2)}{4}. \quad (\text{A.6})$$

If we have the ability to toggle the reference field  $E_R(\mathbf{r})$  off, then we can directly measure  $|E_M(\mathbf{r})|^2$ . Therefore, with four phase measurements and one amplitude measurement we can remove the amplitude of the reference field from the product in Eq. A.6 to obtain

$$E_M(\mathbf{r})e^{-i\phi(\mathbf{r})} = |E_M(\mathbf{r})| \exp \left( i \text{Arg} \left[ \frac{I(\mathbf{r}, 0) - I(\mathbf{r}, \pi)}{4} + i \frac{I(\mathbf{r}, 3\pi/2) - I(\mathbf{r}, \pi/2)}{4} \right] \right), \quad (\text{A.7})$$

where  $\phi(\mathbf{r})$  is the phase pattern of the reference.

### A.1.2 Building A Transmission Matrix

From the four-phase plus one-amplitude measurement, our next goal is to construct a transmission matrix (or interchangeably a field-reconstruction matrix). To this end, consider the case of an experimental system with a spatial light modulator, with  $N$  macro-pixels, and a CCD camera, with  $M$  pixels, juxtaposed about a linear-scattering medium. The field-mapping relationship from the SLM macro-pixels to the CCD pixels can be described by the following  $M \times N$  complex-valued matrix:

$$\mathbf{T} \equiv \begin{pmatrix} t_{1,1} & t_{1,2} & \cdots & t_{1,N} \\ t_{2,1} & t_{2,2} & \cdots & t_{2,N} \\ \vdots & \vdots & \ddots & \vdots \\ t_{M,1} & t_{M,2} & \cdots & t_{M,N} \end{pmatrix}. \quad (\text{A.8})$$

With this representation, displaying a phase-modulation pattern on the SLM is equivalent to multiplying the transmission matrix from the right by a  $N$ -length column,  $e^{i\vec{\theta}_N}$ , with the

resulting field incident on the CCD taking the form of a  $M$ -length column,  $\vec{E}_M$ , i.e.

$$\vec{E}_M = \mathbf{T}e^{i\vec{\theta}_N} \Rightarrow \begin{pmatrix} E_1 \\ E_2 \\ \vdots \\ E_M \end{pmatrix} = \begin{pmatrix} t_{1,1} & t_{1,2} & \cdots & t_{1,N} \\ t_{2,1} & t_{2,2} & \cdots & t_{2,N} \\ \vdots & \vdots & \ddots & \vdots \\ t_{M,1} & t_{M,2} & \cdots & t_{M,N} \end{pmatrix} \begin{pmatrix} e^{i\theta_1} \\ e^{i\theta_2} \\ \vdots \\ e^{i\theta_N} \end{pmatrix}. \quad (\text{A.9})$$

Experimentally, the goal is to determine the elements of the transmission matrix up to a global-phase term along each row  $m$ . The most *conceptually* simple way to accomplish this is to use a planewave reference beam –created by a beamsplitter in the laser path before the SLM– and sequentially perform a four-phase plus one-amplitude measurement for each of the SLM macro-pixels. In order to *only* display a single macro-pixel on the SLM, one simply needs to display a diffraction grating everywhere outside the specific macro-pixel: with a period smaller than the macro-pixel size. Furthermore, because the reference beam is the same for each macro-pixel, the relative phase term in Eq. A.7 will be the same for each measurement. Unfortunately, the conceptually simple method of measuring a transmission matrix in the macro-pixel basis is ill-advised experimentally: due to signal-to-noise considerations, as well as the reality of stray light in experiments. The simplest workaround is to use a different measurement basis on the SLM. To understand how this works, note that the field measurement of a single macro-pixel on the SLM is equivalent to multiplying our representation of the transmission matrix by a column of the identity matrix:  $\mathbf{I}$ . As such, physically measuring the transmission matrix in the macro-pixel basis is mathematically equivalent to multiplying the transmission matrix by the identity matrix  $\mathbf{T} = \mathbf{T}\mathbf{I}$ . Because any orthonormal basis described by the matrix  $\mathbf{U}$  is simply related to the identity matrix,  $\mathbf{U}\mathbf{U}^{-1} = \mathbf{I}$ , the mathematical relation for measuring the transmission matrix can be represented as  $\mathbf{T} = \mathbf{T}\mathbf{U}\mathbf{U}^{-1}$ . In this expression, the matrix product  $\mathbf{T}\mathbf{U} \equiv \mathbf{T}_{\mathbf{U}}$  physically represents measuring the transmission matrix in the  $\mathbf{U}$  basis. Therefore,

the simple expression

$$\mathbf{T} = \mathbf{T}_U \mathbf{U}^{-1} \quad (\text{A.10})$$

can be used to transform any transmission matrix measured using the vectors of the  $\mathbf{U}$  basis into the macro-pixel representation of the transmission matrix. Conventionally the Hadamard basis is used to measure the transmission matrix [72]. Where the single pixel basis can be defined by taking the columns of the identity matrix, the Hadamard basis can be defined by taking the columns of a Hadamard matrix. A square Hadamard matrix of dimension  $2^k$  can be recursively defined by  $\mathbf{H}_1 = 1$ ,

$$\mathbf{H}_2 = \begin{pmatrix} 1 & 1 \\ 1 & -1 \end{pmatrix}, \quad (\text{A.11})$$

and

$$\mathbf{H}_{2^k} = \begin{pmatrix} \mathbf{H}_{2^{k-1}} & \mathbf{H}_{2^{k-1}} \\ \mathbf{H}_{2^{k-1}} & -\mathbf{H}_{2^{k-1}} \end{pmatrix}. \quad (\text{A.12})$$

The Hadamard basis is advantageous because it is orthogonal, yet the elements in the basis-vectors are either 1 or -1. Because all of the macro-pixels on the SLM are used simultaneously when measuring the transmission matrix with the Hadamard basis, the measured signal strength is  $N$  times higher than when measuring the transmission matrix in the single macro-pixel basis. As shown in Eq. A.10, once the transmission matrix has been measured in the Hadamard basis, it can be converted into the spatial representation by a basis transformation: or in fact, any other basis representation desired. The one limitation of working with the Hadamard basis is the dimensional restriction to  $2^k$ . If this

is undesirable, one can alternatively use the columns of the following  $N \times N$  matrix:

$$\tilde{\mathbf{H}}_N \equiv \begin{pmatrix} 1 & -1 & -1 & \cdots & -1 \\ 1 & 1 & -1 & \cdots & -1 \\ 1 & 1 & 1 & \cdots & -1 \\ \vdots & \vdots & \vdots & \ddots & \vdots \\ 1 & 1 & 1 & \cdots & 1 \end{pmatrix}. \quad (\text{A.13})$$

In some experiments a planewave reference beam is impractical. When this is the case, a self-reference technique can be used [112]. In this measurement, half of the SLM macro-pixels are fixed and used as a reference field; while the transmission matrix elements associated with the other half of the SLM macro-pixels are measured. Upon completion, the function of each region is switched and the measurement is repeated with the reversed rolls. This results in two matrices with *different* relative phase values at each camera pixel: according to Eq. A.7. A third interference measurement between the reference patterns can be used to correct this relative phase difference, and the two matrices can be stitched together to form a single matrix. Note, that in the experimental setups shown in Chapters 2-5 it is advantageous to further modify the relative phase on each CCD pixel when using a self-reference technique. Because of the approximate Fourier transform relationship between the SLM and CCD; each SLM macro-pixel is approximately a plane wave in the CCD plane. As such, multiplying all of the matrix columns by the conjugated phase of one of the matrix columns (associated with one of the central macro-pixels on the SLM) results in a planewave relative-phase pattern in this setup.

Until this point, the matrix measurement protocols described are close to standard. We have developed the following modification to the standard techniques in order to reduce error in the measured matrix. Specifically, we average over independent matrix measurements of the same system. Empirically, we have found that superimposing the same

random-phase pattern onto the complete set of basis vectors used in a single transmission matrix measurement, i.e. for the basis shown in Eq. A.13

$$\tilde{\mathbf{H}}_N \Rightarrow \begin{pmatrix} e^{i\theta_1} & -e^{i\theta_1} & -e^{i\theta_1} & \dots & -e^{i\theta_1} \\ e^{i\theta_2} & e^{i\theta_2} & -e^{i\theta_2} & \dots & -e^{i\theta_2} \\ e^{i\theta_3} & e^{i\theta_3} & e^{i\theta_3} & \dots & -e^{i\theta_3} \\ \vdots & \vdots & \vdots & \ddots & \vdots \\ e^{i\theta_N} & e^{i\theta_N} & e^{i\theta_N} & \dots & e^{i\theta_N} \end{pmatrix}, \quad (\text{A.14})$$

and varying the superimposed phase pattern between matrix measurements is more effective than repeating the same measurement multiple times. This is because the measurement error –caused by low signal– is uncorrelated between the different transmission matrix measurements. While this lengthens the measurement time, experimental artifacts such as drift can be accounted and corrected for by periodically measuring test/reference patterns to track changes in the system.

## A.2 Transmission Matrix Validation

To check the error of our transmission matrix measurements, we compare a customized speckle pattern predicted by the measured transmission matrix, in Fig. A.1(a), with the corresponding experimentally measured speckle pattern, in Fig. A.1(b). The difference between the two intensity patterns is 9.7% without any data processing or manipulation; which is typical for transmission matrices measured using our technique. Because the customized properties of the speckle patterns are statistical –both the intensity PDF and the spatial intensity correlation function– they are robust to minor differences between the measured and predicted speckle patterns. For example, in (c) we compare the intensity PDF of predicted speckle patterns, green dashed line, with the intensity PDF of the cor-

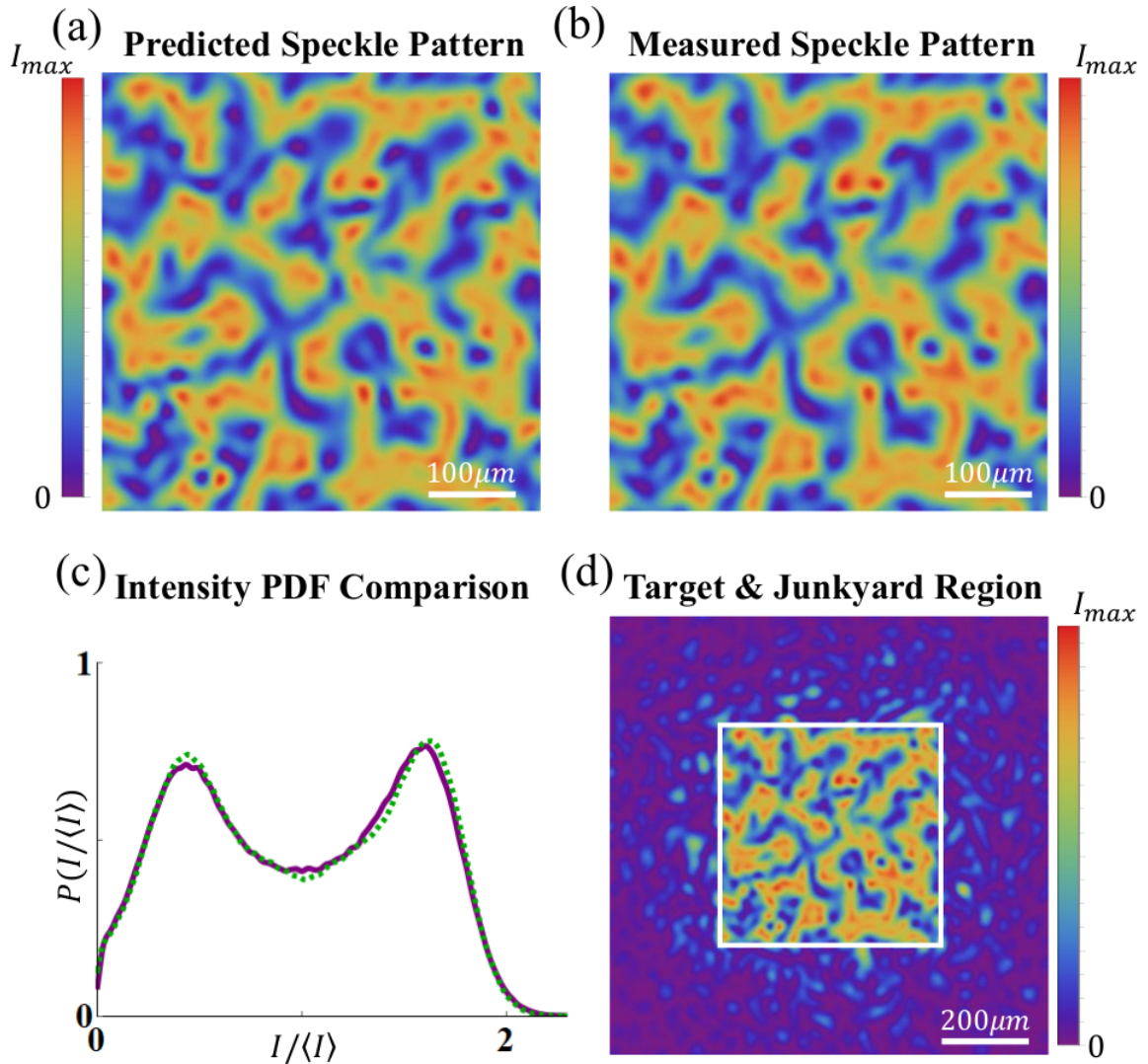


Figure A.1: **Transmission matrix validation.** An example customized speckle pattern predicted by our transmission matrix (a) is juxtaposed with the corresponding experimentally measured speckle pattern (b). The difference between the two intensity patterns is 9.7%. In (c) we compare the intensity PDF of predicted speckle patterns, green dashed line, with the intensity PDF of the corresponding measured speckle patterns, purple solid line, for an ensemble of 100 speckles patterns like those shown in (a) and (b). The difference between the two intensity PDFs is 3.7%. In (d) we present a measured image of the speckles in both the target region and the junkyard region. The white square denotes the boundary of the target region.

responding measured speckle patterns, purple solid line, for an ensemble of 100 speckles patterns like those shown in (a) and (b). The difference between the two intensity PDFs is just 3.7%: less than the difference between the two speckle patterns. This is because the averaging inherent to calculating the respective intensity PDFs suppresses, rather than compounds, the effects of fluctuations/deviations between the two patterns.

The speckle pattern shown in Fig. A.1(b) is located within the target region. However, the speckles in the region outside of it –which we call the junkyard– have distinct statistical properties relative to those in the target region. Fig. A.1(d) is a measured speckle pattern including both the target region and the junkyard. The image encompasses the complete Fourier plane of the SLM. While the central target region (denoted by the white square) adheres to the desired intensity PDF and spatial intensity correlations, the speckles in the junkyard region do not. Though the precise statistical properties of the speckles in the junkyard region depend on the details of the target region’s speckles, they approximately adhere to Rayleigh statistics and are devoid of non-local correlations.

### **A.3 Effect Of Transmission Matrix Error On Customized PDFs**

In this section, we perform a theoretical assessment on how experimental error in the transmission matrix measurement effects the intensity PDFs of the customized speckle patterns (using data from Chapter 2). Due to measurement noise and temporal decorrelation of the experimental setup (ambient temperature drift and/or laser instability), the measured transmission matrix,  $\mathbf{T}_m$ , differs from the actual transmission matrix,  $\mathbf{T}_a$ , that produces the measured speckle pattern. Their difference is:

$$\Delta\mathbf{T} = \mathbf{T}_m - \mathbf{T}_a. \tag{A.15}$$

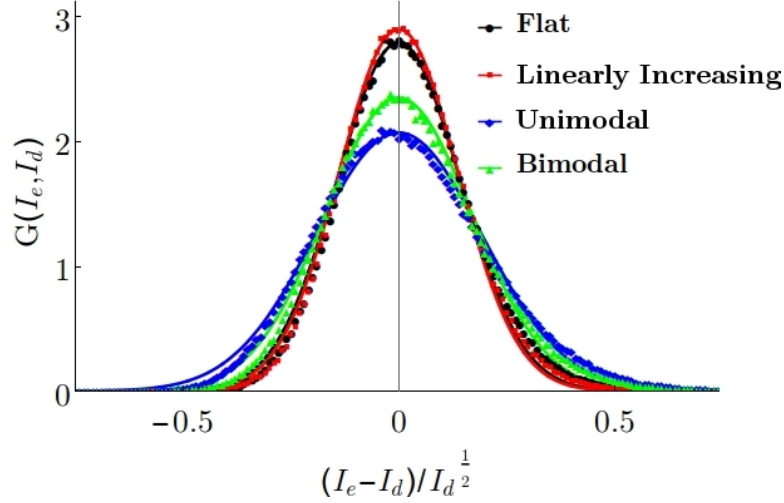


Figure A.2: **Measured speckle pattern error in Chapter 2.** The statistical distribution of  $(I_e - I_d)/\sqrt{I_d}$ , extracted from the experimental data in Chapter 2 (symbols), is fit well by the Gaussian distribution  $G(I_e, I_d)$  in Eq. A.19 (lines). The fitting parameter is given by  $a = 0.020$  for the uniform PDF (black),  $a = 0.019$  for the linearly increasing PDF (red),  $a = 0.037$  for the PDF with a single peak (blue) and  $a = 0.029$  for the bimodal PDF (green).

$\mathbf{T}_m$  is used in the numerical optimization to obtain the SLM field  $\vec{\Psi}_s$  to create the target speckle intensity-pattern

$$\vec{I}_d = |\mathbf{T}_m \vec{\Psi}_s|^2. \quad (\text{A.16})$$

The measured speckle intensity-pattern is

$$\vec{I}_e = |\mathbf{T}_a \vec{\Psi}_s|^2 \quad (\text{A.17})$$

The difference between the two intensities, to the first order in  $\Delta\mathbf{T}$ , is

$$\vec{I}_e - \vec{I}_d = 2\Re[(\mathbf{T}_m \vec{\Psi}_s)(\Delta\mathbf{T} \vec{\Psi}_s)^*] = 2\Re[\sqrt{\vec{I}_d} e^{i\vec{\theta}_d} (\Delta\mathbf{T} \vec{\Psi}_s)^*], \quad (\text{A.18})$$

where  $\mathbf{T}_m \vec{\Psi}_s = \sqrt{\vec{I}_d} e^{i\vec{\theta}_d}$ . Assuming the scalar elements of  $\Delta\mathbf{T}$  are uncorrelated with those in  $\vec{\Psi}_s$ , then the scalar quantities of  $(\vec{I}_e - \vec{I}_d)/\sqrt{\vec{I}_d} = 2\Re[(\Delta\mathbf{T} \vec{\Psi}_s)^*]$  will obey

Gaussian statistics, as verified experimentally in Fig. A.2. The statistical distribution for  $(I_e - I_d)/\sqrt{I_d}$  is:

$$G(I_e, I_d) = A \exp \left[ \frac{-(I_e - I_d)^2}{2aI_d} \right] \quad (\text{A.19})$$

where  $a$  is a coefficient that quantifies the experimental error, and  $A$  is the normalization constant given by  $\int_0^\infty G(I_e, I_d) dI_d = 1$ . Therefore, the normalized expression for  $G(I_e, I_d)$  is

$$G(I_e, I_d) = \frac{\exp \left[ \frac{-(I_e)^2 - (I_d)^2}{2aI_d} \right]}{2I_e K_1[I_e/a]} \quad (\text{A.20})$$

where  $K_1$  is the Bessel function of the first kind.

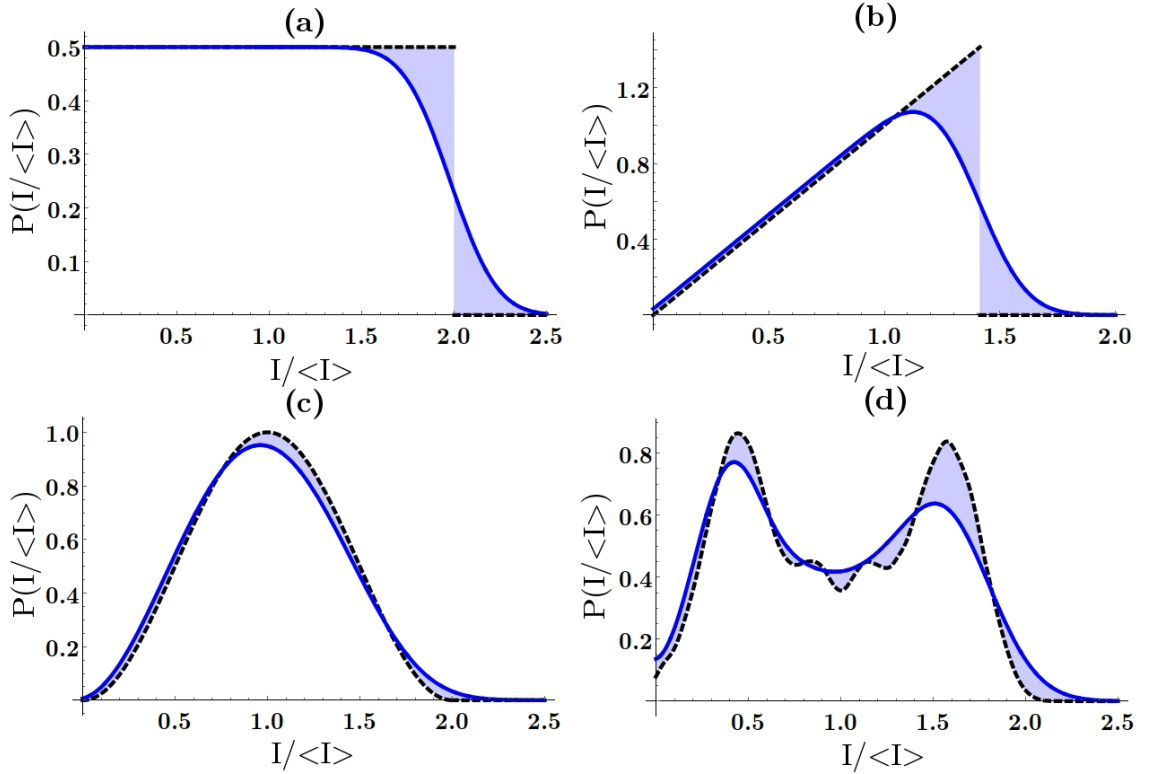


Figure A.3: **Predicted effect of error on PDFs.** The deviation (shaded area) of the intensity PDF (blue solid line) from the target one (black dashed line) is reproduced numerically by Eq. A.21. (a-d) for the four PDFs shown in Fig. 2.5.

The probability density function of the measured speckled intensity  $\bar{F}(I_e)$  is equal to the target distribution  $F(I_d)$  convolved with the error function  $G(I_e, I_d)$  in Eq.(A.20):

$$\bar{F}(I_e) = \int_0^{\infty} F(I_d)G(I_e, I_d)dI_d \quad (\text{A.21})$$

The convolution corresponds to an averaging of  $F(I_d)$  over adjacent values of  $I_d$ . Consequently, the measured PDF  $\bar{F}(I_e)$  displays more discrepancy in the region where  $F(I_d)$  changes rapidly. Since  $G(I_e, I_d)$  is wider at larger  $I_e$ , the averaging effect is stronger, leading to a larger error at higher intensity. These effects are confirmed in Fig. A.3, where we plot Eq.(A.21) for the four PDFs shown in Fig. 2.5 of Chapter 2. For the uniform and linearly increasing PDFs in (a) and (b), the abrupt drop in  $F(I_d)$  at the upper boundary of the intensity range is smoothed out in  $\bar{F}(I_e)$ . In (c), the single-peaked PDF has relatively small error, although the deviation from the target PDF is clearly larger at higher intensity. For the bimodal PDF in (d), the peak at larger intensity is suppressed more due to the stronger averaging effect, and the fine features around the dip in between the two peaks are removed by averaging.

The interested reader may have noticed, there is a significant increase in the fidelity of the customized PDFs in Chapter 4 compared to Chapter 2. This is primarily due to technical improvements made in the transmission matrix measurement process between the two works. In fact, in Chapter 4 the error described in this section is practically non-existent. This can visually be seen in the symmetry of the peaks in the bimodal distribution presented in Fig. A.1(c) compared to the asymmetry in Fig. A.3(d).

# Appendix B

## Random Light In Disordered Media

### B.1 On-Chip Nano Fabrication Process

The on-chip disordered waveguide structures studied in this dissertation were fabricated using resources in the Becton Center Cleanroom at Yale University and the Yale Institute for Nanoscience and Quantum Engineering (YINQE). In this appendix section, the fabrication process is delineated. In short, we use a combination of positive-resist electron-beam lithography and reactive ion etching to create our structures in the top silicon-layer of a silicon-on-insulator chip.

#### Wafer Details

Our fabrication process starts with a 6 inch-in-diameter silicon-on-insulator wafer produced by Soitec (G6P-092-01). The wafer structure consists of a  $220 \pm 20$  nm thick silicon-crystal top-layer, placed on top of an insulating  $3 \mu\text{m}$  thick layer of silicon-dioxide, which resides on a  $\approx 0.7$  mm thick silicon carrier wafer.

## Wafer Partitioning

Before fabricating our on-chip structures, we need to break the 6-inch SOI wafer into smaller rectangular chips: we typically use 3 cm × 2.5 cm. Because surface scratches on the silicon layer result in light loss –which can be detrimental to our structures when uncontrolled– we use the following procedure to protect the top layer of the wafer when breaking it apart and storing the chips.

1. We apply a protective layer of PMMA (495K A11) to the wafer, and spin it at 2000 RPM for 3 minutes.
2. After spinning, the wafer is placed onto a 180 °C hotplate for 60 seconds.
3. After cooling to room temperature, the wafer can be safely cleaved along the crystal axes using a *LatticeAx* device and partitioned into multiple rectangular chips.

## Protective Resist Removal

Around one day before fabricating structures on the chip, the PMMA resist is removed using the following cleaning-procedure. Note that in all of the following steps the top-layer of the wafer is facing upright and carbon-fiber tipped tweezers are used to handle the chip to avoid damaging the surface.

1. We immerse the chip in an acetone solution in a beaker (with a 99.5%+ acetone purity), and place the beaker into an ultrasonic bath for 2 minutes.
2. We remove the chip from the acetone solution, and directly submerge the chip into a beaker with a *Super Methanol<sup>TM</sup>* solution (with a 99.99%+ methanol purity), and place the beaker into an ultrasonic bath for 2 minutes.

3. We remove the chip from the methanol solution, and directly submerge it into a beaker with a *Super Isopropanol<sup>TM</sup>* solution (with a 99.99%+ isopropanol purity), and place the beaker into an ultrasonic bath for 2 minutes.
4. We remove the chip from the isopropanol solution and submerge it in a beaker filled with deionized water, and place the beaker in an ultrasonic tank for 2 minutes.
5. We remove the chip from the beaker and place it under a steady stream of deionized water, with the top surface facing the source. The chip is removed and reinserted until no water droplets adhere to the top surface: indicating the removal of nearly all particles from the surface.

After removing the chip from the deionized water stream, and drying it with filtered nitrogen gas, we inspect the top surface of the chip (with an optical microscope) for any remaining particles or remnants of the resist. Generally, particles appear as black spots while resist remnants appear as colorful non-uniformities on the surface of the chip. If anything is found, the above steps are repeated using new chemical solutions.

## **Chip Thickness Measurement**

At this point, it is important to ascertain the precise thickness of the top silicon layer of the chip in the area we intend to etch our structures: because the thickness can alter the optical performance of the structures. While the chips cleaved from the center of the 6-inch SOI wafer tend to have a uniformly thick top-layer, this is not always the case for chips cleaved from the edges: due to the wafer's manufacturing process. We measure and record the surface-layer thickness at different points across the chip using a *Filmetrics F54-UV Reflectometer*. If the top layer of the chip is uniformly 220-nm-thick, across the region of interest, it is suitable for fabrication.

## **Electron-Beam Resist Application**

Once the chip is deemed suitable for fabrication, the next step is applying the electron-beam resist onto the chip via the following steps. We use the positive resist *CSAR 62* manufactured by *Allresist*, however, this can be interchanged with *ZEP* manufactured by *Zeon Chemicals*.

1. We mount the chip onto a vacuum sealed spinner and coat the top with *CSAR 62*: administered via a syringe with a 0.22  $\mu\text{m}$  filter.
2. The chip is spun at 2000 RPM for 2 min, resulting in the formation of a 600-nm-thick layer of resist on top of the chip.
3. After spinning, we directly place the wafer onto a 180 °C hotplate for 3 minutes, to remove any residual solvent.

Once the electron-beam resist is applied to the chip, we store the chip in a desiccating container until the electron-beam exposure.

## **Electron-Beam Exposure**

We use a *Raith EBPG 5000+* electron-beam lithography system to expose the resist layer on top of the chip. Because we work with a positive resist, the electron-beam is used to directly write the structures we wish to etch away (the holes, photonic crystals and trenches). We write our structures using an electron-beam with a 20nm spot-size, providing a dose of 600  $\mu\text{C}/\text{cm}^2$ , and a 5 nm writing-grid size.

## **Resist Development**

After the electron-beam exposure we develop the resist using the following procedure.

1. We pour a solution of xylenes (with a 98.5%+ purity), chilled to 4 °C, into a beaker also chilled to 4 °C.
2. While holding the chip from the corner with a pair of tweezers –away from exposed regions in the resist– we stir the sample around in the xylenes-solution for 1 minute and 15 seconds.
3. We immediately transfer the chip into a solution of *Super Isopropanol<sup>TM</sup>* (with a 99.99%+ isopropanol purity) –while still holding the corner with tweezers– and stirring for 1 minute 15 seconds.
4. The chip is dried with filtered nitrogen gas. Optionally, it can be placed onto a 130 °C hotplate for 2 minutes **after** drying completely.

Once the development process is complete, we store the chip in a desiccating container until the reactive ion etching.

## **Reactive Ion Etching**

After the waveguide structures are chemically developed into the resist, we transfer the patterns to the top layer of the chip using reactive ion etching (chlorine plasma) in an *Oxford Instruments Plasm Pro 100* system. Before etching the chip, the chamber is conditioned by performing a chlorine plasma process with the carrier wafer –without the chip inserted– which runs at least twice the anticipated length of the etching process. During this process we verify that the chlorine plasma exhibits a light blue color. Afterwards we run a chlorine plasma process with a small test silicon-on-insulator chip, for half the anticipated etching times. Using a *Filmetrics F54-UV Reflectometer* we measure the top-layer thickness of the test-chip, before and after the chlorine plasma process, to calibrate the silicon etching rate of the machine. We use the measured etch rate to determine the duration

of the chlorine plasma process for our main-chip. Our goal is to ensure that the 100 nm holes are etched completely through the top-silicon-layer of the chip without significantly degrading the sidewalls of the larger structures by over-etching.

## **Final Sample Cleave & Resist Removal**

Finally, we cleave the chip so that the edge is separated from the disordered structures by  $\approx 1.5$  cm of empty waveguiding structures. After cleaving, we remove the remaining resist from the chip using the following process. Note that we hold the chip from the corner with carbon fiber tipped tweezers, and gently stir it when in solution.

1. We immerse the chip into a 1-methyl-2-pyrrolidinone solution in a beaker (with 99.7%+ purity) for 2 minutes.
2. We immerse the chip into an acetone solution in a beaker (with a 99.5%+ acetone purity) for 2 minutes.
3. We remove the chip from the acetone solution, and directly submerge the chip into a beaker with a *Super Methanol<sup>TM</sup>* solution (with a 99.99%+ methanol purity) for 2 minutes.
4. We remove the chip from the methanol solution, and directly submerge it into a beaker with a *Super Isopropanol<sup>TM</sup>* solution (with a 99.99%+ isopropanol purity) for 2 minutes.
5. We remove the chip from the isopropanol solution, and place it under a steady stream of deionized water, with the top surface facing the source. The chip is removed and reinserted until no water droplets form outside the area of the fabricated structures.
6. The chip is dried with filtered nitrogen gas.

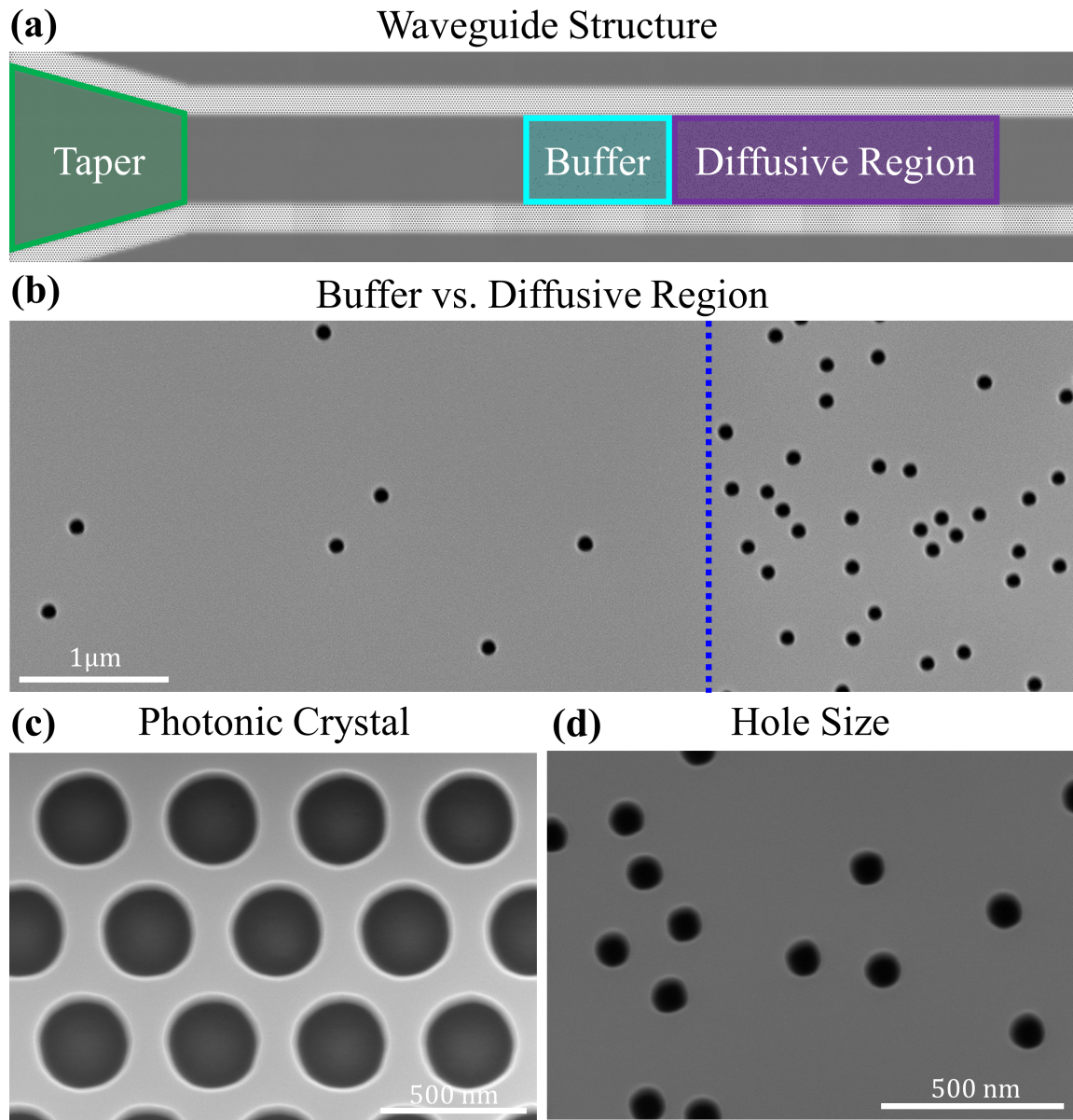


Figure B.1: **Scanning electron microscope (SEM) images of a 2D diffusive waveguide.** In (a) we show a composite SEM image which outlines the structures we etch into a silicon-on-insulator wafer when fabricating our structures. A SEM image of the interface between the buffer and diffusive regions is marked by the blue dashed line in (b). Close-up images of the photonic crystal sidewall and randomly-distributed holes are shown in (c) and (d).

## B.2 Disordered Waveguide Design

Figure B.1 shows a schematic of our two-dimensional (2D) disordered waveguide structures. The major components are the tapered waveguide, the buffer region, and the diffusive region. The air holes (diameter = 100 nm), which induce light scattering in the buffer and diffusive regions, are randomly distributed with a minimum (edge-to-edge) distance of 50 nm. The diffusive region has 5250 holes, which results in an air filling fraction in the Si of 5.5%. The number of air holes in the buffer region is 260, and the air filling fraction is 0.55%. The sidewalls of the waveguide consist of a trigonal lattice of air holes (radius = 155 nm, lattice constant = 440 nm). They provide a 2D complete bandgap for TE polarized light (used in the experiment) within the wavelength range of 1120 nm to 1580 nm [186].

The probe light is injected from the side/edge of the wafer into a ridge waveguide (width = 300  $\mu\text{m}$ , length = 15 mm). It then enters a tapered waveguide (tapering angle =  $15^\circ$ ). The tapered waveguide width decreases gradually from 300  $\mu\text{m}$  to 15  $\mu\text{m}$ . The tapering results in waveguide mode coupling and conversion [183]. To avoid light leakage, the tapered waveguide has photonic crystal sidewalls.

## B.3 Optical Setup

Fig. B.2 is a detailed schematic of the experimental setup used in Chapters 6 & 7. Continuous-wave (CW) output from a tunable laser (Keysight 81960A) –operating around 1554 nm– is linearly polarized and split into two beams. One beam illuminates the phase modulating surface of a phase-only SLM (Hamamatsu LCoS X10468), while the other is used as a reference beam. A one-dimensional (1D) phase-modulation pattern is displayed on the SLM, consisting of 128 macropixels. Each macropixel consists of  $4 \times 800$  regular pixels on the

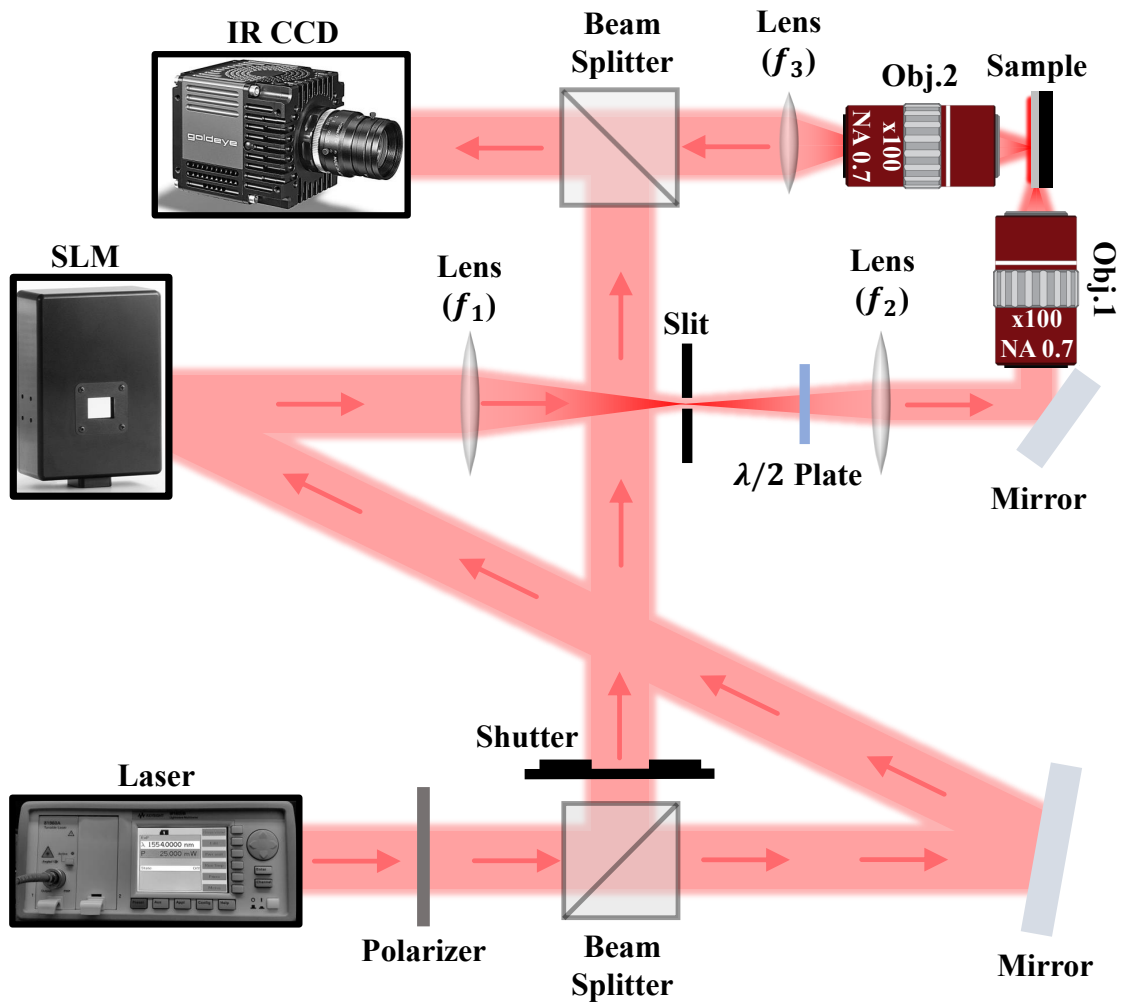


Figure B.2: **A depiction of our experimental setup.** Monochromatic light from our laser is linearly polarized and split into two beams. One beam illuminates the phase modulating surface of a spatial light modulator (SLM), while the other is used as a reference beam. The SLM is used to control the input wavefront in our diffusive waveguide structures. A beam splitter merges the light collected from the top of our sample with the reference beam on an IR CCD. The focal length of the three lenses used in this setup are:  $f_1 = 400$  mm,  $f_2 = 75$  mm, and  $f_3 = 100$  mm.

SLM. Using two lenses with focal lengths of  $f_1 = 400$  mm and  $f_2 = 75$  mm, we image the field on the SLM plane onto the back focal plane of a long-working-distance objective (**Obj. 1**) (Mitutoyo M Plan APO NIR HR100 $\times$ , Numerical Aperture = 0.7). To prevent the unmodulated light from entering the objective lens, we display a binary diffraction grating within each macropixel to shift the modulated light away from the unmodulated light in the focal plane of the  $f_1$  lens. Using a slit in the same focal plane, we block everything except the phase-modulated light in the first diffraction order. Before the  $f_2$  lens, we insert a half-wave ( $\lambda/2$ ) plate to flip the polarization of light so that it is TE polarized relative to the input waveguides of our sample. The side of our SOI wafer is placed at the front focal plane of **Obj. 1** and illuminated with the Fourier transform of the phase-modulation pattern displayed on the SLM. From the top of the wafer, a second long-working-distance objective (**Obj. 2**) (Mitutoyo M Plan APO NIR HR100 $\times$ ) collects light scattered out-of-plane from the on-chip structures. We use a third lens with a focal length of  $f_3 = 100$  mm together with **Obj. 2** to magnify the sample image by  $\times 50$ . With a second beam splitter, we combine the light collected from the sample and the reference beam. Their interference patterns are recorded with an IR CCD camera (Allied Vision Goldeye G-032 Cool). Note, that in Chapter 8 we modified the setup to only allow a single polarization component of the light collected by **Obj. 2** to reach the CCD: by inserting a polarizing beamsplitter.

## B.4 Fluctuations & Correlations of Transmission Eigenchannels

In the following section, supplementary information pertaining the analysis in Chapter 6 is provided.

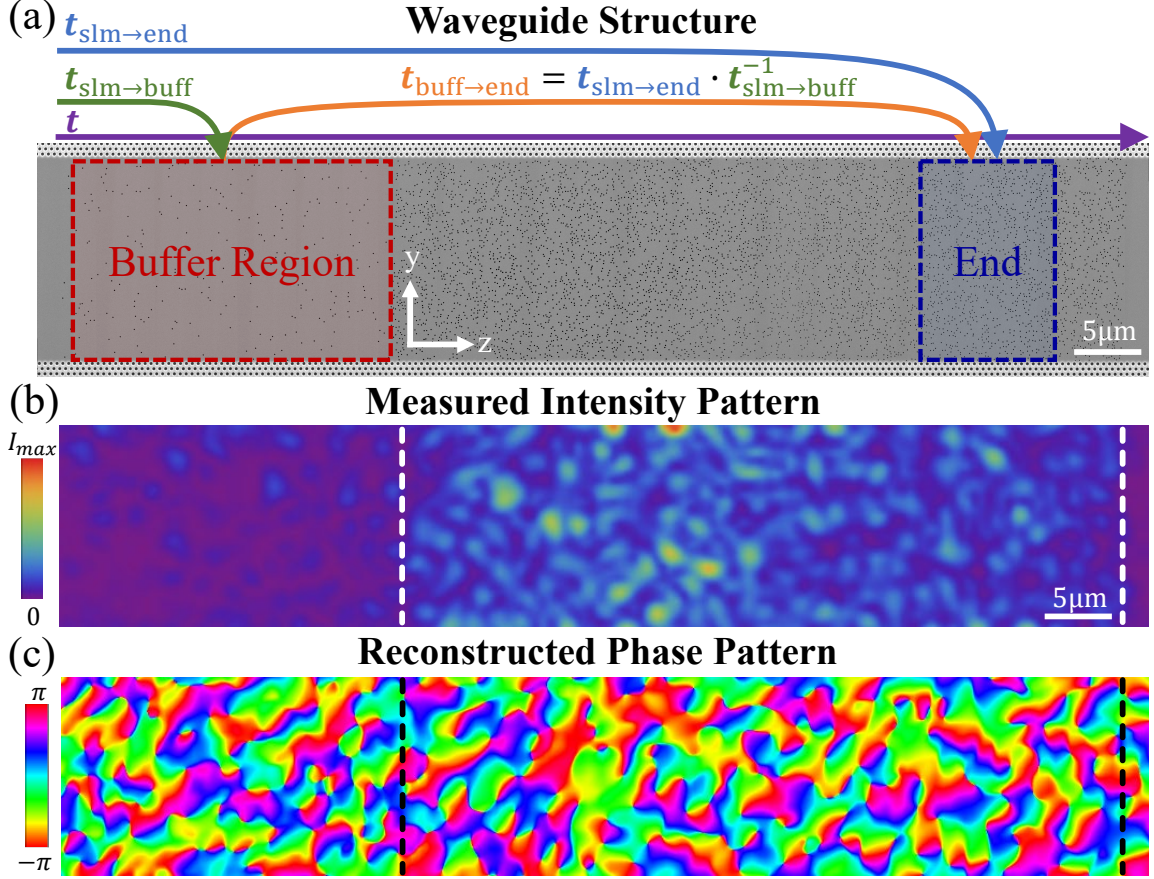


Figure B.3: **Waveguide structure and full-field measurement.** A composite SEM image of a diffusive waveguide is shown in (a). In (b) the 2D intensity pattern of a measured high-transmission eigenchannel is shown. Using our interferometric setup, we can reconstruct the phase of the light field inside the diffusive waveguide in (c). In (b-c) the edges of the diffusive region are marked by the vertical dashed lines.

#### B.4.1 Transmission Matrix Measurement

With the interferometric setup described in Section B.3, we can measure the field distribution of light scattered out-of-plane from within our diffusive waveguides: for any phase-modulation pattern displayed on the SLM. To do this, we first measure the 2D intensity distribution of the scattered light by blocking the reference beam with a shutter (see Fig.B.3(b) for an example). Then using the reference beam in our setup, we retrieve the phase profile of the scattered light with a four-phase measurement (as described in Sec-

tion A.1 of the appendix). Fig. B.3(c) shows the spatial distribution of the recovered phase pattern of the light field across a diffusive waveguide.

By measuring the complex field throughout the waveguide for an orthogonal set of phase patterns displayed on the SLM, we can construct two matrices  $t_{\text{slm} \rightarrow \text{buff}}$  and  $t_{\text{slm} \rightarrow \text{end}}$ , which map the field from the SLM surface to the buffer and to the far end of the disordered waveguide, respectively. To construct the matrix relating the field in the buffer region to the field near the end of the diffusive waveguide,  $t_{\text{buff} \rightarrow \text{end}}$ , we define the field-mapping matrix between the two regions  $t_{\text{buff} \rightarrow \text{end}} \equiv t_{\text{slm} \rightarrow \text{end}} t_{\text{slm} \rightarrow \text{buff}}^{-1}$ . To calculate the inverse of  $t_{\text{slm} \rightarrow \text{buff}}$ , we use Moore-Penrose matrix inversion. In this operation we only take the inverse of the 55 highest singular values of  $t_{\text{slm} \rightarrow \text{buff}}$ , and set the inverse of the remaining singular values to zero. This restriction is imposed because our diffusive waveguide only has 55 transmission eigenchannels.

## B.4.2 Transmission Eigenchannel Profile Measurement

In total, we measure the transmission eigenchannel intensity profiles of 13 independent realizations. We obtain these measurements from two samples with different random hole configurations. To generate independent system realizations from the same random hole configuration, we vary the wavelength of the input light beyond the spectral correlation width of the diffusive region: 0.4 nm. Over a wavelength span of 3 nm, we vary the input wavelength of our laser in increments of 0.5 nm. We choose the specific wavelength range of the measurement –for each random hole configuration– such that the effective dissipation in the diffusive region is minimal and homogeneous over the wavelength range. While our waveguide structure has a width of 15  $\mu\text{m}$ , we only use the central 10  $\mu\text{m}$  region of the waveguide’s out-of-plane-scattered light when performing our measurements to avoid artifacts from light scattered out-of-plane from the photonic crystal boundaries.

### B.4.3 Transmission Eigenchannel Numerical Simulations

In our numerical simulations, we use the Kwant simulation package [188]. We simulate a two-dimensional (2D) rectangular waveguide geometry, which is defined using a tight-binding model for scalar waves on a square grid. At the waveguide boundaries, which are reflective, the grid is terminated. The leads are attached to the open ends of the waveguide, allowing for computation of the complete scattering  $S$  matrix of the system and the wave field throughout the bulk of the system: under an excitation by an arbitrary combination of field amplitudes for the propagating modes. The width  $W$  of the simulated system is selected so that the number of waveguide modes  $N$  matches the number found in the experiment. Once  $W$  is chosen, the length of the disordered waveguide is determined by the ratio  $L/W$  of the waveguides used in the experiment. Due to the low filling fraction of the air holes in the experimental waveguides, both in the buffer region and in the main disordered region, we assume that the number of propagating modes is equal to  $N$ .

Scattering is introduced by a randomly (box distribution) fluctuating real-valued on-site ‘energy’ in the tight-binding model, see Refs. [183, 246]. The addition of a positive imaginary constant to the same term simulates the effect of absorption. In our previous works, we confirmed that the process of vertical leakage due to the holes in our disordered waveguides can be modeled via absorption in a 2D system [183, 186, 205]. The actual material absorption in our experimental system is negligible. By a proper choice of these parameters, we can match the experimental values for the transport mean free path  $\ell_t$  and the diffusive dissipation length  $\xi_a$ .

To model the weakly scattering ‘buffer’ region, we reduce the scattering (the amplitude of the on-site fluctuation) so that transport mean free path is reduced by a factor of 10. The latter corresponds to a 10 times reduction in the areal density of the air holes in the buffer region. Furthermore, because the out-of-plane scattering loss is reduced 10 times, the

diffusive dissipation length is also reduced by the same factor.

The buffer region is incorporated into the experimental waveguides to measure  $t_{\text{buff} \rightarrow \text{end}}$  of the diffusive waveguide, which is not a direct measurement of the field transmission matrix  $t$ . We numerically simulate the eigenchannels of both matrices to confirm their depth profiles are equivalent. The matrix  $t$  is obtained from the incident and transmitted fields in the left and right leads without the buffer. To compute  $t_{\text{buff} \rightarrow \text{end}}$ , we compute the auxiliary matrices  $t_{\text{in} \rightarrow \text{buff}}$  and  $t_{\text{in} \rightarrow \text{end}}$ . The former matrix relates the incident fields in the left lead to the fields at  $2 \times N$  randomly selected points within a  $10 \mu\text{m} \times 20 \mu\text{m}$  region centered in the buffer region (of an area  $15 \mu\text{m} \times 25 \mu\text{m}$ ). The chosen points are at least  $2.5 \mu\text{m}$  separate from each other or any boundary/interface. The second auxiliary matrix  $t_{\text{in} \rightarrow \text{end}}$  relates the impinging fields in the left lead to the fields at  $2 \times N$  randomly selected points within a  $10 \mu\text{m} \times 10 \mu\text{m}$  region at the end of the diffusive waveguide. Again all points are at least  $2.5 \mu\text{m}$  (which is on the order of  $\ell_t$ ) spaced. In the last step, we compute  $t_{\text{buff} \rightarrow \text{end}} = t_{\text{in} \rightarrow \text{end}} t_{\text{in} \rightarrow \text{buff}}^{-1}$ , where  $t_{\text{in} \rightarrow \text{buff}}^{-1}$  is calculated with the Moore-Penrose pseudo-inverse.

To calculate the spatial structure of the transmission eigenchannels, we perform a singular value decomposition on the  $t$  matrix, and use the right singular vectors as input fields in the left lead to excite individual eigenchannels. For the matrix  $t_{\text{buff} \rightarrow \text{end}}$ , its right singular vectors are transformed to the incident fields in the left lead by multiplying  $t_{\text{in} \rightarrow \text{buff}}^{-1}$ . To further mimic the phase-only modulation of the SLM in the experiment, we only keep the phases of the incident fields, and set the field magnitudes equal. We calculate all eigenchannels for  $t$  and  $t_{\text{buff} \rightarrow \text{end}}$  for an ensemble of 1000 disorder configurations of the waveguides. The numerical results are presented in Figs. 6.3, 6.4, & 6.5 in Chapter 6.

To compare the variance  $\tilde{C}_\alpha$  and covariance  $\tilde{C}_{\alpha\beta}$  numerically calculated from  $t_{\text{buff} \rightarrow \text{end}}$  to the experimentally-measured ones, we need to account for some experimental limitations and imperfections. On one hand, the finite spatial resolution of our detection op-

tics effectively enlarges the speckle grain size of the field measured inside the diffusive waveguide. This reduction in the number of speckle grains increases the fluctuations of the cross-section-averaged intensity. On the other hand, the combined effects of sample drift during measurements and the presence of two linear polarizations in the light scattered out-of-plane from our sample; decrease the fluctuations of the cross-section-averaged intensity. For random incident wavefronts, the spatially-averaged intensity variance of our experimental measurements is  $\text{var}[I(z)] = 0.59$ , compared to  $\text{var}[I(z)] = 0.64$  from the numerical simulations of  $t_{\text{buff} \rightarrow \text{end}}$ . For all eigenchannels, we re-scale the numerical  $\text{var}[I_\alpha(z)]$  and  $\tilde{C}_{\alpha\beta}$  by the multiplicative factor  $0.59/0.64$ , in order to compare them to the experimental values. While we applied the re-scaling factor to the fluctuations and correlations calculated from numerical simulations of  $t_{\text{buff} \rightarrow \text{end}}$ , we did not apply it to the results from simulations of  $t$ .

### B.4.4 Identification Of Experimental Transmission Eigenchannels

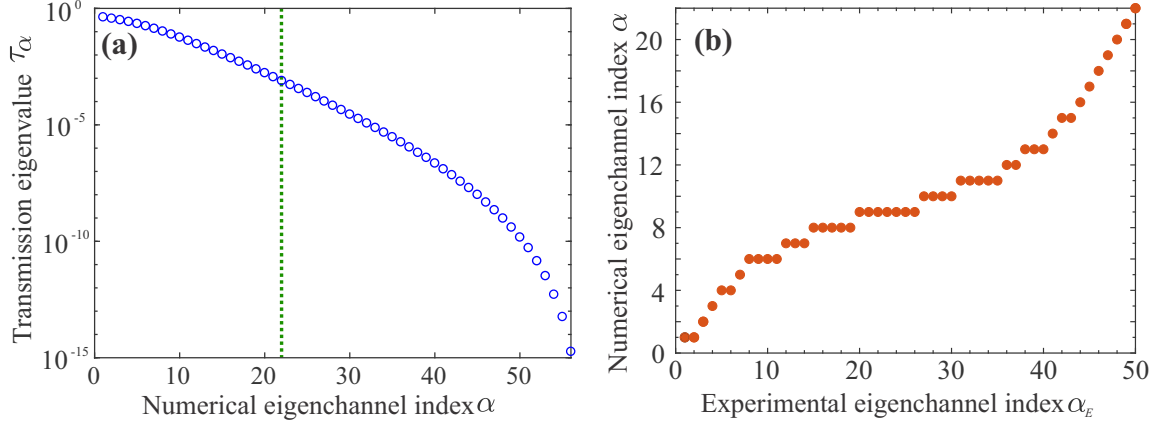


Figure B.4: **Transmission eigenvalue mapping.** Calculated transmission eigenvalues, as a function of eigenchannel index  $\alpha$ , are shown in (a). In (b), we show the mapping between the experimentally-measured eigenchannel profiles with index  $\alpha_E$  and the first 22 (in the order of decreasing transmittance) eigenchannels with index  $\alpha$  found in the numerical simulations based on the  $t_{\text{buff} \rightarrow \text{end}}$  matrix.

In this section, we analyze the normalized eigenchannel profiles measured in the experiment  $\langle I_{\alpha_E}(z) \rangle$  and the numerical simulations  $\langle I_\alpha(z) \rangle$ . For each experimental eigenchannel with an index of  $\alpha_E \in [1 \dots 55]$ , we identify the corresponding numerical eigenchannel with an index that minimizes the difference  $\int_0^L (\langle I_{\alpha_E}(z) \rangle - \langle I_\alpha(z) \rangle)^2 dz$ . We do *not* use any eigenchannel-specific adjustments/fits in this identification. This process gives the mapping of  $\alpha_E$  to  $\alpha$ , shown in Fig. B.4. A few experimental eigenchannels are redundant, particularly in the range  $\alpha \in [6 \dots 15]$ , and no eigenchannels with  $\alpha > 22$  are observed experimentally. We attribute this to the finite signal-to-noise ratio in the experimental data. The eigenchannels with  $\alpha > 22$  have a transmittance less than  $\sim 0.25\%$ , thus they are overwhelmed by the experimental noise.

We use the redundancy of the experimental eigenchannels in Fig. B.4 to enlarge the statistical ensemble. In other words, statistical averages  $\langle \dots \rangle$  for the  $\alpha$ -th eigenchannel –that correspond to multiple  $\alpha_E$ – include averaging over both disorder configurations and

different  $\{\alpha_E\}$ .

### B.4.5 Transmission Eigenchannel Variance

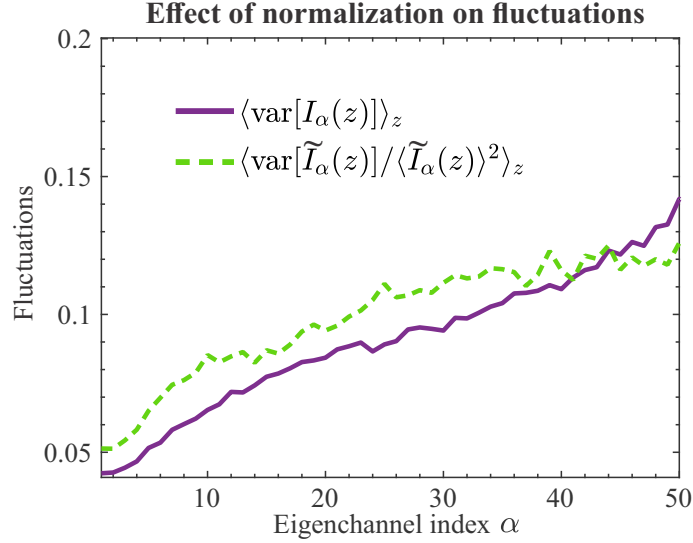


Figure B.5: **Transmission eigenchannel variance comparison.** We compare the variance of eigenchannel profiles calculated with the normalized intensity (purple solid line) to the intensity variance normalized by the mean intensity  $\langle \text{var}[\tilde{I}_\alpha(z)] / \langle \tilde{I}_\alpha(z) \rangle^2 \rangle_z$  squared (green dashed line). They show similar growth with the eigenchannel index  $\alpha$ .

In Chapter 6, we present the realization-to-realization fluctuations of the eigenchannels' normalized intensity profiles. For each eigenchannel, the measured intensity profile  $\tilde{I}(z)$  is normalized to  $I(z) = \tilde{I}(z) / [(1/L) \int_0^L \tilde{I}(z') dz']$ . Using a different normalization procedure, we check the effect of our normalization on the eigenchannel fluctuations using numerical simulations of  $t$ . For an eigenchannel  $\alpha$ , the variance  $\text{var}[\tilde{I}_\alpha(z)] = \langle \delta \tilde{I}_\alpha^2(z) \rangle$  of the unnormalized intensity fluctuation  $\delta \tilde{I}_\alpha(z) = \tilde{I}_\alpha(z) - \langle \tilde{I}_\alpha(z) \rangle$  can be normalized by dividing the square of the mean intensity  $\langle \tilde{I}_\alpha(z) \rangle^2$  at the same depth  $z$ . Then this ratio  $\text{var}[\tilde{I}_\alpha(z)] / \langle \tilde{I}_\alpha(z) \rangle^2$  can be averaged over all  $z$ . In Fig. B.5, we compare this quantity to the variance of the normalized intensity profile,  $\tilde{C}_\alpha$ , calculated in Chapter 6. Both exhibit an increase with the eigenchannel index  $\alpha$ . Their similar trend confirms that the stronger

fluctuations for lower-transmission eigenchannels are due to the intrinsic properties of the transmission eigenchannels.

## B.5 Deposition Eigenchannels

In the following section, supplementary information pertaining the analysis in Chapter 7 is provided.

### B.5.1 Deposition Eigenchannel Numerical Simulations

Again, we use the Kwant simulation package [188] to perform numerical simulations of wave transport in a two-dimensional (2D) rectangular waveguide geometry. The geometry of the numerical simulations is chosen to match the experimental parameters of  $W/\lambda$  (width of the waveguide normalized by wavelength),  $L/\lambda$  (length of the waveguide), and  $N$  (number of waveguide modes). The refractive index in the input (empty) waveguide matches the average index in the disordered region, thus the number of propagating modes in the disordered waveguide is also  $N$ . Furthermore, the strength of the disorder and (spatially uniform) absorption coefficient are selected to match the macroscopical physical parameters in the experiment: specifically, the transport mean free path  $\ell$  and diffusive absorption length  $\xi_a$ . We also simulate the disordered waveguides without loss by setting  $\xi_a = \infty$ . Statistical averaging over 1000 disorder configurations is performed for all numerical results shown in Chapter 7.

#### Transmission Eigenchannels

We calculate the field transmission matrix  $t$  in the basis of the empty (input) waveguide modes.  $t$  is normalized so that when light with a unit flux in the  $n$ -th waveguide mode is incident on the disordered region,  $|t_{mn}|^2$  is equal to the amount of flux carried away by

the  $m$ -th waveguide mode in transmission. We also compute the wavefunction  $E_n(y, z)$  describing the complex field distribution throughout the system, when excited via the  $n$ -th waveguide mode.

Transmission eigenchannels are computed by performing a singular value decomposition of the transmission matrix so that  $t_{mn} = \sum_{\alpha=1}^N U_{m\alpha}^{(T)} \cdot \tau_{\alpha}^{1/2} \cdot V_{\alpha n}^{(T)*}$ . Here,  $\hat{U}^{(T)}$  and  $\hat{V}^{(T)}$  are unitary matrices and  $\tau_{\alpha}$  are the transmission eigenvalues. The disorder-specific incident wavefront given by the  $\alpha$ -th column of the matrix  $\hat{V}^{(T)}$  excites the  $\alpha$ -th transmission eigenchannel with the field distribution  $E_{\alpha}^{(T)}(y, z) = \sum_{n=1}^N V_{\alpha n}^{(T)} E_n(y, z)$  inside the system with the transmittance given by  $\tau_{\alpha}$ . The depth intensity profile is computed by integrating over the transverse coordinate  $y$  followed by averaging over disorder realizations: denoted by angular brackets  $I_{\alpha}^{(T)}(z) = \left\langle \int_0^W \left| E_{\alpha}^{(T)}(y, z) \right|^2 dy \right\rangle$ .

## Deposition Matrix

We provide two definitions for the deposition matrix  $\mathcal{Z}$  defined in Chapter 7. While the first definition is more general, the second one reduces to the transmission matrix at the output. For both definitions, the deposition eigenchannels are introduced based on the singular value decomposition of the deposition matrix

$$\mathcal{Z}_{mn}(z_D) = \sum_{\alpha=1}^N U_{m\alpha}^{(D)}(z_D) \zeta_{\alpha}^{1/2}(z_D) V_{\alpha n}^{(D)*}(z_D). \quad (\text{B.1})$$

The spatial structure of  $\alpha$ -th deposition eigenchannel inside the system is given by

$$E_{\alpha}^{(D)}(y, z; z_D) = \sum_{n=1}^N V_{\alpha n}^{(D)}(z_D) E_n(y, z). \quad (\text{B.2})$$

The depth intensity profile is computed by integrating over the transverse coordinate  $y$  as well as the disorder realizations

$$I_\alpha^{(D)}(z; z_D) = \left\langle \int_0^W |E_\alpha^{(D)}(y, z; z_D)|^2 dy \right\rangle. \quad (\text{B.3})$$

Numerically we compare the eigenvalues  $\zeta(z_D)$  of the deposition matrices  $\mathcal{Z}(z_D)$  defined previously for a thin slice at depth  $z_D$  inside the disordered waveguide. As shown in Fig. B.6, the probability density function (PDF) of deposition eigenvalues  $P(\zeta)$  is almost identical for the two definitions at most depths inside the disordered waveguide. Only close to the very end  $L - z_D < \ell$  do the two PDFs differ; one remains single peaked while the other becomes bimodal and converges to the PDF of the transmission eigenvalues.

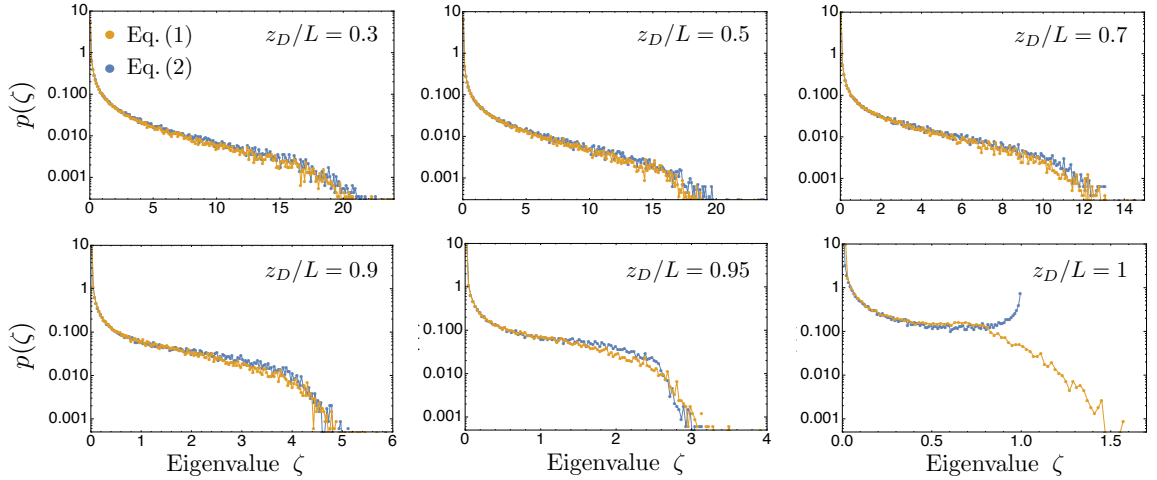


Figure B.6: **Comparison between deposition eigenvalue definitions.** Comparison of the eigenvalue distributions  $p(\zeta)$  of the operators  $\mathcal{Z}^\dagger \mathcal{Z}$  defined by Eq. (7.1) and Eq. (7.2), evaluated at different depths  $z_D/L$  of a disordered waveguide (length  $L = 50 \mu\text{m}$ , width  $W = 30 \mu\text{m}$ , transport mean free path  $\ell = 3.3 \mu\text{m}$ ). Noticeable differences are observed only at  $z_D$  very close to  $L$ , where  $p(\zeta)$  converges to the bimodal distribution of transmission eigenvalues for the operator  $\mathcal{Z}^\dagger \mathcal{Z}$  defined by Eq. (7.2) only. The two distributions still coincide for  $z_D/L = 0.95$  (panel 5), which corresponds to  $L - z_D < \ell$ .

To illustrate the close relationship between the two definitions of the deposition matrix, we compare the trace of  $\mathcal{Z}^\dagger \mathcal{Z}$ , which corresponds to the sum of their eigenvalues,

$Tr[\mathcal{Z}^\dagger \mathcal{Z}] = \sum_m \zeta_m$ . For the first definition, we switch to the waveguide mode basis and find the trace

$$Tr[\mathcal{Z}(z_D)^\dagger \mathcal{Z}(z_D)] = \sum_{n=1}^N \sum_{m=1}^{\infty} |\mathcal{Z}_{mn}(z_D)|^2, \quad (\text{B.4})$$

where  $\mathcal{Z}_{mn}(z_D) = \int_0^W \chi_m(y) E_n(y, z_D) dy$  is obtained by projecting the internal field distribution, excited by a unit flux input to the  $n$ -th waveguide mode, onto the  $m$ -th waveguide mode at the cross-section  $z = z_D$ . With the second definition of  $\mathcal{Z}(z_D)$ , the trace

$$Tr[\mathcal{Z}^\dagger(z_D) \mathcal{Z}(z_D)] = \sum_{n=1}^N \sum_{m=1}^N v_m |\mathcal{Z}_{mn}(z_D)|^2 \quad (\text{B.5})$$

differs from the first one in two ways: (i) the summation over  $m$  runs only over the propagating modes of the waveguide, and (ii) the prefactor  $v_m$  introduces a weight for different modes. Using the Fisher-Lee formula [247], one can show that the trace for the second definition at  $z_D = L$  is equal to the dimensionless conductance  $g = \sum_m \tau_m$ .

## B.5.2 Analytical Predictions

### Filtered Random Matrix (FRM) Model

In Chapter 7, we make the ansatz that  $\mathcal{Z}(z_D)$  has the same spectrum as a filtered matrix  $\tilde{t}$  drawn from a larger virtual transmission matrix  $t_0$ . The matrix  $\tilde{t}$  is obtained by keeping a fraction  $m < 1$  of rows and columns in  $t_0$ . In Ref. [202], it is shown that the eigenvalue distribution of the matrix  $\tilde{t}^\dagger \tilde{t}$  is given by  $p_{\tilde{t}^\dagger \tilde{t}}(x) = -\lim_{\eta \rightarrow 0^+} \text{Im} g_{\tilde{t}^\dagger \tilde{t}}(x + i\eta)$ , where the resolvent  $g_{\tilde{t}^\dagger \tilde{t}}(w)$  is the solution of the implicit equation:

$$g_{\tilde{t}^\dagger \tilde{t}}(w) = \frac{w m g_{\tilde{t}^\dagger \tilde{t}}(w) + 1 - m}{w m^2 g_{\tilde{t}^\dagger \tilde{t}}(w)} g_{t_0^\dagger t_0} \left[ \frac{[w m g_{\tilde{t}^\dagger \tilde{t}}(w) + 1 - m]^2}{w m^2 g_{\tilde{t}^\dagger \tilde{t}}(w)^2} \right]. \quad (\text{B.6})$$

Since  $t_0$  represents the transmission matrix of a virtual opaque and disordered medium, the resolvent  $g_{t_0^\dagger t_0}(w)$  is [202]:

$$g_{t_0^\dagger t_0}(w) = \frac{1}{w} - \frac{\bar{\tau}_0}{w\sqrt{1-w}} \text{Arctanh} \left[ \frac{\text{Tanh}(1/\bar{\tau}_0)}{\sqrt{1-w}} \right], \quad (\text{B.7})$$

where  $\bar{\tau}_0$  is the mean of  $p_{t_0^\dagger t_0}(x)$ . Hence, the eigenvalue distribution  $p(\zeta)$  of  $\mathcal{Z}^\dagger(z_D)\mathcal{Z}(z_D)$  is parametrized by  $m$  and  $\bar{\tau}_0$  only. In particular, the variance of  $p(\zeta)$  is

$$\frac{\text{Var}(\zeta)}{\langle \zeta \rangle^2} = m \left( \frac{2}{3\bar{\tau}_0} - 1 \right) + 1 - m. \quad (\text{B.8})$$

In our model, we take  $m = \langle \zeta(L) \rangle / \langle \zeta(z_D) \rangle = \langle \tau \rangle / \langle \zeta(z_D) \rangle \leq 1$  and  $\bar{\tau}_0$  solution of Eq. (B.8). In this way, the full distribution  $p(\zeta)$  becomes parametrized by its first two moments,  $\langle \zeta \rangle$  and  $\langle \zeta^2 \rangle$ . To obtain the FRM predictions in Fig. 7.2(a) of Chapter 7 and Fig. B.7 here, we solve Eq. (B.6) with  $\langle \zeta \rangle$  and  $\langle \zeta^2 \rangle$  as input parameters evaluated numerically. The good agreement between the FRM prediction and numerical distributions validates our model.

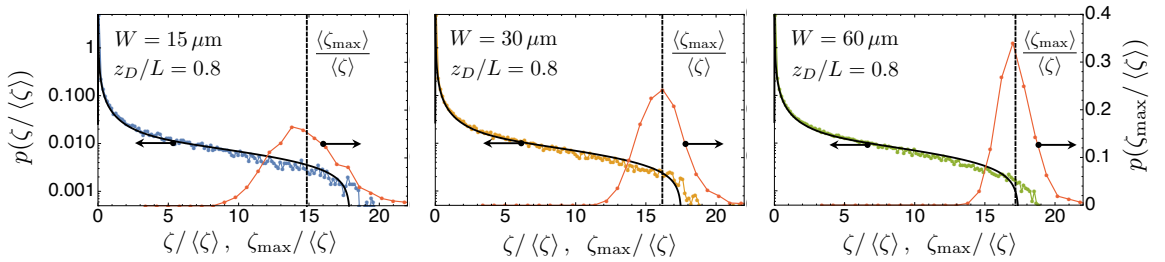


**Figure B.7: Width-dependence of deposition eigenvalues.** Deposition eigenvalue distribution  $p(\zeta)$  at depth  $z_D = 0.8L$  of a disordered waveguide of length  $L = 50 \mu\text{m}$  and width  $W = 15, 30, 50 \mu\text{m}$ . Analytical FRM predictions (solid black lines) are compared with numerical results (dots) obtained from the solution of the wave equation for  $10^3$  realizations of the disordered waveguide with a transport mean free path  $\ell = 3.3 \mu\text{m}$ . The distribution of the largest eigenvalue  $p(\zeta_{\max})$  is superimposed (red dots connected by red line) to reveal the convergence of  $\zeta_{\max}$  towards the upper edge of  $p(\zeta)$  in the limit  $g = N \langle \tau \rangle \gg 1$  ( $W = 15, 30, 50 \mu\text{m}$  correspond to  $g = 5, 10, 15$ ). The value  $\langle \zeta_{\max} \rangle$  is indicated with dashed vertical line.

In Ref. [202], it is also shown that the edges  $x^*$  of the distribution  $p_{\bar{i}\dagger\bar{i}}(x)$  are given by  $x^* = \xi^* \left[ 1 + (m - 1)/\xi^* g_{t_0\dagger t_0}(\xi^*) \right]^2$ , where  $\xi^*$  is the solution of

$$\left. \frac{dg_{t_0\dagger t_0}(\xi)}{d\xi} \right|_{\xi^*} = \frac{g_{t_0\dagger t_0}(\xi^*)}{2\xi^*} \frac{-(1-m)^2 + \xi^{*2} g_{t_0\dagger t_0}(\xi^*)^2}{(1-m)^2 - (1-m)\xi^* g_{t_0\dagger t_0}(\xi^*)}. \quad (\text{B.9})$$

We solve this equation to find the values of the upper edge  $x^*$  represented in Fig. 7.2(b) of Chapter 7, where it is compared to  $\langle \zeta_{\max} \rangle$ . In the limit of large matrix size ( $N \rightarrow \infty$ ), we expect that the upper edge of  $p(\zeta)$  and  $\langle \zeta_{\max} \rangle$  coincide. This is illustrated in Fig. B.7, where we present the distributions  $p(\zeta)$  and  $p(\zeta_{\max})$  for three waveguide widths  $W$ , at a fixed depth  $z_D = 0.8L$ . As  $W$  increases,  $p(\zeta)$  is almost unaffected because  $\text{Var}(\zeta)$  marginally depends on  $W$ , whereas the distribution  $p(\zeta_{\max})$  shrinks and  $\langle \zeta_{\max} \rangle$  converges towards the upper edge from below. Convergence is reached for all depths  $z_D$  in the limit of large conductance ( $g = N \langle \tau \rangle \gg 1$ ), as illustrated in Fig. B.8.

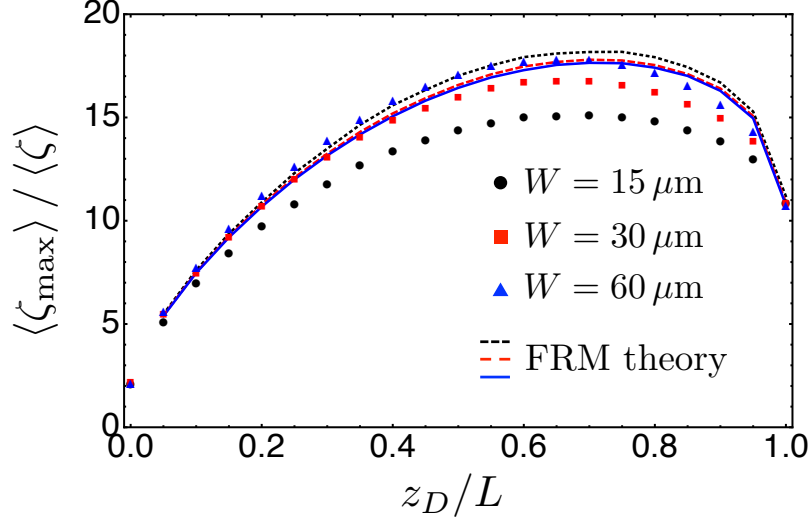


Figure B.8: **Width-dependence of maximum deposition eigenvalues.** Symbols (circles, squares, triangles) represent the ensemble average of the largest deposition eigenvalue  $\langle \zeta_{\max} \rangle$  at different depth  $z_D/L$  for three waveguide width  $W = 10, 30, 60 \mu\text{m}$ . Other parameters are identical to the parameters in Fig. B.7. Solid lines of matched colors are analytical predictions for the upper edge of  $p(\zeta)$  evaluated with the numerical mean  $\langle \zeta \rangle$  and variance  $\text{Var}[\zeta]$ . The agreement between the numerical data and the analytical predictions improves with increasing waveguide width.

### First Two Moments Of $p(\zeta)$

The first moment  $\langle \zeta(z_D) \rangle$  of the distribution  $p(\zeta)$  is proportional to the mean intensity  $\langle I(z_D) \rangle$  deposited at depth  $z_D$  under random wavefront illumination. We can approximate it by the steady state solution of the diffusion equation with an isotropic source located at an injection depth  $z_{\text{in}} \sim \ell$  away from the front surface of the disordered waveguide boundary,  $\partial_z^2 \langle \zeta(z) \rangle = A\delta(z - z_{\text{in}})$ , where  $A$  is a constant to be evaluated below. This equation must be complemented with boundary conditions:  $\langle \zeta(z=0) \rangle = z_0 \partial_z \langle \zeta(z=0) \rangle$  and  $\langle \zeta(z=L) \rangle = -z_0 \partial_z \langle \zeta(z=L) \rangle$ , where  $z_0$  is the extrapolation length ( $z_0 = \pi\ell/4$  in 2D and  $z_0 = 2\ell/3$  in 3D). The solution is a linear function of  $z_D$ ,

$$\langle \zeta(z_D) \rangle = A \frac{(z_{\text{in}} + z_0)(L + z_0 - z_D)}{L + 2z_0}, \quad (\text{B.10})$$

for  $z_D > z_{\text{in}}$ . The constant  $A$  being fixed by our choice of normalization  $\langle \zeta(z = L) \rangle = \langle \tau \rangle = 2z_0/(L + 2z_0)$ , we get

$$\langle \zeta(z_D) \rangle = 2(1 - \langle \tau \rangle) \left(1 - \frac{z_D}{L}\right) + \langle \tau \rangle, \quad (\text{B.11})$$

which is independent of the precise value of  $z_{\text{in}}$ . The agreement of this prediction with numerical simulations is excellent, as shown in Fig. B.9(a).

The variance  $\text{Var}(\zeta) = \langle \zeta(z_D)^2 \rangle - \langle \zeta(z_D) \rangle^2$  of the eigenvalue distribution  $p(\zeta)$  can be related to intensity fluctuation  $\langle I(z_D)^2 \rangle - \langle I(z_D) \rangle^2$ . Using the singular value decomposition of the deposition matrix  $\mathcal{Z} = U^{(D)} \hat{\zeta}^{1/2} V^{(D)\dagger}$ , the cross-section integrated intensity deposited by a waveguide mode  $n$  is  $I_n(z_D) = \sum_{\alpha} |V_{n\alpha}^{(D)}|^2 \zeta_{\alpha}(z_D)$ . The evaluation of the first two moments of  $I_n(z_D)$  is straightforward using the isotropy hypothesis for the disordered waveguide [86, 248]. This amounts to considering that  $V$  is uniformly distributed over the unitary group and is independent of  $\hat{\zeta}$ . We find

$$\langle I_n(z_D) \rangle = \frac{1}{N} \langle \text{Tr}(\hat{\zeta}) \rangle, \quad (\text{B.12})$$

$$\langle I_n^2(z_D) \rangle = \frac{1}{N^2 - 1} \left(1 - \frac{1}{N}\right) \left[ \langle \text{Tr}(\hat{\zeta})^2 \rangle + \langle \text{Tr}(\hat{\zeta}^2) \rangle \right]. \quad (\text{B.13})$$

In the limit  $N \gg 1$ , the leading order is

$$\begin{aligned} \text{Var}[I_n(z_D)] &\simeq \frac{1}{N^2} \left[ \langle \text{Tr}(\hat{\zeta}^2) \rangle - \frac{1}{N} \langle \text{Tr}(\hat{\zeta})^2 \rangle \right] \\ &\simeq \frac{1}{N^2} \left[ \langle \text{Tr}(\hat{\zeta}^2) \rangle - \frac{1}{N} \langle \text{Tr}(\hat{\zeta}) \rangle^2 \right]. \end{aligned} \quad (\text{B.14})$$

This result is independent of the waveguide mode index  $n$ , and also holds for random

wavefront illumination. We conclude that

$$\frac{\text{Var}[\zeta(z_D)]}{\langle \zeta(z_D) \rangle^2} \simeq N \frac{\text{Var}[I(z_D)]}{\langle I(z_D) \rangle^2}. \quad (\text{B.15})$$

Finally, the intensity fluctuations at depth  $z_D$  are computed by decomposing the field  $E(z_D)$  involved in  $I(z_D) = |E(z_D)|^2$  as a sum of propagators along all possible scattering trajectories [203]. The intensity fluctuations are composed of a small Gaussian field contribution  $C_1 = 1/N$ , and dominated by the non-Gaussian contribution  $C_2(z_D)$ ,

$$\frac{\text{Var}[I(z_D)]}{\langle I(z_D) \rangle^2} = C_1 + C_2(z_D), \quad (\text{B.16})$$

with

$$C_2(z) = \frac{2}{gL \langle I(z) \rangle^2} \int_0^L dz' \langle I(z') \rangle^2 [\partial_{z'} K(z, z')]^2. \quad (\text{B.17})$$

The mean intensity is  $\langle I(z) \rangle = \int_0^L dz' e^{-z'/\ell} K(z, z')$ , where  $K(z, z')$  is the Green's function of the diffusion equation  $\partial_z^2 K(z, z') = \delta(z - z')$ , with boundary conditions  $\partial_z K(0, z') = K(0, z')/z_0$  and  $\partial_z K(L, z') = -K(L, z')/z_0$ . The solution is

$$K(z, z') = \frac{(z^- + z_0)(L + z_0 - z^+)}{L + 2z_0}, \quad (\text{B.18})$$

with  $z^- = \min(z, z')$  and  $z^+ = \max(z, z')$ . In the limit  $L \gg \ell$ , the correlator  $C_2(z)$  takes the simple form [205]

$$C_2(z) \simeq \frac{2}{3g} \frac{z(3L - 2z)}{L^2}, \quad (\text{B.19})$$

where  $g = N \langle \tau \rangle$  is the dimensionless conductance of the disordered waveguide.

By combining Eqs. (B.15) and (B.16), we finally obtain an analytical expression for

the normalized variance of the eigenvalues of the deposition matrix,

$$\frac{\text{Var}[\zeta(z_D)]}{\langle \zeta(z_D) \rangle^2} \simeq 1 + NC_2(z_D). \quad (\text{B.20})$$

Figure B.9(b) shows a good agreement between the simulation results and our prediction based on Eq. (B.17).

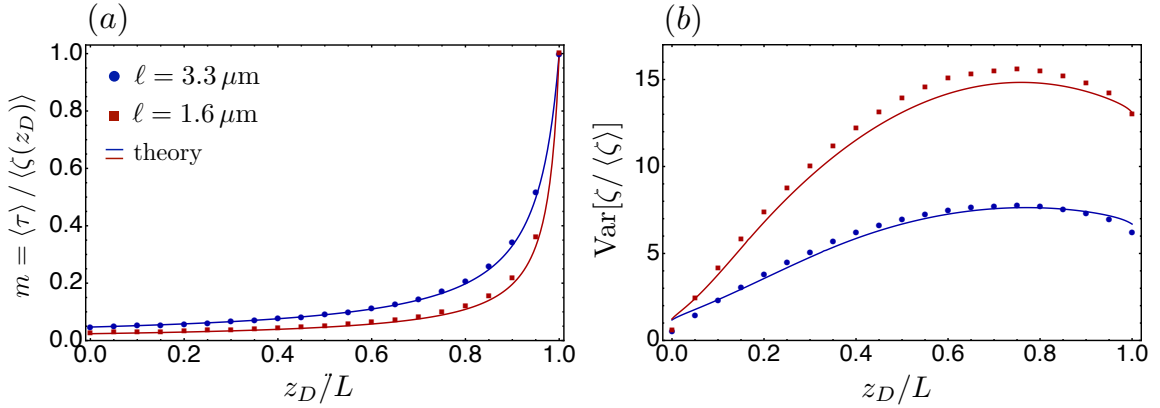


Figure B.9: **FRM filtering ratio.** (a) Effective filtering ratio  $m = \langle \tau \rangle / \langle \zeta(z_D) \rangle$  of the FRM model versus depth  $z_D/L$ . Numerical results (dots) are compared with the analytical prediction  $m = 1 / [2(1 / \langle \tau \rangle - 1)(1 - z_D/L) + 1]$  (solid lines with matched colors); (b) Variance  $\text{var}[\zeta / \langle \zeta \rangle] = \langle \zeta^2 \rangle / \langle \zeta \rangle^2 - 1$  of the eigenvalue distribution  $p(\zeta)$  vs. depth  $z_D/L$ . Numerical results (dots) are compared with intensity fluctuations  $NC_2(z_D) + 1$  evaluated analytically (solid lines of matched colors) for two values of transport mean free path  $\ell = 1.6, 3.3 \mu\text{m}$ . The disordered waveguide dimensions are  $L = 50 \mu\text{m}$  and  $W = 15 \mu\text{m}$ .

When comparing with the experimental data in Fig. 7.3(d), the effect of absorption is included in Eq. (B.17). This is accomplished by substitution of the Green's function which accounts for absorption

$$\partial_z^2 K(z, z') - \frac{K(z, z')}{\xi_a^2} = \delta(z - z'), \quad (\text{B.21})$$

where  $\xi_a$  is the diffusive absorption length.

### B.5.3 Upper Edge Of $p(\zeta)$

In Chapter 7, we argue that the maximal enhancement of energy deposition  $\langle \zeta_{\max} \rangle / \langle \zeta \rangle$  depends, for most depths  $z_D$ , only on the long-range intensity-intensity correlation function  $C_2(z_D)$ . To prove this property, we first note that  $m = \langle \tau \rangle / \langle \zeta(z_D) \rangle$  becomes quickly smaller than unity for  $z_D < L$ , as long as  $\langle \tau \rangle \ll 1$  [see Fig. B.9(a)]. This allows us to perform an expansion of the FRM solution in the limit  $m \rightarrow 0$ . Using

$$g_{t_0^\dagger t_0}(w) \simeq \frac{1 - \bar{\tau}_0}{w} - \frac{i\pi\bar{\tau}_0}{2w\sqrt{1-w}}, \quad (\text{B.22})$$

and expanding Eq. (B.9) to leading order, we find

$$\frac{\langle \zeta_{\max}(z_D) \rangle}{\langle \zeta(z_D) \rangle} \simeq \frac{[(\gamma - 1)^{2/3} + (\pi/2)^{2/3}]^2 [\gamma - 1 + (\pi/2)^{2/3}(\gamma - 1)^{1/3}]}{\gamma(\gamma - 1)^{1/3}} + \mathcal{O}(m), \quad (\text{B.23})$$

which depends on  $\gamma = m/\bar{\tau}_0$  only. According to Eq. (B.8),

$$\gamma \simeq \frac{3}{2} \left( \frac{\text{Var}[\zeta(z_D)]}{\langle \zeta(z_D) \rangle^2} - 1 \right) \simeq \frac{3NC_2(z_D)}{2}. \quad (\text{B.24})$$

Hence,  $\langle \zeta_{\max} \rangle / \langle \zeta \rangle$  depends only on  $C_2(z_D)$  only. Since  $\gamma \sim NC_2(z_D) \gg 1$  for  $\langle \tau \rangle \sim \ell/L \ll 1$ , we can further expand Eq. (B.23) as

$$\frac{\langle \zeta_{\max}(z_D) \rangle}{\langle \zeta(z_D) \rangle} \simeq \gamma + 3 \left( \frac{\pi}{2} \right)^{2/3} \gamma^{1/3} - 2 + \mathcal{O}(\gamma^{-1/3}). \quad (\text{B.25})$$

This shows that the energy enhancement slowly converges to  $\gamma$  in the limit  $L/\ell \gg 1$ .

## B.5.4 Deposition Eigenchannel Experimental Measurements

### Deposition Matrix Measurement

To begin with, the experimental measurement of the deposition matrix largely follows the experimental measurement of the transmission matrix in Appendix B.4.1. For a given disordered waveguide configuration, we sequentially apply a complete set of orthogonal phase-fronts to the SLM and record the 2D field distribution throughout the waveguide for each input. Based on these field measurements, we construct a linear matrix that relates the field pattern at the SLM to the field distribution anywhere inside the waveguide: the field reconstruction matrix. From this, we create two matrices  $\mathcal{Z}_{\text{SLM} \rightarrow \text{Buff}}$  and  $\mathcal{Z}_{\text{SLM} \rightarrow R}$ , which map the field from the SLM surface to the buffer region in front of the main disordered region and to the deposition area of interest  $R$  inside it.

With these two matrices, we build the deposition matrix relating the field in the buffer region to the field in the deposition region:  $\mathcal{Z}_{\text{Buff} \rightarrow R} \equiv \mathcal{Z}_{\text{SLM} \rightarrow R} \mathcal{Z}_{\text{SLM} \rightarrow \text{Buff}}^{-1}$ . Again, to calculate the inverse of  $\mathcal{Z}_{\text{SLM} \rightarrow \text{Buff}}$ , we use Moore-Penrose matrix inversion. Similarly, the inverse matrix is calculated using the 55 highest singular values of  $\mathcal{Z}_{\text{SLM} \rightarrow \text{Buff}}$  and the remaining singular values are set to zero.

As shown in Fig. 7.3(a) of Chapter 7, the energy deposition regions are four  $10 \mu\text{m} \times 10 \mu\text{m}$  areas inside the disordered waveguide. To avoid artifacts from light scattered out-of-plane from the photonic-crystal sidewalls, the deposition regions are kept away from the waveguide boundaries. Since each deposition area is relatively large and contains many speckle grains, the effect of incident wavefront shaping on increasing/decreasing out-of-plane scattered light into the camera is reduced. Therefore, optimizing the input wavefront to the waveguide predominantly enhance/suppress the amount of energy deposited into the target region. This is confirmed by our numerical simulation with realistic parameters, as detailed in the next subsection.

## Deposition Eigenchannel Characterization

To experimentally excite a single deposition eigenchannel, we first calculate the singular vectors of the deposition matrix,  $\mathcal{Z}_{\text{Buff} \rightarrow \text{R}}$ , using a singular value decomposition. We then convert the singular vectors of  $\mathcal{Z}_{\text{Buff} \rightarrow \text{R}}$  into SLM phase-modulation patterns by multiplying each vector by the pseudoinverse of the matrix from the SLM to the buffer region,  $\mathcal{Z}_{\text{SLM} \rightarrow \text{Buff}}^{-1}$ , and retain the resulting phase-modulation patterns. By displaying one of the phase patterns on the SLM, we excite the corresponding deposition eigenchannel in the diffusive waveguide. For a given disorder configuration and region of interest, we record the 2D spatial intensity profiles of every eigenchannel of  $\mathcal{Z}_{\text{Buff} \rightarrow \text{R}}$ . From each eigenchannel measurement, we integrate the 2D intensity pattern over the waveguide cross-section (along  $y$ ) to obtain the deposition eigenchannel's depth profile. While our waveguide structure has a width of 15  $\mu\text{m}$ , we only use the central 10  $\mu\text{m}$  region of the waveguide's out-of-plane-scattered light to avoid artifacts from out-of-plane scattering by the photonic-crystal boundaries.

After measuring 55 of the deposition eigenchannel profiles of  $\mathcal{Z}_{\text{Buff} \rightarrow \text{R}}$  with the highest eigenvalues (for a given disorder configuration) we need to mitigate the influence of 'noisy eigenchannels' and properly normalize the eigenchannel profiles. While our waveguides have 55 deposition eigenchannels (for a given region of interest) the limited dynamic range of our CCD camera makes the deposition eigenchannels with small eigenvalues experimentally inaccessible. The missing information needed to reconstruct these deposition eigenchannels is replaced with measurement noise, and therefore the corresponding 'noisy eigenchannels' are equivalent to random inputs. Additionally, this effect leads to a slight shuffling in the order of the measured eigenchannels based on their eigenvalues.

To account for redundant eigenchannel measurements, induced by measurement noise, as well as the inability to experimentally control the norm of the input flux, we conduct

numerical simulations in order to normalize and sort the measured deposition eigenchannel depth profiles. The simulated waveguides have identical parameters and dimensions to the experimental ones. We compute the deposition matrices that map the incident fields to the fields within four target regions  $R_1 - R_4$ . Since  $2N$  points are chosen randomly inside each region, the deposition matrix is rectangular with dimensions  $2N \times N$ . We compute the ensemble-averaged eigenchannel profiles from the numerical simulations to normalize and determine the correct order of measured eigenchannel profiles. First, we normalize all of the experimental and numerical profiles to have a mean value of one, and spatially overlap them. Then, for each experimental profile, we calculate its absolute difference from every numerical profile and assign the correct order based on the minimum difference. Once we have the correct order of the experimental eigenchannel, we renormalize it according to the unit input flux. In this process, we remove the ‘noisy eigenchannels’ with the intermediate eigenvalues, whose depth profiles resemble those of random input wavefronts. In this way, we are able to sort out the deposition eigenchannels of a single realization. We repeat this process for multiple disorder realizations –generated using different wavelengths and random hole configurations– and ensemble-average the depth profiles of deposition eigenchannels with the same indices. As in Section B.4.2, we measure the deposition eigenchannel profiles of 13 independent system realizations: for each of four target regions at different spatial locations in the waveguide. We obtain these measurements from two waveguides with different random arrays of air holes. To generate independent system realizations from the same hole configuration, we vary the wavelength of the input light beyond the spectral correlation width of the diffusive light, which is estimated to be 0.4 nm. Over a wavelength span of 3 nm, we vary the input wavelength of our laser in increments of 0.5 nm. We choose the specific wavelength range of the measurement –for each random hole configuration– such that the effective dissipation by out-of-plane scattering is minimal and nearly constant over the probe wavelength

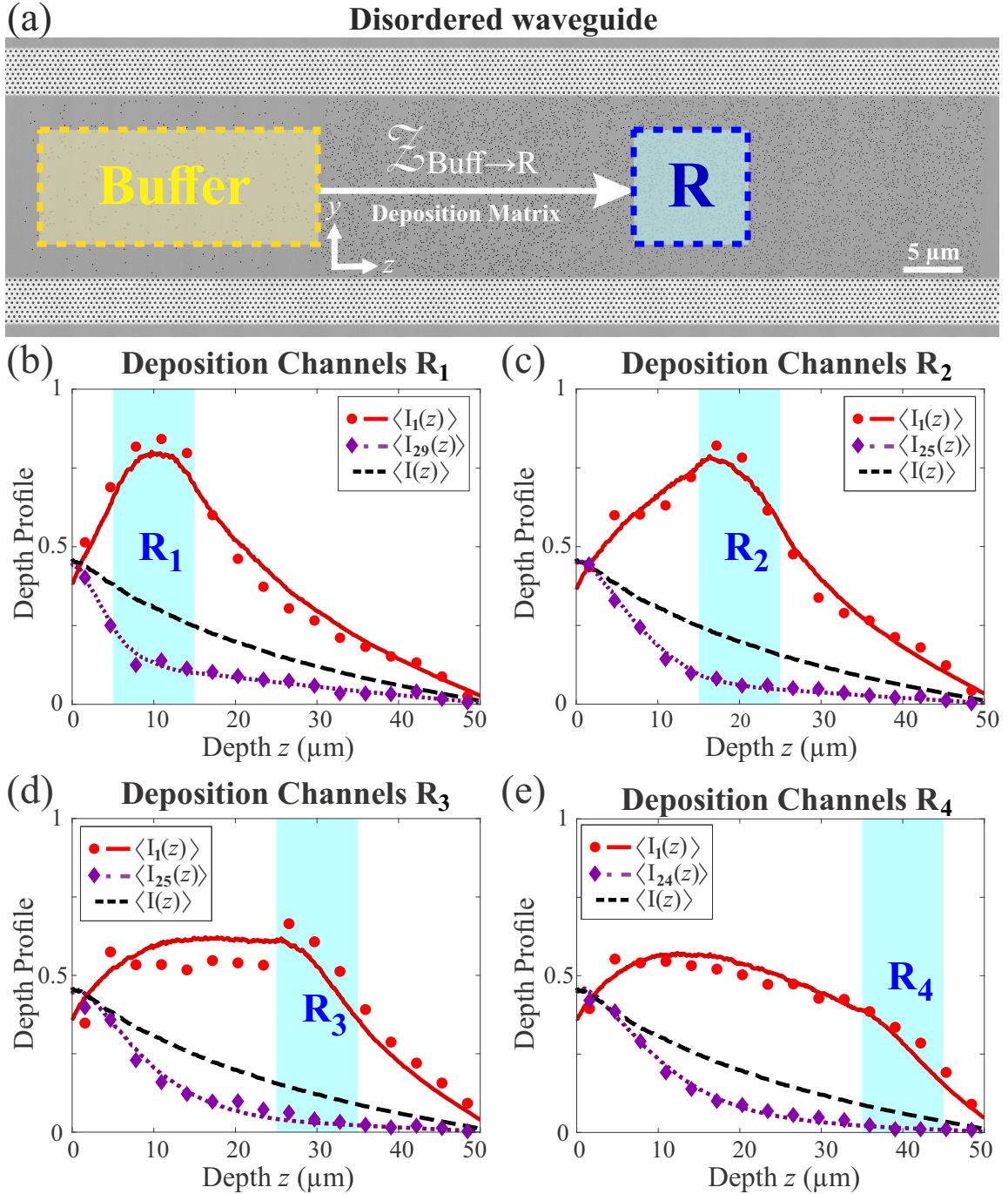


Figure B.10: **Experimental measurement of deposition eigenchannels.** A composite SEM image of an on-chip disordered waveguide is presented in (a) with a delineation of the buffer region and a deposition region superimposed. In (b-e) the maximally enhancing/suppressing (red-dots/purple-diamonds) deposition eigenchannel profiles, measured experimentally, are juxtaposed with numerically simulated profiles (red-solid and purple-dashed lines): for four target regions centered at 10, 20, 30, and 40  $\mu\text{m}$ .

range. Because of minor structural differences, pertaining to the fabrication process, one sample has a smaller acceptable wavelength range.

In Figures B.10(b-e), the maximal enhancing/suppressing energy deposition eigenchannel profiles (red-dots/purple-diamonds), measured experimentally, are juxtaposed with numerically simulated profiles (red-solid and purple-dashed lines): for all four target regions centered at 10, 20, 30 and 40  $\mu\text{m}$ . The cross-section integrated intensities are averaged axially (along  $z$ ) over one transport mean free path to reduce fluctuations. The black dashed line represents the cross-section integrated intensity profile of random illumination patterns in our system,  $\langle I(z) \rangle$ . The depth profiles of the maximal energy deposition eigenchannels (with the largest eigenvalues) are well above  $\langle I(z) \rangle$ : both within the target region and beyond. Similarly, the depth profiles of the minimal energy deposition eigenchannels (with the smallest eigenvalues) are notably lower than  $\langle I(z) \rangle$ , both inside and outside the target region.

# Bibliography

- [1] N. Bender, H. Yilmaz, Y. Bromberg, and H. Cao, “Customizing speckle intensity statistics,” *Optica* **5**, 595–600 (2018). 1, 9, 49, 60
- [2] N. Bender, H. Yilmaz, Y. Bromberg, and H. Cao, “Introducing non-local correlations into laser speckles,” *Opt. Express* **27**, 6057–6067 (2019). 1, 4, 30
- [3] N. Bender, H. Yilmaz, Y. Bromberg, and H. Cao, “Creating and controlling complex light,” *APL Photon.* **4**, 110806 (2019). 1, 45
- [4] N. Bender, M. Sun, H. Yilmaz, J. Bewersdorf, and H. Cao, “Circumventing the optical diffraction limit with customized speckles,” *Optica* **8**, 122–129 (2021). 1, 67
- [5] N. Bender, A. Yamilov, H. Yilmaz, and H. Cao, “Fluctuations and correlations of transmission eigenchannels in diffusive media,” *Physical Review Letters* **125**, 165901 (2020). 1, 6, 90, 106, 115, 117
- [6] N. Bender, A. Yamilov, A. Goetschy, H. Yilmaz, C. W. Hsu, and H. Cao, “Depth-targeted energy deposition deep inside scattering media,” (2021). 1, 105
- [7] J. W. Goodman, “Some fundamental properties of speckle,” *J. Opt. Soc. Am.* **66**, 1145–1150 (1976). 3, 9
- [8] J. W. Goodman, *Speckle Phenomena in Optics: Theory and Applications, Second Edition* (SPIE, 2020). 3, 9, 22, 23, 29, 32
- [9] J. C. Dainty, “An introduction to ‘Gaussian’ speckle,” *Proc. Soc. Photo-Opt. Instrum. Eng.* **243**, 2–8 (1980). 3, 9, 25
- [10] J. C. Dainty, *Laser Speckle and Related Phenomena*, Topics in Applied Physics (Springer Berlin Heidelberg, 2013). 3, 9, 23, 32
- [11] I. Freund, “‘1001’ correlations in random wave fields,” *Waves in Random Media* **8**, 119–158 (1998). 3, 32
- [12] J. C. Dainty, “Some statistical properties of random speckle patterns in coherent and partially coherent illumination,” *J. Mod. Opt.* **17**, 761–772 (1970). 3, 9

- [13] B. M. Levine and J. C. Dainty, “Non-Gaussian image plane speckle: measurements from diffusers of known statistics,” *Opt. Commun.* **45**, 252–257 (1983). 3, 9
- [14] J. W. Goodman, “Dependence of image speckle contrast on surface roughness,” *Opt. Commun.* **14**, 324–327 (1975). 3, 9
- [15] H. Fujii and T. Asakura, “Effect of surface roughness on the statistical distribution of image speckle intensity,” *Opt. Commun.* **11**, 35–38 (1974). 3, 4, 9, 32
- [16] H. Fujii and T. Asakura, “Statistical properties of image speckle patterns in partially coherent light,” *Nouv. Rev. Opt.* **6**, 5–14 (1975). 3, 9
- [17] E. Jakeman and J. G. McWhirter, “Non-Gaussian scattering by a random phase screen,” *Appl. Phys. B* **26**, 125–131 (1981). 3, 9
- [18] E. Jakeman, “Speckle statistics with a small number of scatterers,” *Opt. Eng.* **23**, 234453 (1984). 3, 9
- [19] H. M. Pedersen, “The roughness dependence of partially developed, monochromatic speckle patterns,” *Opt. Commun.* **12**, 156–159 (1974). 3, 9
- [20] K. A. O’Donnell, “Speckle statistics of doubly scattered light,” *J. Opt. Soc. Am.* **72**, 1459–1463 (1982). 3, 9
- [21] H. Funamizu and J. Uozumi, “Generation of fractal speckles by means of a spatial light modulator,” *Opt. Express* **15**, 7415–7422 (2007). 4, 32
- [22] T. Yoshimura, K. Kato, and K. Nakagawa, “Surface-roughness dependence of the intensity correlation function under speckle-pattern illumination,” *J. Opt. Soc. Am. A* **7**, 2254–2259 (1990). 4, 32
- [23] R. Fischer, I. Vidal, D. Gilboa, R. R. B. Correia, A. C. Ribeiro-Teixeira, S. D. Prado, J. Hickman, and Y. Silberberg, “Light with tunable non-Markovian phase imprint,” *Phys. Rev. Lett.* **115**, 073901 (2015). 4, 32
- [24] R. Chriki, G. Barach, C. Tradanosky, S. Smartsev, V. Pal, A. A. Friesem, and N. Davidson, “Rapid and efficient formation of propagation invariant shaped laser beams,” *Opt. Express* **26**, 4431–4439 (2018). 4, 32
- [25] L. Waller, G. Situ, and J. W. Fleischer, “Phase-space measurement and coherence synthesis of optical beams,” *Nat. Photon.* **6**, 474–479 (2012). 4, 32
- [26] C. Sun, L. Waller, D. V. Dylov, and J. W. Fleischer, “Spectral dynamics of spatially incoherent modulation instability,” *Phys. Rev. Lett.* **108**, 263902 (2012). 4, 32
- [27] D. Di Battista, D. Ancora, G. Zacharakis, G. Ruocco, and M. Leonetti, “Hyperuniformity in amorphous speckle patterns,” *Opt. Express* **26**, 15594–15608 (2018). 4, 32

- [28] D. B. Phillips, R. He, Q. Chen, G. M. Gibson, and M. J. Padgett, “Non-diffractive computational ghost imaging,” *Opt. Express* **24**, 14172–14182 (2016). 4
- [29] D. Li, D. P. Kelly, and J. T. Sheridan, “K speckle: space-time correlation function of doubly scattered light in an imaging system,” *J. Opt. Soc. Am. A* **30**, 969–978 (2013). 4
- [30] S. Pau, S. N. Dixit, and D. Eimerl, “Electro-optic control of correlations in speckle statistics,” *J. Opt. Soc. Am. B* **11**, 1498–1503 (1994). 4
- [31] T. Yoshimura and K. Fujiwara, “Statistical properties of doubly scattered image speckle,” *J. Opt. Soc. Am. A* **9**, 91–95 (1992). 4, 32
- [32] S. Kubota and J. W. Goodman, “Very efficient speckle contrast reduction realized by moving diffuser device,” *Appl. Opt.* **49**, 4385–4391 (2010). 4
- [33] Y. Bromberg and H. Cao, “Generating non-Rayleigh speckles with tailored intensity statistics,” *Phys. Rev. Lett.* **112**, 213904 (2014). 4, 9, 25, 39
- [34] R. Fischer, I. Vidal, D. Gilboa, R. R. B. Correia, A. C. Ribeiro-Teixeira, S. D. Prado, J. Hickman, and Y. Silberberg, “Light with tunable non-Markovian phase imprint,” *Phys. Rev. Lett.* **115**, 073901 (2015). 4
- [35] J. P. Amaral, E. J. S. Fonseca, and A. J. Jesus-Silva, “Tailoring speckles with Weibull intensity statistics,” *Phys. Rev. A* **92**, 063851 (2015). 4
- [36] H. E. Kondakci, A. Szameit, A. F. Abouraddy, D. N. Christodoulides, and B. E. A. Saleh, “Sub-thermal to super-thermal light statistics from a disordered lattice via deterministic control of excitation symmetry,” *Optica* **3**, 477–482 (2016). 4
- [37] X. Li, Y. Tai, H. Li, J. Wang, H. Wang, and Z. Nie, “Generation of a super-Rayleigh speckle field via a spatial light modulator,” *App. Phys. B* **122**, 82 (2016). 4
- [38] M. Guillon, B. C. Forget, A. J. Foust, V. De Sars, M. Ritsch-Marte, and V. Emiliani, “Vortex-free phase profiles for uniform patterning with computer-generated holography,” *Opt. Express* **25**, 12640–12652 (2017). 4, 32
- [39] S. Akbar, R. Fickler, M. J. Padgett, and R. W. Boyd, “Generation of caustics and rogue waves from nonlinear instability,” *Phys. Rev. Lett.* **119**, 203901 (2017). 4
- [40] C. Ventalon and J. Mertz, “Dynamic speckle illumination microscopy with translated versus randomized speckle patterns,” *Opt. Lett.* **14**, 7198–7209 (2006). 4, 45, 66, 68
- [41] J. Gateau, T. Chaigne, O. Katz, S. Gigan, and E. Bossy, “Improving visibility in photoacoustic imaging using dynamic speckle illumination,” *Opt. Lett.* **38**, 5188–5191 (2013). 4, 45, 66, 68

- [42] J.-E. Oh, Y.-W. Cho, G. Scarcelli, and Y.-H. Kim, “Sub-Rayleigh imaging via speckle illumination,” *Opt. Lett.* **38**, 682–684 (2013). 4, 45, 66, 68
- [43] T. Chaigne, J. Gateau, M. Allain, O. Katz, S. Gigan, A. Sentenac, and E. Bossy, “Super-resolution photoacoustic fluctuation imaging with multiple speckle illumination,” *Optica* **3**, 54–57 (2016). 4, 45, 66
- [44] E.-F. Zhang, W.-T. Liu, and P.-X. Chen, “Ghost imaging with non-negative exponential speckle patterns,” *J. Opt.* **17**, 085602 (2015). 4, 45, 66
- [45] K. Kuplicki and K. W. C. Chan, “High-order ghost imaging using non-Rayleigh speckle sources,” *Opt. Express* **24**, 26766–26776 (2016). 4, 45, 66
- [46] S. Zhang, W. Wang, R. Yu, and X. Yang, “High-order correlation of non-Rayleigh speckle fields and its application in super-resolution imaging,” *Laser Phys.* **26**, 055007 (2016). 4, 45, 66
- [47] F. Jendrzejewski, A. Bernard, K. Müller, P. Cheinet, V. Josse, M. Piraud, L. Pezzé, L. Sanchez-Palencia, A. Aspect, and P. Bouyer, “Three-dimensional localization of ultracold atoms in an optical disordered potential,” *Nat. Phys.* **8**, 398–403 (2012). 4
- [48] K. Dholakia and T. Čižmár, “Shaping the future of manipulation,” *Nat. Photon.* **5**, 335–342 (2011). 4
- [49] G. Volpe, L. Kurz, A. Callegari, G. Volpe, and S. Gigan, “Speckle optical tweezers: micromanipulation with random light fields,” *Opt. Express* **22**, 18159–18167 (2014). 4
- [50] G. Volpe, G. Volpe, and S. Gigan, “Brownian motion in a speckle light field: tunable anomalous diffusion and selective optical manipulation,” *Sci. Rep.* **4**, 3936 (2014). 4
- [51] J. Beverunge and S. U. Egelhaaf, “Experimental creation and characterization of random potential-energy landscapes exploiting speckle patterns,” *Phys. Rev. A* **93**, 013806 (2016). 4
- [52] K. M. Douglass, S. Sukhov, and A. Dogariu, “Superdiffusion in optically controlled active media,” *Nat. Photon.* **6**, 834–837 (2012). 4
- [53] C. Bechinger, R. Di Leonardo, H. Löwen, C. Reichhardt, G. Volpe, and G. Volpe, “Active particles in complex and crowded environments,” *Rev. Mod. Phys.* **88**, 045006 (2016). 4, 32, 46, 66
- [54] E. Pinçe, S. K. Velu, A. Callegari, P. Elahi, S. Gigan, G. Volpe, and G. Volpe, “Disorder-mediated crowd control in an active matter system,” *Nat. Commun.* **7**, 10907 (2016). 4

- [55] A. P. Mosk, A. Lagendijk, G. Lerosey, and M. Fink, “Controlling waves in space and time for imaging and focusing in complex media,” *Nat. Photon.* **6**, 283 (2012). 5, 6, 105
- [56] S. Rotter and S. Gigan, “Light fields in complex media: mesoscopic scattering meets wave control,” *Rev. Mod. Phys.* **89**, 015005 (2017). 5, 6, 90, 91, 105
- [57] H. Yu, J. Park, K. Lee, J. Yoon, K. Kim, S. Lee, and Y. K. Park, “Recent advances in wavefront shaping techniques for biomedical applications,” *Curr. Appl. Phys.* **15**, 632–641 (2015). 5, 91, 105
- [58] S. Yoon, M. Kim, M. Jang, Y. Choi, W. Choi, S. Kang, and W. Choi, “Deep optical imaging within complex scattering media,” *Nat. Rev. Phys.* **2**, 141–158 (2020). 5, 6, 105
- [59] J. Yoon, M. Lee, K. Lee, N. Kim, J. M. Kim, J. Park, H. Yu, C. Choi, W. Do Heo, and Y. Park, “Optogenetic control of cell signaling pathway through scattering skull using wavefront shaping,” *Sci. Rep.* **5**, 1–7 (2015). 5, 105
- [60] H. Ruan, J. Brake, J. E. Robinson, Y. Liu, M. Jang, C. Xiao, C. Zhou, V. Gradinaru, and C. Yang, “Deep tissue optical focusing and optogenetic modulation with time-reversed ultrasonically encoded light,” *Sci. Adv.* **3**, eaao5520 (2017). 5, 105
- [61] M. Pernot, J.-F. Aubry, M. Tanter, A.-L. Boch, F. Marquet, M. Kujas, D. Seilhean, and M. Fink, “In vivo transcranial brain surgery with an ultrasonic time reversal mirror,” *J. Neurosurg.* **106**, 1061–1066 (2007). 5, 105
- [62] S. F. Liew, S. M. Popoff, S. W. Sheehan, A. Goetschy, C. A. Schmuttenmaer, A. D. Stone, and H. Cao, “Coherent control of photocurrent in a strongly scattering photoelectrochemical system,” *ACS Photon.* **3**, 449–455 (2016). 5, 91, 105
- [63] A. Ishimaru, *Wave propagation and scattering in random media*, vol. 2 (Academic press New York, 1978). 6
- [64] R. Horstmeyer, H. Ruan, and C. Yang, “Guidestar-assisted wavefront-shaping methods for focusing light into biological tissue,” *Nat. Photon.* **9**, 563–571 (2015). 6, 7, 105
- [65] I. M. Vellekoop, “Feedback-based wavefront shaping,” *Opt. Express* **23**, 12189–12206 (2015). 6, 7, 91, 105, 106
- [66] M. Kim, W. Choi, Y. Choi, C. Yoon, and W. Choi, “Transmission matrix of a scattering medium and its applications in biophotonics,” *Opt. Express* **23**, 12648–12668 (2015). 6
- [67] Z. Shi, M. Davy, and A. Z. Genack, “Statistics and control of waves in disordered media,” *Opt. Express* **23**, 12293–12320 (2015). 6

- [68] J.-H. Park, J. Park, K. Lee, and Y. Park, “Disordered optics: Exploiting multiple light scattering and wavefront shaping for nonconventional optical elements,” *Adv. Mater.* **32**, 1903457 (2020). 6
- [69] V. Ntziachristos, “Going deeper than microscopy: the optical imaging frontier in biology,” *Nat. Methods* **7**, 603–614 (2010). 6
- [70] E. H. Kennard *et al.*, *Kinetic theory of gases*, vol. 483 (McGraw-hill New York, 1938). 6
- [71] H. Yılmaz, C. W. Hsu, A. Yamilov, and H. Cao, “Transverse localization of transmission eigenchannels,” *Nat. Photon.* **13**, 352–358 (2019). 6, 91, 106
- [72] S. M. Popoff, G. Lerosey, R. Carminati, M. Fink, A. C. Boccara, and S. Gigan, “Measuring the transmission matrix in optics: an approach to the study and control of light propagation in disordered media,” *Phys. Rev. Lett.* **104**, 100601 (2010). 6, 16, 106, 141
- [73] W. Choi, A. P. Mosk, Q. H. Park, and W. Choi, “Transmission eigenchannels in a disordered medium,” *Phys. Rev. B* **83**, 134207 (2011). 6, 91, 106, 115, 117
- [74] M. Kim, Y. Choi, C. Yoon, W. Choi, J. Kim, Q.-H. Park, and W. Choi, “Maximal energy transport through disordered media with the implementation of transmission eigenchannels,” *Nat. Photon.* **6**, 581–585 (2012). 6, 91, 106
- [75] H. Yu, T. R. Hillman, W. Choi, J. O. Lee, M. S. Feld, R. R. Dasari, and Y. K. Park, “Measuring large optical transmission matrices of disordered media,” *Phys. Rev. Lett.* **111**, 153902 (2013). 6, 91, 106
- [76] S. M. Popoff, A. Goetschy, S. F. Liew, A. D. Stone, and H. Cao, “Coherent control of total transmission of light through disordered media,” *Phys. Rev. Lett.* **112**, 133903 (2014). 6, 91, 106, 112
- [77] B. Gérardin, J. Laurent, A. Derode, C. Prada, and A. Aubry, “Full transmission and reflection of waves propagating through a maze of disorder,” *Phys. Rev. Lett.* **113**, 173901 (2014). 6, 91, 106
- [78] M. Davy, Z. Shi, J. Park, C. Tian, and A. Z. Genack, “Universal structure of transmission eigenchannels inside opaque media,” *Nat. Commun.* **6**, 6893 (2015). 6, 91, 106, 115, 117
- [79] C. W. Hsu, S. F. Liew, A. Goetschy, H. Cao, and A. D. Stone, “Correlation-enhanced control of wave focusing in disordered media,” *Nat. Phys.* **13**, 497–502 (2017). 6, 16, 91, 106
- [80] C. W. Hsu, A. Goetschy, Y. Bromberg, A. D. Stone, and H. Cao, “Broadband coherent enhancement of transmission and absorption in disordered media,” *Phys. Rev. Lett.* **115**, 223901 (2015). 6, 106

- [81] O. N. Dorokhov, “On the coexistence of localized and extended electronic states in the metallic phase,” *Solid State Commun.* **51**, 381–384 (1984). 6, 91
- [82] Y. Imry, “Active transmission channels and universal conductance fluctuations,” *Europhys. Lett.* **1**, 249–256 (1986). 6, 91
- [83] P. Mello, P. Pereyra, and N. Kumar, “Macroscopic approach to multichannel disordered conductors,” *Ann. Phys.* **181**, 290–317 (1988). 6, 91
- [84] J. B. Pendry, A. MacKinnon, and A. B. Pretre, “Maximal fluctuations - a new phenomenon in disordered systems,” *Physica A* **168**, 400–407 (1990). 6, 91
- [85] Y. V. Nazarov, “Fluctuations of transmission distribution in disordered conductors,” *Phys. Rev. Lett.* **76**, 2129–2132 (1996). 6, 91
- [86] C. W. Beenakker, “Random-matrix theory of quantum transport,” *Rev. Mod. Phys.* **69**, 731–808 (1997). 6, 90, 91, 109, 173
- [87] I. M. Vellekoop and A. Mosk, “Focusing coherent light through opaque strongly scattering media,” *Opt. Lett.* **32**, 2309–2311 (2007). 7, 105
- [88] Z. Yaqoob, D. Psaltis, M. S. Feld, and C. Yang, “Optical phase conjugation for turbidity suppression in biological samples,” *Nat. Photon.* **2**, 110–115 (2008). 7, 105
- [89] I. M. Vellekoop, E. Van Putten, A. Lagendijk, and A. Mosk, “Demixing light paths inside disordered metamaterials,” *Opt. Express* **16**, 67–80 (2008). 7, 105
- [90] X. Xu, H. Liu, and L. V. Wang, “Time-reversed ultrasonically encoded optical focusing into scattering media,” *Nat. Photon.* **5**, 154–157 (2011). 7, 105
- [91] B. Judkewitz, Y. M. Wang, R. Horstmeyer, A. Mathy, and C. Yang, “Speckle-scale focusing in the diffusive regime with time reversal of variance-encoded light (TROVE),” *Nat. Photon.* **7**, 300–305 (2013). 7, 105
- [92] M. Fink, D. Cassereau, A. Derode, C. Prada, P. Roux, M. Tanter, J.-L. Thomas, and F. Wu, “Time-reversed acoustics,” *Rep. Prog. Phys.* **63**, 1933 (2000). 7, 105
- [93] I. M. Vellekoop and A. P. Mosk, “Universal optimal transmission of light through disordered materials,” *Phys. Rev. Lett.* **101**, 120601 (2008). 7, 91, 106
- [94] G. Maret and P. Wolf, “Multiple light scattering from disordered media. the effect of brownian motion of scatterers,” *Zeitschrift für Physik B Condensed Matter* **65**, 409–413 (1987). 8, 120
- [95] D. J. Pine, D. A. Weitz, P. M. Chaikin, and E. Herbolzheimer, “Diffusing wave spectroscopy,” *Physical review letters* **60**, 1134 (1988). 8, 120

- [96] D. A. Boas, L. Campbell, and A. G. Yodh, “Scattering and imaging with diffusing temporal field correlations,” *Physical review letters* **75**, 1855 (1995). 8, 120
- [97] D. A. Boas and A. G. Yodh, “Spatially varying dynamical properties of turbid media probed with diffusing temporal light correlation,” *JOSA A* **14**, 192–215 (1997). 8, 120
- [98] A. P. Gibson, J. C. Hebden, and S. R. Arridge, “Recent advances in diffuse optical imaging,” *Physics in medicine & biology* **50**, R1 (2005). 8, 120
- [99] T. Durduran, R. Choe, W. B. Baker, and A. G. Yodh, “Diffuse optics for tissue monitoring and tomography,” *Reports on Progress in Physics* **73**, 076701 (2010). 8, 120
- [100] E. M. Buckley, A. B. Parthasarathy, P. E. Grant, A. G. Yodh, and M. A. Franceschini, “Diffuse correlation spectroscopy for measurement of cerebral blood flow: future prospects,” *Neurophotonics* **1**, 011009 (2014). 8, 120
- [101] J. Gunther and S. Andersson-Engels, “Review of current methods of acousto-optical tomography for biomedical applications,” *Frontiers of Optoelectronics* **10**, 211–238 (2017). 8, 120
- [102] J. P. Angelo, S.-J. K. Chen, M. Ochoa, U. Sunar, S. Gioux, and X. Intes, “Review of structured light in diffuse optical imaging,” *Journal of biomedical optics* **24**, 071602 (2018). 8, 120
- [103] J. Xu, A. K. Jahromi, and C. Yang, “Diffusing wave spectroscopy: a unified treatment on temporal sampling and speckle ensemble methods,” *APL Photonics* **6**, 016105 (2021). 8, 120, 121
- [104] K. Wapenaar, J. Brackenhoff, and J. Thorbecke, “Green’s theorem in seismic imaging across the scales,” *Solid Earth* **10**, 517–536 (2019). 8, 120
- [105] P. M. Shearer, *Introduction to seismology* (Cambridge university press, 2019). 8, 120
- [106] N. Nakata, L. Gualtieri, and A. Fichtner, *Seismic ambient noise* (Cambridge University Press, 2019). 8, 120
- [107] F. F. Jobsis, “Noninvasive, infrared monitoring of cerebral and myocardial oxygen sufficiency and circulatory parameters,” *Science* **198**, 1264–1267 (1977). 8, 120
- [108] T. Durduran and A. G. Yodh, “Diffuse correlation spectroscopy for non-invasive, micro-vascular cerebral blood flow measurement,” *Neuroimage* **85**, 51–63 (2014). 8, 120

- [109] A. T. Eggebrecht, S. L. Ferradal, A. Robichaux-Viehoever, M. S. Hassanpour, H. Dehghani, A. Z. Snyder, T. Hershey, and J. P. Culver, “Mapping distributed brain function and networks with diffuse optical tomography,” *Nature photonics* **8**, 448–454 (2014). 8, 120
- [110] R. W. Gerchberg and O. W. Saxton, “A practical algorithm for the determination of the phase from image and diffraction plane pictures,” *Optik* **35**, 237–246 (1972). 14
- [111] M. Reicherter, T. Haist, E. U. Wagemann, and H. J. Tiziani, “Optical particle trapping with computer-generated holograms written on a liquid-crystal display,” *Opt. Lett.* **24**, 608–610 (1999). 16
- [112] J. Yoon, K. Lee, J. Park, and Y. Park, “Measuring optical transmission matrices by wavefront shaping,” *Opt. Express* **23**, 10158–10167 (2015). 16, 142
- [113] S. G. Johnson, “The NLOpt nonlinear-optimization package,” *ab-initio. mit.edu/nlopt* (2011). 18
- [114] J. Nocedal, “Updating quasi-Newton matrices with limited storage,” *Math. Comp.* **35**, 773–782 (1980). 18
- [115] R. H. Brown and R. Q. Twiss, “Correlation between photons in two coherent beams of light,” *Nature* **177**, 27–29 (1956). 30
- [116] R. Pecora, *Dynamic light scattering: applications of photon correlation spectroscopy* (Springer Science & Business Media, 2013). 30
- [117] L. Mandel and E. Wolf, *Optical coherence and quantum optics* (Cambridge University, 1995). 30
- [118] E. Akkermans and G. Montambaux, *Mesoscopic Physics of Electrons and Photons* (Cambridge University Press, Cambridge, UK, 2007). 30
- [119] M. J. Stephen and G. Cwilich, “Intensity correlation functions and fluctuations in light scattered from a random medium,” *Phys. Rev. Lett.* **59**, 285–287 (1987). 30
- [120] P. A. Mello, E. Akkermans, and B. Shapiro, “Macroscopic approach to correlations in the electronic transmission and reflection from disordered conductors,” *Phys. Rev. Lett.* **61**, 459–462 (1988). 30, 32
- [121] A. Z. Genack, N. Garcia, and W. Polkosnik, “Long-range intensity correlation in random media,” *Phys. Rev. Lett.* **65**, 2129–2132 (1990). 30
- [122] J. F. de Boer, M. P. van Albada, and A. Lagendijk, “Transmission and intensity correlations in wave propagation through random media,” *Phys. Rev. B* **45**, 658–666 (1992). 30

- [123] F. Scheffold, W. Härtl, G. Maret, and E. Matijević, “Observation of long-range correlations in temporal intensity fluctuations of light,” *Phys. Rev. B* **56**, 10942–10952 (1997). 30
- [124] P. Sebbah, R. Pnini, and A. Z. Genack, “Field and intensity correlation in random media,” *Phys. Rev. E* **62**, 7348–7352 (2000). 30
- [125] G. Cwilich, L. S. Froufe-Pérez, and J. J. Sáenz, “Spatial wave intensity correlations in quasi-one-dimensional wires,” *Phys. Rev. E* **74**, 045603 (2006). 30
- [126] A. Yamilov, “Relation between channel and spatial mesoscopic correlations in volume-disordered waveguides,” *Phys. Rev. B* **78**, 045104 (2008). 30
- [127] S. Feng, C. Kane, P. A. Lee, and A. D. Stone, “Correlations and fluctuations of coherent wave transmission through disordered media,” *Phys. Rev. Lett.* **61**, 834–837 (1988). 30, 91
- [128] T. Strudley, T. Zehender, C. Blejean, E. P. Bakkers, and O. L. Muskens, “Mesoscopic light transport by very strong collective multiple scattering in nanowire mats,” *Nat. Photon.* **7**, 413–418 (2013). 30
- [129] A. Dogariu and R. Carminati, “Electromagnetic field correlations in three-dimensional speckles,” *Phys. Rep.* **559**, 1–29 (2015). 31
- [130] M. I. Akhlaghi and A. Dogariu, “Tracking hidden objects using stochastic probing,” *Optica* **4**, 447–453 (2017). 31, 44, 46
- [131] J. Bertolotti, E. G. van Putten, C. Blum, A. Lagendijk, W. L. Vos, and A. P. Mosk, “Non-invasive imaging through opaque scattering layers,” *Nature* **491**, 232–234 (2012). 31
- [132] J. Mertz, “Optical sectioning microscopy with planar or structured illumination,” *Nat. Methods* **8**, 811–819 (2011). 31, 46, 68
- [133] J. Billy, V. Josse, Z. Zuo, A. Bernard, B. Hambrecht, P. Lugan, D. Clément, L. Sanchez-Palencia, P. Bouyer, and A. Aspect, “Direct observation of Anderson localization of matter waves in a controlled disorder,” *Nature* **453**, 891–894 (2008). 31, 46, 66
- [134] K. Dholakia and T. Čižmár, “Shaping the future of manipulation,” *Nat. Photon.* **5**, 335–342 (2011). 32, 46, 66
- [135] R. Berkovits and S. Feng, “Correlations in coherent multiple scattering,” *Phys. Rep.* **238**, 135–172 (1994). 32
- [136] D. Di Battista, G. Zacharakis, and M. Leonetti, “Enhanced adaptive focusing through semi-transparent media,” *Sci. Rep.* **5**, 17406 (2015). 32

- [137] R. Barakat, “Clipped correlation functions of aperture integrated laser speckle,” *Appl. Opt.* **25**, 3885–3888 (1986). 32
- [138] M. Giglio, M. Carpineti, and A. Vailati, “Space intensity correlations in the near field of the scattered light: A direct measurement of the density correlation function  $g(r)$ ,” *Phys. Rev. Lett.* **85**, 1416–1419 (2000). 32
- [139] A. Labeyrie, “Attainment of diffraction limited resolution in large telescopes by fourier analysing speckle patterns in star images,” *Astron. Astrophys.* **6**, 85–87 (1970). 38
- [140] R. C. Kuhn, O. Sigwarth, C. Miniatura, D. Delande, and C. A. Müller, “Coherent matter wave transport in speckle potentials,” *New J. Phys.* **9**, 161 (2007). 43
- [141] L. Pezzé, M. R. de Saint-Vincent, T. Bourdel, J.-P. Brantut, B. Allard, T. Plisson, A. Aspect, P. Bouyer, and L. Sanchez-Palencia, “Regimes of classical transport of cold gases in a two-dimensional anisotropic disorder,” *New J. Phys.* **13**, 095015 (2011). 43
- [142] M. Robert-de Saint-Vincent, J.-P. Brantut, B. Allard, T. Plisson, L. Pezzé, L. Sanchez-Palencia, A. Aspect, T. Bourdel, and P. Bouyer, “Anisotropic 2D diffusive expansion of ultracold atoms in a disordered potential,” *Phys. Rev. Lett.* **104**, 220602 (2010). 43
- [143] E. Mudry, K. Belkebir, J. Girard, J. Savatier, E. Le Moal, C. Nicoletti, M. Allain, and A. Sentenac, “Structured illumination microscopy using unknown speckle patterns,” *Nat. Photonics* **6**, 312–315 (2012). 45, 68
- [144] S. Dong, P. Nanda, R. Shiradkar, K. Guo, and G. Zheng, “High-resolution fluorescence imaging via pattern illuminated Fourier ptychography,” *Opt. Express* **22**, 20856–20870 (2014). 45, 68
- [145] L.-H. Yeh, L. Tian, and L. Waller, “Structured illumination microscopy with unknown patterns and a statistical prior,” *Biomed. Opt. Express* **8**, 695–711 (2017). 45, 68
- [146] M. Pascucci, S. Ganesan, O. Tripathi, O. Katz, V. Emiliani, and M. Guillon, “Compressive three-dimensional super-resolution microscopy with speckle-saturated fluorescence excitation,” *Nat. Commun.* **10**, 1327 (2019). 46, 66, 68, 88, 89
- [147] M. Leonetti and C. Conti, “Observation of three dimensional optical rogue waves through obstacles,” *Appl. Phys. Lett.* **106**, 254103 (2015). 65
- [148] S. W. Hell and J. Wichmann, “Breaking the diffraction resolution limit by stimulated emission: stimulated-emission-depletion fluorescence microscopy,” *Opt. Lett.* **19**, 780–782 (1994). 67
- [149] S. W. Hell, “Far-field optical nanoscopy,” *Science* **316**, 1153–1158 (2007). 67

- [150] S. W. Hell and M. Kroug, “Ground-state-depletion fluorescence microscopy: a concept for breaking the diffraction resolution limit,” *Appl. Phys. B* **60**, 495–497 (1995). 67
- [151] T. Grotjohann, I. Testa, M. Leutenegger, H. Bock, N. T. Urban, F. Lavoie-Cardinal, K. I. Willig, C. Eggeling, S. Jakobs, and S. W. Hell, “Diffraction-unlimited all-optical imaging and writing with a photochromic GFP,” *Nature* **478**, 204–208 (2011). 67
- [152] M. Hofmann, C. Eggeling, S. Jakobs, and S. W. Hell, “Breaking the diffraction barrier in fluorescence microscopy at low light intensities by using reversibly photoswitchable proteins,” *Proc. Natl. Acad. Sci. U.S.A* **102**, 17565–17569 (2005). 67
- [153] A. Chmyrov, J. Keller, T. Grotjohann, M. Ratz, E. d’Este, S. Jakobs, C. Eggeling, and S. W. Hell, “Nanoscopy with more than 100,000 ‘doughnuts’,” *Nat. Methods* **10**, 737–740 (2013). 67
- [154] E. H. Rego, L. Shao, J. J. Macklin, L. Winoto, G. A. Johansson, N. Kamps-Hughes, M. W. Davidson, and M. G. Gustafsson, “Nonlinear structured-illumination microscopy with a photoswitchable protein reveals cellular structures at 50-nm resolution,” *Proc. Natl. Acad. Sci. U.S.A* **109**, E135–E143 (2012). 67
- [155] M. Pascucci, G. Tessier, V. Emiliani, and M. Guillon, “Superresolution imaging of optical vortices in a speckle pattern,” *Phys. Rev. Lett.* **116**, 093904 (2016). 68, 88
- [156] J. H. Shapiro, “Computational ghost imaging,” *Phys. Rev. A* **78**, 061802 (2008). 68
- [157] O. Katz, Y. Bromberg, and Y. Silberberg, “Compressive ghost imaging,” *Appl. Phys. Lett.* **95**, 131110 (2009). 68
- [158] Y. Bromberg, O. Katz, and Y. Silberberg, “Ghost imaging with a single detector,” *Phys. Rev. A* **79**, 053840 (2009). 68
- [159] J. Min, J. Jang, D. Keum, S.-W. Ryu, C. Choi, K.-H. Jeong, and J. C. Ye, “Fluorescent microscopy beyond diffraction limits using speckle illumination and joint support recovery,” *Sci. Rep.* **3**, 1–6 (2013). 68
- [160] M. Kim, C. Park, C. Rodriguez, Y. Park, and Y.-H. Cho, “Superresolution imaging with optical fluctuation using speckle patterns illumination,” *Sci. Rep.* **5**, 16525 (2015). 68
- [161] H. Yilmaz, E. G. van Putten, J. Bertolotti, A. Lagendijk, W. L. Vos, and A. P. Mosk, “Speckle correlation resolution enhancement of wide-field fluorescence imaging,” *Optica* **2**, 424–429 (2015). 68
- [162] N. Meitav, E. N. Ribak, and S. Shoham, “Point spread function estimation from projected speckle illumination,” *Light Sci. Appl.* **5**, e16048–e16048 (2016). 68

- [163] M. Zhang, H. Chang, Y. Zhang, J. Yu, L. Wu, W. Ji, J. Chen, B. Liu, J. Lu, Y. Liu *et al.*, “Rational design of true monomeric and bright photoactivatable fluorescent proteins,” *Nat. Methods* **9**, 727–729 (2012). 69, 71
- [164] M. R. Dennis, “Topological singularities in wave fields,” Ph.D. thesis, University of Bristol (2001). 81
- [165] W. Wang, S. G. Hanson, Y. Miyamoto, and M. Takeda, “Experimental investigation of local properties and statistics of optical vortices in random wave fields,” *Phys. Rev. Lett.* **94**, 103902 (2005). 81
- [166] S. Zhang and A. Z. Genack, “Statistics of diffusive and localized fields in the vortex core,” *Phys. Rev. Lett.* **99**, 203901 (2007). 81
- [167] L. de Angelis, “The singular optics of random light: a 2D vectorial investigation,” Ph.D. thesis, Delft University of Technology (2018). 81
- [168] X. Hao, C. Kuang, T. Wang, and X. Liu, “Phase encoding for sharper focus of the azimuthally polarized beam,” *Opt. Lett.* **35**, 3928–3930 (2010). 88
- [169] S. Galiani, B. Harke, G. Vicidomini, G. Lignani, F. Benfenati, A. Diaspro, and P. Bianchini, “Strategies to maximize the performance of a STED microscope,” *Opt. Express* **20**, 7362–7374 (2012). 88
- [170] A. P. Mosk, A. Lagendijk, G. Lerosey, and M. Fink, “Controlling waves in space and time for imaging and focusing in complex media,” *Nat. Photon.* **6**, 283–292 (2012). 90, 91
- [171] J.-L. Pichard, N. Zanon, Y. Imry, and A. D. Stone, “Theory of random multiplicative transfer matrices and its implications for quantum transport,” *J. Phys. (France)* **51**, 587–609 (1990). 91, 101
- [172] Z. Shi and A. Z. Genack, “Transmission eigenvalues and the bare conductance in the crossover to anderson localization,” *Phys. Rev. Lett.* **108**, 043901 (2012). 91
- [173] B. L. Altshuler, P. A. Lee, and R. A. Webb, eds., *Mesoscopic Phenomena in Solids* (North Holland, Amsterdam, 1991). 91
- [174] C. W. J. Beenakker and B. Rejaei, “Nonlogarithmic repulsion of transmission eigenvalues in a disordered wire,” *Phys. Rev. Lett.* **71**, 3689–3692 (1993). 91
- [175] R. Berkovits and S. Feng, “Correlations in coherent multiple scattering,” *Phys. Rep.* **238**, 135 – 172 (1994). 91
- [176] M. Caselle, “Distribution of transmission eigenvalues in disordered wires,” *Phys. Rev. Lett.* **74**, 2776–2779 (1995). 91
- [177] C. W. J. Beenakker, *Applications of random matrix theory to condensed matter and optical physics* (Oxford University Press, 2011), chap. 35,36. 91

- [178] M. Kim, W. Choi, C. Yoon, G. H. Kim, and W. Choi, “Relation between transmission eigenchannels and single-channel optimizing modes in a disordered medium,” *Opt. Lett.* **38**, 2994–2996 (2013). 91
- [179] J. Bosch, S. A. Goorden, and A. P. Mosk, “Frequency width of open channels in multiple scattering media,” *Opt. Express* **24**, 26472–26478 (2016). 91
- [180] A. Peña, A. Girschik, F. Libisch, S. Rotter, and A. Chabanov, “The single-channel regime of transport through random media,” *Nat. Commun.* **5**, 1–8 (2014). 91
- [181] R. Sarma, A. Yamilov, S. F. Liew, M. Guy, and H. Cao, “Control of mesoscopic transport by modifying transmission channels in opaque media,” *Phys. Rev. B* **92**, 214206 (2015). 91
- [182] O. S. Ojambati, H. Yılmaz, A. Lagendijk, A. P. Mosk, and W. L. Vos, “Coupling of energy into the fundamental diffusion mode of a complex nanophotonic medium,” *New J. Phys.* **18**, 043032 (2016). 91
- [183] R. Sarma, A. G. Yamilov, S. Petrenko, Y. Bromberg, and H. Cao, “Control of energy density inside a disordered medium by coupling to open or closed channels,” *Phys. Rev. Lett.* **117**, 086803 (2016). 91, 94, 115, 117, 156, 161
- [184] P. Hong, O. S. Ojambati, A. Lagendijk, A. P. Mosk, and W. L. Vos, “Three-dimensional spatially resolved optical energy density enhanced by wavefront shaping,” *Optica* **5**, 844–849 (2018). 91, 115, 117
- [185] A. M. Paniagua-Diaz, A. Ghita, T. Vettenburg, N. Stone, and J. Bertolotti, “Enhanced deep detection of raman scattered light by wavefront shaping,” *Opt. Express* **26**, 33565–33574 (2018). 91
- [186] A. G. Yamilov, R. Sarma, B. Redding, B. Payne, H. Noh, and H. Cao, “Position-dependent diffusion of light in disordered waveguides,” *Phys. Rev. Lett.* **112**, 023904 (2014). 92, 156, 161
- [187] A. A. Lisyansky and D. Livdan, “Influence of internal reflection on correlation of intensity fluctuation in random media,” *Phys. Rev. B* **47**, 14157–14164 (1993). 95
- [188] C. W. Groth, M. Wimmer, A. R. Akhmerov, and X. Waintal, “Kwant: a software package for quantum transport,” *New J. Phys.* **16**, 063065 (2014). 97, 109, 132, 161, 166
- [189] Z. Shi and A. Z. Genack, “Dynamic and spectral properties of transmission eigenchannels in random media,” *Phys. Rev. B* **92**, 184202 (2015). 104
- [190] X. Cheng and A. Z. Genack, “Focusing and energy deposition inside random media,” *Opt. Lett.* **39**, 6324–6327 (2014). 106

- [191] T. Chaigne, O. Katz, A. C. Boccara, M. Fink, E. Bossy, and S. Gigan, “Controlling light in scattering media non-invasively using the photoacoustic transmission matrix,” *Nat. Photon.* **8**, 58–64 (2014). 106
- [192] P. Ambichl, A. Brandstötter, J. Böhm, M. Kühmayer, U. Kuhl, and S. Rotter, “Focusing inside disordered media with the generalized Wigner-Smith operator,” *Phys. Rev. Lett.* **119**, 033903 (2017). 106
- [193] M. Horodyski, M. Kühmayer, A. Brandstötter, K. Pichler, Y. V. Fyodorov, U. Kuhl, and S. Rotter, “Optimal wave fields for micromanipulation in complex scattering environments,” *Nat. Photon.* **14**, 149–153 (2020). 106
- [194] S. Jeong, Y.-R. Lee, W. Choi, S. Kang, J. H. Hong, J.-S. Park, Y.-S. Lim, H.-G. Park, and W. Choi, “Focusing of light energy inside a scattering medium by controlling the time-gated multiple light scattering,” *Nat. Photon.* **12**, 277–283 (2018). 106
- [195] A. Badon, D. Li, G. Lerosey, A. C. Boccara, M. Fink, and A. Aubry, “Smart optical coherence tomography for ultra-deep imaging through highly scattering media,” *Sci. Adv.* **2**, e1600370 (2016). 106
- [196] O. Katz, F. Ramaz, S. Gigan, and M. Fink, “Controlling light in complex media beyond the acoustic diffraction-limit using the acousto-optic transmission matrix,” *Nat. Commun.* **10**, 1–10 (2019). 106
- [197] M. Durand, S. M. Popoff, R. Carminati, and A. Goetschy, “Optimizing light storage in scattering media with the dwell-time operator,” *Phys. Rev. Lett.* **123**, 243901 (2019). 106
- [198] W. Lambert, L. A. Cobus, T. Frappart, M. Fink, and A. Aubry, “Distortion matrix approach for ultrasound imaging of random scattering media,” *Proc. Natl. Acad. Sci. U.S.A* **117**, 14645–14656 (2020). 106
- [199] A. Badon, V. Barolle, K. Irsch, A. C. Boccara, M. Fink, and A. Aubry, “Distortion matrix concept for deep optical imaging in scattering media,” *Sci. Adv.* **6**, eaay7170 (2020). 106
- [200] D. Bouchet, S. Rotter, and A. P. Mosk, “Maximum information states for coherent scattering measurements,” *Nat. Phys.* pp. 1–5 (2021). 106
- [201] V. A. Marchenko and L. A. Pastur, “Distribution of eigenvalues for some sets of random matrices,” *Math. USSR Sbornik* **1**, 457 (1967). 111
- [202] A. Goetschy and A. D. Stone, “Filtering random matrices: the effect of incomplete channel control in multiple scattering,” *Phys. Rev. Lett.* **111**, 063901 (2013). 111, 169, 170, 171

- [203] M. C. van Rossum and T. M. Nieuwenhuizen, “Multiple scattering of classical waves: microscopy, mesoscopy, and diffusion,” *Rev. Mod. Phys.* **71**, 313–371 (1999). 111, 174
- [204] R. Pnini and B. Shapiro, “Fluctuations in transmission of waves through disordered slabs,” *Phys. Rev. B* **39**, 6986–6994 (1989). 112
- [205] R. Sarma, A. Yamilov, P. Neupane, B. Shapiro, and H. Cao, “Probing long-range intensity correlations inside disordered photonic nanostructures,” *Phys. Rev. B* **90**, 014203 (2014). 112, 161, 174
- [206] O. S. Ojambati, A. P. Mosk, I. M. Vellekoop, A. Lagendijk, and W. L. Vos, “Mapping the energy density of shaped waves in scattering media onto a complete set of diffusion modes,” *Opt. Express* **24**, 18525–18540 (2016). 115, 117
- [207] M. Koirala, R. Sarma, H. Cao, and A. Yamilov, “Inverse design of perfectly transmitting eigenchannels in scattering media,” *Phys. Rev. B* **96**, 054209 (2017). 115, 117
- [208] P. Fang, C. Tian, L. Zhao, Y. P. Bliokh, V. Freilikher, and F. Nori, “Universality of eigenchannel structures in dimensional crossover,” *Phys. Rev. B* **99**, 094202 (2019). 115, 117
- [209] A. Yodh and B. Chance, “Spectroscopy and imaging with diffusing light.” *Physics today* **48**, 34–40 (1995). 120
- [210] F. Roddier, *Adaptive Optics in Astronomy* (Cambridge University Press, 1999). 120
- [211] R. Mallart and M. Fink, “Adaptive focusing in scattering media through sound-speed inhomogeneities: The van cittert zernike approach and focusing criterion,” *The Journal of the Acoustical Society of America* **96**, 3721–3732 (1994). 120
- [212] M. J. Booth, “Adaptive optics in microscopy,” *Philosophical Transactions of the Royal Society A: Mathematical, Physical and Engineering Sciences* **365**, 2829–2843 (2007). 120
- [213] J.-L. Robert and M. Fink, “Green’s function estimation in speckle using the decomposition of the time reversal operator: Application to aberration correction in medical imaging,” *The Journal of the Acoustical Society of America* **123**, 866–877 (2008). 120
- [214] A. Aubry and A. Derode, “Random matrix theory applied to acoustic backscattering and imaging in complex media,” *Physical review letters* **102**, 084301 (2009). 120
- [215] A. Aubry and A. Derode, “Multiple scattering of ultrasound in weakly inhomogeneous media: Application to human soft tissues,” *The Journal of the Acoustical Society of America* **129**, 225–233 (2011). 120

- [216] C. Papadacci, M. Tanter, M. Pernot, and M. Fink, “Ultrasound backscatter tensor imaging (bti): analysis of the spatial coherence of ultrasonic speckle in anisotropic soft tissues,” *IEEE transactions on ultrasonics, ferroelectrics, and frequency control* **61**, 986–996 (2014). 120
- [217] S. Shahjahan, A. Aubry, F. Rupin, B. Chassignole, and A. Derode, “A random matrix approach to detect defects in a strongly scattering polycrystal: How the memory effect can help overcome multiple scattering,” *Applied Physics Letters* **104**, 234105 (2014). 120
- [218] S. Kang, S. Jeong, W. Choi, H. Ko, T. D. Yang, J. H. Joo, J.-S. Lee, Y.-S. Lim, Q.-H. Park, and W. Choi, “Imaging deep within a scattering medium using collective accumulation of single-scattered waves,” *Nature Photonics* **9**, 253–258 (2015). 120
- [219] S. Kang, P. Kang, S. Jeong, Y. Kwon, T. D. Yang, J. H. Hong, M. Kim, K.-D. Song, J. H. Park, J. H. Lee, M. J. Kim, K. H. Kim, and W. Choi, “High-resolution adaptive optical imaging within thick scattering media using closed-loop accumulation of single scattering,” *Nature communications* **8**, 1–10 (2017). 120
- [220] W. Lambert, L. A. Cobus, T. Frappart, M. Fink, and A. Aubry, “Distortion matrix approach for ultrasound imaging of random scattering media,” *Proceedings of the National Academy of Sciences* **117**, 14645–14656 (2020). 120
- [221] W. Lambert, L. A. Cobus, M. Couade, M. Fink, and A. Aubry, “Reflection matrix approach for quantitative imaging of scattering media,” *Physical Review X* **10**, 021048 (2020). 120
- [222] K. Aki, “Space and time spectra of stationary stochastic waves, with special reference to microtremors,” *Bulletin of the Earthquake Research Institute* **35**, 415–456 (1957). 121
- [223] J. F. Claerbout, “Synthesis of a layered medium from its acoustic transmission response,” *Geophysics* **33**, 264–269 (1968). 121
- [224] T. L. Duvall, S. Jefferies, J. Harvey, and M. Pomerantz, “Time–distance helioseismology,” *Nature* **362**, 430–432 (1993). 121
- [225] J. Rickett and J. Claerbout, “Acoustic daylight imaging via spectral factorization: Helioseismology and reservoir monitoring,” *The leading edge* **18**, 957–960 (1999). 121
- [226] K. Wapenaar, D. Draganov, J. Thorbecke, and J. Fokkema, “Theory of acoustic daylight imaging revisited,” in “SEG Technical Program Expanded Abstracts 2002,” (Society of Exploration Geophysicists, 2002), pp. 2269–2272. 121
- [227] M. Campillo and A. Paul, “Long-range correlations in the diffuse seismic coda,” *Science* **299**, 547–549 (2003). 121

- [228] A. Derode, E. Larose, M. Tanter, J. De Rosny, A. Tourin, M. Campillo, and M. Fink, “Recovering the green’s function from field-field correlations in an open scattering medium (I),” *The Journal of the Acoustical Society of America* **113**, 2973–2976 (2003). 121
- [229] R. Snieder, “Extracting the green’s function from the correlation of coda waves: A derivation based on stationary phase,” *Physical Review E* **69**, 046610 (2004). 121
- [230] N. M. Shapiro, M. Campillo, L. Stehly, and M. H. Ritzwoller, “High-resolution surface-wave tomography from ambient seismic noise,” *Science* **307**, 1615–1618 (2005). 121
- [231] P. Roux, K. G. Sabra, W. A. Kuperman, and A. Roux, “Ambient noise cross correlation in free space: Theoretical approach,” *The Journal of the Acoustical Society of America* **117**, 79–84 (2005). 121
- [232] K. G. Sabra, P. Gerstoft, P. Roux, W. Kuperman, and M. C. Fehler, “Extracting time-domain green’s function estimates from ambient seismic noise,” *Geophysical Research Letters* **32** (2005). 121
- [233] E. Larose, L. Margerin, A. Derode, B. van Tiggelen, M. Campillo, N. Shapiro, A. Paul, L. Stehly, and M. Tanter, “Correlation of random wavefields: An interdisciplinary review,” *Geophysics* **71**, SI11–SI21 (2006). 121
- [234] G. Bensen, M. Ritzwoller, and N. M. Shapiro, “Broadband ambient noise surface wave tomography across the united states,” *Journal of Geophysical Research: Solid Earth* **113** (2008). 121
- [235] D. Draganov, X. Campman, J. Thorbecke, A. Verdel, and K. Wapenaar, “Reflection images from ambient seismic noise,” *Geophysics* **74**, A63–A67 (2009). 121
- [236] F.-C. Lin, M. H. Ritzwoller, and R. Snieder, “Eikonal tomography: surface wave tomography by phase front tracking across a regional broad-band seismic array,” *Geophysical Journal International* **177**, 1091–1110 (2009). 121
- [237] R. L. Weaver and O. I. Lobkis, “Ultrasonics without a source: Thermal fluctuation correlations at mhz frequencies,” *Physical Review Letters* **87**, 134301 (2001). 121
- [238] O. I. Lobkis and R. L. Weaver, “On the emergence of the green’s function in the correlations of a diffuse field,” *The Journal of the Acoustical Society of America* **110**, 3011–3017 (2001). 121
- [239] G. Dietsche, M. Ninck, C. Ortoff, J. Li, F. Jaillon, and T. Gisler, “Fiber-based multispeckle detection for time-resolved diffusing-wave spectroscopy: characterization and application to blood flow detection in deep tissue,” *Applied optics* **46**, 8506–8514 (2007). 121

- [240] W. Zhou, O. Kholiqov, S. P. Chong, and V. J. Srinivasan, “Highly parallel, interferometric diffusing wave spectroscopy for monitoring cerebral blood flow dynamics,” *Optica* **5**, 518–527 (2018). 121
- [241] E. J. Sie, H. Chen, E.-F. Saung, R. Catoen, T. Tieceke, M. A. Chevillet, and F. Marsili, “High-sensitivity multispeckle diffuse correlation spectroscopy,” *Neurophotonics* **7**, 035010 (2020). 121
- [242] J. Xu, A. K. Jahromi, J. Brake, J. E. Robinson, and C. Yang, “Interferometric speckle visibility spectroscopy (isvs) for human cerebral blood flow monitoring,” *APL Photonics* **5**, 126102 (2020). 121
- [243] W. Liu, R. Qian, S. Xu, P. Chandra Konda, J. Jönsson, M. Harfouche, D. Borycki, C. Cooke, E. Berrocal, Q. Dai *et al.*, “Fast and sensitive diffuse correlation spectroscopy with highly parallelized single photon detection,” *APL Photonics* **6**, 026106 (2021). 121
- [244] W. Cui, C. Kumar, and B. Chance, “Experimental study of migration depth for the photons measured at sample surface,” in “Time-Resolved Spectroscopy and Imaging of Tissues,” , vol. 1431 (International Society for Optics and Photonics, 1991), vol. 1431, pp. 180–191. 121, 126
- [245] P. N. den Outer, T. M. Nieuwenhuizen, and A. Lagendijk, “Location of objects in multiple-scattering media,” *J. Opt. Soc. Am. A* **10**, 1209–1218 (1993). 125
- [246] A. Yamilov, S. Petrenko, R. Sarma, and H. Cao, “Shape dependence of transmission, reflection, and absorption eigenvalue densities in disordered waveguides with dissipation,” *Phys. Rev. B* **93**, 100201(R) (2016). 161
- [247] D. S. Fisher and P. A. Lee, “Relation between conductivity and transmission matrix,” *Phys. Rev. B* **23**, 6851–6854 (1981). 169
- [248] P. A. Mello, “Averages on the unitary group and applications to the problem of disordered conductors,” *J. Phys. A* **23**, 4061–4080 (1990). 173